TUNING THE ELECTRONIC AND SPINTRONIC PROPERTIES OF GRAPHENE BY DOPING AND ATOM ADSORPTION

ALEXANDRE PACHOUD

(*M.ASt in Physics, University of Cambridge*)

A THESIS SUBMITTED

FOR THE DEGREE OF DOCTOR OF PHILOSOPHY

GRADUATE SCHOOL FOR INTEGRATIVE SCIENCES AND ENGINEERING

NATIONAL UNIVERSITY OF SINGAPORE

(2014)

DECLARATION

I hereby declare that the thesis is my original work and it has been written by me in its entirety.

I have duly acknowledged all the sources of information which have been used in the thesis.

This thesis has also not been submitted for any degree in any university previously.

Alexandre Pachoud

29 January 2014

ACKNOWLEDGEMENTS

I wish to thank Professor Barbaros Özyilmaz for his supervision of the experimental side of my research. He patiently introduced me to the world of experimental physics, which was not a small task given my previous inexperience in this field. Thanks to his support, I gained a much better understanding of the constraints inherent to real samples and equipments. I believe this will help me for the rest of my career.

I am also grateful to Professor Antonio Castro Neto for his supervision of the theoretical aspects of my work. Working under him was a privilege, due to his broad knowledge and deep understanding of a multitude of topics.

Special thanks to Doctor Aires Ferreira, whose guidance, enthusiasm, and pedagogical skills were critical for my research. I am certain he will become a great Professor. I am also extremely grateful to Doctor Manu Jaiswal, who basically taught me much of what I know in experimental physics. Working with him was very stimulating.

I am especially indebted to my colleague and friend Fabio Hipolito, whose support was key to this thesis. Having him as a colleague also made my coffee breaks more interesting.

Many thanks to Professor Kian Ping Loh and Doctor Yu Wang for their help with sample preparation.

I also wish to thank my colleagues Doctor Jayakumar Balakrishnan, Mr Gavin Kok Wai Koon, Mr Chee Tat Toh, Dr Jong Hak Lee, Ms Kaiwen Zhang, Mr Zhao Xiangming, Mr Ahmet Ahmet Avsar, Mr Henrik Andersen, Mr Wu Jing, Mr Orhan Kahya, Dr. Ajit Patra, Dr. Surajit Saha, Dr. Lanfei Xie, Dr. Guangxin Ni, Dr. Miguel Dias Costa, Dr Alexandre Carvalho, Dr Dario Bahamon, Dr. Gareth Wyn Jones, Dr Hennrik Schmidt, Dr. Jeil Jung, Dr. Joao Nuno Rodrigues, Dr. Li Linjun, Dr. Mirco Milletari, Ms. Lidia Carvalho Gomes, Mr. Manuel Rodrigues for their countless interactions and support.

Contents

ABSTRACT

The work described in this thesis reports on the possibilities of tuning the electronic and spintronic properties of graphene by doping and atom adsorption. Novel experimental and theoretical results are presented, showing how deeply graphene properties can be transformed. In a first part, we study graphene doped to ultra-high charge carrier density regimes by means of a polymer-electrolyte gating technique. We show how the temperature-dependence of the resistivity is affected by large Fermi energies. Possible implications for intrinsic superconductivity in graphene are discussed. In a second part, we show how graphene, a very good conductor in its pristine form, can be turned into a granular metal by chemical functionalization. We report the observation of multiple inelastic and elastic co-tunneling conduction mechanisms such granular graphene systems, fabricated by hydrogenation of free-standing graphene sheets. Even though multiple inelastic co-tunneling has already been observed in conventional granular metals, this is, to the best of our knowledge, the first time multiple elastic co-tunneling is observed. These conduction mechanisms comprising series of virtual tunneling events, show deviations from established theories. However, they are consistent with a theory developed for granular Dirac materials, and presented in this thesis. Finally, we theoretically study the modifications of graphene's spintronic properties by atom adsorption. We show that atoms adsorbed in hollow position can lead to the appearance of strong and gate-tunable Spin Hall Effect, while certain atoms adsorbed on graphene in top-position can induce a large Anomalous Hall Effect.

List of Figures

LIST OF PUBLICATIONS AND MANUSCRIPTS

[1] A. Pachoud, M. Jaiswal, Y. Wang, B-H. Hong, J-H. Ahn, K.P. Loh, and B. Özyilmaz, *Multiple Virtual*
Tunneling of Dirac Fermions in Granular Graphene, Nature Scientific Reports **3**, 3404 (2013).

[2] A. Pachoud, A. Ferreira and A.H. Castro Neto, *Ultra-Sensitivity of Graphene's Dirac Fermions to Atomic-*
Scale Shapes, Physical Review Letters (to be submitted).

[3] A. Pachoud, A. Ferreira and A.H. Castro Neto, *Scattering theory of SO-active adatoms on graphene*,
Physical Review B (to be submitted).

[4] G.X. Ni, Y. Zheng, S. Bae, H.R. Kim, A. Pachoud, Y.S. Kim, C.L. Tan, D. Im, J-H. Ahn, B.H. Hong, and
B. Özyilmaz, *Quasi-Periodic Nanoripples in Graphene Grown by Chemical Vapor Deposition and Its Impact*
on Charge Transport, ACS Nano, **6**, 1158 (2012).

[5] T.Y. Yang, J. Balakrishnan, F. Volmer, A. Avsar, M. Jaiswal, J. Samm, S.R. Ali, A. Pachoud, M. Zeng,
M. Popinciuc, G. Guntherodt, B. Beschoten, and B. Özyilmaz, *Observation of Long Spin-Relaxation Times*
in Bilayer Graphene at Room Temperature, Physical Review Letters, **107**, 047206 (2011).

[6] A. Pachoud, M. Jaiswal, P.K. Ang, K.P. Loh, and B. Özyilmaz, *Graphene transport at high carrier densities*
using a polymer electrolyte gate, Europhysics Letters **92**, 27001 (2010).

Chapter 1

Introduction

1.1 Graphene, versatile material

Graphene [1], an atomically-thin two-dimensional hexagonal lattice of carbon atoms is known for its high room-temperature mobility, its transparency, and the exotic quantum phenomena it hosts [2], from Klein tunneling [3] to anomalous quantum Hall effect [4]. It is also the strongest material ever measured [6], and yet is flexible and elastic. Due to its low intrinsic spin-orbit coupling, graphene is widely seen as a possible high-performance spin-preserving wire for spintronic applications. Novel two-dimensional heterostructures combining graphene with other two-dimensional crystals [7] such as boron nitride and molybdenum disulfide led to new interesting phenomena such as Dirac fermions cloning [8]. Some of these multi-layer structures also exhibit strong Coulomb drag phenomena [9] and enhanced light-matter interactions for photovoltaic applications [10]. Novel transistors based on vertical graphene heterostructures [10, 11, 12, 13] with high on/off ratio [11] or negative differential conductance [12] were recently demonstrated. The list of possibilities offered by graphene alone or combined with other two-dimensional crystals in heterostructures is really impressive and impossible to fully cover in an introductory chapter or even the entire thesis. However, the characteristics we already mentioned illustrate

how versatile graphene can be, promising applications in many fields such as electronics, spintronics, optics, mechanical engineering, and opto-electronics.

1.2 Graphene, chameleon material

In spite of the rich physics of graphene and all its promised applications, the "Wonder Material" has its shortcomings. Its tiny spin-orbit coupling may make it a good candidate as wire for spin transmission, it cannot be used as active material for spin-processing in its pristine form. Moreover, the vanishingly small density of states [2] in quasi-neutral graphene makes it an unlikely host of many interesting correlated electron states. Last but not least, the ability of graphene Dirac fermions to Klein-tunnel [3] through potential barriers makes it hard to fabricate conventional horizontal transistors and large, scalable two-dimensional arrays of quantum dots, which combined with graphene natural transparency, bendability and elasticity would enable exciting flexible electronics and strain-sensing applications. Though a possible route to compensate these disadvantages may involve the fabrication of novel Van Der Waals heterostructures [7], it is worth exploring methods which at the time of writing seem simpler, such as ultra-high doping by polymer-electrolyte gating techniques, or the adsorption of various atoms on the graphene scaffold to transform graphene properties at will. This approach is the object of the present thesis. Before describing our results in the following chapters, we briefly summarize the basic experimental techniques used to fabricate and characterize graphene samples, as they will frequently be refered to in the remainder of our thesis.

1.3 Basic experimental techniques to fabricate and characterize graphene devices

1.3.1 Exfoliation from graphite

Graphene is an abundant and natural material, which can be extracted from graphite by exfoliation. The realization that this could be achieved by extremely simple means allowed scientists to intensively study this atomically-thin material, since 2004. The method [1], known as "Scotch tape technique", consists in the following steps:

(i) Insert a thin piece of graphite between two adhesive tapes - sticky faces on graphite.
(ii) Peel the tapes off. Thinner graphite flakes are now on both tapes.
(iii) Select the tape with the thinnest flakes, and cover it with another adhesive tape.
(iv) Repeat steps (i), (ii), and (iii) until resulting tapes contain transparent graphite flakes.
(v) Apply a tape with transparent flakes on a Si/SiO_2wafer.
(vi) Gently rub the upper face of the tape with a tweezer for few minutes.
(vii) Peel the tape off

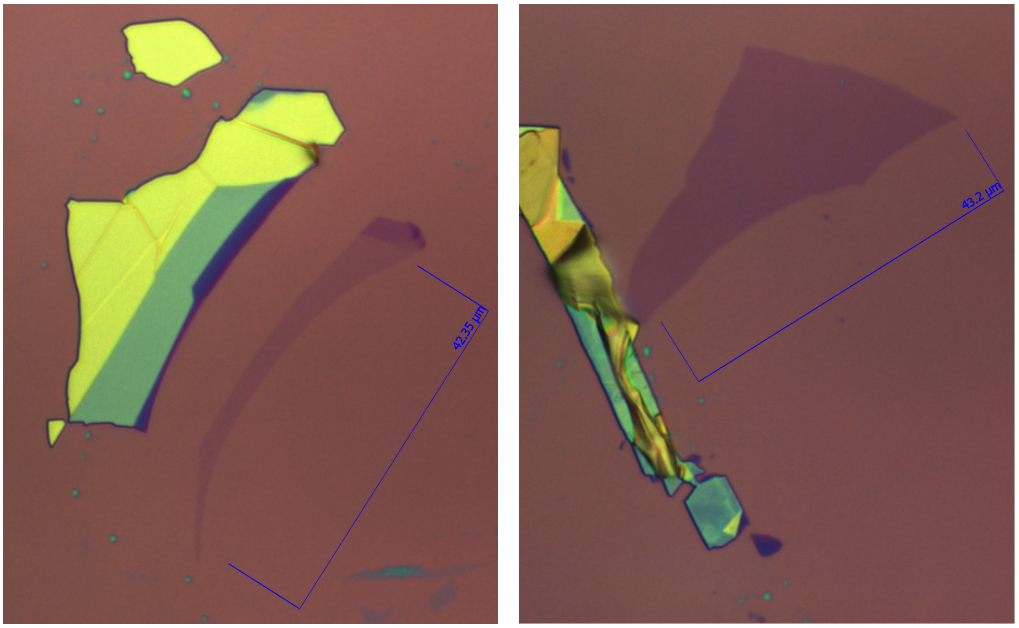

Figure 1.3.1: Optical pictures of exfoliated single-layer (left) and bilayer (right) graphene on a SiO_2/Si wafer, with a 300 nm-thick silicon oxide layer.

If done well, steps (i) to (vii) leave many few-layer graphite flakes on the silicon oxide surface. Some of these flakes are even monolayer graphite, i.e. graphene. Critically, graphene layers are visible under conventional optical microscopes for wafers with silicon oxide layers with a thickness of ≈ 90 nm or ≈ 300 nm [29]. This is the reason why these thicknesses are often selected in practice (and in all the experiments reported in this thesis!). Typical optical pictures of graphene and bilayer graphene obtained by exfoliation from graphite are shown in Figure 1.3.1.

1.3.2 Chemical Vapour Deposition

While the "Scotch tape technique" allowed the number of academic works on graphene to quickly grow, this method can not be used for industrial production, given its extremely small yield. For this reason, chemical vapour deposition (CVD) methods have be developed [89], to produce large-area graphene in a systematic way. Typically, graphene is grown at high temperature (~ 1000 °C) on metallic substrates such as copper [89] and nickel [19]. In order to fabricate graphene-based transistors or other devices, the substrate is then chemically

etched away, and graphene is transferred onto an insulator such as silicon oxide.

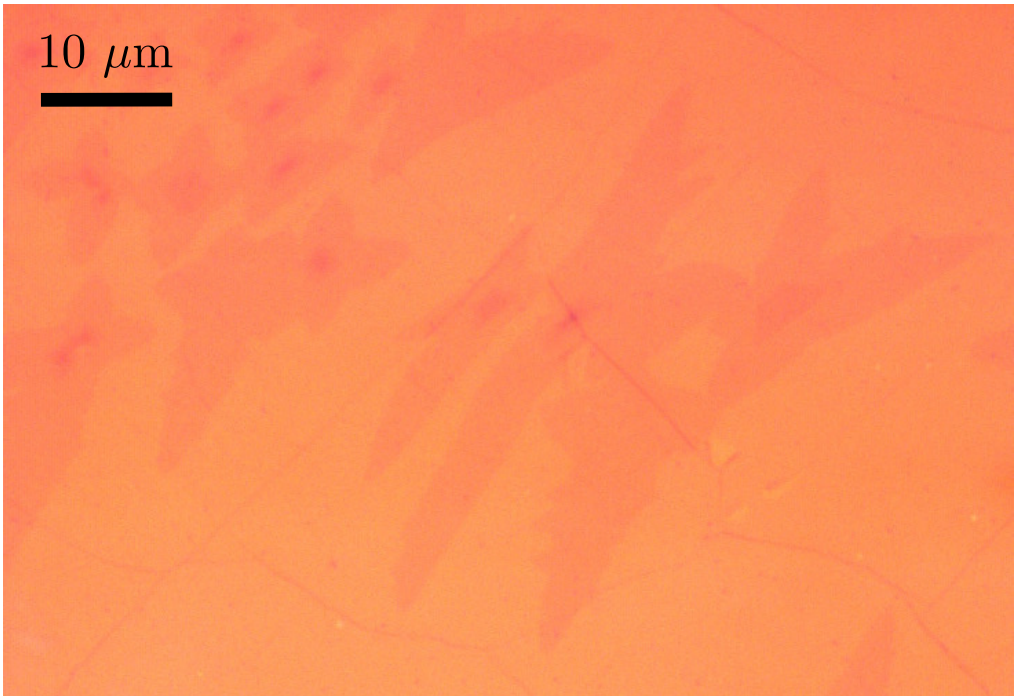

Figure 1.3.2: CVD graphene (background) entirely covering a SiO_2/Si wafer. Some "islands" of multilayer graphene are visible.

Figure 1.3.2 shows an optical picture of CVD graphene grown on copper and transferred on a SiO_2/Si wafer. Many variations of this method to grow and transfer CVD graphene exist and have been reported by many authors.

1.3.3 Electron beam lithography

After selecting suitable graphene samples either prepared by exfoliation from graphite or chemical vapor deposition, we may fabricate devices for electron transport experiments. These devices usually consist in graphene channels contacted with gold/chromium electrodes, and lie on a SiO_2/Si wafer. A voltage bias V_g between the p-doped silicon layer and the gold/chromium electrodes allows to tune the graphene Fermi level, while graphene's conductance is measured with the electrodes. Fabrication methods for these devices are standard, and typically employ electron-beam lithography. Here, we summarize the fabrication process used for the work presented in this thesis.

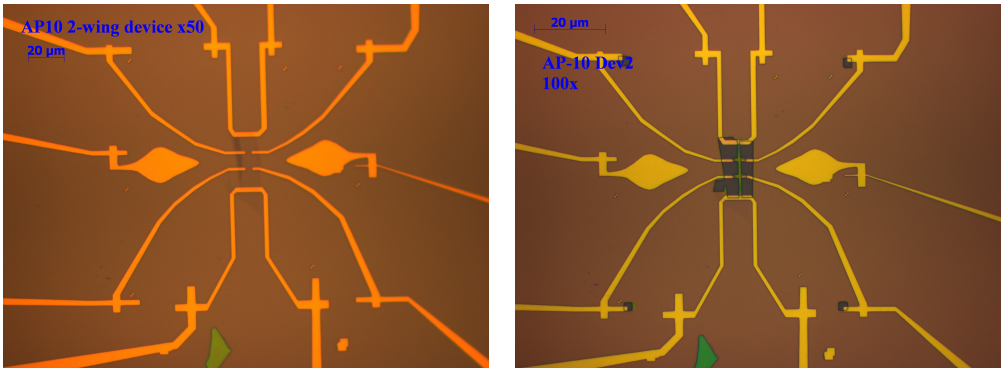

Figure 1.3.3: Typical graphene device fabricated by standard electron-beam lithography, after gold/chromium evaporation and lift-off (left picture). The graphene flake is then etched into a proper Hall bar by writting a PMMA etch-mask (right) with electron-beam lithography and subsequently exposing the sample to oxygen plasma.

We first spin-coat poly-methyl methacrylate (PMMA) on the silicon oxide wafer, and then shine an electron-beam around the area of interest (a graphene flake for instance). At this stage, the region of PMMA exposed to the electron-beam is an array of symbols, called alignement markers. PMMA being a positive photoresist, a subsequent bath of methyl isobutyl ketone (MIBK) and isopropyl alcohol (IPA) leads to the removal of the exposed PMMA region. Patterning these alignment markers is particularly useful. With them carved on the spin-coated PMMA film, we are equipped with a frame relative to which electrodes can be patterned. This approach generally improves the device patterning precision greatly. Next, optical pictures of the graphene sample together with clearly visible alignment markers are taken, and used to design the device electrodes with the Design CAD software. Created design files are then loaded to the nanometer pattern generator (NPGS) software driving the electron-beam setup (we use a FEI Nano SEM 230). The electron-beam is then projected on the wafer, along the designed electrodes. After this second electron-beam step, the wafer is bathed in a MIBK/IPA solution again for development. We end up with a patterned PMMA film on the graphene/SiO_2/Si system. If everything went well, these patterns have the desired electrode shapes. Subsequent thermal evaporation of chromium and gold, followed by a lift-off step (consisting

in leaving the wafer in acetone more than 10 hours) then yields a graphene device with its electrodes. An optical picture of a typical device after lift-off is shown in Figure 1.3.3(a). To give the graphene channel a proper geometry (a Hall bar for instance), a step of oxygen-plasma etching might be needed. In this case, a third elecron-beam step is needed to fabricate a protective PMMA mask, as shown in Figure 1.3.3(b).

1.3.4 Raman spectroscopy

Raman spectroscopy is a powerful characterization method. This versatile technique is very popular among graphene physicists [14], and is used to measure important properties of fabricated samples such as the number of graphene layers in ultra-thin graphite films [15], crystallinity [97, 99], density of charges [31], and degree of mechanical strain [16]. Covering all possible applications of Raman spectroscopy to graphene goes beyond the scope of this section and the present thesis. We will nonetheless summarize key results on Raman spectroscopy applied to graphene.

Typical Raman measurements consist in shining a laser of frequency ν_i on a sample. Incidents photons excite some electrons in the sample, which then may experience scattering events with phonons and/or defects before recombining with a hole while emitting a photon of frequency ν_f. These outgoing photons are detected by the Raman setup, which measures the intensity of outgoing light $\mathcal{I}_{Raman}$ as a function $\nu_f - \nu_i$. The $\mathcal{I}_{Raman}(\nu_f - \nu_i)$ spectrum is a footprint of the sample which reflects important scattering mechanisms. These scattering events give rise to characteristic peaks in the $\mathcal{I}_{Raman}(\nu_f - \nu_i)$ spectrum and can thus be identified.

We now list key scattering events probed by a Raman measurement of single-layer graphene. We first start with scattering processes yielding the most visible peaks in graphene Raman spectra, called G, $2D$ and $2D'$ peaks corresponding to $\nu_f - \nu_i \approx 1580$ cm^{-1}, $\nu_f - \nu_i \approx 2700$ cm^{-1} and $\nu_f - \nu_i \approx 3240$

cm^{-1} respectively. The G-peak arises from scattering of laser-excited electrons with low-momentum phonon modes situated in the Brilloin zone centre [18] and of energy ~ 1580 cm^{-1}. The $2D$- and $2D'$- peaks originate from higher-order scattering processes involving two phonons [15, 17]. Scattering with two phonons of energy $\omega \sim 1350$ cm^{-1}(respectively $\omega' \sim 1620$ cm^{-1}) and with opposite momenta before electron-hole recombination leads to the $2D$-peak (respectively $2D'$-peak), located at $\nu_f - \nu_i = 2\omega$ (respecively $\nu_f - \nu_i = 2\omega'$). The G-, $2D$- and $2D'$-peaks are measured in pristine graphene. Additional peaks can be observed in Raman spectra of defective graphene, where other Raman processes are possible. These peaks are called D and D' and require excited electrons to experience scattering with both a phonon and a defect [15, 17]. More precisely, the D-peak (respectively D'-peak) arises from scattering of excited electrons with a phonon of energy $\omega \sim 1350$ cm^{-1}(respectively $\omega' \sim 1620$ cm^{-1}) and high-momentum $\vec{q}$ (respectively low-momentum $\vec{q}$) followed by inter-valley (respectively intra-valley) scattering due to an impurity, prior to electron-hole recombination. The D- and D'-peaks, located at $\nu_f - \nu_i = \omega$ and $\nu_f - \nu_i = \omega'$ are important to analyse the crystallinity of graphene samples, as these peak allow to estimate the amount of defects. Such a method will be used later in this thesis.

1.3.5 Electron transport measurements in a Variable Temperature Insert (VTI) coupled with a magnet

The electron transport data presented in this thesis are measured at variable temperatures and magnetic fields. Temperatures typically range from ~ 2 K up to room temperature, while the magnetic field can be tuned between -9T and 9T. In order to perform these measurements, we load our devices inside a vacuum probe. The probe is then introduced in a variable-temperature insert cryostat coupled to a superconducting magnet. Electrometers, resistance meters, voltage and current sources, as well as lock-in amplifiers are electrically

connected to the probe, itself connected to our nanofabricated devices by wire-bonding.

Chapter 2

Transport properties of graphene at high electron densities

2.1 Electronic structure of graphene

Graphene is a honeycomb lattice of carbon atoms comprising two inequivalent triangular sublattices, A and B. Within a first-nearest neighbor tight-binding model, one can easily calculate the valence and conduction bands of graphene π-electrons. These results are well-documented and known to all graphene physicists [20, 2]. For the sake of presenting a self-contained thesis, we will nonetheless briefly rederive them, starting from graphene Hamiltonian

$$H_0 = -t \sum_{\langle i,j \rangle} (a_i^\dagger b_j + b_j^\dagger a_i) \tag{2.1.1}$$

where $t \approx 2.7$ eV is graphene first-nearest neighbor hopping integral, $a_i^\dagger$ and $b_i^\dagger$ create an electron in site i of the A and B sublattices. In equation 2.1.1, $\langle i, j \rangle$ refers to neighboring sites i and j belonging to the A and B sublattice respectively. Noting $\vec{\alpha}_i$ (respectively $\vec{\beta}_j$) the position vector corresponding site

$i \in A$ (respectively $j \in B$), and N the number of carbon atoms in each sublattice, operators a_i ans b_i can be written as

$$a_i = \frac{1}{\sqrt{N}} \sum_{\vec{k}} e^{-i\vec{k}.\vec{\alpha}_i} a_{\vec{k}} \tag{2.1.2}$$

$$b_i = \frac{1}{\sqrt{N}} \sum_{\vec{k}} e^{-i\vec{k}.\vec{\beta}_i} b_{\vec{k}} \tag{2.1.3}$$

where $a^\dagger_{\vec{k}}$ and $b^\dagger_{\vec{k}}$ create an electron of momentum $\vec{k}$ in the A and B sublattice respectively. Using equations 2.1.2 and 2.1.3 we can diagonalise H_0 in momentum space.

$$\begin{aligned} H_0 &= -\frac{t}{N} \sum_{\vec{k}} \sum_{\langle i,j \rangle} \left[e^{-i\vec{k}.(\vec{\beta}_j - \vec{\alpha}_i)} a^\dagger_{\vec{k}} b_{\vec{k}} + e^{i\vec{k}.(\vec{\beta}_j - \vec{\alpha}_i)} b^\dagger_{\vec{k}} a_{\vec{k}} \right] \\ &= \sum_{\vec{k}} \left[\phi^*(\vec{k}) a^\dagger_{\vec{k}} b_{\vec{k}} + \phi(\vec{k}) b^\dagger_{\vec{k}} a_{\vec{k}} \right] \end{aligned} \tag{2.1.4}$$

where

$$\phi(\vec{k}) = -t \sum_{l=1,2,3} e^{i\vec{k}.\vec{\delta}_l} \tag{2.1.5}$$

In equation 2.1.5, vectors $\vec{\delta}_l$ connect an atom of the A-sublattice to its nearest neighbors. Noting $\vec{e}_x$ and $\vec{e}_y$ unit vectors along the zig-zag and armchair directions forming a direct basis, we have $\vec{\delta}_1 = \frac{a_0}{2}(\sqrt{3}\vec{e}_x + \vec{e}_y)$, $\vec{\delta}_2 = \frac{a_0}{2}(-\sqrt{3}\vec{e}_x + \vec{e}_y)$ and $\vec{\delta}_3 = -a_0\vec{e}_y$, where $a_0 \approx 1.42$ Å is the distance between nearest carbon atoms. The quadratic form $\mathcal{Q}(\vec{k}) = \phi^*(\vec{k}) a^\dagger_{\vec{k}} b_{\vec{k}} + \phi(\vec{k}) b^\dagger_{\vec{k}} a_{\vec{k}}$ can easily be written as

$$\begin{aligned} \mathcal{Q}(\vec{k}) &= |\phi(\vec{k})| \left(\frac{a_{\vec{k}} + \frac{\phi^*(\vec{k})}{|\phi(\vec{k})|} b_{\vec{k}}}{\sqrt{2}} \right)^\dagger \left(\frac{a_{\vec{k}} + \frac{\phi^*(\vec{k})}{|\phi(\vec{k})|} b_{\vec{k}}}{\sqrt{2}} \right) \\ &- |\phi(\vec{k})| \left(\frac{a_{\vec{k}} - \frac{\phi^*(\vec{k})}{|\phi(\vec{k})|} b_{\vec{k}}}{\sqrt{2}} \right)^\dagger \left(\frac{a_{\vec{k}} - \frac{\phi^*(\vec{k})}{|\phi(\vec{k})|} b_{\vec{k}}}{\sqrt{2}} \right) \end{aligned} \tag{2.1.6}$$

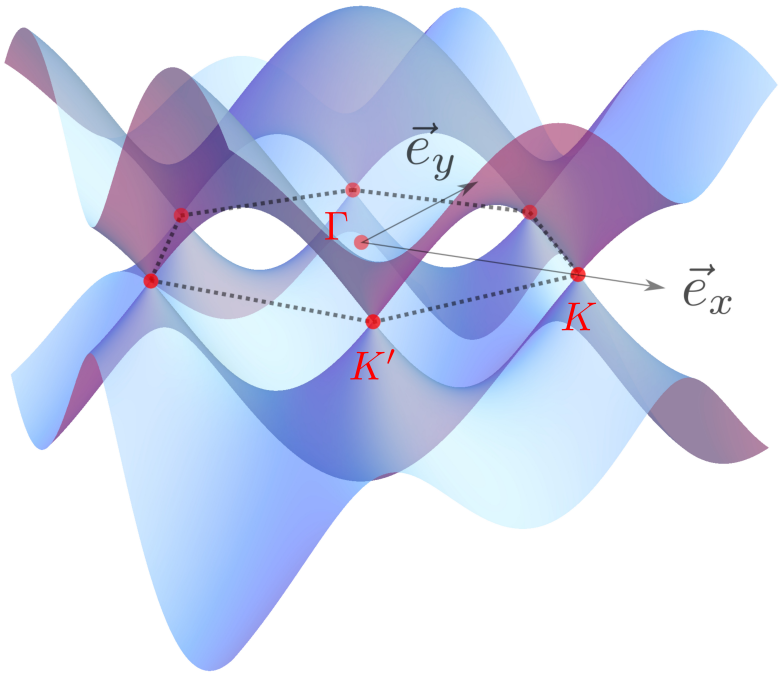

Figure 2.1.1: Graphene single-electron energy spectrum. K and K' points are indicated, as well as the Γ-point, the Brillouin zone centre.

providing a natural diagonalisation basis for H_0 where $\mathcal{E}_\pm(\vec{k}) = \pm|\phi(\vec{k})|$ are the conduction $(+)$ and valence $(-)$ band energy dispersion relations. Correspondingly, operators

$$\Psi_{\pm,\vec{k}} = \frac{a_{\vec{k}} \pm \frac{\phi^*(\vec{k})}{|\phi(\vec{k})|} b_{\vec{k}}}{\sqrt{2}} \tag{2.1.7}$$

annihilate a quasi-particle of crystal momentum $\vec{k}$ and energy $\mathcal{E}_\pm(\vec{k})$. Using explicit forms for vectors $\vec{\delta}_l$, we obtain

$$\mathcal{E}_\pm(\vec{k}) = \pm t\sqrt{3 + 2\cos(\sqrt{3}a_0 k_x) + 4\cos(\frac{\sqrt{3}}{2}a_0 k_x)\cos(\frac{3}{2}a_0 k_y)} \tag{2.1.8}$$

Energy bands $\mathcal{E}_\pm(\vec{k})$ are plotted in Figure 2.1.1, where it can be seen that conduction and valence bands meet at the corners of the Brillouin zone. The two inequivalent corners, the K and K' points, are called Dirac points, because in their vicinity, $\mathcal{E}_\pm(\vec{k})$ have a conic geometry, similarly to the dispersion relation

of relativistic Dirac particles. More precisely, for vectors $\vec{q}$ of norm much smaller than $1/a_0$, we have

$$\phi(\lambda\overrightarrow{\Gamma K} + \vec{q}) = \lambda\hbar v_F q e^{i\lambda\theta} \tag{2.1.9}$$

$$\mathcal{E}_{\pm}(\lambda\overrightarrow{\Gamma K} + \vec{q}) = \pm\hbar v_F q \tag{2.1.10}$$

where $\lambda = \pm 1$ is the valley index, θ is the angle between $\vec{q}$ and $\overrightarrow{\Gamma K}$, and $v_F = 3a_0 t/2\hbar$ is the Fermi velocity. For a band index $s = \pm 1$ and a valley index $\lambda = \pm 1$, corresponding eigensates describing the so-called graphene Dirac fermions read

$$\Psi^{\dagger}_{s,\lambda\overrightarrow{\Gamma K}+\vec{q}}|0\rangle = \frac{a^{\dagger}_{\vec{k}} + s\frac{\phi(\vec{k})}{|\phi(\vec{k})|}b^{\dagger}_{\vec{k}}}{\sqrt{2}}|0\rangle = \frac{|A,\vec{k}\rangle + s.\lambda e^{i\lambda\theta}|B,\vec{k}\rangle}{\sqrt{2}} \tag{2.1.11}$$

where $|A,\vec{k}\rangle = a^{\dagger}_{\vec{k}}|0\rangle$ and $|B,\vec{k}\rangle = b^{\dagger}_{\vec{k}}|0\rangle$. Most of the interesting phenomena in graphene, such as Klein tunneling [3] and anomalous quantum Hall effect [4], arise from its linear dispersion relation 2.1.10 and corresponding Dirac fermion states 2.1.11. Due to graphene linear spectrum, its charge carriers have zero effective mass in the low-energy limit, which makes graphene an ideal platform for the observation of Bose-Einstein condensates of excitons at high temperatures [21]. However, this also means that neutral graphene is not an intrinsic superconductor due to a linearly vanishing density of states at low energy ϵ,

$$\mathcal{D}(\epsilon) = \frac{2}{\pi}\frac{\epsilon}{(\hbar v_F)^2} \tag{2.1.12}$$

making the BCS critical temperature

$$T_c(\epsilon) = 1.14\Theta_D e^{-1/\mathcal{D}(\epsilon)V_{e-ph}}, \tag{2.1.13}$$

where V_{e-ph} is the electron-phonon coupling, exponentially small in spite of graphene's exceptionnally high Debye temperature $\Theta_D \approx 2300$ K.

Nonethelss, it is worth noting that graphene's atomically thin character

makes its Fermi energy widely tunable, and that graphene devices could then become superconducting upon applying a large enough gate voltage. In particular, the graphene spectrum has a particular topology in the vicinity of the mid-points of the first Brillouin zone edges, or M-points. These high-energy points, situated at an energy t away from the Dirac points, are saddle points. Close to these M-points, the Fermi surface becomes singular and the the Fermi velocity $\frac{1}{\hbar}\nabla_{\vec{k}}\mathcal{E}$ vanishes, leading to a diverging density of states, or van Hove singularity, as shown in Appendix (see section 2.4.1). It is therefore expected to have a considerably enhanced $T_c(\epsilon_F)$ as the Fermi energy approaches t. Clearly, such a high energy level $t \approx 2.7$ eV is unreachable by conventional methods employing a silicone oxide gate. Silicone oxide is limited not only by his small dielectric constant $\epsilon_{SiO_2} \approx 3.9$, but also by a breakdown field of $F_{max} \approx 0.5$ V/nm, above which it becomes irreversibly damaged. Such constraints would lead to a maximum charge carrier density of the order of 10^{13}/cm^2 and corresponding maximum Fermi energy of ~ 400 meV. However, other methods, such as polymer-electrolyte gating [31], provide better prospects and could be used to obtain much higher electronic densities. With such techniques, approaching graphene's van Hove singularities seems feasible, but is challenging and can be seen as a long-term goal.

A very important preliminary step is to explore how graphene properties change upon raising the Fermi level to ultra-high values. Electron transport experiments are expected to capture much of the change, as significantly increasing the electronic density is predicted to transform the temperature dependence of graphene resistivity [23, 24, 25]. Besides, as the Fermi level increases, the Fermi surface should morph from circular to trigonal, thereby altering the graphene propagator and hence the way charges scatter with typical defects. Last but not least, going to ultra-high charge carrier densities n should considerably diminish the resistivity terms ρ_{CI} and ρ_{ad} originating from charged impurities and adatoms due to their well-known $\propto 1/n$ dependence [22, 2],

perhaps allowing the observation of terms arising from interesting many-body effects, usually dominated by ρ_{CI} and ρ_{ad}. We devote the remainder of this chapter to the study of graphene at ultra-high charge carrier densities, by first reviewing some theoretical aspects of this regime and then presenting our electron transport experiments.

2.2 Electron-phonon scattering in graphene

We now review the interaction between graphene Dirac fermions and acoustic phonons, as it evolves with charge carrier density and is expected to lead to measurable effects in charge transport experiments. We aim to calculate the electron-phonon scattering rate and corresponding resistivity, in particular its temperature-dependence. This section is essentially a detailed re-derivation of the main results from E.H. Hwang and S. Das Sarma [23], Stauber et al [25] and Kaasbjerg et al [24]. We start with the following Hamiltonian,

$$H_{tot} = H_0 + H_{e-ph} \tag{2.2.1}$$

where H_0 describes previously studied prisitine graphene Hamiltonian, and H_{e-ph} is the electron-phonon interaction term [48]:

$$H_{e-ph} = D \sum_{\vec{q}} \sqrt{\frac{\hbar}{2\rho_m \mathcal{A}_{gr} \omega_{\vec{q}}}} \, \|\vec{q}\| \, \hat{\rho}(\vec{q})(c_{\vec{q}} + c^{\dagger}_{-\vec{q}}) \tag{2.2.2}$$

where ρ_m is graphene mass density, $\mathcal{A}_{gr}$ is the graphene sheet area and D is the deformation-potential coupling constant. $c_{\vec{q}}$ is the annihilation operator for phonons of momentum $\vec{q}$ and frequency $\omega_{\vec{q}}$.In equation 2.2.2,$\hat{\rho}(\vec{q})$ is the Fourier transform of the electron density operator

$$\rho(\vec{r}) = \psi^{\dagger}_A(\vec{r})\psi_A(\vec{r}) + \psi^{\dagger}_B(\vec{r})\psi_B(\vec{r}) \tag{2.2.3}$$

and therefore,

$$\hat{\rho}(\vec{q}) = \int \frac{d^2\vec{k}}{(2\pi)^2} \left\{ \tilde{\psi}_A^\dagger(\vec{k})\tilde{\psi}_A(\vec{k}+\vec{q}) + \tilde{\psi}_B^\dagger(\vec{k})\tilde{\psi}_B(\vec{k}+\vec{q}) \right\} \tag{2.2.4}$$

Here, we only consider coupling to longitudinal acoustic phonons, since other phonons of graphene either couple too weakly with graphene charge carriers or carry too much energy to have a significant occupation number n_{BE} below room temperature. The relevant phonon energy dispersion is therefore linear in momentum,

$$\omega_{\vec{q}} = v_s q \tag{2.2.5}$$

with $v_s = 2 \times 10^4$ m/s. To calculate transition probabilities $\mathcal{P}_{e-ph}(\vec{k}_i \to \vec{k}_f)$ for a the deflection of a charge carrier's momentum from $\vec{k}_i$ to $\vec{k}_f$ due to the absorption or emission of a phonon, we use the Fermi golden rule. We thus need to calculate the matrix element $\langle \vec{k}_f | H_{e-ph} | \vec{k}_i \rangle$ with

$$|\vec{k_{i,f}}\rangle = \frac{1}{\sqrt{2\mathcal{A}_{gr}}} (\tilde{\psi}_A^\dagger(\vec{k}_{i,f}) + e^{i\theta_{i,f}} \tilde{\psi}_B^\dagger(\vec{k}_{i,f}))|0\rangle \tag{2.2.6}$$

where $\theta_{i,f}$ is the angle of momentum $\vec{k}_{i,f}$ with respect to some axis $\vec{u}$. Using fermions anti-commutation property, we easily obtain

$$\langle \vec{k}_f | \hat{\rho}(\vec{q}) | \vec{k}_i \rangle = \frac{1 + e^{i(\theta_i - \theta_f)}}{2} (2\pi)^2 \delta(\vec{k}_f - \vec{k}_i + \vec{q}) \tag{2.2.7}$$

and hence:

$$\langle \vec{k}_f | H_{e-ph} | \vec{k}_i \rangle = D \sqrt{\frac{\hbar}{2\rho_m \mathcal{A}_{gr} \omega_{\vec{k}_i - \vec{k}_f}}} \left\| \vec{k}_i - \vec{k}_f \right\| \frac{1 + e^{i(\theta_i - \theta_f)}}{2} \tag{2.2.8}$$

Since $v_s \ll v_F$, acoustic phonons carry small energies compared to graphene electrons, and electron-acoustic phonon scattering can be considered elastic.

At finite Fermi level, we can thus write $k_i \approx k_f$ and

$$|\langle \vec{k}_f | H_{e-ph} | \vec{k}_i \rangle|^2 \approx \frac{\hbar D^2 k_i}{\rho_m \mathcal{A}_{gr} v_s} \left| \sin\left(\frac{\theta_i - \theta_f}{2}\right) \right| \cos^2\left(\frac{\theta_i - \theta_f}{2}\right) \tag{2.2.9}$$

Noting $\vec{q} = \vec{k}_f - \vec{k}_i$, the Fermi golden rule gives:

$$\begin{aligned} \mathcal{P}_{e-ph}(\vec{k}_i \to \vec{k}_f) &= \frac{2\pi}{\hbar} |\langle \vec{k}_f | H_{e-ph} | \vec{k}_i \rangle|^2 \Big\{ n_{BE}(\omega_{\vec{q}}) \delta(\mathcal{E}(\vec{k}_i) - \mathcal{E}(\vec{k}_f) + \omega_{\vec{q}}) \\ &+ x_{BE}(\omega_{\vec{q}}) \delta(\mathcal{E}(\vec{k}_i) - \mathcal{E}(\vec{k}_f) - \omega_{\vec{q}}) \Big\} \end{aligned} \tag{2.2.10}$$

where $x_{BE}(\omega_{\vec{q}})$ verifies the detailed balance principle

$$\begin{aligned} |\langle \vec{k}_f | H_{e-ph} | \vec{k}_i \rangle|^2 f_{FD}(\mathcal{E}(\vec{k}_i))(1 - f_{FD}(\mathcal{E}(\vec{k}_f) + \omega_{\vec{q}})) n_{BE}(\omega_{\vec{q}}) \\ = |\langle \vec{k}_i | H_{e-ph} | \vec{k}_f \rangle|^2 f_{FD}(\mathcal{E}(\vec{k}_f) + \omega_{\vec{q}}) \\ \times (1 - f_{FD}(\mathcal{E}(\vec{k}_i))) x_{BE}(\omega_{\vec{q}}) \end{aligned} \tag{2.2.11}$$

reflecting that at equilibrium, the probability for an electron to scatter from $\vec{k}_i$ to $\vec{k}_f$ upon absorbing a phonon is equal to the probability to scatter from $\vec{k}_f$ to $\vec{k}_i$ by emitting a phonon. In equation 2.2.11, $f_{FD}(\epsilon)$ and $n_{BE}(\omega)$ are the Fermi-Dirac and Bose-Einstein distributions,

$$f_{FD}(\epsilon) = \frac{1}{1 + e^{\frac{\epsilon - \epsilon_F}{k_B T}}} \tag{2.2.12}$$

and

$$n_{BE}(\omega) = \frac{1}{e^{\frac{\hbar\omega}{k_B T}} - 1} \tag{2.2.13}$$

and ϵ_F is the Fermi level. Electron-acoustic phonon scattering being quasi-elastic, we have $\mathcal{E}(\vec{k}_f) \approx \mathcal{E}(\vec{k}_i)$ and $|\langle \vec{k}_f | H_{e-ph} | \vec{k}_i \rangle|^2 \approx |\langle \vec{k}_i | H_{e-ph} | \vec{k}_f \rangle|^2$, leading to

$$x_{BE}(\omega_{\vec{q}}) \approx \frac{f_{FD}(\mathcal{E}(\vec{k}_i))(1 - f_{FD}(\mathcal{E}(\vec{k}_i) + \omega_{\vec{q}}))}{f_{FD}(\mathcal{E}(\vec{k}_i) + \omega_{\vec{q}})(1 - f_{FD}(\mathcal{E}(\vec{k}_i)))} n_{BE}(\omega_{\vec{q}}) \tag{2.2.14}$$

which simplifies to

$$x_{BE}(\omega_{\vec{q}}) \approx n_{BE}(\omega_{\vec{q}}) + 1 \tag{2.2.15}$$

The total transport scattering rate for an electron of initial momentum $\vec{k}_i$ is therefore

$$\begin{aligned} \mathcal{P}_{e-ph}(\vec{k}_i) &= \sum_{\vec{k}_f} \mathcal{P}_{e-ph}(\vec{k}_i \to \vec{k}_f)(1 - \cos(\theta_i - \theta_f)) \\ &\approx g_s \mathcal{A}_{gr} \int \frac{d^2\vec{k}_f}{(2\pi)^2}(1 - f_{FD}(\mathcal{E}(\vec{k}_f))) \\ &\quad \mathcal{P}_{e-ph}(\vec{k}_i \to \vec{k}_f)(1 - \cos(\theta_i - \theta_f)) \end{aligned} \tag{2.2.16}$$

where g_s accounts for the spin-degeneracy. Here, we do not take the valley degeneracy g_v into account as we neglect inter-valley scattering. The rate $\mathcal{P}_{e-ph}(\vec{k}_i)$ depends on k_i but not on θ_i because the electron-phonon scattering amplitude depends on the scattering angle $\theta_f - \theta_i$ but not on individual angular variables θ_i and θ_f. $\mathcal{P}_{e-ph}$ can therefore be seen as a function of the incoming electron energy $\mathcal{E}(\vec{k}_i)$ only. We shall now calculate the energy-averaged scattering rate $\langle \mathcal{P}_{e-ph} \rangle_{\epsilon_F}$ for an electron at the Fermi level, by summing $\mathcal{P}_{e-ph}(\vec{k}_i)$ over $\vec{k}_i$ and dividing by the typical number of states N_{scatt} involved in the scattering process. N_{scatt} is the number of states within $k_B T$ around the Fermi level ϵ_F,

$$N_{scatt} \sim 2\mathcal{A}_{gr}\mathcal{D}(\epsilon_F)k_B T \tag{2.2.17}$$

and

$$\begin{aligned} \langle \mathcal{P}_{e-ph} \rangle_{\epsilon_F} &= \frac{g_s \mathcal{A}_{gr}}{N_{scatt}} \int d\epsilon \mathcal{D}(\epsilon) f(\epsilon) \mathcal{P}_{e-ph}(\epsilon) \\ &= \frac{g_s \mathcal{A}_{gr}^2}{N_{scatt}} \int d\epsilon \mathcal{D}(\epsilon) f(\epsilon) \times \\ &\quad \int \frac{d^2\vec{k}_f}{(2\pi)^2}(1 - f_{FD}(\mathcal{E}(\vec{k}_f)))\mathcal{P}_{e-ph}(\vec{k}_i \to \vec{k}_f)(1 - \cos(\theta_i - \theta_f)) \end{aligned} \tag{2.2.18}$$

Using equations 2.2.9, 2.2.10, 2.2.15 and 2.2.16, we obtain with $\varphi = \theta_f - \theta_i$,

$$\begin{aligned}\langle \mathcal{P}_{e-ph}(\epsilon_F)\rangle &= \frac{2\pi g_s \mathcal{A}_{gr}}{\hbar N_{scatt}} \frac{\hbar D^2 k_i}{\rho_m v_s} \int_0^{2\pi} \frac{d\varphi}{2\pi}(1-\cos\varphi)\left|\sin\left(\frac{\varphi}{2}\right)\right| \cos^2\left(\frac{\varphi}{2}\right) \times \\ &\int_0^{+\infty} \frac{k_f dk_f}{2\pi}(1 - f_{FD}(\mathcal{E}(\vec{k}_f))) \times \\ &\int_{-\infty}^{+\infty} d\epsilon \mathcal{D}(\epsilon) f(\epsilon) \Big\{ n_{BE}(\omega_{\vec{q}})\delta(\mathcal{E}(\vec{k}_i) - \mathcal{E}(\vec{k}_f) + \omega_{\vec{q}}) \\ &(n_{BE}(\omega_{\vec{q}}) + 1)\delta(\mathcal{E}(\vec{k}_i) - \mathcal{E}(\vec{k}_f) - \omega_{\vec{q}})\Big\} \end{aligned} \tag{2.2.19}$$

Writing $k_i \approx k_f \approx \frac{\epsilon_F}{\hbar v_F}$ and $\mathcal{D}(\epsilon) \approx \mathcal{D}(\epsilon_F)$ in the above-integrand, equation 2.2.19 simplifies to

$$\begin{aligned}\langle \mathcal{P}_{e-ph}\rangle_{\epsilon_F} &\approx \frac{g_s D^2 \mathcal{A}_{gr}}{N_{scatt}} \frac{\epsilon_F^2 \mathcal{D}(\epsilon_F)}{\rho_m (\hbar v_F)^3 v_s} \int_0^{2\pi} \frac{d\varphi}{2\pi}(1-\cos\varphi)\left|\sin\left(\frac{\varphi}{2}\right)\right| \cos^2\left(\frac{\varphi}{2}\right) \times \\ &\int_{-\infty}^{+\infty} d\epsilon f(\epsilon) \{ n_{BE}(\omega_{\vec{q}})(1 - f_{FD}(\epsilon + \omega_{\vec{q}})) \\ &+ (n_{BE}(\omega_{\vec{q}}) + 1)(1 - f_{FD}(\epsilon - \omega_{\vec{q}}))\} \end{aligned} \tag{2.2.20}$$

Functions $f_{FD}(\epsilon)(1 - f_{FD}(\epsilon \pm \omega_{\vec{q}}))$ have two series of simple poles, $\epsilon_n = 2k_B T i(\frac{\pi}{2} + n\pi)$ and $\epsilon'_n = \mp\omega + 2ik_B T(\frac{\pi}{2} + n\pi)$ so that applying the residue theorem easily gives

$$\int_{-\infty}^{+\infty} d\epsilon f_{FD}(\epsilon)(1 - f_{FD}(\epsilon \pm \omega_{\vec{q}})) = \hbar\omega_{\vec{q}}(\Theta(\pm\omega_{\vec{q}}) + n_{BE}(\omega_{\vec{q}})) \tag{2.2.21}$$

where Θ is the unit-step function. Equation 2.2.20 can thus be rewritten as

$$\begin{aligned}\langle \mathcal{P}_{e-ph}(\epsilon_F)\rangle_{\epsilon_F} &\approx \frac{g_s \hbar D^2 \mathcal{A}_{gr}}{N_{scatt}} \frac{\epsilon_F^2 \mathcal{D}(\epsilon_F)}{\rho_m (\hbar v_F)^3 v_s} \\ &\times \int_0^{2\pi} \frac{d\varphi}{2\pi}(1-\cos\varphi)\left|\sin\left(\frac{\varphi}{2}\right)\right| \\ &\cos^2\left(\frac{\varphi}{2}\right) \omega_{\vec{q}} n_{BE}(\omega_{\vec{q}})(n_{BE}(\omega_{\vec{q}}) + 1) \end{aligned} \tag{2.2.22}$$

Since the energy exchanged between phonons and electrons is $\omega_{\vec{q}} = 2k_F v_s \left|\sin\left(\frac{\varphi}{2}\right)\right|$, where k_F is the Fermi momentum, a typical temperature scale emerges, the

Bloch-Grüneisen temperature

$$T_{BG} = \frac{2\hbar v_s k_F}{k_B} \tag{2.2.23}$$

If $T \gg T_{BG}$, then all states of graphene Fermi surface can be scattered to any other state of the Fermi surface by absorbing or emitting an acoustic phonon, and one expects the scattering rate $\langle \mathcal{P}_{e-ph}(\epsilon_F) \rangle_{\epsilon_F}$ to be significant. In this regime, we have

$$n_{BE}(\omega_{\vec{q}}) = \left(\exp\left(\frac{T_{BG}}{T} \left| \sin\left(\frac{\varphi}{2}\right) \right| \right) - 1 \right)^{-1} \approx \frac{T}{T_{BG} \left| \sin\left(\frac{\varphi}{2}\right) \right|} \gg 1 \tag{2.2.24}$$

and the integral in equation 2.2.22 can be calculated easily, to yield

$$\langle \mathcal{P}_{e-ph}(\epsilon_F) \rangle_{\epsilon_F} \approx \frac{g_s \hbar D^2 \mathcal{A}_{gr}}{N_{scatt}} \frac{\epsilon_F^2 \mathcal{D}(\epsilon_F)}{\rho_m (\hbar v_F)^3 v_s} \frac{k_F v_s}{2} \left(\frac{T}{T_{BG}} \right)^2 \tag{2.2.25}$$

We can simplify the above-equation further using equation 2.2.17, to end up with:

$$\langle \mathcal{P}_{e-ph}(\epsilon_F) \rangle_{\epsilon_F} \approx \frac{D^2}{8\hbar^3} \frac{\epsilon_F}{\rho_m v_F^2 v_s^2} k_B T \tag{2.2.26}$$

In the opposite limit $T \ll T_{BG}$, the acoustic phonon occupation number is exponentially small and the Fermi surface becomes extremely sharp, leading to quenched phonon absorption and emission rates. In this limit, one thus expects a vanishingly small electron-phonon scattering rate. More precisely,

$$n_{BE}(\omega_{\vec{q}}) \approx e^{-\frac{T_{BG}}{T} \left| \sin\left(\frac{\varphi}{2}\right) \right|} \tag{2.2.27}$$

and the integral in equation 2.2.22 can be approximated by

$$\begin{aligned} \langle \mathcal{P}_{e-ph}(\epsilon_F) \rangle_{\epsilon_F} &\approx \frac{2 g_s \hbar D^2 \mathcal{A}_{gr}}{N_{scatt}} \frac{\epsilon_F^2 \mathcal{D}(\epsilon_F)}{\rho_m (\hbar v_F)^3 v_s} \frac{T_{BG}}{\hbar} \\ &\times \int_0^{2\pi} \frac{d\varphi}{2\pi} \sin^4\left(\frac{\varphi}{2}\right) \cos^2\left(\frac{\varphi}{2}\right) e^{-\frac{T_{BG}}{T} \left| \sin\left(\frac{\varphi}{2}\right) \right|} \end{aligned}$$

Doing the change of variables $u = \frac{T_{BG}}{T}\left|\sin\left(\frac{\varphi}{2}\right)\right|$, we have

$$\begin{aligned}
&\int_0^{2\pi} \frac{d\varphi}{2\pi} \sin^4\left(\frac{\varphi}{2}\right) \times \\
\cos^2\left(\frac{\varphi}{2}\right) e^{-\frac{T_{BG}}{T}\left|\sin\left(\frac{\varphi}{2}\right)\right|} &= 2\left(\frac{T}{T_{BG}}\right)^5 \int_0^{\frac{T_{BG}}{T}} duu^4(1-(\frac{T}{T_{BG}}u)^2)^{1/2}e^{-u} \\
&\approx 2\left(\frac{T}{T_{BG}}\right)^5 \int_0^{+\infty} duu^4 e^{-u} \\
&= 48\left(\frac{T}{T_{BG}}\right)^5
\end{aligned}$$

and finally,

$$\left\langle \mathcal{P}_{e-ph}(\epsilon_F)\right\rangle_{\epsilon_F} \approx \frac{6D^2}{\hbar^4}\frac{(k_B T)^4}{k_F \epsilon_F \rho_m v_s^5} \tag{2.2.28}$$

The rate $\left\langle \mathcal{P}_{e-ph}(\epsilon_F)\right\rangle_{\epsilon_F}$ is equal to the inverse average electron-phonon scattering time $1/\left\langle \tau_{e-ph}\right\rangle$. The corresponding conductivity, given by the well-known formula

$$\sigma_{e-ph} = \frac{e^2 v_F^2}{2}\mathcal{D}(\epsilon_F)\left\langle \tau_{e-ph}\right\rangle, \tag{2.2.29}$$

scales as $\propto (k_F^3 T^4)^{-1}$ in the Bloch-Grüneisen regime $T \ll T_{BG}$ while it does not depend on k_F and is inversly proportional to temperature in the the high-temperature regime $T \gg T_{BG}$. At fixed temperature T, the crossover form the $\sigma_{e-ph} \propto T^{-1}$ regime to the Bloch-Grüneisen regime occurs when the graphene Fermi surface becomes too large for acoustic phonon scattering to connect any two states of the Fermi surface around a given valley, K or K'. Experimentally, observing this crossover can be used as evidence for reaching ultra-high charge-carrier densities.

2.3 Electronic properties of graphene in the ultra-high doping regime

2.3.1 Summary of our experimental results

We report the study of graphene devices in Hall-bar geometry, gated with a polymer electrolyte. High densities of $6 \times 10^{13}/cm^2$ are consistently reached, significantly higher than with conventional back-gating. The mobility follows an inverse dependence on density, which can be correlated to a dominant scattering from resonant scatterers. Furthermore, our measurements show a Bloch-Grüneisen regime until 100 K (at $6.2 \times 10^{13}/cm^2$), consistent with an increase of the density. Ubiquitous in our experiments is a small upturn in resistivity around $3 \times 10^{13}/cm^2$, whose origin is discussed. We identify two potential causes for the upturn: the renormalization of Fermi velocity and an electrochemically-enhanced scattering rate.

2.3.2 Introduction

Since its first exfoliation from graphite in 2004 [1], graphene transport properties have mainly been studied in the vicinity of the Dirac point, where the dispersion relation is linear and the electrons behave as massless Dirac particles [3, 4, 5]. For technical reasons, the electrical properties of graphene have rarely been measured at densities beyond 10^{13} /cm^2. But the physics of graphene may well be as exciting at high charge carrier densities as it is in the vicinity of the Dirac point. As the chemical potential is shifted away from the Dirac point, the description of electrons as massless Dirac particles becomes less valid and corrections are needed to describe the physics [26, 27]. Besides, recent angle resolved photoemission spectroscopy (ARPES) experiments [26] show that potassium- and calcium-doped graphene have extended van Hove singularities (VHS), a feature also present in the cuprate energy-bands and suspected by

some to be responsible for their high-Tc superconducting transitions [26, 28]. However, the extended VHS of cuprates are easily accessible, whereas their graphene counterparts lie at ~ 2 eV above the Dirac points, corresponding to electron densities greater than 2×10^{14} /cm^2.

Experimentally, the realization of high carrier densities in graphene devices is limited by the requirement of thin dielectrics with high capacitance. These materials are however prone to dielectric breakdown at gate voltages required for achieving high doping. In addition the growth and identification of graphene on various substrates remains challenging [29]. The conventional SiO_2 back-gate, while being suitable for identifying graphene flakes, cannot lead to carrier densities greater than 10^{13} /cm^2 in graphene. The use of high-κ dielectrics has also been considered for achieving high doping [30], although this approach has been less successful. The present work uses a polymer electrolyte gate to achieve high-doping. When a potential difference is applied between two electrodes in an electrochemical cell, the ions move in the polymer matrix according to their charge polarity and accumulate to form an electric-double layer at the electrode interface. Such nanometer-size gate has a very high capacitance and can induce counter charges of equivalent density on graphene. Polymer electrolyte top-gating has been previously used to demonstrate the sensitivity of the Raman spectrum to high carrier densities in graphene [31, 32].

2.3.3 Polymer Electrolyte Gating

In this work, we study the electronic properties of graphene Hall devices gated with a polymer electrolyte and track the deviations from Dirac physics through density and temperature dependent transport measurements. The Hall measurements demonstrate the effectiveness of the electrolyte system in realizing high carrier densities in graphene. From transport measurements, we evaluate the relative contributions to graphene resistivity induced by different scattering mechanisms. Monolayer graphene flakes are prepared by mechanical exfoliation

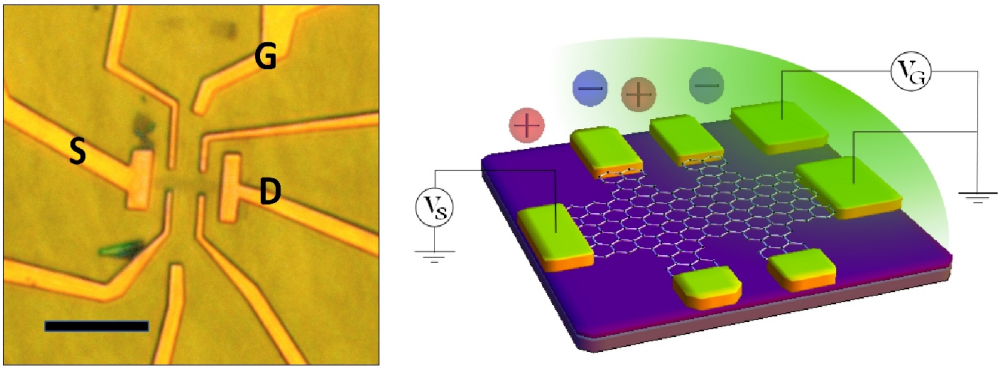

Figure 2.3.1: Optical image and schematic of graphene device in Hall-bar configuration, coated with polymer electrolyte [S = Source, D = Drain, G = Polymer Electrolyte Gate]. Scale bar: 10 µm.

on Si/SiO_2 substrates. The device measurements are performed on standard Hall bar and four-terminal structures fabricated with electron-beam lithography. A schematic of the device is shown in fig. 2.3.1. In addition to the electrodes on the graphene flake, Au/Cr electrodes of large surface area are also patterned within the plane of the device structure at few micron separations. While several designs for polymer electrolyte gating rely on evaporation of top gate-electrode or insertion of a Pt or Au wire in the polymer matrix [31, 33], the present design does not require positioning of the top-contact. The in-plane gate electrode can be simultaneously patterned lithographically along with the graphene contacts. Migration of metal atoms into the polymer matrix may happen in case of evaporated top contact and this contamination is also prevented. The polymer electrolyte, an aqueous dispersion of polyethylene oxide (PEO) and lithium perchlorate is then drop cast on the device and bake-dried.

The graphene resistance is measured at low frequencies (13 Hz) in the four-terminal configuration under low vacuum conditions. A plot showing the modulation of graphene resistivity (ρ) with applied polymer electrolyte gate voltage V_g at room temperature is shown in fig. 2.3.2(a). Due to the large interfacial capacitance arising from a nearby layer of counter ions, it is possible to obtain a large and reversible modulation in graphene resistance with the

application of small voltages. The measurements are restricted to a maximum gate leakage of ~ 1 nA. At high gate voltages (or gate leakage currents) the devices show a breakdown due to electrochemical reactions. Since the polymer is hygroscopic, the presence of adsorbed residual water contributes importantly to this leak [34], but at the same time allows a better ionic mobility. Significantly lower leakage current is observed, when the device is cooled below the ice-point of water. In addition, we note that the sweep rate of gate voltage must be slow enough to allow equilibration of the ion double layer atop graphene and measure a stabilized value of resistivity. The typical mobility of our pristine graphene samples at low doping is in the range 4000-7000 $cm^2/V.s$. Upon addition of the polymer electrolyte, the mobility of graphene remains larger than 3000 $cm^2/V.s$ at $n \sim 10^{13}/cm^2$. The slope of graphene resistance $\frac{dR}{dV_g}$ (measured at half the value of maximum resistance) gated with silicon-oxide back-gate is typically 150 Ω/V. This slope is enhanced significantly to ~ 3500 Ω/V when the polymer electrolyte gate is used. Upon sweeping the electrolyte gate voltage, a typical on-off ratio of 30-40 is obtained. The sharp resistance slope and high on-off ratio value are indicative of high-doping in graphene. At zero gate-voltage, graphene is found to be in a highly electron-doped low-resistance state and the charge neutrality point is shifted by -3 to -5 V. Such doping may be attributed to a higher concentration of Li^+ ions adsorbed in the vicinity of graphene, since the graphene has small hole-doping prior to the coating of polymer electrolyte [see fig 2.3.2(a)]. The G-band Raman peak for graphene shows a shift of 6-7 cm^{-1} upon addition of the polymer electrolyte as well as a reduction in full-width at half-maximum (FWHM) [see fig. 2.3.2(b)], which further supports the electron-doping of graphene [31].

Ubiquitous in our measurements is a small upturn in resistivity observed at high gate voltages [see inset of Fig. 2.3.2(a)]. This upturn is consistently observed in 6 graphene devices on 5 different wafers and across several sweeps for the same sample. To characterize the nature of transport at high-doping and

examine the contributions to graphene resistivity, we performed Hall measurements. The room temperature resistivity ρ and Hall mobility μ of graphene devices are plotted as a function of the carrier density in fig. 2.3.3(a) and 2.3.3(b) respectively, for two devices. The mobility shows a continuous decrease between 1×10^{13}/cm^2 and 6×10^{13}/cm^2 , $\mu \sim 1/n$, indicating that ρ approaches a saturation value. As in the low density regime ($n \leq 10^{13}$/cm^2), the factors determining the total resistivity include charged impurities (both from underlying substrate and from electrolyte ions), defects on the graphene lattice and phonons [5, 35, 36, 37, 38]. While these contributions have been examined at low densities, their relative contributions at high densities can be significantly different due to high screening from carriers in graphene.

2.3.4 Contributions to graphene resistivity

In this experiment, graphene is sandwiched between the SiO_2 substrate below and the polymer layer above. The number of electrolyte ions in the vicinity of the graphene sheet increases with the electron density, unlike the number of charged impurities at the SiO_2/graphene interface which remains constant. To estimate the contribution of the ions to the total resistivity of graphene, it is necessary to know their distribution in the vicinity of the graphene sheet, which is hard to obtain experimentally. Theoretically, the Poisson-Boltzmann equation is often used to describe the ion distribution in electrolyte systems [31]. However, the concentration of ions estimated from this model diverges at the graphene/polymer interface while the concentration of ions is limited by the finite ionic radius, the space occupied by the polymer, and the formation of electrolyte-polymer complex. To take this into account, modified Poisson-Boltzmann equations are generally applied and/or cutoff concentrations c_{max} introduced [39]. Following the latter approach, we modeled the ion-induced resistivity of graphene [see Appendix]. With a polymer packing density $f \leq 80\%$ and an electrolyte ion effective radius around 1 nm, c_{max} takes values between

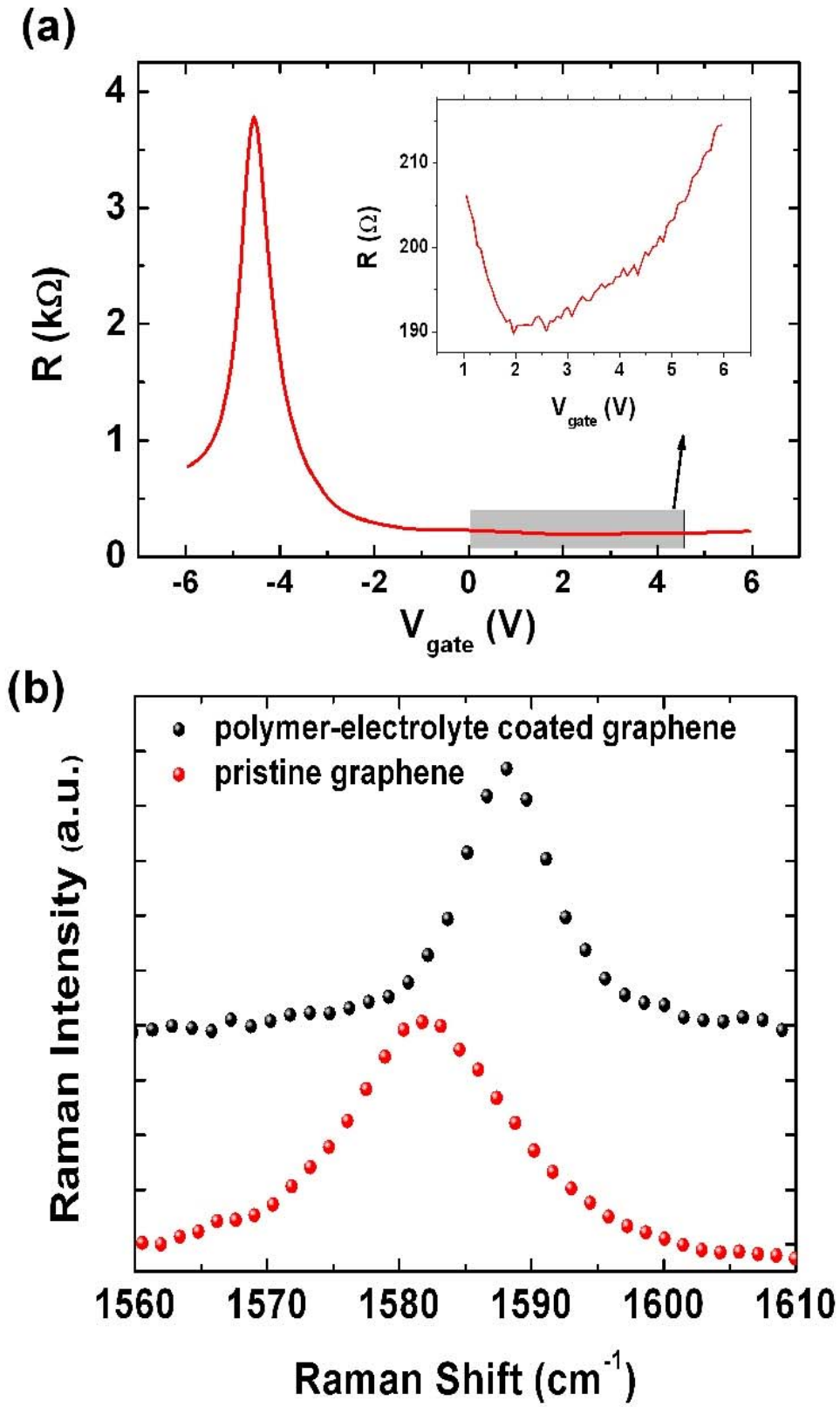

Figure 2.3.2: (a) Resistance vs. polymer gate voltage for sample 1 [Inset: R vs. V_g in the low resistance region, showing an upturn in the device resistance] (b) G-band Raman-shift for pristine graphene (red) and polymer-electrolyte coated graphene (black).

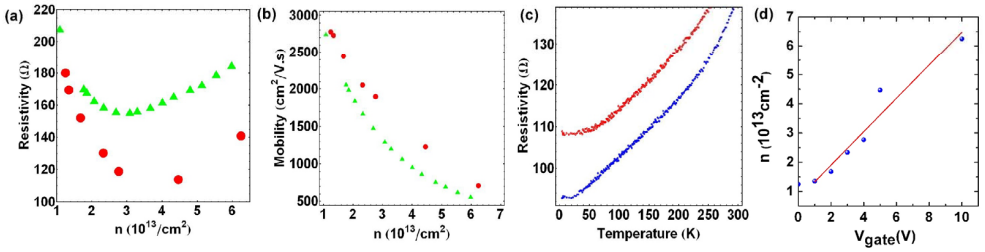

Figure 2.3.3: (a) Resistivity vs. carrier concentration for Sample 1 (red) and Sample 2 (green). (b) Hall mobility vs. carrier concentration for the same 2 samples at T = 295 K. (c) Resistivity vs. Temperature at two different densities: $n \sim 6.2 \times 10^{13}/cm^2$ (red), $n \sim 2.5 \times 10^{13}/cm^2$ (blue) (d) Carrier concentration vs. applied gate bias; Slope of the linear fit gives an estimate of the gate capacitance of the electrolyte gating, $C \approx 1$ μF/cm^2.

10^{25} /m^3 and 5×10^{25} /m^3 . The polymer dielectric constant is $\epsilon \sim 5$ [31]. The concentration of ions in the bulk polymer matrix is estimated to be about 5×10^{24}/m^3. The gate voltage dependence of carrier density is plotted in Fig. 2.3.3(d). This can be used to experimentally estimate the total gate capacitance (polymer capacitance and quantum capacitance in series), which is of the order of ~ 1 μF/cm^2 [see fig. 3(d)]. Second, we consider the influence of charged impurities from the SiO_2 substrate on the graphene resistivity. This requires an estimate of the charged impurity density n_{imp} in the substrate, which can be obtained from a linear fit to the $\sigma - n$ plot at low densities for our graphene samples, prior to the addition of the polymer [38]. This evaluation may be an upper limit since other scatterers can also contribute to a linear density dependence of conductivity at low density [36]. However, by considering this upper bound, we can at least estimate the maximum contribution of charged substrate impurities to graphene resistivity. We obtained an average value of $n_{imp} \sim 7 \times 10^{11}$ /cm^2 for our samples. Therefore, calculations based on the semi-classical Boltzmann formalism lead to a maximum contribution of few Ohms for $n \geq 10^{13}$/cm^2. The contribution from substrate impurities is significantly lower than from electrolyte ions in the polymer matrix.

The electrolyte ion distribution discussed above is almost temperature-independent since the ions are practically frozen below the ice-point of wa-

ter. Therefore, the phonon contribution ρ_{phonon} can be extracted from the temperature dependence of the graphene resistivity at high-doping. The resistivity versus temperature measurements are shown for Sample 1 down to 4 K in fig. 2.3.3(c). The upturn of resistivity observed at room temperature persists down to 4 K, since the resistivity at higher doping remains larger than the resistivity at lower doping throughout this range of temperature. The temperature-dependent part of the resistivity can be fitted by a T^4 law at low temperature, up to T ∼70 K and ∼100K for $n = 2.5 \times 10^{13}$/cm^2 and $n = 6.2 \times 10^{13}$/cm^2 respectively. This power-law dependence can be associated to a Bloch-Grüneisen regime, characterized by a strong suppression of the acoustic phonon scattering rate for $T \ll T_{BG}$, where $T_{BG} = 2\hbar v_s k_F/k_B$ is the Bloch-Grüneisen temperature, v_s the speed of sound in graphene and k_F the Fermi momentum [40]. The density of phonons being governed by the Bose-Einstein law, T_{BG} defines the temperature scale below which the acoustic phonon absorption rate vanishes. Besides, the lower the temperature, the sharper the Fermi distribution and lower the acoustic phonon emission rate. These two factors lead to a complete suppression of the acoustic-phonon induced resistivity in theBloch-Grüneisen regime $T \ll T_{BG}$. Further, these acoustic phonons are known to be the lowest-energy phonons graphene electrons scatter with [37], which ensures that all phonon scattering is suppressed around 4K. Previous measurements down to 20 K and at much lower densities $n = 2 \times 10^{12}$ to $n = 6 \times 10^{12}$, do not show the Bloch-Grüneisen regime [37]. Since $T_{BG} \propto \sqrt{n}$, the observation of a T^4 law to higher temperatures (up to 100 K) in our experiment is consistent with theoretical predictions. We also observe a linear regime (or non-degenerate regime) between 100 K and 170 K with a slope of $\rho_{tot}(T) \sim 0.13$ Ω/K, as the temperature becomes comparable to T_{BG} (240 - 420 K), consistent with previous observations at lower densities [37]. Above 200 K, the resistivity becomes a super-linear function of the temperature, indicating that the electrons start to scatter with additional

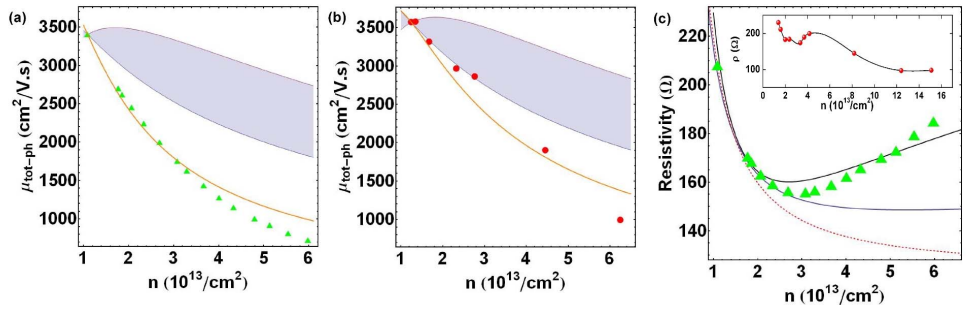

Figure 2.3.4: (a) Room temperature Hall mobility μ_{tot-ph} vs. carrier density for Sample 2. Green triangles represent experimental data, shaded blue region represents all possible μ_{tot-ph} curves that cross the first data point but do not include resistivity contribution from unitary scatterers. Orange curve is a theoretical fit after including this contribution. (b) Mobility μ_{tot-ph} vs. carrier density for Sample 1 (experimental data in red circles) (c) Resistivity vs. n for Sample 2 (experimental data in green triangles). Best fits of $\rho_{tot} = \rho_{ion} + \rho_{ph} + \rho_d + \rho_0$ to resistivity data: without Fermi velocity renormalization (dashed red curve); With electron-electron interaction induced renormalization, for $e^2/4\kappa v\hbar \approx 0.11$ (solid blue curve); By doubling the e-e interaction coupling constant (solid black curve). This may reflect the need to include the renormalization from several other interactions as discussed in the text. [Inset: Resistivity vs. n for Sample 3]

phonons, as previously discussed in the literature [35, 37, 41] for experiments at lower charge carrier densities. Finally, an estimate of ρ_{phonon} is obtained as: $\rho_{phonon} \approx \rho(295K) - \rho(4K)$, which is equal to 40 to 47 Ω. This almost constant phonon induced resistivity contributes to the observed $1/n$ dependence of mobility. However, even after subtracting ρ_{phonon} from the total resistivity, the resulting mobility $\mu_{tot-ph} = (1/\mu_{tot} - 1/\mu_{ph})^{-1}$ still shows such dependence [see fig. 2.3.4(a), 2.3.4(b)]. This indicates that other scattering mechanisms are also responsible for it, as discussed below.

We now consider the resistivity induced by defects in the graphene lattice. Strong-potential defects such as vacancies and certain adatoms lead to a density-dependent resistivity of the form,

$$\rho_d = \frac{h n_d}{4e^2 n \ln^2(R_0\sqrt{\pi n})} \tag{2.3.1}$$

where $R_0 \approx 1.4$ Å and n_d are the size and density of these defects. Using

typical values for n_d [36], this leads to a contribution of the order of 1 kΩ near the Dirac point. This logarithmic correction leads to a sublinear defect conductivity at high density, and contributes to the decrease in mobility at high doping. However, the increase of $ne\rho_d$ with charge carrier density is too slow to reproduce the mobility behavior, as shown in fig. 2.3.4. To explain the latter, we thus consider scatterers inducing a *constant* resistivity ρ_0, such as *small* short-range potentials. This scattering mechanism corresponds to a potential of the form, $V_{scatt}(\vec{r}) = V_0\delta(\vec{r})$ with small V_0. To estimate ρ_0, we fitted the theoretical expression

$$\mu_{tot-ph}(n) = 1/(ne(\rho_{ion}(n) + \rho_d(n) + \rho_0)) \tag{2.3.2}$$

to the corresponding data [fig. 2.3.4(a), (b)], giving a typical value of $\sim 100\ \Omega$. Therefore the mobility analysis shows that ρ_0 is the most important contribution to the resistivity of our samples at high doping.

So far we have discussed the contributions to the graphene resistivity from ions, phonons and point-defects. These contributions are either nearly constant (phonons and small short-range potentials) or rapidly vanishing with density (charged impurities and resonant scatterers). It is thus surprising to consistently observe an upturn in resistivity in a finite density window near $n \sim 3\times10^{13}$/cm^2 [see fig. 2.3.3(a), 2.3.4(c)]. Note that at higher densities (1.6×10^{14}/cm^2), the resistivity decreases, then saturates, as shown for one sample (Sample 3) [see inset of fig. 2.3.4(c)]. Below, we consider possible corrections to the resistivity terms to model this observed dependence on density. At first, we note that phonons and point-defects make up most of the graphene resistivity for $n \geq 3 \times 10^{13}$ /cm^2. Therefore, it is tempting to attribute the upturn to corrections to these terms. Experimentally, the phonon contribution does not increase with density, which makes point-defects the likely cause of the upturn. We therefore examine the various factors that determine ρ_0 to identify possible underlying mechanisms driving the observed upturn. Theoretically, ρ_0 is given

by [36, 40]:

$$\rho_0(n_0, V_0, v_F) = \frac{h n_0 V_0^2}{8e^2(\hbar v_F)^2} \tag{2.3.3}$$

where V_0 is the average impurity potential, n_0 the density of point-defects of potential $\sim V_0$ and v_F is the Fermi velocity. We examine the three factors n_0, V_0 and v_F for corrections to resistivity induced by point-defects. One possible explanation could be the electrochemically-induced creation of new defects in graphene, δn_0, upon application of gate volatge. However, this does not appear very plausible since the onset of upturn is seen in some samples already at small gate voltages (e.g. $V_g \sim 2$ V, $I_g \leq 50$ pA for Sample 1). At low voltages, the resistivity is stable and shows negligible time dependence, precluding the formation of new defects which would be a time-dependent process. Furthermore, this resistivity increase is reversible with gate voltage and distinguishable from an irreversible increase seen at much higher gate voltages ($V_g \geq 10$ V), which is likely to be related to electrochemical processes. A different explanation is related to the modification of the local scattering potential V_0 at the sites where Li^+ couples to the carbon lattice to form complexes. These coupling sites may invlove a finte density of pre-existing defects on the carbon lattice (e.g. edges, vacancies), which could explain the density-dependence of resistivity after the upturn [see fig. 2.3.4(c)], as these sites get saturated with complex formation. A more interesting source for a resistivity upturn is related to the renormalization of Fermi velocity v_F. This renormalization has been previously shown by scanning tunneling spectroscopy for graphene on graphite and ARPES measurements on epitaxial graphene on silicon carbide substrates in our range of densities [42, 26]. A density-dependent renormalization of the Fermi-velocity, v_F can lead to corrections to an otherwise constant ρ_0. The Fermi velocity is expected to be renormalized by direct electron-electron, Fröhlich, electron-phonon and electron-impurity interactions [5, 40, 43, 44, 45, 46, 47]. The direct electron-electron interaction is responsible for an increase of the Fermi velocity near the Dirac point, following $v \to v(1 - e^2 \ln(2a\sqrt{\pi n})/(4\kappa v\hbar))$ but

this can only partially explain an increase in resistivity in our range of densities [fig. 2.3.4(c)]. Other factors such as Fröhlich and electron-phonon interactions and disorders contribute equally to this decrease of Fermi velocity. These factors when considered together can potentially explain the magnitude of the observed increase in resistivity [see fig.2.3.4(c)] [5, 40, 43, 44, 45, 46, 47]. By keeping the concentration of electrolyte ions in the compact layer c_{max} around 10^{25}/m^3 and density of strong-potential defects n_d around 10^{11}/cm^2, it is possible to fit the $\rho - n$ curves of our samples by varying the bare defect resistivity of unitary scatterers r_0 around $100\ \Omega$, provided that this renormalization of the Fermi velocity is taken into account. The upturn is essentially a result of the competition between a decreasing ρ_{ion} and an increasing ρ_0. Therefore, the charge carrier density corresponding to the onset of the upturn increases with the ratio c_{max}/r_0. Besides, the decrease in Fermi velocity induced by the above-mentioned interactions, slows down at higher densities ($n \sim 10^{14}$/cm^2), potentially leading to a saturation of ρ_0 [see inset of fig. 2.3.4(c)] [43, 45, 48, 49, 47]. It also follows that for samples with a large enough c_{max}/r_0, the upturn is expected to be suppressed. Finally, note that the Fermi velocity dependence of the phonon-induced resistivity and the renormalization of the former do not contradict the fact that the $\rho - T$ curves [see fig.2.3.3(c)] remain almost parallel in the linear regime. Due to the screening of the Coulomb interaction between carbon atoms, the sound velocity and the deformation potential decrease with charge carrier density. This limits the influence of a decrease of Fermi velocity on $\rho(T)$. Before we conclude, note that at low densities ($n \leq 5 \times 10^{12}$/cm^2), the graphene resistivity is already strongly density-dependent from Coulomb and strong potential defect scattering. Thus any corrections arising from density-dependent renormalization of Fermi velocity in the low density regime are hard to discern in transport measurements.

2.3.5 Concluding remarks

In summary, we have demonstrated high electron densities 6.2×10^{13}/cm^2 in graphene with a polymer electrolyte gate. A Bloch-Grüneisen regime was observed between 4 K and 100 K, a clear sign of large Fermi temperatures. The density-dependence of the mobility and resistivity of our samples were analyzed by considering various scattering mechanisms: Coulomb scattering from the electrolyte ions, electron-phonon scattering, and electron-impurity scattering. Vacancies, cracks and certain adatoms are important scatterers in the low density regime. However, low-potential point-defects are the most important scatterers in our range of densities ($n \geq 10^{13}$/cm^2), as suggested by the $1/n$ density dependence of mobility. The resistivity versus carrier density graphs, obtained from Hall measurements, show an upturn for densities around 3×10^{13}/cm, and possible corrections to resistivity originating from point-defects are discussed. While the devices reported in this paper allowed to reach electron densities significantly higher than obtained with conventional dielectrics, further improvements are needed to explore the physics of graphene in the vicinity of the van Hove singularity.

2.4 Appendix

2.4.1 Density of states at the van Hove filling

Here, we briefly derive an asymptotic formula for the density of states in graphene as the Fermi level ϵ_F approaches t from below. By symmetry, all M-points contribute equally to the density of states $\mathcal{D}(\epsilon)$ of graphene, so that we can choose to calculate the contribution from the saddle point situated at $(\frac{\pi}{\sqrt{3}a_0}, \frac{\pi}{3a_0})$ in the Brillouin zone. In the vicinity of this M-point, graphene's

conduction band locally takes the form

$$\mathcal{E}(\vec{q}) = \frac{3ta_0^2}{2}(q_x^2 + \sqrt{3}q_x q_y + \frac{2}{3}p_m^2) \tag{2.4.1}$$

where $\vec{q}$ is measured from M and $p_m = 1/a_0$. Close to M, the Fermi velocity vanishes linearly in q_x and q_y:

$$\nabla_{\vec{k}}\mathcal{E} \approx \frac{3}{2}ta_0^2 \begin{pmatrix} 2q_x + \sqrt{3}q_y \\ \sqrt{3}q_y \end{pmatrix} \tag{2.4.2}$$

Accounting for the spin degeneracy g_s, the resulting density of states reads [50]

$$\mathcal{D}_M(\epsilon) \approx \frac{g_s}{(2\pi)^2}\int_{\mathcal{L}(\epsilon_F)} \frac{dl}{\left\|\nabla_{\vec{k}}\mathcal{E}(l)\right\|} \tag{2.4.3}$$

where the integration is done over the Fermi surface, approximated by a hyperbola. This approximation is valid close to the M-point, where the Fermi surface $\mathcal{L}(\epsilon_F)$ is described by the following equation:

$$2q_x = -\sqrt{3}q_y \pm \sqrt{3(q_y^2 - q_{min}^2)} \tag{2.4.4}$$

with

$$q_{min} = \frac{2\sqrt{2}}{3}\sqrt{\frac{t-\epsilon_F}{t}}p_m \tag{2.4.5}$$

Writing $q_y = q_{min} + Q$ with $q_{min} \gg Q \geq 0$, we have $dl = \sqrt{dq_x^2 + dq_y^2} \approx \sqrt{\frac{3q_{min}}{8Q}}dQ$ and $\left\|\nabla_{\vec{k}}\mathcal{E}(l)\right\| \approx \frac{3ta_0^2}{2}\sqrt{6q_{min}Q + 3q_{min}^2}$ and introducing a cut-off Q_{max} for Q, we obtain:

$$\begin{aligned} \mathcal{D}_M(\epsilon) &\approx \frac{4g_s}{(2\pi)^2}\int_0^{Q_{max}} \sqrt{\frac{3q_{min}}{8Q}}\frac{dQ}{\frac{3ta_0^2}{2}\sqrt{6q_{min}Q + 3q_{min}^2}} \\ &\approx \frac{g_s p_m}{(2\pi)^2\hbar v_F}\int_0^{2Q_{max}/q_{min}} \frac{du}{\sqrt{u}\sqrt{1+u}} \\ &\sim \frac{g_s p_m}{2(2\pi)^2\hbar v_F}\ln\left(\frac{t}{t-\epsilon}\right) \end{aligned} \tag{2.4.6}$$

Therefore, the total density of states $\mathcal{D}(\epsilon_F)$ diverges logarithmically as $\epsilon_F \to t^-$.

2.4.2 Resistivity induced by electrolyte ions

The resistivity induced by the electrolyte ions of the polymer is modeled within the framework of Boltzmann theory. Away from the Dirac point, the resistivity is given by

$$\rho = 2/(e^2 v_F^2(n)\mathcal{D}(n)\tau(n)) \tag{2.4.7}$$

where v_F is the Fermi velocity, $\mathcal{D}(n)$ the density of states, and $\tau(n)$ the scattering relaxation time. We compute the scattering rate induced by a 2D layer of charged particles situated at a distance z above the graphene plane by using a screened scattering potential,

$$V_c(q,z) = \frac{2\pi e^2 e^{-qz}}{\kappa(q+q_{TF})} \tag{2.4.8}$$

In a classic Poisson-Boltzmann approach where the steric effects are not taken into account, the concentration of ions diverges in the vicinity of the graphene sheet. However, as the gate voltage is applied, charged ions form a compact layer of thickness λ_c and concentration c_{max} atop graphene [39]. The total scattering rate τ^{-1} is obtained by integrating over the compact layer and the corresponding resistivity reads

$$\rho_{ion}(n) = \frac{\pi\hbar c_{max} I_{ion}}{8e^2(\pi n)^{3/2}} \tag{2.4.9}$$

where

$$I_{ion} = \int_0^1 du \frac{u\sqrt{1-u^2}}{\left(1+\frac{2u}{q_s}\right)^2}(1-e^{-4\lambda_c k_F u}) \approx 0.13 \tag{2.4.10}$$

since the exponential factor is small for typical values of compact layer thickness ($\lambda_c \sim 10$ nm) and graphene carrier densities ($k_F \approx 1$ nm^{-1}) in our experiment.

Chapter 3

Virtual Tunneling in Granular Graphene

3.1 Why study granular graphene?

Granular metals are arrays of conducting grains or dots seperated by an insulating medium. The granules are usually mesoscopic, have a distinct electronic structure but a significant energy-level spacing due to electron confinement. These systems have been studied for decades [51] due to their rich correlated electron physics and numerous applications, ranging from strain- and bio-sensing to photovoltaic applications [52]. Ordinary granular metals are prepared by thermal evaporation of metallic and insulating materials onto a substrate [53], or self-assembly of colloidal nanocrystals [54, 55, 56].

An excellent conductor in its pristine state, graphene can be transformed into an insulator by adsorption of atoms on its lattice. The most prominent exemples are graphene oxide [57], fluorinated graphene [94] and hydrogenated graphene [90]. Interestingly, adatoms on graphene often tend to form electrically insulating clusters [58], so that it is possible to fabricate granular metals by functionalizing graphene with adatoms. We call such systems granular graphene. Given graphene's elasticity and transparency, granular graphene can

be extremely interesting for strain-sensing and opto-electronic applications.

It is also worth noting that fully hydrogenated graphene systems, called graphane, are predicted to be high-temperature superconductors [123]. However, fully hydrogenated graphene has proven hard to sythesize, and to the best of our knowledge, graphane has never been realized. Fabricating granular graphene by hydrogenation is therefore both a more easily achievable goal and very interesting in its own right, as it may exhibit percolative superconductivity. From this perspective, we propose to study the electronic properties of heavily hydrogenated graphene in this chapter. While the next section is devoted to the theoretical study of the main transport mechanisms in granular metals in general and granular graphene in particular, subsequent sections report on experimental methods and results regarding hydrogenated graphene. Using theoretical results derived for granular graphene, it will be shown that our hydrogenated graphene samples have a granular metal behavior exhibiting interesting properties.

3.2 Electron transport in granular metals: a theoretical perspective

The main electron transport mechanisms in granular metals have been an outstanding puzzle in mesoscopic physics for decades [51, 52]. At low-enough temperatures, the conductivity σ_{GM} of granular metals has a temperature-dependence similar to the Efros-Shklovskii variable-range hopping law

$$\sigma_{GM}(T) \propto e^{-\sqrt{\frac{T_0}{T}}} \tag{3.2.1}$$

for some typical temperature T_0. Systematically observed in experiments, this behavior has long been intriguing because the insulating matrix in which granules are embedded makes the overlap between wave-functions of electrons local-

ized in non-neighboring granules vanishingly small. Moreover, this phenomenon has also been observed when all granules have similar dimensions [59], *a priori* making the *bare* density of states at the Fermi level zero, while a finite bare density of states is necessary for the Efros-Shklovskii variable-range hopping [60] mechanism to take place. Theoretically, a better understanding of the main conduction mechanisms in granular metals emerged only recently, in the works of Beloborodov et al. [84, 82], Zhang and Shklovskii [61], and Feigel'man and Ioselevich [83]. In this section, we review the main conduction mechanisms in conventional two-dimensional granular metals whose dots have a parabolic energy spectrum, and derive new results for granular graphene, whose granules are graphene dots and hence have a linear energy spectrum.

3.2.1 Model Hamiltonian

A typical granular metal or quantum dots array, sketched in Figure 3.2.1, is essentially parameterized by the average dot diameter ξ, intra-dot density of states $\mathcal{D}$, effective dielectric constant κ and the inter-dot tunneling amplitudes, whose magnitudes depend on overlaps between intra-dot eigenstates. We neglect the overlap between wavefunctions of electrons localized in non-neighboring dots, and hence any *direct* tunneling process between distant dots. Besides, the typical distance between neighboring dots is assumed to be small compared to ξ.

Granular metals can thus be described by a Hamiltonian H reading as the sum of individual dot Hamiltonians H_D^i and tunneling terms H_T^{ij} connecting dot i to neighboring dot j. In other words, H reads [84, 83]:

$$H = \sum_{i=1}^{N_D} H_D^i + \sum_{\langle i,j \rangle} H_T^{i.j} = H_D + H_T \tag{3.2.2}$$

where N_D is the number of dots int the studied array. Moreover, the single-dot Hamiltonian H_D^i can be written as the sum of a term describing a virtually

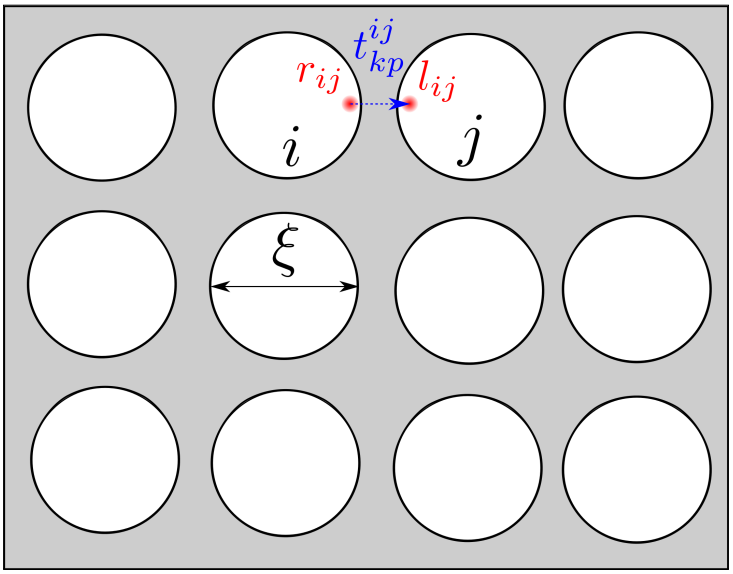

Figure 3.2.1: Cartoon representation of a granular metal. White disks represent conducting dots while the gray area corresponds to the insulating medium. Tunneling between state k in dot i and state p in dot j is depicted as a blue arrow, and has a tunneling integral t_{ij}^{kp}. Points between which tunneling occur are shown in red.

non-interacting electron in dot i, a term accounting for Coulomb interactions with other electrons in the system, and a term arising from possible external electrostatic potentials:

$$H_D^i = \sum_k \epsilon_{k,i} c_{k,i}^\dagger c_{k,i} + \sum_j E_c^{i,j} \hat{n}_i \hat{n}_j + \hat{n}_i e V_i \tag{3.2.3}$$

where $c_{k,i}^\dagger$ creates a particle in state k in the i^{th} dot, and

$$\hat{n}_i = \sum_k c_{k,i}^\dagger c_{k,i} \tag{3.2.4}$$

is the number operator of dot i. In equation 3.2.3, E_c^{ij} arises from the Coulomb interaction between dots i and j, and $E_c^{i,j} = e^2/\kappa r_{ij}$ if $i \neq j$ and $E_c^{ij} = e^2/\kappa\xi$ if $i = j$. Besides, V_i is the external electrostatic potential in dot i, originating from the gate voltage, source-drain bias and possible charged impurities in the substrate or sample. $\epsilon_{k,i}$ is the single-electron energy (equal to zero at the Fermi level) corresponding to state k in graphene dot number i. We besides

assume that tunneling terms $H_T^{i,j}$ are of the form

$$H_T^{i,j} = \sum_{k,p} t_{kp}^{ij} c_{p,j}^{\dagger} c_{k,i} \tag{3.2.5}$$

Following [62, 64], we write

$$t_{kp}^{ij} = t\psi_{p,j}^{*}(l_{ij})\psi_{k,i}(r_{ij}) \tag{3.2.6}$$

where $\psi_{k,i}$is the wave function of state k in dot i. From an idealized point-contact picture, $l_{ij}$and r_{ij} are the coordinates of the points between which tunneling from dot i to dot j typically occurs. We can now describe the main conduction mechanisms in granular metals described by Hamiltonian H, assuming that $|t|$ is much smaller than the typical charging energy E_c^{ii}, and that the corresponding tunneling conductance is much smaller than the intra-dot conductivity.

3.2.2 Sequential tunneling

At temperatures T larger than the average charging energy, the main conduction mechanism is known as sequential tunneling, and leads to a conductivity exhibiting an activated behavior [106]

$$\sigma_{GM}(T) \propto e^{-\frac{U}{k_B T}} \tag{3.2.7}$$

where U is an energy scale of the order of the dot charging energy. In the sequential tunneling regime, thermally excited charge carriers can pay the charging energy cost to tunnel to a neighboring grain, hence leading to the above activated behavior. However, as T becomes much small than the dot charging energy, σ_{GM} is exponentially suppressed and sequential tunneling may not remain the dominant conduction mechanism.

3.2.3 Multiple inelastic co-tunneling

We now focus on cases where the temperature is much smaller than the charging energy. We treat the tunneling hamiltonian H_T as a small perturbation and calculate the probability amplitudes for the dominant transport mechanisms connecting two given distant dots i and f. Such transport mechanisms can involve different electrons inelastically tunneling between neighboring dots along a chain of dots linking i and f, a single electron elastically hopping from i to f via multiple intermediate virtual tunneling events, or a combination of both inelastic and elastic processes. Inelastic processes require a finite temperature or electric field, while elastic processes can occur at vanishingly small temperature or electric field. For the sake of simplicity, we will consider only two cases: either all intermediate tunneling events are inelastic and involve a distinct charge carrier, or only one charge carrier elastically hops from the initial to the final grain. While the former, called multiple inelastic mechanism, is expected to dominate at sufficiently high temperatures or electric fields, the latter, coined multiple elastic mechanism, should dominate in the limit of vanishingly small temperatures or electric fields. Both process types are depicted in Figure 3.2.2. Intuitively, hybrid phenomena involving a combination of inelastic and elastic processes should be crossover phenomena, dominating only in narrow intervals of temperatures or fields [83]. We first treat the case of multiple inelastic co-tunneling. Multiple elastic co-tunneling will be discussed later, in section 3.2.4.

3.2.3.1 Rate of multiple inelastic co-tunneling: a general expression

We first derive a general expression for the multiple inelastic co-tunneling rate in a granular metal, without assuming any particular intra-dot energy spectrum. Here, we follow a perturbative approach similar to the work of Feigel'man and Ioselevich [83]. Given the nature of multiple inelastic co-tunneling, we need to consider multiple charge-carriers. We consider N grains forming a chain,

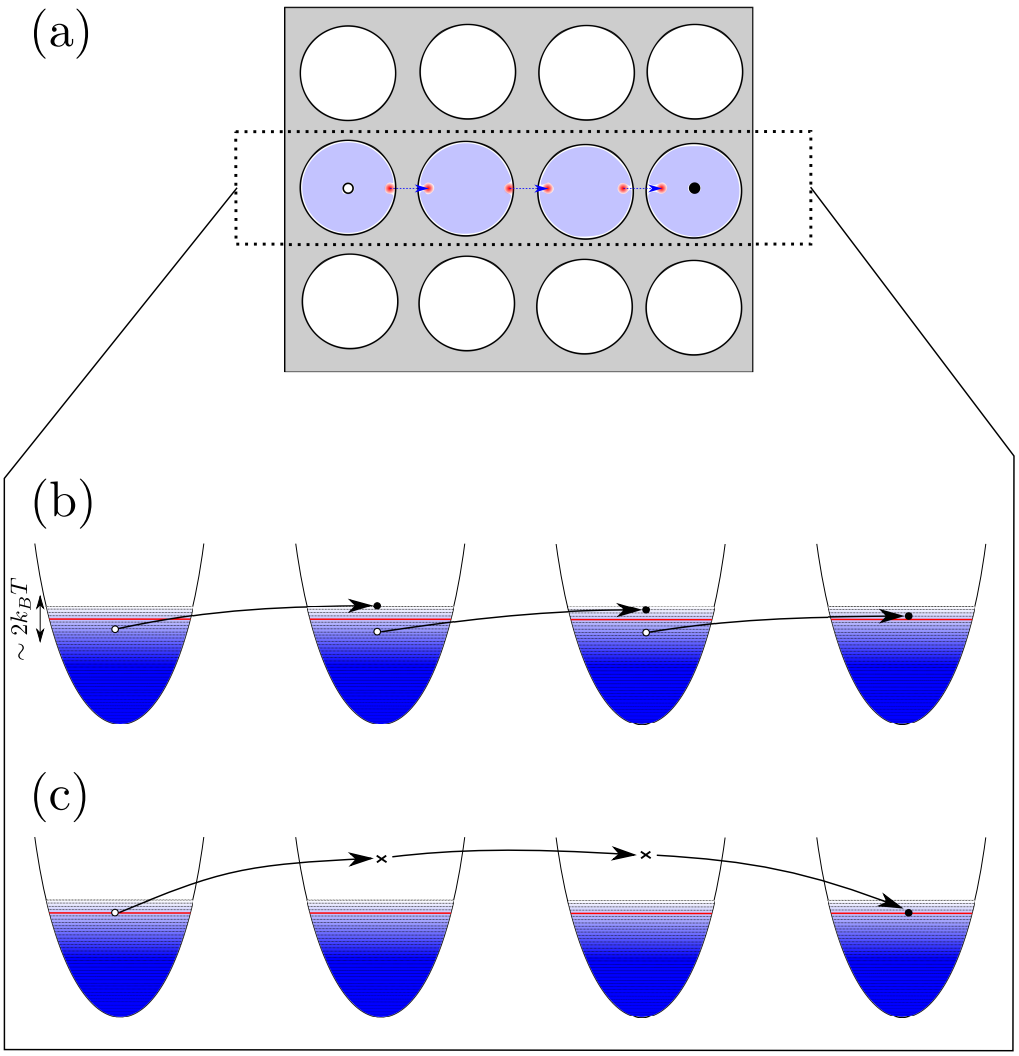

Figure 3.2.2: Schematic of multiple inelastic (b) and elastic (c) co-tunneling mechansims for a two-dimensional granular metal (a) with parabolic dot spectrum. In (a), dots involved in high-order conduction mechanisms (b) and (c) are shown in blue. In (a), (b) and (c) electrons (holes) are represented by black disks (circles). In (b) and (c), the Fermi level is represented by a red solid line. The gadient of blue represents the density of occupied states at finite temperature T, from fully occupied (dark blue) to empty (white). Dashed lines are energy levels (almost unoccupied levels are not shown). In (c), crosses represent the intermediate energy levels through which the electron tunnels.

numbered from 1 to N. Let $|\psi_{k_1,1}\rangle$, $|\psi_{k_2,2}\rangle$, ..., $|\psi_{k_N,N}\rangle$ be eigenstates of grains 1, 2, ..., N respectively, of eigenenergies $\epsilon_{k_1,1}$, $\epsilon_{k_2,2}$, ...,$\epsilon_{k_N,N}$. We also set $|\psi\rangle = |\psi_{k_1,1}\rangle|\psi_{k_2,2}\rangle...|\psi_{k_N,N}\rangle$. We thus have:

$$H_D|\psi\rangle = \sum_{i=1}^{N}(\epsilon_{k_i,i} + \mathcal{E}_i)|\psi\rangle \tag{3.2.8}$$

where $\mathcal{E}_i$ is the electrostatic energy of an electron in dot i:

$$\mathcal{E}_i = \sum_j E_c^{i,j} n_i n_j + n_i e V_i \tag{3.2.9}$$

where n_i is the number of electrons in dot i. We aim to calculate the actual N-particle eigenstate $|\psi_{tot}\rangle$ of H seen as a perturbation of $|\psi\rangle$ in the small tunneling amplitude limit. We write

$$|\psi_{tot}\rangle = |\psi\rangle + |\delta\psi\rangle \tag{3.2.10}$$

and

$$H|\psi_{tot}\rangle = E_{tot}|\psi_{tot}\rangle \tag{3.2.11}$$

where E_{tot} is the energy of the pertubed state $|\psi_{tot}\rangle$. E_{tot} is generally different from

$$E_0 = \sum_{i=1}^{N}(\epsilon_{k_i,i} + \mathcal{E}_i) \tag{3.2.12}$$

since we consider inelastic tunneling. However, the difference $E_{tot} - E_0 = \delta E_0$ is small compared to E_0. We have:

$$(H_D + H_T)|\delta\psi\rangle + H_T|\psi\rangle = \delta E_0|\psi\rangle + E_{tot}|\delta\psi\rangle \tag{3.2.13}$$

leading to

$$\begin{aligned} |\delta\psi\rangle &= (E_0 - H_D - (H_T - \delta E_0) + i\eta)^{-1}(H_T - \delta E_0)|\psi\rangle \\ &= G_{tot}(E_{tot})(H_T - \delta E_0)|\psi\rangle \end{aligned} \tag{3.2.14}$$

Since

$$G_{tot}(E_{tot}) = \sum_{n=0}^{+\infty} (G_0(E_0)(H_T - \delta E_0))^n G_0(E_0) \tag{3.2.15}$$

we have:

$$|\delta\psi\rangle = \sum_{n=1}^{+\infty} (G_0(E_0)(H_T - \delta E_0))^n |\psi\rangle \tag{3.2.16}$$

The probability amplitude for the transition from initial state $|\psi\rangle$ to final state $|\psi_f\rangle = |\psi_{k'_1,1}\rangle|\psi_{k'_2,2}\rangle...|\psi_{k'_N,N}\rangle$ is $\mathcal{A}(\vec{k},\vec{k'}) = \langle\psi_f|\delta\psi\rangle$. During multiple inelastic co-tunneling, the electron tunneling in a dot is different from the electron tunneling out of this dot, and hence $|\psi_{k_i,i}\rangle \neq |\psi_{k'_i,i}\rangle$ for all i. Therefore,

$$\mathcal{A}(\vec{k},\vec{k'}) = \sum_{n\geq N} \langle\psi_f|(G_0(E_0)(H_T - \delta E_0))^n|\psi\rangle \tag{3.2.17}$$

Both δE_0 and $|t|$ are small compared to the graphene grains charging energy, so that the dominant term in equation 3.2.17 is $\langle\psi_f|(G_0(E_0)(H_T - \delta E_0))^N|\psi\rangle$. Because for all i, $|\psi_{k_i,i}\rangle \neq |\psi_{k'_i,i}\rangle$, δE_0 does not contribute to the probability amplitude for MIC events $|\psi\rangle \to |\psi_f\rangle$, and we obtain:

$$\begin{aligned} \mathcal{A}(\vec{k},\vec{k'}) &\approx \langle\psi_f|(G_0(E_0)H_T)^N|\psi\rangle \\ &= \langle\psi_f| \sum_{i_1,i_2,...,i_{N-1}} G_0(E_0)H_T^{(i_{N-1})}G_0(E_0)H_T^{(i_{N-2})}...G_0(E_0)H_T^{(i_1)}|\psi\rangle \end{aligned} \tag{3.2.18}$$

where $H_T^{(i_p)}$ are all possible tunneling terms of H_T connecting adjacent grains along the path $1 \to 2 \to ... \to N$. In the above equation, only terms with pairwise distinct $H_T^{(i_p)}$ tunneling operators, connecting states $|\psi_{k_i,i}\rangle$ to states $|\psi_{k'_{i+1},i+1}\rangle$, contribute to the probability amplitude $\mathcal{A}(\vec{k},\vec{k'})$. However, all possible orderings of tunneling events $|\psi_{k_i,i}\rangle \to |\psi_{k'_{i+1},i+1}\rangle$ along the path $1 \to 2 \to ... \to N$ are allowed. Each operator $G_0(E_0)H_T^{(i_k)}$ in

$$G_0(E_0)H_T^{(i_{N-1})}G_0(E_0)H_T^{(i_{N-2})}...G_0(E_0)H_T^{(i_1)}|\psi\rangle$$

brings an extra factor of $\left[E_0 - E_{exc}^{(k)}(i_1, i_2, ..., i_k)\right]^{-1}$ where $E_{exc}^{(k)}(i_1, i_2, ..., i_k)$ is the energy of the excited state $G_0(E_0)H_T^{(i_k)}...G_0(E_0)H_T^{(i_1)}|\psi\rangle$ after k elementary tunneling events $i_1, i_2, ..., i_k$. Assuming both the temperature T and electric fields $E_{bias} = \frac{V_{i+1}-V_i}{\xi}$ are small, i.e. $k_BT \ll e^2/\kappa\xi$and $e\xi E_{bias} \ll e^2/\kappa\xi$, each elementary tunneling event increases the energy by an amount of the order of $\sim e^2/\kappa\xi$. Noting $\bar{E}_c$ the average excitation energy added by a tunneling event, $E_{exc}^{(k)}(i_1, i_2, ..., i_k) \approx E_0 + k\bar{E}_c$ and each term in equation 3.2.18 is proportional to $(-1)^{N-1}\left((N-1)!\bar{E}_c^{N-1}\right)^{-1}$. Since only $|\psi_{k_i,i}\rangle \to |\psi_{k'_{i+1},i+1}\rangle$ transitions contribute to probability amplitude $\mathcal{A}(\vec{k}, \vec{k}')$, each non-zero term in equation 3.2.18 has the same numerator

$$t^{N-1}(\psi_{k_1,1}(r_1)\psi^*_{k'_2,2}(l_2))\times(\psi_{k_2,2}(r_2)\psi^*_{k'_3,3}(l_3))\times...\times(\psi_{k_{N-1},N-1}(r_{N-1})\psi^*_{k'_N,N}(l_N))$$

Taking into account the $(N-1)!$ different tunneling orderings, we obtain:

$$\mathcal{A}(\vec{k}, \vec{k}') \approx (-1)^{N-1}\left(\frac{t}{\bar{E}_c}\right)^{N-1}\prod_{i=1}^{N-1}(\psi_{k_i,i}(r_i)\psi^*_{k'_{i+1},i+1}(l_{i+1})) \tag{3.2.19}$$

The total probability of multiple inelastic co-tunneling along the path $1 \to 2 \to ... \to N$ is thus:

$$\mathcal{P}_{in,N} = \sum_{\vec{k},\vec{k}'}|\mathcal{A}(\vec{k}, \vec{k}')|^2 \tag{3.2.20}$$

Chaotic dots are well described by Gaussian ensembles, either Gaussian Unitary Ensemble (GUE) or the Gaussian Orthogonal Ensemble (GOE). In other words, the energy level statistics and corresponding wavefunctions are not correlated, and for a given state of wavefunction ψ, and given points $\vec{r}$ and $\vec{r}'$ in the dot, $\psi(\vec{r})$ and $\psi(\vec{r}')$ are identically distributed random variables having Gaussian probability distributions [65]. Performing an ensemble average $\langle ... \rangle$ on $\mathcal{P}_{in,N}$,

we obtain:

$$\langle \mathcal{P}_{in,N} \rangle = \left(\frac{|t|^2}{\bar{E}_c^2} \right)^{N-1} \sum_{\vec{k},\vec{k'}} \prod_{i=1}^{N-1} \langle |\psi_{k_i,i}(r_i)|^2 \rangle \left\langle |\psi_{k'_{i+1},i+1}(l_{i+1})|^2 \right\rangle \tag{3.2.21}$$

We now evaluate sums over k_i and k'_{i+1} by means of integrals. Noting $\mathcal{D}(\epsilon)$ the areal density of states in dots, and $f_{FD}(\epsilon)$ the Fermi-Dirac distribution, we do the following substitutions at finite temperature:

$$\sum_{k_i} \to \int_{-\infty}^{+\infty} d\epsilon_i \xi^2 \mathcal{D}(\epsilon_i) f_{FD}(\epsilon_i) \tag{3.2.22}$$

and

$$\sum_{k'_i} \to \int_{-\infty}^{+\infty} d\epsilon'_i \xi^2 \mathcal{D}(\epsilon'_i)(1 - f_{FD}(\epsilon'_i)) \tag{3.2.23}$$

We also write the sum $\sum_{\vec{k},\vec{k'}}$ such that the tunneling events $1 \to 2$ and $N - 1 \to N$ involve a charge carrier leaving the fixed ground state $k_1^{(0)}$ in dot 1 and reaching the excited state k_N^{ex} in dot N respectively. Noting Δ the energy difference between the charge carrier leaving dot 1 and the charge carrier reaching dot N, we obtain, since $\langle |\psi_{k_i,i}(r_i)|^2 \rangle = \left\langle |\psi_{k'_{i+1},i+1}(l_{i+1})|^2 \right\rangle = \xi^{-2}$:

$$\langle \mathcal{P}_{in,N} \rangle = \xi^{-4} \left(\frac{|t|^2}{\bar{E}_c^2} \right)^{N-1} f_{FD}(\epsilon_{k_1^{(0)},1})(1 - f_{FD}(\epsilon_{k_N^{ex},N})) \mathcal{I}_N(\Delta, T) \tag{3.2.24}$$

with

$$\begin{aligned} \mathcal{I}_N(\Delta, T) = & \prod_{i=1}^{N-1} \int_{-\infty}^{+\infty} d\epsilon_i \mathcal{D}(\epsilon_i) f_{FD}(\epsilon_i) \int_{-\infty}^{+\infty} d\epsilon'_i \mathcal{D}(\epsilon'_i)(1 - f_{FD}(\epsilon'_i)) \\ & \delta \left(\sum_{i=1}^{N-1} (\epsilon'_{i+1} - \epsilon_i) - \Delta \right) \end{aligned} \tag{3.2.25}$$

where $\delta \left(\sum_{i=1}^{N-1} (\epsilon'_{i+1} - \epsilon_i) - \Delta \right)$ enforces the energy conservation. Here, the energy conservation of the N-particle state is a clear idealization. During

multiple inelastic co-tunneling, individual charge carriers involved in the process virtually tunnel to a neighboring dot, before relaxing their energy. The energy relaxation can be done by phonon adsorption or emission, electron-electron interaction, or by interacting with electron-hole pairs created by the inelastic co-tunneling process itself [84]. While in the latter case, the energy conservation of the N-particle state applies, it is not strictly enforced when phonons are emitted or absorbed, or when energy is relaxed to other charge carriers in the system. For these reasons, a more accurate calculation would replace the δ-function by a peak-function F exhibiting a maximum at zero [66, 67, 68]. For the sake of simplicity, we will nonetheless follow Beloborodov et al and Feigel'man and Ioselevich [84, 83], and consider a delta function.

We now estimate the multiple integral $\mathcal{I}_N(\Delta, T)$. Using the Fourier representation of the Dirac δ function,

$$\begin{aligned}\delta\left(\sum_{i=1}^{N-1}(\epsilon'_{i+1}-\epsilon_i)-\Delta\right) &= \int_{-\infty}^{+\infty}\frac{dt}{2\pi\hbar}\exp\left[i\left(\sum_{i=1}^{N-1}(\epsilon'_{i+1}-\epsilon_i)-\Delta\right)t/\hbar\right] \\ &= \int_{-\infty}^{+\infty}\frac{dt}{2\pi\hbar}e^{-i\Delta t/\hbar}\prod_{i=1}^{N-1}e^{i(\epsilon'_{i+1}-\epsilon_i)t/\hbar} \qquad (3.2.26)\end{aligned}$$

we rewrite $\mathcal{I}_N(\Delta, T)$ as:

$$\begin{aligned}\mathcal{I}_N(\Delta,T) &= \int_{-\infty}^{+\infty}\frac{dt}{2\pi\hbar}e^{-i\Delta t/\hbar}\prod_{i=1}^{N-1}\int_{-\infty}^{+\infty}d\epsilon_i\mathcal{D}(\epsilon_i)f_{FD}(\epsilon_i)e^{-i\epsilon_i t/\hbar} \\ &\quad \prod_{i=1}^{N-1}\int_{-\infty}^{+\infty}d\epsilon'_i\mathcal{D}(\epsilon'_i)(1-f_{FD}(\epsilon'_i))e^{i\epsilon'_{i+1}t/\hbar} \qquad (3.2.27)\end{aligned}$$

For materials whose density of states is even in energy, such as graphene at half-filling, we have

$$\int_{-\infty}^{+\infty}d\omega\mathcal{D}(\omega)(1-f_{FD}(\omega))e^{i\omega t/\hbar} = \int_{-\infty}^{+\infty}d\omega\mathcal{D}(\omega)f_{FD}(\omega)e^{-i\omega t/\hbar} \qquad (3.2.28)$$

and hence:

$$\mathcal{I}_N(\Delta,T)=\int_{-\infty}^{+\infty}\frac{dt}{2\pi\hbar}e^{-i\Delta t/\hbar}\left(\int_{-\infty}^{+\infty}d\omega\mathcal{D}(\omega)f_{FD}(\omega)e^{-i\omega t/\hbar}\right)^{2(N-2)} \tag{3.2.29}$$

We next apply it to the particular cases of parabolic-band dots and granular Dirac materials, whose grains have a linear spectrum.

3.2.3.2 The case of parabolic-band two-dimensional electron gases

We first investigate the case of a constant density of states, $\mathcal{D}(\omega)=2\mathcal{D}_0$, where $\mathcal{D}_0$ is the density of states per spin, valid for parabolic-band two-dimensional electron gases. In this case, we have:

$$\mathcal{I}_N(\Delta,T)=\mathcal{D}_0^{2(N-2)}\int_{-\infty}^{+\infty}\frac{dt}{2\pi\hbar}e^{-i\Delta t/\hbar}\mathcal{F}(T,t)^{2(N-2)} \tag{3.2.30}$$

where

$$\mathcal{F}(T,t)=2\int_{-\infty}^{+\infty}d\omega f_{FD}(\omega)e^{-i\omega t/\hbar} \tag{3.2.31}$$

$\mathcal{F}(T,t)$ can be evaluated easily using the residue theorem. The poles ω_n of $f_{FD}(\omega)$ are located on the imaginary axis and read, for all integers n:

$$\omega_n=2ik_BT(\frac{\pi}{2}+n\pi) \tag{3.2.32}$$

so that:

$$\mathcal{F}(T,t)=4i\pi k_BT\sum_{n=0}^{+\infty}\frac{e^{-\omega_n/2k_BT}e^{-i\omega_nt/\hbar}}{\sinh(\omega_n/2k_BT)} \tag{3.2.33}$$

$$\begin{aligned}\mathcal{F}(T,t) &= 4i\pi k_BT\sum_{n=0}^{+\infty}\frac{e^{-\omega_n/2k_BT}e^{-i\omega_nt/\hbar}}{\sinh(\omega_n/2k_BT)}\\ &= \frac{2i\pi k_BT}{\sinh(\pi k_BTt/\hbar)}\end{aligned} \tag{3.2.34}$$

Therefore,

$$\mathcal{I}_N(\Delta,T)=\mathcal{D}_0^{2(N-2)}\int_{-\infty}^{+\infty}\frac{dt}{2\pi\hbar}e^{-i\Delta t/\hbar}\left(\frac{2i\pi k_BT}{\sinh(\pi k_BTt/\hbar)}\right)^{2(N-2)} \tag{3.2.35}$$

The integrand in equation 3.2.35 has zero as a pole of order $2(N-2)$. Nevertheless, this problem can be cured by integrating in the lower or upper half of the complex plane, i.e. doing the substitution:

$$\int_{-\infty}^{+\infty}\rightarrow\int_{-\infty+i\eta}^{+\infty+i\eta} \tag{3.2.36}$$

where $\eta=0^{\pm}$. Noticing that

$$\mathcal{I}_N(\Delta,T)=\mathcal{D}_0^{2(N-2)}\int_{-\infty+i\eta}^{+\infty+i\eta}\frac{dt}{2\pi\hbar}e^{-i\Delta t/\hbar}\left(\frac{2\pi k_BT}{\cosh(\pi k_BTt/\hbar+i\pi/2)}\right)^{2(N-2)} \tag{3.2.37}$$

and doing the change of variable $\tau=t+\frac{i\hbar}{2k_BT}$, we obtain:

$$\mathcal{I}_N(\Delta,T)=e^{-\Delta/2k_BT}\mathcal{D}_0^{2(N-2)}\int_{-\infty+i\eta+\frac{i\hbar}{2k_BT}}^{+\infty+i\eta+\frac{i\hbar}{2k_BT}}\frac{d\tau}{2\pi\hbar}e^{-i\Delta\tau/\hbar}\left(\frac{2\pi k_BT}{\cosh(\pi k_BT\tau/\hbar)}\right)^{2(N-2)} \tag{3.2.38}$$

Performing a second change of variable, $u=\exp(-2\pi k_BT\tau/\hbar)$ leads to:

$$\mathcal{I}_N(\Delta,T)=-\frac{e^{-\Delta/2k_BT}}{(2\pi)^2k_BT}\left[4\pi k_BT\mathcal{D}_0\right]^{2(N-2)}\int_{D_\eta}du\frac{u^{N-3+i\Delta/2\pi k_BT}}{(1+u)^{2N}} \tag{3.2.39}$$

where the integration domain D_η corresponds to the semi-infinite line $]-\infty,0]$ rotated by an angle of η. Choosing $\eta>0$, the integral over D_η can be replaced by an integral over $[0,+\infty[$ because the integrand does not admit any pole other than -1. This leads to:

$$\mathcal{I}_N(\Delta,T)=\frac{e^{-\Delta/2k_BT}}{(2\pi)^2k_BT}\left[4\pi k_BT\mathcal{D}_0\right]^{2(N-2)}\int_{0}^{+\infty}du\frac{u^{N-3+i\Delta/2\pi k_BT}}{(1+u)^{2N}} \tag{3.2.40}$$

In equation 3.2.40, we recognize the Euler Beta function,

$$B(N-2+i\Delta/2\pi k_BT, N-2-i\Delta/2\pi k_BT) = \int_0^{+\infty} du \frac{u^{N-3+i\Delta/2\pi k_BT}}{(1+u)^{2N}} \tag{3.2.41}$$

which can easily be written in terms of Euler Gamma functions,

$$\begin{aligned} &B(N-2+i\Delta/2\pi k_BT, \\ &\quad N-2-i\Delta/2\pi k_BT) \\ &\qquad = \frac{\Gamma(N-2+i\Delta/2\pi k_BT)\Gamma(N-2-i\Delta/2\pi k_BT)}{\Gamma(2(N-2))} \\ &\qquad = \frac{|\Gamma(N-2+i\Delta/2\pi k_BT)|^2}{\Gamma(2(N-2))} \end{aligned} \tag{3.2.42}$$

Putting all pieces together, we finally end up with:

$$\langle \mathcal{P}_{in,N} \rangle = \frac{|t|^2 \mathcal{W} \xi^{-4}}{(2\pi)^2 \bar{E}_c^2 k_BT} e^{-\Delta/2k_BT} \left(\frac{4\pi k_BT \mathcal{D}_0 |t|}{\bar{E}_c} \right)^{2N_{int}} \frac{|\Gamma(N_{int}+i\Delta/2\pi k_BT)|^2}{\Gamma(2N_{int})} \tag{3.2.43}$$

with $\mathcal{W} = f_{FD}(\epsilon_{k_1^{(0)},1})(1-f_{FD}(\epsilon_{k_N^{ex},N}))$. In equation 3.2.43, $N_{int} = N-2$ is the number of intermediate grains standing between initial and final dots involved in the multiple inelastic co-tunneling (MIC) process. Introducing the dimensionless inter-grain conductance

$$g = \pi |t|^2 \mathcal{D}_0^2 \tag{3.2.44}$$

equation 3.2.43 suggests the existence of an effective elementary inelastic tunneling probability

$$p_{in} = 16\pi g \left(\frac{k_BT}{\bar{E}_c} \right)^2 \tag{3.2.45}$$

which is vanishingly small in the low-temperature regime $k_BT \ll \bar{E}_c$ in which MIC nonetheless dominates the "orthodox" sequential tunneling mechanism. We can further simplify equation 3.2.43 by invoking the Efros-Shklovskii argument [60]: because of the unavoidable Coulomb interaction between an

electron excited from ground state and the corresponding hole left behind, the density of states $\nu(\epsilon)$ of the entire granular system must vanish at the Fermi level E_F. In two-dimensions in particular, the density of states at E_F vanishes linearly in energy,

$$\nu(\epsilon) \sim \left(\frac{\kappa}{e^2}\right)^2 |\epsilon - E_F| \tag{3.2.46}$$

and correspondingly, we have:

$$\Delta \sim \frac{Ce^2}{\kappa N_{int}\xi} \tag{3.2.47}$$

for some constant C of the order of unity. Defining the "charging temperature" $T_c = \frac{e^2}{\kappa\xi}$ and probability prefactor

$$\alpha = \frac{|t|^2 \mathcal{W} \xi^{-4}}{(2\pi)^2 \bar{E}_c^2 k_B T} \tag{3.2.48}$$

the MIC probability now reads:

$$\langle \mathcal{P}_{in,N} \rangle = \alpha p_{in}^{N_{int}} \frac{|\Gamma(N_{int} + i\Delta/2\pi k_B T)|^2}{\Gamma(2N_{int})} \exp\left(-\frac{CT_c}{2N_{int}T}\right) \tag{3.2.49}$$

So far, N_{int} was a free parameter of the problem. However, the measured MIC-induced conductivity of a large-enough two-dimensional granular metal in the insulating regime is necessarily dominated by almost optimally conducting pathways. Corresponding pathways comprise links of $\sim N_{int} + 2$ grains, such that N_{int} maximizes $\langle \mathcal{P}_{in,N} \rangle$, or equivalently the "action" [84]:

$$\varphi(N_{int}) = N_{int} \ln p_{in} + 2 \ln |\Gamma(N_{int} + i\Delta/2\pi k_B T)| - \ln \Gamma(2N_{int}) - \frac{CT_c}{2N_{int}T} \tag{3.2.50}$$

Applying Stirling formula in the limit of low temperatures T and large N_{int}, we have $\ln\Gamma(2N_{int}) = \ln(\pi/N_{int})/2 + 2N_{int}\ln(2N_{int}) - 2N_{int}$ and

$$\begin{aligned}\ln\left(|\Gamma(N_{int}+i\Delta/2\pi k_BT)|^2\right) &\approx \ln(2\pi) + (N_{int}-\frac{1}{2})\ln\left(N_{int}^2+\left(\frac{\Delta}{2\pi k_BT}\right)^2\right)\\ &- \frac{\Delta}{\pi k_BT}\arctan\left(\frac{\Delta}{2\pi N_{int}k_BT}\right) \qquad (3.2.51)\end{aligned}$$

In this double limit, we can easily find the number of intermediate grains $N_{int} = N_{hop}$ which typically maximizes the action, by requiring:

$$\frac{\partial\varphi}{\partial N_{int}}(N_{hop}) = \ln\left(\frac{p_{in}}{4}\right) + 2 + \ln(1+x^2) + \pi x(1+\frac{2}{\pi}\arctan x) = 0 \quad (3.2.52)$$

where we set

$$x = \frac{\Delta}{2\pi N_{hop}k_BT} \qquad (3.2.53)$$

Equation 3.2.52 indicates that x must be large at low temperatures, when p_{in} is vanishingly small. More precisely,

$$x \approx \frac{1}{2\pi}\ln\left(\frac{1}{p_{in}}\right) \qquad (3.2.54)$$

and hence

$$N_{hop} \approx \sqrt{\frac{CT_c}{\ln\left(\frac{1}{p_{in}}\right)T}} \qquad (3.2.55)$$

Since the action reads

$$\begin{aligned}\varphi(N_{int}) &\approx N_{int}\left(\ln p_{in} + \ln\left(1+\left(\frac{\Delta}{2\pi N_{int}k_BT}\right)^2\right) + 2 - 2\ln 2\right)\\ &- \frac{\Delta}{2k_BT}\left(1+\frac{2}{\pi}\arctan\left(\frac{\Delta}{2\pi N_{int}k_BT}\right)\right) \qquad (3.2.56)\end{aligned}$$

equation 3.2.52 directly implies that the action takes the maximum value:

$$\begin{aligned}\varphi(N_{hop}) &\approx -\frac{\Delta}{k_B T}(1+\frac{2}{\pi}\arctan x)\\ &\approx -\frac{2\Delta}{k_B T}\end{aligned} \tag{3.2.57}$$

and finally, using equation 3.2.55, we end up with:

$$\varphi(N_{hop}) = -\sqrt{4C\ln\left(\frac{1}{p_{in}}\right)\frac{T_c}{T}} \tag{3.2.58}$$

This strinkingly resembles the Efros-Shklokski law $\varphi_{ES} \propto -T^{-1/2}$, except that the charging temperature T_c is renormalized by a weakly temperature-dependent factor of $4C\ln\left(\frac{1}{p_{in}}\right)$ which logarithmically diverges as $T \to 0$K. Though the underlying mechanism behind multiple inelastic co-tunneling is clearly different from Efros-Shklovskii variable-range hopping mechanism [104], it yields a conductivity with the same temperature-dependence and hence provides a compelling explanation for experimental results obtained so far in granular metals. Besides, action $\varphi(N_{hop})$ has a much smaller magnitude than E_c/T in the $T \ll E_c$ regime, showing that multiple inelastic co-tunneling dominates over sequential tunneling in the small temperature limit.

Similarly, the typical hopping distance $N_{hop}\xi$ and corresponding action φ can be calculated for a finite electric field E_{sd} induced by the source-drain voltage and at $T = 0$K. In this case, equation 3.2.35 simply becomes

$$\begin{aligned}\mathcal{I}_N(\Delta,T) &= \mathcal{D}_0^{2N_{int}}\int_{-\infty+i\eta}^{+\infty+i\eta}\frac{dt}{2\pi\hbar}e^{-i\Delta t/\hbar}\left(\frac{2i\hbar}{t}\right)^{2N_{int}}\\ &= \frac{(4\mathcal{D}_0^2\Delta^2)^{N_{int}}}{|\Delta|(2N_{int}-1)!}\end{aligned} \tag{3.2.59}$$

and hence:

$$\langle\mathcal{P}_{in,N}(T=0)\rangle = \frac{\mathcal{W}\xi^{-4}|t|^2}{(2N_{int}-1)!|\Delta|\bar{E}_c^2}\left(\frac{4\mathcal{D}_0^2\Delta^2|t|^2}{\bar{E}_c^2}\right)^{N_{int}} \tag{3.2.60}$$

The difference Δ in energy between the initial and final states is now essentially due to the electric field E_{sd},

$$\Delta \approx e\xi E_{sd} N_{int} \tag{3.2.61}$$

so that

$$\langle \mathcal{P}_{in,N}(T=0) \rangle = \frac{2\mathcal{W}\xi^{-4}|t|^2}{e\xi|E_{sd}|\bar{E}_c^2} \left(\frac{(2N_{int})^{2N_{int}-1}}{(2N_{int}-1)!} \right) \left(\frac{g(e\xi E_{sd})^2}{\pi \bar{E}_c^2} \right)^{N_{int}} \tag{3.2.62}$$

and the effective elementary inelastic tunneling probability now becomes

$$p_{in}(T=0) = \frac{g}{\pi} \left(\frac{e\xi E_{sd}}{\bar{E}_c} \right)^2 \tag{3.2.63}$$

The typical number of intermediate grains involved in an MIC event at $T = 0$K and finite E_{sd} can easily be computed. Unlike the non-zero temperatures case, MIC events at finite E_{sd} and $T = 0$K always involve

$$N_{hop}(T=0) \approx \sqrt{\frac{CT_c}{eE_{sd}\xi}} \tag{3.2.64}$$

grains, due to both the equality $\Delta \approx e\xi E_{sd} N_{int}$ expressing the typical bias between initial and final grains, and the Efros-Shklovski constraint $\Delta \sim CT_c/N_{int}$. Using the Stirling approximation, we thus obtain

$$\langle \mathcal{P}_{in,N}(T=0) \rangle \propto e^{2N_{hop}} e^{N_{hop} \ln p_{in}(0)}, \tag{3.2.65}$$

which in the low-field limit $e\xi E_{sd} \ll \bar{E}_c$ becomes:

$$\langle \mathcal{P}_{in,N}(T=0) \rangle \propto \exp\left(-\sqrt{\frac{C \ln^2 p_{in}(0) T_c}{eE_{sd}\xi}} \right) \tag{3.2.66}$$

Again $\langle \mathcal{P}_{in,N}(T=0) \rangle$ has the same electric-field dependence as the Efros-Shklovskii variable-range hopping conductivity at $T = 0$ K.

3.2.3.3 The case of graphene at low Fermi energy

We next calculate $\langle \mathcal{P}_{in,N} \rangle$ for granular graphene, when the Fermi level lies close to the Dirac point. We now have $\mathcal{D}(\omega) = \frac{2}{\pi} \frac{|\omega|}{(\hbar v_F)^2}$, and:

$$\mathcal{I}_{gr,N}(\Delta, T) = \left(\frac{1}{\pi(\hbar v_F)^2} \right)^{2N_{int}} \int_{-\infty}^{+\infty} \frac{dt}{2\pi\hbar} e^{-i\Delta t/\hbar} \mathcal{F}_{gr}(T,t)^{2N_{int}} \quad (3.2.67)$$

with

$$\mathcal{F}_{gr}(T,t) = 2 \int_{-\infty}^{+\infty} d\omega |\omega| f_{FD}(\omega) e^{-i\omega t/\hbar} \quad (3.2.68)$$

At finite temperature T, $\mathcal{F}_{gr}(T,t)$ reads:

$$\begin{aligned} \mathcal{F}_{gr}(T,t) &= \frac{k_B T^2}{2} \left(\psi^{(1)} \left(-\frac{ik_B T t}{2\hbar} \right) - \psi^{(1)} \left(\frac{1}{2} - \frac{ik_B T t}{2\hbar} \right) \right. \\ &+ \left. \psi^{(1)} \left(\frac{1}{2} + \frac{ik_B T t}{2\hbar} \right) - \psi^{(1)} \left(1 + \frac{ik_B T t}{2\hbar} \right) \right) \end{aligned} \quad (3.2.69)$$

where $\psi^{(1)}$ is the first derivative of the digamma function. For the sake of simplicity, we calculate $\mathcal{I}_{gr,N}(\Delta, T)$ at $T = 0$K, as

$$\mathcal{F}_{gr}(T = 0K, t) = -\frac{2\hbar^2}{t^2} \quad (3.2.70)$$

In the zero-Kelvin limit, we thus have:

$$\mathcal{I}_{gr,N}(\Delta, T = 0K) = \left(\frac{2\hbar^2}{\pi(\hbar v_F)^2} \right)^{2N_{int}} \int_{-\infty+i\tau}^{+\infty+i\tau} \frac{dt}{2\pi\hbar} e^{-i\Delta t/\hbar} t^{-4N_{int}} \quad (3.2.71)$$

where τ is an infinitesimal real time. The only pole of the above integrand is 0, and it is of order 1. Applying the residue theorem, we easily obtain

$$\mathcal{I}_{gr,N}(\Delta, T = 0K) = \frac{1}{|\Delta|(4N_{int} - 1)!} \left(\frac{2\Delta^2}{\pi(\hbar v_F)^2} \right)^{2N_{int}} \quad (3.2.72)$$

where the sign of τ has been chosen such that the winding number and Δ are of opposite sign. We therefore end up with the following MIC probability:

$$\langle \mathcal{P}^{gr}_{in,N}(T=0)\rangle = \frac{\xi^{-4}\mathcal{W}|t|^2}{|\Delta|\bar{E}_c^2(4N_{int}-1)!}\left(\frac{2\Delta^2|t|}{\pi(\hbar v_F)^2\bar{E}_c}\right)^{2N_{int}} \tag{3.2.73}$$

This expression can be further simplified. Introducing the N_{int}-independent prefactor $\alpha' = \xi^{-4}\mathcal{W}|t|^2/e\xi|E_{sd}|\bar{E}_c^2$ and the typical level spacing in graphene dots $\Delta_0 = \hbar v_F/\xi$, we obtain, given that $\Delta \approx e\xi E_{sd}N_{int}$:

$$\langle \mathcal{P}^{gr}_{in,N}(T=0)\rangle = \frac{\alpha'(4N_{int})^{4N_{int}-1}}{(4N_{int}-1)!}\left(\frac{e^2E_{sd}^2|t|}{8\pi\Delta_0^2\bar{E}_c}\right)^{2N_{int}} \tag{3.2.74}$$

For granular graphene with the Fermi level close to the Dirac point, the effective elementary inelastic tunneling probability thus reads, at $T = 0$K:

$$p^{gr}_{in}(0) = g\left(\frac{e^2E_{sd}^2\xi^2}{8\pi\Delta_0\bar{E}_c}\right)^2 \tag{3.2.75}$$

In the low electric-field limit, we thus recover a result similar to equation 3.2.66,

$$\langle \mathcal{P}^{gr}_{in,N}(T=0)\rangle \propto \exp\left(-\sqrt{\frac{C\ln^2 p^{gr}_{in}(0)T_c}{eE_{sd}\xi}}\right) \tag{3.2.76}$$

Since in graphene, $\bar{E}_c \sim \frac{e^2}{\kappa\xi}$ is of the same order of magnitude as $\Delta_0 = \frac{\hbar v_F}{\xi}$,

$$\begin{aligned}\ln(p^{gr}_{in}(0)) &= 2\ln\left(\frac{\bar{E}_c}{\Delta_0}\right) + 2\ln p_{in}(0) - \ln(64g)\\ &\sim 2\ln p_{in}(0) - \ln(64g)\end{aligned} \tag{3.2.77}$$

Therefore, for "moderately" insulating granular graphene, $g \sim 10^{-2}$ to 10^{-1}, the E_{sd}-dependence of the conductance $G_{gr}(E_{sd})$ is expected to be close to the E_{sd}-dependence of the conductance $G_{para}(E_{sd})$ for granular parabolic-band 2DEGs. Theoretically, both $\ln G_{gr}(E_{sd})$ and $\ln G_{para}(E_{sd})$ have a $\sim \sqrt{E_0/E_{sd}}$ behavior with similar values of E_0. Naturally, the same situation is expected at

finite temperatures, i.e. comparable $G_{gr}(T)$ and $G_{para}(T)$, with experimentally indistinguishable temperature dependences.

3.2.3.4 Fluctuations of multiple inelastic cotunneling

In previous paragraphs, we calculated the average probability of MIC, and derived an expression for the conductance G_{MIC} associated with this transport mechanism, both for parabolic-band grains and graphene grains. It was shown that G_{MIC} has similar temperature and electric-field dependences as the Efros-Shklovskii law, though the underlying transport mechanisms are different. Unlike Efros-Shklovskii variable-range hopping in amorphous media, single MIC events in granular metals involve multiple charge-carriers which "cooperatively" tunnel between neighboring grains. We thus expect a much larger temperature-dependence for the mesoscopic fluctuations of $\ln G_{MIC}$ compared to the case of Efros-Shklovskii variable-range hopping. To verify this intuitive picture, we aim to derive in this section a probability distribution for the probability of multiple inelastic cotunneling, i.e. calculating $\mathbb{P}(P_{MIC} = p)$.

Setting

$$S_{i,\pm}(\vec{\rho},\tau) = \sum_{\epsilon_{k_i,i}} f_{FD}(\pm\epsilon_{k_i,i}) e^{\mp i\epsilon_{k_i,i}\tau/\hbar} |\psi_{k_i,i}(\vec{\rho})|^2 \tag{3.2.78}$$

and using results from the previous section, the probability of MIC along a path $1 \to 2 \to ... \to N$ reads:

$$\mathcal{P}_{in,N} = \frac{\mathcal{W}}{\xi^4} \left(\frac{|t|^2}{\bar{E}_c^2}\right)^{N-1} \int_{-\infty}^{+\infty} \frac{d\tau}{2\pi} e^{-i\Delta\tau/\hbar} \prod_{i=2}^{N-1} S_{i,\pm}(\vec{r}_i,\tau) S_{i,\pm}(\vec{l}_i,\tau) \tag{3.2.79}$$

Given two independent random vectors with M components $(X_1, X_2, ..., X_M)$ and $(Y_1, Y_2, ..., Y_M)$, and assuming that $Y_1, ..., Y_{\mathsf{M}}$ are identically distributed random variables, then

$$L = \sum_{i=1}^{M} X_i Y_i \tag{3.2.80}$$

and

$$\tilde{L} = \left(\sum_{i=1}^{M} X_i \right) \frac{1}{M} \sum_{i=1}^{M} Y_i \tag{3.2.81}$$

have asymptotically the same probability distributions in the $M \to +\infty$ limit. This is easily shown by comparing n-order moments $\langle L^n \rangle$ and $\left\langle \tilde{L}^n \right\rangle$, which in the $M \gg 1$ limit verify:

$$\langle L^n \rangle \sim \left\langle \tilde{L}^n \right\rangle \sim \sum_{i_1, i_2, ... i_n} \langle X_{i_1} X_{i_2} ... X_{i_n} \rangle \langle Y \rangle^n \tag{3.2.82}$$

Based on this observation, we can write:

$$S_{i,\pm}(\vec{\rho}, \tau) \approx \frac{\xi^2}{N_{th}} \left(\int_{-\infty}^{+\infty} d\epsilon \mathcal{D}(\epsilon) f_{FD}(\pm\epsilon) e^{\mp i\epsilon\tau/\hbar} \right) \mathcal{S}_{th,i}(\vec{\rho}, T) \tag{3.2.83}$$

with

$$\mathcal{S}_{th,i}(\vec{\rho}, T) = \sum_{|\epsilon_{k_i,i} - E_F| \lesssim k_B T} |\psi_{\epsilon_{k_i,i}}(\vec{\rho})|^2 \tag{3.2.84}$$

where N_{th} is the typical number of energy levels within $\sim k_B T$ around the Fermi level E_F. If dots are described by the Gaussian Orthogonal (Unitary) Ensemble, then eigenvectors are real (complex) and $\mathcal{S}_{th,i}(T)$ is the sum of βN_{th} identically distributed random real Gaussian variables of mean 0 and standard deviation $\sigma \sim \xi^{-1}$ with $\beta = 1$ ($\beta = 2$). Therefore, random variables $\mathcal{S}_{th,i}(\vec{\rho}, T)$ follow a chi-squared law

$$\mathbb{P}(\mathcal{S}_{th,i}(\vec{\rho}, T) = s) = \frac{s^{\frac{\beta N_{th}}{2} - 1} e^{-\frac{s}{2\sigma^2}}}{2^{\beta N_{th}/2} \sigma^{\beta N_{th}} \Gamma(\beta N_{th}/2)}, \tag{3.2.85}$$

and $\mathcal{P}_{in,N}$ is a product of $2N_{int}$ such random variables:

$$\mathcal{P}_{in,N} = \mathcal{W} \xi^{4(N_{int}-1)} \mathcal{I}_N(\Delta, T) \left(\frac{|t|^2}{\bar{E}_c^2} \right)^{N-1} \prod_{i=2}^{N-1} \mathcal{S}_{th,i}(\vec{r}_i, T) \mathcal{S}_{th,i}(\vec{l}_i, T) \tag{3.2.86}$$

The natural measure of conductance fluctuations in strongly disordered systems is the standard deviation of log-conductance, $\sigma_{\ln G}$. We thus need to

calculate the standard deviation $\sigma_{\ln S}$ of $\ln\left(\mathcal{S}_{th,i}(\vec{\rho},T)\right)$. We have:

$$\begin{aligned}\left\langle \ln\left(\mathcal{S}_{th,i}(\vec{\rho},T)\right)\right\rangle &= \int_{-\infty}^{+\infty} dx \frac{x e^{\frac{\beta N_{th}}{2}x} e^{-\frac{e^x}{2\sigma^2}}}{2^{\beta N_{th}/2}\sigma^{\beta N_{th}}\Gamma(\beta N_{th}/2)} \\ &= \ln(2\sigma^2) + \psi\left(\frac{\beta N_{th}}{2}\right)\end{aligned}$$

where again, ψ is the digamma function. Similarly calculating the second moment $\left\langle \ln^2\left(\mathcal{S}_{th,i}(\vec{\rho},T)\right)\right\rangle$, we easily obtain

$$\left\langle \ln^2\left(\mathcal{S}_{th,i}(\vec{\rho},T)\right)\right\rangle - \left\langle \ln\left(\mathcal{S}_{th,i}(\vec{\rho},T)\right)\right\rangle^2 = \psi^{(1)}\left(\frac{\beta N_{th}}{2}\right) \tag{3.2.87}$$

As soon as $x \gtrsim 1$, $\psi^{(1)}(x) \approx 1/x$. This approximation is accurate and does not require to be in the $x \gg 1$ limit to be valid. We can thus write

$$\sigma_{\ln S} \approx \sqrt{\frac{2}{\beta N_{th}}} \tag{3.2.88}$$

even when only few intra-dot energy levels exist within $\sim k_B T$ around the Fermi level. We can thus calculate the standard deviation $\sigma_{\ln \mathcal{P}}$ of $\ln\left(\mathcal{P}_{in,N}\right)$ for $N_{int} = N_{hop}$ in the small temperatures limit, when $N_{hop} \propto T^{-1/2}$ becomes large and the central limit theorem can be applied, while equation 3.2.88 remains valid in spite of small N_{th}. Since in addition $N_{th} \propto T$ for parabolic-band 2DEGs and $N_{th} \propto T^2$ (see appendix, section 3.5.6) for graphene close to the Dirac point, we end up with

$$\sigma_{\ln \mathcal{P}} \propto \sqrt{\frac{N_{hop}}{N_{th}}} \tag{3.2.89}$$

at low-enough temperatures. We now have to relate $\sigma_{\ln \mathcal{P}}$ at the scale of a hopping distance $N_{hop}\xi$ to the the fluctuations in log-conductance $\sigma_{\ln G}$ at the scale of an entire array of dots. This can be achieved by mapping the granular system to a resistor network whose vertices correspond to initial and final grains

i and f involved in MIC events, and edges are resistors of conductance

$$g_{MIC}^{i\to f} = g_0 e^{-\lambda X_{i\to f}} \tag{3.2.90}$$

where $g_{MIC}^{i\to f}$ is the MIC-induced conductance between grains i and f, $X_{i\to f}$ is a random variable with uniform distribution in $[0,1]$. In equation 3.2.90,

$$\lambda = 2\sqrt{3}\sigma_{\ln \mathcal{P}} \tag{3.2.91}$$

and

$$g_0 = \gamma_0 \exp\left(\frac{\lambda}{2} - \sqrt{\frac{\mathcal{K}_{in} T_c}{T}}\right) \tag{3.2.92}$$

where γ_0 is a numerical prefactor, $\mathcal{K}_{in}$ is such that $\langle \ln \mathcal{P}_{in,N} \rangle = -\sqrt{\frac{\mathcal{K}_{in} T_c}{T}}$. With such definitions, $\left\langle \ln g_{MIC}^{i\to f} \right\rangle = \langle \ln \mathcal{P}_{in,N} \rangle$ up to a constant, and $\ln g_{MIC}^{i\to f}$ has a standard deviation of $\sigma_{\ln \mathcal{P}}$. The advantage of operating this mapping to a random resistor network model is that the latter has been very well studied [70]. In particular, networks whose elementary random conductances follow the law described by equation 3.2.90 have a random resistivity $R_\square$ following a log-normal law [118, 114],

$$\mathbb{P}(R_\square = \rho) = \frac{1}{\sqrt{2\pi}\mu\rho} \exp\left(-\frac{\ln^2(g_e \rho)}{2\mu^2}\right) \tag{3.2.93}$$

where $\mu \sim \frac{\lambda^\nu}{l}$, $l = L/N_{hop}\xi$ is the granular system size L in units of the hopping distance $N_{hop}\xi$ and $\nu = 4/3$ is the critical exponent of the percolation correlation length in two dimensions. In equation 3.2.93, $g_e = g_0 e^{-p_c \lambda}$ where p_c is the percolation threshold. For a two-dimensional random resistor bond network, $p_c = 1/2$ and g_e is simply

$$g_e = \gamma_0 \exp\left(-\sqrt{\frac{\mathcal{K}_{in} T_c}{T}}\right) \tag{3.2.94}$$

which directly implies from equation 3.2.93 that the average granular system

conductivity $G_\square$ is g_e, an expected result. Most importantly, we obtain from equation 3.2.93 that the standard deviation of $\ln G_\square$ is $\sigma_{\ln G} = \mu$, and therefore:

$$\sigma_{\ln G} \propto N_{hop}\sigma^{\nu}_{\ln \mathcal{P}} \tag{3.2.95}$$

We thus have $\sigma_{\ln G} \propto N_{hop}^{1+\frac{\nu}{2}} N_{th}^{-\frac{\nu}{2}}$, which leads to $\sigma_{\ln G} \propto T^{-\frac{3\nu+2}{4}} \approx T^{-3/2}$ for parabolic-band dots and $\sigma_{\ln G} \propto T^{-\frac{5\nu+2}{4}} \approx T^{-13/6}$ for graphene grains with small Fermi energy. In the low-temperature limit, the fluctuations in log-conductance are much larger for granular metals with graphene grains than granular metals with parabolic-band grains. Interestingly, this means that the intra-grain energy spectrum can be distinguished in electron transport experiements in which the percolation network is tuned, for instance by means of a gate voltage. The above-results also show that experimentally, multiple inelastic co-tunneling can be easily distinguished from Efros-Shklovskii variable-range hopping. Though these transport mechanisms yield average conductances with similar temperature dependences, their fluctuations have drastically different behavior. More precisely, Efros-Shklovskii variable-range hopping leads to much less temperature-dependent conductance fluctuations, $\sigma^{ES}_{\ln G} \propto T^{-a}$ with $a < 1$, as shown by several authors [113].

3.2.4 Multiple elastic co-tunneling

Until now, we have shown that while sequential tunneling is the dominant electron-transport mechanism at temperatures T typically larger than the dots charging energy, multiple inelastic co-tunneling yields much larger conductivities as $k_B T \ll e^2/\kappa\xi$ and $e\xi E_{sd} \ll e^2/\kappa\xi$. However, MIC itself should become irrelevant at low temperatures and low electric fields. In this case, multiple elastic co-tunneling (MEC), introduced earlier, should become more important. In this section, we quantitatively study MEC, which involves only one electron. We can thus deal with single-electron states.

We first write the Schrödinger equation for a quasi-particle in the initial

dot, numbered as 1. At the Fermi level E_F,

$$(H_D + H_T)(\psi_1 + \delta\psi_1) = E_F(\psi_1 + \delta\psi_1) \tag{3.2.96}$$

where ψ_1 is the eigenstate of the quasi-particle in dot 1, and $\delta\psi_1$ is a perturbation to this state induced by the small tunneling term H_T. $\delta\psi_1$ thus reflects the possibility for the considered quasi-particle to be outside dot 1, and spans the entire granular system. By definition, ψ_1 obeys the Schrödinger equation:

$$H_D\psi_1 = E_F\psi_1 \tag{3.2.97}$$

Combining equations 3.2.96 and 3.2.97 thus yields:

$$(E_F\mathbb{I} - H_D - H_T)\delta\psi_1 = H_T\psi_1 \tag{3.2.98}$$

and hence:

$$\delta\psi_1 = G_{tot}(E_F)H_T\psi_1 \tag{3.2.99}$$

where $G_{tot}(E_F)$ is the total Green operator

$$G_{tot}(E_F) = \lim_{\eta\to 0^+}(E_F\mathbb{I} - H_D - H_T + i\eta)^{-1} \tag{3.2.100}$$

The perturbed Green operator can be simply related to the unperturbed one,

$$G_0(E_F) = \lim_{\eta\to 0^+}(E_F\mathbb{I} - H_D + i\eta)^{-1} \tag{3.2.101}$$

through the equation:

$$G_{tot}(E_F)^{-1} = G_0(E_F)^{-1} - H_T \tag{3.2.102}$$

A series expansion thus yields:

$$\delta\psi_1 = \sum_{n=1}^{+\infty} (G_0(E_F)H_T)^n \psi_1 \tag{3.2.103}$$

We assume that initial and final dots are connected by a path, comprising $N-2$ intermediate dots, which conducts exponentially better than all other paths linking initial and final dots. Dots along this path are numbered from 1 to N. The probability amplitude for a multiple elastic co-tunneling event between state ψ_N in final dot N and state ψ_1 thus reads:

$$\begin{aligned} \mathcal{A}(\psi_1 \to \psi_N) &= \sum_{n=1}^{+\infty} \langle \psi_N | (G_0(E_F)H_T)^n | \psi_1 \rangle \\ &\approx \langle \psi_N | (G_0(E_F)H_T)^N | \psi_1 \rangle \end{aligned} \tag{3.2.104}$$

Discarding all terms corresponding to dots outside the most conducting path and noting

$$\Delta E = \left(\prod_{i=1}^{N} (E_c n_i^2 + e\varphi_i n_i) \right)^{1/n} - E_F, \tag{3.2.105}$$

we obtain:

$$\mathcal{A}(\psi_1 \to \psi_N) \approx \sum_{p_2, p_3, \ldots, p_{N-1}} \frac{t^{1,2}_{p_1,p_2} \times t^{2,3}_{p_2,p_3} \times \ldots \times t^{N-1,N}_{p_{N-1},p_N}}{(-\epsilon_{p_2,2} - \Delta E + i\eta) \times \ldots \times (-\epsilon_{p_N,N} - \Delta E + i\eta)} \tag{3.2.106}$$

The corresponding probability $\mathcal{P}(\psi_1 \to \psi_N)$ thus verifies:

$$\begin{aligned} \mathcal{P}(\psi_1 \to \psi_N) \propto\ & |t|^{2(N-2)} \sum_{p_2,\ldots,p_{N-1}} \sum_{q_2,\ldots,q_{N-1}} \\ & \prod_{n=2}^{N-1} \frac{\psi_{p_n}(l_n)\psi^*_{p_n}(r_n)\psi^*_{q_n}(l_n)\psi_{q_n}(r_n)}{(\epsilon_{p_n,n} + \Delta E + i\eta)(\epsilon_{q_n,n} + \Delta E - i\eta)} \end{aligned} \tag{3.2.107}$$

where l_n (respectively r_n) labels the point of dot n through which the considered quasi-particle enters (respectively leaves) by tunneling. We model Hamil-

tonians H_D^i describing individual dots by random matrices in the orthogonal or unitary ensemble. In each grain, eigenvectors corresponding to different eigenstates are thus independtly distributed Gaussian variables, and eigenvectors and eigenvalues are uncorrelated. Besides, individual components of each eigenvector are independently distributed Gaussian variables, in the large-dot limit [65]. In other words,

$$\langle \psi_k^*(s)\psi_{k'}(s')\rangle = \frac{\delta_{k,k'}\delta_{s,s'}}{\mathcal{A}_{dot}} \tag{3.2.108}$$

where $\langle ...\rangle$ is the appropriate ensemble average and $\mathcal{A}_{dot} \approx \xi^2$ is the typical dot area. Ensemble-averaging the transition probability $\mathcal{P}(\psi_1 \to \psi_N)$, we obtain:

$$\begin{aligned}\langle \mathcal{P}(\psi_1 \to \psi_N)\rangle \quad \propto \quad & |t|^{2(N-2)} \sum_{p_2,\ldots,p_{N-1}} \sum_{q_2,\ldots,q_{N-1}} \\ & \prod_{n=2}^{N-1} \frac{\left\langle \psi_{p_n}(l_n)\psi_{q_n}^*(l_n)\right\rangle \left\langle \psi_{q_n}(r_n)\psi_{p_n}^*(r_n)\right\rangle}{(\epsilon_{p_n,n}+\Delta E+i\eta)(\epsilon_{q_n,n}+\Delta E-i\eta)}\end{aligned} \tag{3.2.109}$$

Using equation 3.2.108, equation 3.2.109 simplifies to:

$$\langle \mathcal{P}(\psi_1 \to \psi_N)\rangle \propto \frac{|t|^{2(N-2)}}{\mathcal{A}_{dot}^{2(N-2)}} \sum_{p_2,\ldots,p_{N-1}} \prod_{n=2}^{N-1} \frac{1}{(\epsilon_{p_n,n}+\Delta E)^2} \tag{3.2.110}$$

$$\begin{aligned}\langle \mathcal{P}(\psi_1 \to \psi_N)\rangle \quad &\propto \quad \frac{|t|^{2(N-2)}}{\mathcal{A}_{dot}^{2(N-2)}} \sum_{p_2,\ldots,p_{N-1}} \prod_{n=2}^{N-1} \frac{1}{(\epsilon_{p_n,n}+\Delta E)^2} \\ &\propto \quad \frac{|t|^{2(N-2)}}{\mathcal{A}_{dot}^{2(N-2)}} \prod_{n=2}^{N-1} \sum_{p_n} \frac{1}{(\epsilon_{p_n,n}+\Delta E)^2}\end{aligned} \tag{3.2.111}$$

Equation 3.2.111 can be simplified using the areal density of states $\mathcal{D}(\epsilon)$ at energy ϵ:

$$\sum_{p_n} \frac{1}{(\epsilon_{p_n,n}+\Delta E)^2} \approx \int_0^{+\infty} \frac{\mathcal{A}_{dot}\mathcal{D}(\epsilon)d\epsilon}{(\epsilon+\Delta E)^2} \tag{3.2.112}$$

Equation 3.2.112 is valid in the $T = 0$ K limit, where Fermi-Dirac distributions can be replaced by step-functions. We do not include the effect of finite temperatures as the leading-order term is temperature-independent. The MEC rate therefore reads:

$$\langle \mathcal{P}(\psi_1 \to \psi_N) \rangle \propto \left(\frac{|t|^2}{\mathcal{A}_{dot}} \int_0^{+\infty} \frac{\mathcal{D}(\epsilon) d\epsilon}{(\epsilon + \Delta E)^2} \right)^{N_{int}} \tag{3.2.113}$$

Equation 3.2.113 is general and can be applied to granular metals with parabolic-band dots or graphene dots. For parabolic-band grains, $\mathcal{D}(\epsilon) = 2\mathcal{D}_0$ is constant, and we obtain:

$$\langle \mathcal{P}_{para}(\psi_1 \to \psi_N) \rangle \propto \left(\frac{2|t|^2 \mathcal{D}_0}{\mathcal{A}_{dot} \Delta E} \right)^{N_{int}} \tag{3.2.114}$$

Introducing the mean level-spacing δ_0, and using equation 3.2.44, we end up with the well-known result [84, 83]

$$\langle \mathcal{P}_{para}(\psi_1 \to \psi_N) \rangle \propto \left(g \frac{\delta_0}{\pi \Delta E} \right)^{N_{int}} \tag{3.2.115}$$

For graphene, the density of states is linear in energy, $\mathcal{D}(\epsilon) = \frac{2}{\pi} \frac{\epsilon}{(\hbar v_F)^2}$. This remains approximately valid in graphene grains and even in chaotic dots [63]. Introducing graphene's half-bandwidth Γ, necessary to make the integral of equation 3.2.113 converge, we obtain the following average MEC rate for granular graphene:

$$\langle \mathcal{P}_{gr}(\psi_1 \to \psi_N) \rangle \propto \left(g_{\hexagon} \left[\ln \left(\frac{\Gamma}{\Delta E} \right) - 1 \right] \right)^{N_{int}} \tag{3.2.116}$$

where we introduced the effective inter-grain dimensionless conductance

$$g_{\hexagon} = \frac{2|t|^2}{\pi \mathcal{A}_{dot} (\hbar v_F)^2} \tag{3.2.117}$$

for granular graphene. In both parabolic-band dots and graphene dots cases,

the MEC rate appears as the N_{int}-th power of a probability, $p_{el}^{para} = g\frac{\delta_0}{\pi\Delta E}$ and $p_{el}^{gr} = g_{\hexagon}\left[\ln\left(\frac{\Gamma}{\Delta E}\right) - 1\right]$ respectively. In both cases, the multiple elastic co-tunneling rate can thus be interpreted as arising from a sequence of independent virtual tunneling events of probability $p_{el}^{para/gr}$. However, one typically has

$$p_{el}^{para} \ll p_{el}^{gr} \tag{3.2.118}$$

because $\delta_0 \ll \Delta E$ while $\Delta E \ll \Gamma$. In other words, the MEC rate is considerably enhanced in granular graphene, compared to conventional granular systems, due to graphene's linearly increasing density of states which partially compensates the decreasing behavior of individual energy levels contribution to the MEC rate, proportional to $1/(\epsilon + \Delta E)^2$.

We can now calculate the MEC-induced conductivity G_{MEC} in a way similar to G_{MIC}, presented in sub-sections 3.2.3.2 and 3.2.3.3. Applying the Mott argument [69], the probability for a charge carrier of initial energy ϵ in grain 1 to hop to grain N with a final energy $\epsilon + \Delta$ is, at small but finite temperature T

$$\mathcal{P}_{MEC}(T) \propto \left(p_{el}^{para/gr}\right)^{N_{int}} e^{-\frac{\Delta}{k_B T}} \tag{3.2.119}$$

where, employing the Efros-Shklovskii argument, $\Delta \approx \frac{Ce^2}{\kappa N_{int}\xi}$. Maximizing $\mathcal{P}_{MEC}(T)$ with respect to N_{int} as done in sub-sections 3.2.3.2 and 3.2.3.3, directly leads to the MEC-induced conductivity

$$G_{MEC}^{para/gr}(T) \propto \exp\left(-\sqrt{\frac{Ce^2 \ln\left(\frac{1}{p_{el}^{para/gr}}\right)}{2\kappa\xi T}}\right) \tag{3.2.120}$$

which again has a temperature-dependence similar to the Efros-Shklovskii variable-range hopping law, in spite of arising from a distinct transport mechanism. At $T = 0$ K and finite electric field E_{sd}, we would find a similar result for $G_{MEC}^{para/gr}(E_{sd})$, with $\sim e\xi E_{sd}$ playing the role of temperature T. In sub-sections

3.2.3.2, 3.2.3.3, as well as the present section 3.2.4, we found two conduction mechanisms, MIC and MEC, which yield larger currents than sequential tunneling in the low-temperature regime $k_B T \ll e^2/\kappa\xi$. An interesting question is to find the range of temperatures in which MIC dominates over MEC. As explained earlier, MEC is expected to dominate over MIC at low-enough temperatures. A typical crossover temperature $T_{cross}^{para/gr}$ can easily be found by solving

$$p_{in}^{para/gr}(T_{cross}^{para/gr}) = p_{el}^{para/gr} \tag{3.2.121}$$

which for conventional granular metals and granular graphene gives a crossover temperature proportional to the geometric average of the mean charging energy $\bar{E}_c$ and the intra-dot level spacing at the Fermi level [82].

3.3 Sample fabrication and characterisation

The previous section was devoted to presenting important theoretical results on granular metals, and comparing our findings for granular graphene to established results on "conventional" granular systems, whose grains are parabolic-band two-dimensional electron gases. We now shift our focus to the experimental part of this chapter. Before presenting our data on hydrogenated graphene and studying its granular character, we first describe two key techniques used for sample fabrication and characterisation.

3.3.1 Graphene hydrogenation

In recent years, hydrogenated graphene has been intensively studied essentially for energy storage applications and understanding better scattering between graphene charge carriers and adatoms [90, 91]. These works mostly focused on graphene hydrogenated on a single face, thereby limiting the concentration of hydrogen atoms adsorbed on the graphene scaffold. However, recent predictions of high-temperature superconductivity in fully hydrogenated graphene and

the possibility to fabricate granular graphene sheets by heavy hydrogenation, are strong incentives to develop methods to hydrogenate suspended graphene. Here, we give a detailed description of the method we used to hydrogenate suspended graphene sheets on both sides and fabricate devices for electron transport measurements. Our method essentially consists in suspending graphene over a grid, then exposing it to a hydrogen plasma in high-vacuum conditions and finally depositing the resulting material onto a silicon oxide wafer for easy fabrication of gold/chromium contacts by standard electron-beam lithography. While in chapter 2, we used exfoliated graphene for our experiments, we now decide to use CVD graphene, given the possibilities it offers in terms of transfer onto a wide range of substrates and structures.

The standard CVD growth technique leads to the synthesis of graphene on both faces of a copper foil. One of these two graphene layers must then be removed to allow an easy chemical etching of the copper foil and a subsequent transfer of the remaining graphene layer. The most widely used technique relies on a layer of polymer - typically PMMA -, spin-coated on one graphene layer, the other one remaining in contact with air. Upon exposure to O_2/Ar plasma, the later is completely etched, while the former stays intact, due to its protective polymer layer. However, this technique is not appropriate to the production of graphane crystals, as unavoidable polymeric residues would drastically limit the hydrogenation. Figure 3.3.1 shows TEM pictures of suspended CVD graphene samples, whose fabrication involved PMMA. The PMMA residues present on the graphene membrane (left picture) cannot be removed by performing thermal annealing at 250°C for 3 hours (right picture), which makes PMMA cluster up and does not lead to its removal.

In order to facilitate the hydrogenation process, we used a polymer-free method to suspend graphene sheets on top of a Transmission Electron Microscopy (TEM) grids. This technique is depicted in Figures 3.3.2 and 3.3.4. It allows transferring CVD graphene from its copper foil to a TEM grid with-

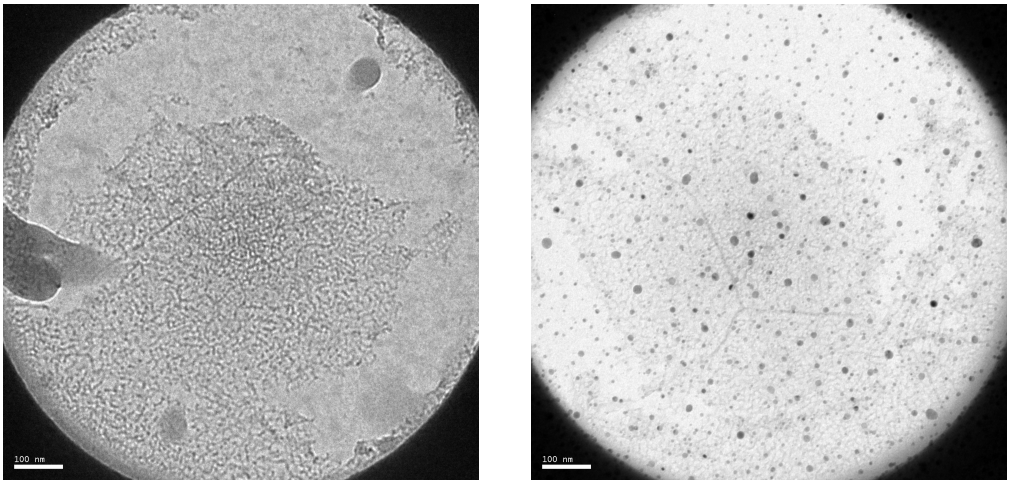

Figure 3.3.1: TEM pictures of suspended CVD graphene prepared with standard PMMA-based methods. Left picture: without thermal annealing. PMMA residues form large puddles over most of the graphene membrane; Right picture: after thermal annealing at 250°C for 3h, graphene residues did not disappear, but clustered up. Scale bars: 100 nm for both pictures.

out using PMMA. Only one chemical is used: a weakly concentrated solution of ammonium persulfate to etch copper. Unlike PMMA, possible ammonium persulfate residues on graphene can be easily removed upon DI water rinsing. After suspension using a gold Quantifoil Micromachined Holey Carbon TEM grid S7/2, graphene is hydrogenated in a high-vacuum chamber and then transferred to a Si/SiO_2 wafer with 90 nm of oxide, which offers an enhanced contrast for hydrogenated graphene.

In what follows, we give practical details regarding our polymer-free suspension and hydrogenation technique. Letters (a) to (i) refer to steps depicted in Figure 3.3.2, while letters (j) to (m) refer to Figure 3.3.4.We first prepare - step (a) - a piece of scotch tape with a hole and cover it with a graphene-coated copper foil.(b) The latter is stamped on the sticky face of the tape. A shell is then pasted on top to form the structure depicted in (c), so that the upper copper foil face is hermetically sealed. This structure is then exposed to argon plasma for 2 min (60W, 20 sccm of flow rate) and O_2/Ar plasma for 2 more minutes (60W, 20 sccm of flow rate for both O_2 and Ar) to etch graphene away from the non-protected side (d). The protective shell is then

removed, and a piece of the suspended copper foil is cut (e) and placed on the surface of a solution of ammonium persulfate (with a typical concentration of 5-10 g/L). At this stage, there is no graphene at the interface between the copper foil and the solution of ammonium persulfate, while a graphene layer lies on the upper copper foil face. A gold Quantifoil Micromachined Holey Carbon TEM grid S7/2 (f, g) is then gently deposited on the floating copper foil, the carbon face being in contact with graphene (h). After few hours, the copper foil is fully etched, leaving the TEM grid alone with a graphene layer attached to its carbon film [71]. The TEM grid is then transferred to a pure DI water beaker for 6 hours in order to rinse the graphene layer (i). Figure 3.3.3 shows an optical picture of a PMMA-free graphene sheet supported by a TEM grid, just after rinsing and drying. A typical TEM picture of a 7 µm $\times$ 7 µm square of suspended graphene is shown in inset, illustrating the cleanliness of the resulting suspended CVD graphene sheets, compared to CVD graphene sheets prepared with standard polymer-based methods, see Figure 3.3.1.

Next, four of these graphene-covered TEM grids (j) are prepared and inserted in a home-made stainless steel TEM-grid holder (k). The holder is then put on a hot plate at 100°C for a few minutes to dry the graphene membranes. To prevent trapped water vapors from damaging graphene layers, the holder is placed on the hot plate in an oblique fashion. The TEM grid holder is then placed in an ultrahigh-vacuum chamber for hydrogenation. Before introduction of a hydrogen plasma, a low pressure of 10^{-9} Torr is typically established. Then a hydrogen plasma is generated by means of a RF Plasma system at 13.56 MHz and 300W. During hydrogenation, the temperature is $\sim 300K$ and the pressure is $\sim 5 \times 10^{-6}$ Torr [91]. After hydrogenation, the graphene-on-TEM-grid samples are taken out of the holder and stamped onto 90 nm SiO2 wafers, the graphene layer being in contact with the oxide (l). A scotch tape is generally pasted on top of the grids, and then gently rubbed for few minutes using a tweezer. Upon delicately removing the grids, some 7 µm $\times$7 µm squares of

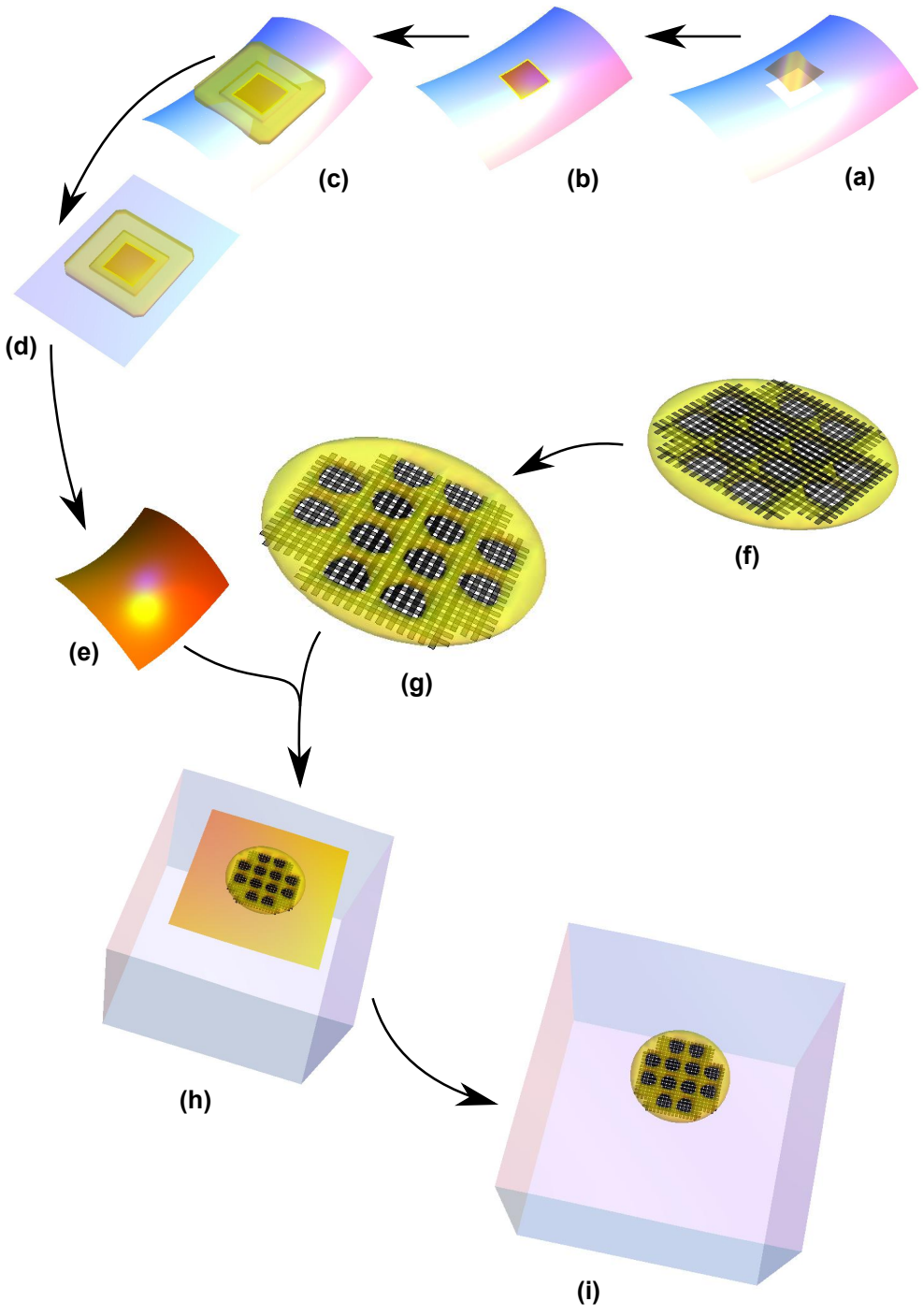

Figure 3.3.2: Polymer-free isolation of CVD graphene from its copper substrate. Steps (a) to (i) are described in the main text.

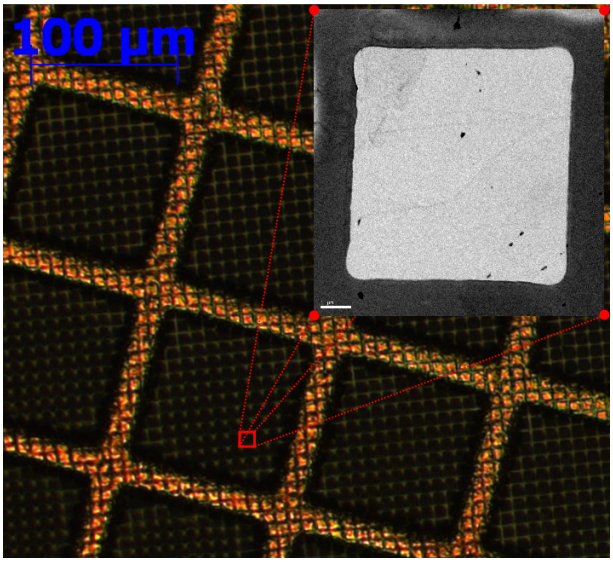

Figure 3.3.3: Typical picture of a Quantifoil TEM grid entirely covered with PMMA-free CVD graphene, after rinsing and drying on a hot plate. Inset: TEM picture of a 7µm × 7µm square of suspended graphene, before hydrogenation. This picture illustrates the exceptional cleanliness of CVD graphene prepared following the method depicted in Figure 2. Scale bare: 1 µm.

graphene are transferred to SiO_2, presumably due to the electrostatic forces at the SiO_2-graphene interface. An optical picture of the typical result is shown in Figure 3.3.4 (m).

The polymer-free fabrication method presented in this section is key for the fabrication of highly hydrogenated graphene samples. However, we also need to have tools to characterize as-produced samples. In particular, we need to know how graphene adatoms are distributed on the graphene lattice. Are they randomly distributed, forming amorphous hydrogenated graphene films, or are they arranged in clusters, possibly giving a granular structure to graphene?

3.3.2 Accessing the sample topology by combining Raman spectroscopy and electron transport measurements

Raman spectroscopy is a convenient method to provide answers to the above question, given its ability to measure the intervalley scattering rate in graphene,

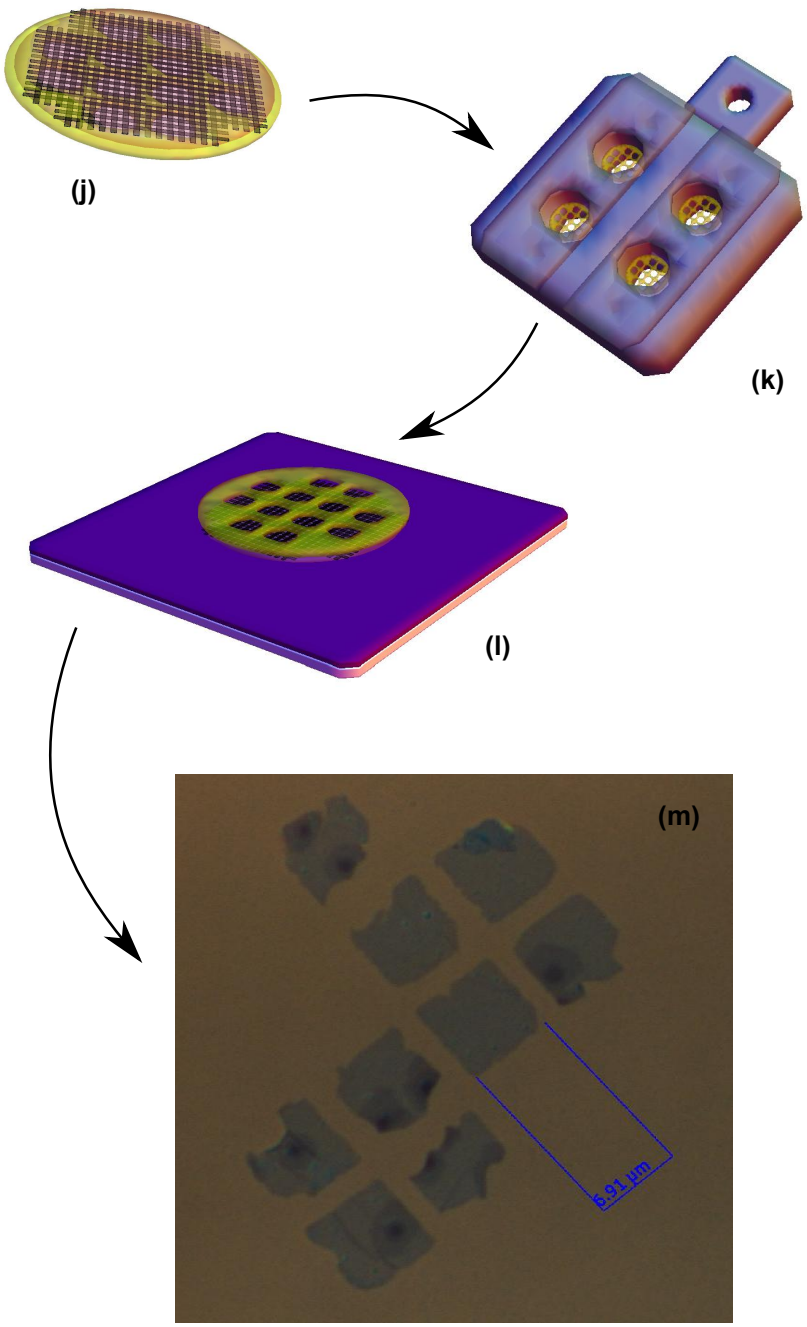

Figure 3.3.4: Schematic illustrating the hydrogenation and deposition of CVD graphene on Si_2O substrate. Steps (j) to (m) are described in the main text.

and hence evaluate the amount of adatoms on the lattice. It was shown by several authors [96, 97] that the ratio of integrated intensities I_D/I_G for the D and G peak in graphene with short-range defects is related to the mean distance L_D between these defects, through the formula:

$$\begin{aligned}\frac{I_D}{I_G} &= F(L_D) = C_A\frac{r_A^2 - r_S^2}{r_A^2 - 2r_s^2}\left(\exp(-\pi r_S^2/L_D^2) - \exp(-\pi(r_A^2 - r_S^2)/L_D^2)\right) \\ &+ C_S(1 - \exp(-\pi r_S^2/L_D^2)) \end{aligned} \tag{3.3.1}$$

Equation 3.3.1 was first established for ion-bombarded graphene [96], but was found to describe chemically-functionalized graphene well [99], at least in situations where adatoms do not cluster and are randomly distributed on the graphene scaffold. In this case, r_S is a fixed parameter giving the radius of a disk centered on the impurity, and within which graphene is structurally disordered. r_A is the typical distance from the structurally disordered area within which electrons excited by the Raman laser contribute to the D peak before recombining with a hole. C_A and C_S are dimensionless prefactors. Experimentally and theoretically, it was found that in such cases, this formula describes the I_D/I_G ratio properly provided r_S, r_A, C_A and C_S typically take the following values: $r_S \sim 2$ nm, $r_A \sim 4$ nm, $C_A \sim 4$ and $C_S \sim 1$. L_D is usually determined by measuring I_D/I_G experimentally and solving $F(L_D) = (I_D/I_G)_{experimental}$.

However, in many realistic situations, defects are not randomly distributed. A degree of correlation often exists [122, 101, 58, 88]. For instance, hydrogen [122, 101] adatoms tend to cluster. But $F(L_D)$ should still adequately describe I_D/I_G provided that:

(i) clusters are randomly distributed,

(ii) clusters have a typical radius r_S,

(iii) the average distance between cluster centres is L_D.

In most experimental situations, the typical cluster size is unknown and

hence both L_D and r_S are unknown. r_A is unknown as well, but simply depends on r_S through $r_A = r_S + \delta$, where δ is the average distance a graphene electron excited by the Raman laser travels before recombining with a hole. We now briefly re-establish the formula $I_D/I_G = F(L_D)$ using arguments similar to Lucchese et al [96], and show that it can be applied to situations satisfying conditions (i), (ii) and (iii). Let $\mathcal{S}_S$ and $\mathcal{S}_A$ be the total area of chemically-functionalized graphene and activated area, respectively. The activated area corresponds to the area of defect-free graphene within which laser-excited electrons have a significant probability of undergoing inter-valley scattering with an adatom before recombining with a hole and emitting a photon. Let $\mathcal{A}$ be the total area of the graphene sheet. Both chemically-functionnalized graphene and the activated zone contribute to the measured I_D/I_G signal a term proportional to their respective area $\mathcal{S}_S$ and $\mathcal{S}_A$. Corresponding proportionality coefficients are different though: $C_S/\mathcal{A}$ and $C_A/\mathcal{A}$. We assume N clusters of adatoms are present on the graphene sheet, and we add an $N+1$th cluster randomly. We further assume that the position of its centre has a uniform probability distribution law. For the sake of simplicity, we assume that only the following two outcomes are possible: (a) the $N+1$-th cluster does not overlap with the N other clusters or (b) the $N+1$-th cluster completely overlaps with another cluster. In other words, we neglect the possibility of a partial overlap between clusters. Consistently, the average increase in $\mathcal{S}_S$ upon adding the $N+1$-th cluster is:

$$\langle \mathcal{S}_S(N+1) - \mathcal{S}_S(N) \rangle = \frac{\mathcal{A} - \mathcal{S}_S(N)}{\mathcal{A}} \times \pi r_S^2 \tag{3.3.2}$$

Correspondingly, the average increase in $\mathcal{S}_A$ reads:

$$\langle \mathcal{S}_A(N+1) - \mathcal{S}_A(N) \rangle = \frac{\mathcal{A} - \mathcal{S}_S(N) - \mathcal{S}_A(N)}{\mathcal{A}} \times \pi (r_A^2 - r_S^2) \tag{3.3.3}$$

Introducing $f_A = \mathcal{S}_A/\mathcal{A}$ and $f_S = \mathcal{S}_S/\mathcal{A}$ and $\sigma = N/\mathcal{A} \approx L_D^{-2}$, we immedi-

ately obtain:

$$\frac{df_S}{d\sigma} = \pi r_S^2(1 - f_S) \tag{3.3.4}$$

and

$$\frac{df_A}{d\sigma} = \pi(r_A^2 - r_S^2)(1 - f_S - f_A) \tag{3.3.5}$$

as in reference [Carbon 48, 1592]. By definition, $f_S(\sigma = 0) = 0$, so that equation 3.3.4 leads to

$$f_S(\sigma) = 1 - e^{-\pi r_S^2 \sigma} \tag{3.3.6}$$

Reinjecting the obtained expression for $f_S(\sigma)$ in equation 3.3.5, we easily obtain (given that $f_A(\sigma = 0) = 0$):

$$f_A(\sigma) = \frac{r_A^2 - r_S^2}{r_A^2 - 2r_s^2}\left(e^{-\pi r_S^2 \sigma} - e^{-\pi(r_A^2 - r_S^2)\sigma}\right) \tag{3.3.7}$$

and hence

$$\begin{aligned} \frac{I_D}{I_G} &= C_A \frac{r_A^2 - r_S^2}{r_A^2 - 2r_s^2}\left(e^{-\pi r_S^2 \sigma} - e^{-\pi(r_A^2 - r_S^2)\sigma}\right) \\ &+ C_S(1 - e^{-\pi r_S^2 \sigma}) \end{aligned} \tag{3.3.8}$$

Equation 3.3.8 is often used to determine L_D assuming no significant clustering takes place, and $r_S \sim 2$ nm is commonly used in practice. Here, r_S is not necessarily small, and shall be extracted from Raman spectra using 3.3.8. Since the localization length ξ is known from electron transport data and is comparable to the crystallite size as V_g lies close to the charge neutrality point [72], one can relate L_D to r_S and ξ. Modelling the clusters network by a square lattice of disks, we have, qualitatively:

$$\sqrt{2}L_D \sim 2r_S + \xi \tag{3.3.9}$$

Injecting 3.3.9 into equation 3.3.8, we obtain, in the $r_S, \delta \ll \xi$ limit:

$$\frac{I_D}{I_G} = \frac{4\pi\delta}{\xi^2} C_A r_S \tag{3.3.10}$$

and

$$\frac{I_D}{I_G} \sim C_S \tag{3.3.11}$$

in the $r_S \gg \xi$ limit. I_D/I_G typically reaches the saturation regime $I_D/I_G \sim C_S$ when

$$r_S \sim \frac{C_S}{C_A} \frac{\xi^2}{4\pi\delta}. \tag{3.3.12}$$

Interestingly, these equations can be used to estimate r_S from Raman spectra provided ξ is known. Estimates of ξ can be obtained by electron transport measurements performed at different temperatures and source-drain voltages. In the next section, we describe our experiments on hydrogenated graphene, and present our data.

3.4 Multiple virtual tunneling of Dirac fermions in granular graphene: experimental results

3.4.1 Summary of our experimental results

Graphene's charge carriers behave as massless Dirac fermions, opening the exciting possibility to observe long-range virtual tunneling of electrons in a solid. In granular metals, electron hops arising from series of virtual transitions are predicted to yield observable currents at low-enough temperatures, but to date experimental evidence is lacking. We report on electron transport in granular graphene films self-assembled by hydrogenation of suspended graphene. While the log-conductance shows a characteristic $T^{-1/2}$ temperature dependence,

cooling the samples below 10K drives a triple crossover: a slope break in log-conductance, simultaneous to a substantial increase in magneto-conductance and onset of large mesoscopic conductance fluctuations. These phenomena are signatures of virtual transitions of electrons between distant localized states, and conductance statistics reveal that the high crossover-temperature is due to the Dirac nature of granular graphene charge carriers.

3.4.2 Introduction

Short-lived particles allowed by Heisenberg's uncertainty principle are called "virtual", but the effects they induce are very real. They lead to vacuum fluctuations and mediate fundamental forces [73], explain the Lamb shift of atomic levels [74], the Casimir effect [74, 75] and possible Hawking radiations [76]. Though unobservable, virtual particles are key ingredients of modern quantum electrodynamics. Considerable research efforts have thus been devoted to measuring the most direct consequences of their existence, such as virtual-to-real photon conversion during dynamic Casimir effect [77]. Quantum dot nanostructures are excellent test beds too, as electron tunneling through virtual states [78, 79, 80] generates background currents observable below $\sim 100mK$ [81]. Interestingly, higher-order currents between distant localized states are predicted to arise from multiple transitions to virtual states in macroscopic granular metals [82, 83, 84], but this phenomenon coined multiple elastic co-tunneling (MEC) has not been observed yet. From this perspective, graphene is a particularly promising material, in which virtual excitations of charges play a special role. They are theoretically predicted to induce Dirac fermions' jittery motion called zitterbewegung [85], and give a minimum conductivity to pristine graphene. In granular form, graphene dots' linear density of states (DOS) [86] means that high-energy virtual states should contribute significantly to elastic co-tunneling currents despite shorter life-times, unlike ordinary granular metals (GM). This not only makes granular graphene the ideal platform for the first

observation of MEC, but also provides a rare opportunity to measure long-range effects mediated by high-energy virtual states.

3.4.3 Results

Recently, chemical functionalization of graphene [87] was reported to be a viable method to produce granular graphene [88], due to the tendency of adatoms to form electrically insulating clusters. At high enough adatoms concentrations, such clusters merge into percolative pathways, effectively partitioning the graphene sheet into weakly-coupled graphene dot arrays, or GM. To conveniently fabricate graphene GMs, we exposed suspended CVD graphene sheets [89] to hydrogen plasma [90, 91], thereby allowing adsorption of sufficiently high concentrations of hydrogen atoms on both sides of the graphene scaffold. We then stamped as-produced doubly-hydrogenated graphene (DHG) films on 90 nm-SiO2 chips. Au/Cr contacts in two- and four-probe geometries were then fabricated. Typical devices are shown in inset of Figure 3.4.1. To observe the charge-neutrality point (CNP) at gate voltages $V_g \sim 0V$, the samples were then vacuum-dried [92] in-situ at 10^{-6} Torr for a day before cooling below 0 °C. We then measured electron transport in 8 devices from room temperature down to 2.4K. After fabrication, samples were loaded in a variable temperature insert coupled to a 9T superconducting magnet. A pressure of $\sim 10^{-6}$ Torr was maintained during the experiments. Electron transport measurements were carried out with a Keithley 6517B Electrometer/High-Resistance Meter. To eliminate possible DC noise, we used the following procedure: for each bias V_{sd}, the source-drain current I_{sd} was measured 10 times at $+V_{sd}$ within ~ 1 s, then 10 times at $-V_{sd}$ within ~ 1 s. The resulting noise-filtered current was then systematically calculated as

$$I_{sd}^{filt} = \frac{\langle I_{sd}(V_{sd})\rangle - \langle I_{sd}(-V_{sd})\rangle}{2} \tag{3.4.1}$$

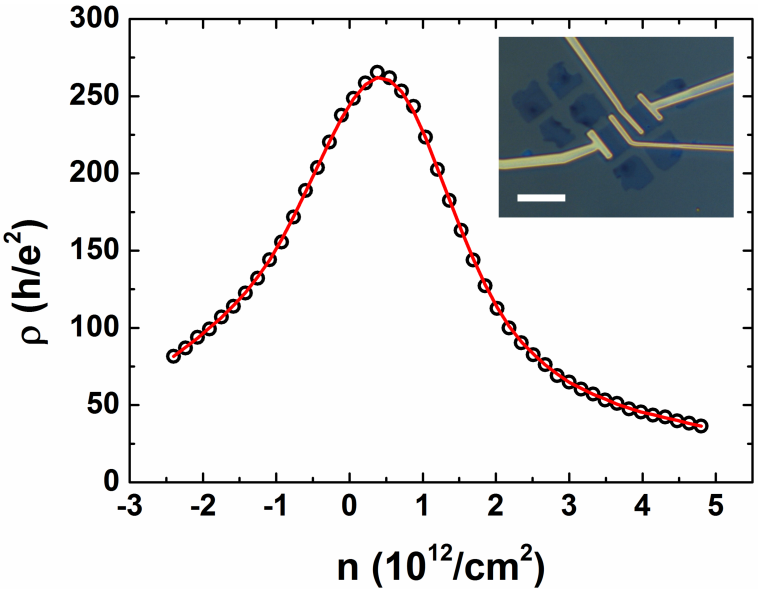

Figure 3.4.1: Sheet resistance against charge density n at room temperature (Device D0). Inset shows an optical picture of typical devices. Scale bar: 10 µm.

where $\langle ... \rangle$ corresponds to the arithmetic average. V_{sd} was sourced by Keithley 6517B or Keithley 6430. Keithley 6430 was systematically used to source the gate voltage V_g. When needed, a fixed source-drain current was sourced with a Keithley 6221, while V_{sd} was measured with Keithley 6517B.

Figure 3.4.1 shows the room-temperature resistance R in units of resistance quantum h/e^2, against charge-carrier density n - determined from the back-gate capacitance - for a typical sample (D0). The R(n) curve has a characteristic graphene-like shape, but is broad and $R(n) \gg 1$ throughout the whole range of measured densities, indicating strong localization.

Next, we measure the conductance G for different bias voltages V_{sd} and temperatures T to extract the typical localization length ξ of our samples. The inset of figure 3.4.2 shows G against V_{sd} at different temperatures T between 2.3K and 20K for device D1. For consistency, all subsequent data shown in this section correspond to the same device D1. Data taken for other devices are reported in section 3.5.1. We observe that above $V_{sd} \sim 0.1V$, G increases with V_{sd} while below, G is bias-independent, indicating an Ohmic behavior. Crucially, $G(V_{sd}, T)$ data can be used to extract ξ without assuming

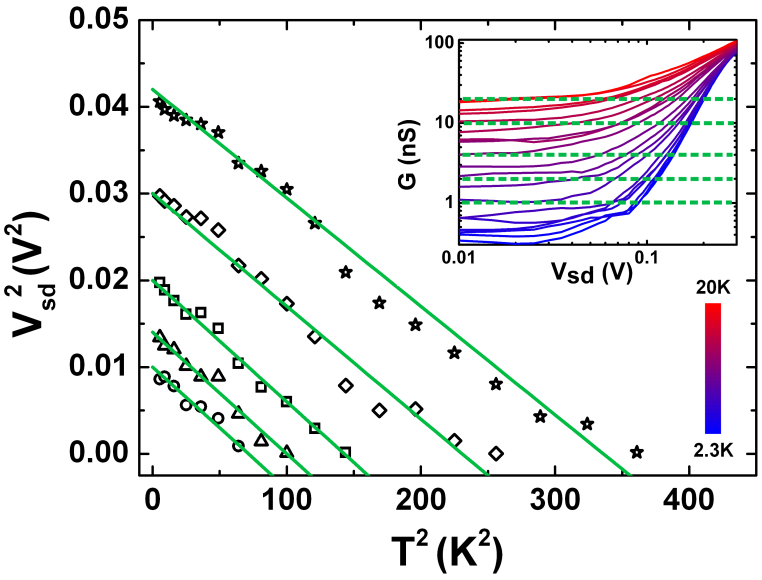

Figure 3.4.2: Constant-conductance V_{sd}^2 vs T^2 domains extracted from conductance G against V_{sd} curves at 2.3K and all temperatures between 3K and 20K in steps of 1K (inset). The solid lines of the main figure are linear fits of slope $\approx -1.4 \times 10^{-4} V^2 K^{-2}$ to $G = 1$ nS (circles), $G = 2$ nS (triangles), $G = 4$ nS (squares), $G = 10$ nS (diamonds) and $G = 20$ nS (stars) domains. These domains correspond to traces represented as green dashed lines in inset.

any particular transport mechanism. Since an electron hopping against the source-drain electric field $E = V_{sd}/L$ over a distance d increases its energy by an amount eEd, it was shown that charge carriers experience an effective temperature

$$T_{eff} = \sqrt{T^2 + \left(\frac{\alpha e \xi V_{sd}}{k_B L}\right)^2} \tag{3.4.2}$$

where $L = 4\mu m$ is the channel length, and $\alpha \approx 0.67$ is a constant [93]. More details regarding the concept of effective temperature and its applicability are given in section 3.5.2. Importantly, T_{eff} uniquely determines G, which implies that constant-conductance domains of (V_{sd}^2, T^2)-space are straight lines of slope $-(\alpha e \xi / k_B L)^2$. Figure 3.4.2 shows such domains extracted from $G(V_{sd}, T)$ data at 1, 2, 4, 10 and 20 nS. As expected, they are well-fitted by straight lines of slope $\approx -1.4 \times 10^{-4} V^2 K^{-2}$, giving $\xi \approx 45nm$.

We now show that our DHG samples have a GM structure by complementing our electric transport measurements with Raman spectroscopy data, presented in figure 3.4.3. The spectrum shown in figure 3.4.3 exhibits a promi-

nent D peak as well as broad $2D$ and $D+D'$ peaks. The D peak partially overlaps with the G peak. The D' peak at $1614\ cm^{-1}$ almost completely merges with the G peak at $\sim 1588\ cm^{-1}$ but can still be resolved as shown by the inset of figure 3.4.3 . These are characteristics of strongly sp^3-hybridized graphene [94]. The D-peak of sp^3-hybridized graphene probes the distribution of sp^3-bonds on the graphene lattice [95]. More precisely, the ratio I_D/I_G of integrated intensities of the D and G peaks is related to the typical adatom cluster size r_S and the mean distance L_D between nearest cluster centers by the formula [96, 97]

$$\begin{aligned}\frac{I_D}{I_G} &= F(r_s, L_D) \\ &= C_A \frac{r_A^2 - r_S^2}{r_A^2 - 2r_S^2}\left(e^{-\pi r_S^2/L_D^2} - e^{-\pi(r_A^2-r_S^2)/L_D^2}\right) \\ &+ C_S\left(1 - e^{-\pi r_S^2/L_D^2}\right) \end{aligned} \tag{3.4.3}$$

discussed in section 3.3.2 where C_A and C_S are constants, $r_A = r_S + \delta$, and δ is the average distance laser-excited electrons travel before recombining with holes. Experimentally, it was shown that $C_A \approx 4$, $C_S \approx 0.9$ and $\delta \approx 2$ nm for a laser of 2.4 eV [98, 99]. By fitting Fano line-shapes [100] to the Raman spectrum peaks, we calculate the peaks integrated intensities and $I_D/I_G \approx 1.8$. This value is clearly inconsistent with a random distribution of isolated adatoms, which would yield $L_D \approx \delta \ll \xi$. Conversely, hydrogen adatoms form clusters of typical radius r_S [101], and since $\xi \approx 45$ nm and $I_D/I_G \approx 1.8$, we find $r_S \gtrsim 30$ nm by using equation 3.3.12, leading to $L_D \sim 2r_S$. In other words, clusters tend to merge, isolating graphene dots of size ξ, and our DHG samples have a GM structure. This agrees with previous studies on graphene quantum dots of size $\sim \xi$ [102] yielding comparable Raman spectra due to edge scattering [98, 103].

Next, we focus on identifying the dominant charge transport mechanisms

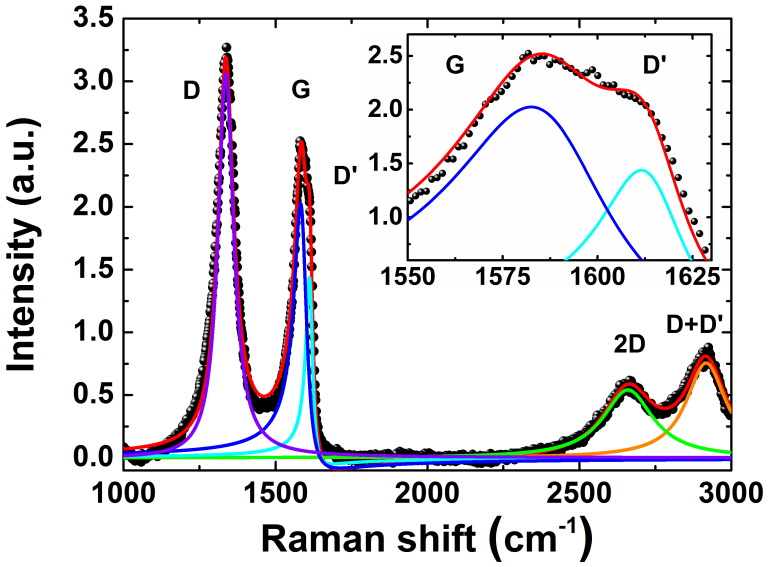

Figure 3.4.3: Raman spectrum (device D1). The data (black) are fitted by a five-peak line-shape (red), sum of Breit-Wigner-Fano peaks: violet (D), blue (G), cyan (D'), green (2D) and orange (D+G). The inset is a zoom on the G and D' peaks.

by analyzing the temperature-dependence of the conductance $G(T)$. More precisely, one expects G to follow a

$$G(T) = G_0 e^{-(T_0/T)^\gamma} \tag{3.4.4}$$

law characteristic of hopping transport, where γ and T_0 depend on the exact hopping mechanism [104]. We thus measured G around CNP for different T between 2.4K and 300K. $G(T)$ is systematically measured in the low-bias Ohmic regime, where both electric-field-driven electron hopping and Joule heating are negligible. We observed a reduced activation energy [105]

$$\beta = \frac{d \ln G}{d \ln T} \tag{3.4.5}$$

linear in $\ln G$ with slope $\approx -1/2$ both for $\ln G < -21.5$ and $\ln G > -19$. More details are given in section 3.5.3. Therefore, we plotted G against $T^{-1/2}$ in figure 3.4.4. Strikingly,

$$\ln G \propto T^{-1/2} \tag{3.4.6}$$

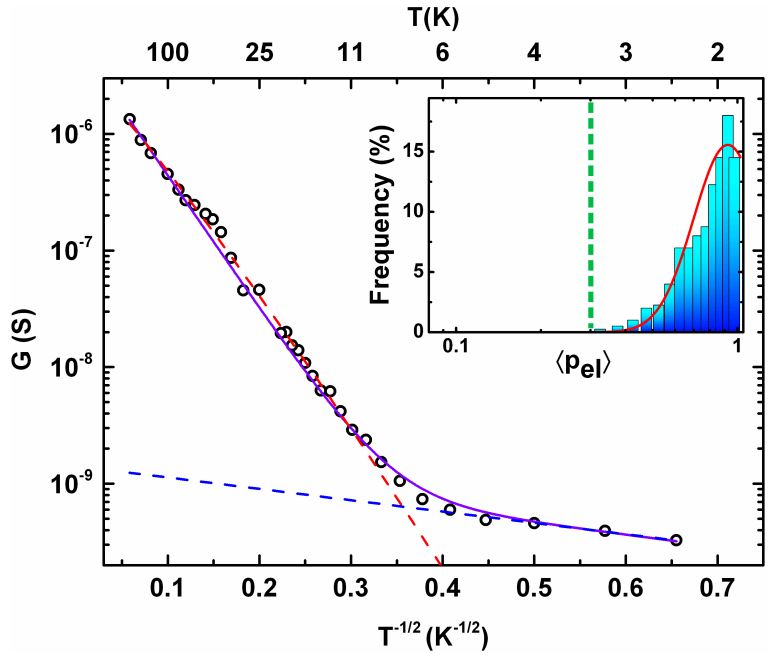

Figure 3.4.4: Low-bias G vs $T^{-1/2}$ at $V_g = 1.5$ V. The violet line is a fit accounting for inelastic and elastic co-tunneling mechanisms as described in main text. The blue (resp. red) dashed line corresponds to the best power law fit for $\ln G$ vs $T^{-1/2}$ below 6K (resp. above 10K). Inset shows a histogram for p_{el} extracted from slopes of $\ln G(T)$ vs $T^{-1/2}$ at different V_g, see section 3.5.4. The red solid line is a guide to the eyes and the dashed green line is an estimate for p_{el} calculated in section 3.2.4.

between 300K and $\approx 12K$, and between $\approx 8K$ and 2.4 K, but with a much smaller slope.

A distinct slope break is thus identified around $T_{cross} = 10$ K. Graphene being atomically thin, this phenomenon certainly does not reflect a decrease in effective sample dimensionality from three to two dimensions [106]. Besides, our measured samples have a channel width $W \approx 6-7$ µm systematically larger than the length $L \leq 5$ µm to avoid any possible 2D to 1D crossover upon lowering the temperature. A $G_0 \exp(-(T_0/T)^\gamma)$ fit both above and below T_{cross} respectively gives $\gamma = 0.56 \pm 0.04$ and $\gamma = 0.495 \pm 0.05$. In these regimes, $G(T)$ is thus neither of the Arrhenius type ($\gamma = 1$) nor of the Mott's 2D variable-range hopping (VRH) type ($\gamma = 1/3$). However, $\gamma = 1/2$ suggests an Efros-Shklovskii (ES) VRH behavior, the 1D Mott VRH being excluded due to the geometry of our devices. Such behavior contrasts with the result of several

earlier studies, in particular [90], performed on strongly localized hydrogenated graphene samples, where the conduction is attributed to 2D Mott VRH. However, these results were obtained for less hydrogenated graphene samples, fabricated by exposing a single graphene face to hydrogen plasma. Conversely, a $\gamma = 1/2$ behavior was already reported in heavily oxidized graphene films [88] with a GM structure. However, the presence of both a gamma-1/2 behavior and a slope break as observed in figure 3.4.4 around 10K has never been observed before, to the best of our knowledge. While a crossover between two $\gamma = 1/2$ regimes with different slopes is not expected in standard VRH theories [104], it is predicted for granular systems [82], each regime reflecting a distinct transport mechanism illustrated in figure 3.4.5: multiple inelastic co-tunneling (MIC) at high temperatures and multiple elastic co-tunneling (MEC) at low temperatures. During MIC, multiple electrons simultaneously tunnel from the Fermi sea of a grain to an excited state of a neighboring grain, along a string of grains ultimately left in an excited state, thus requiring a finite temperature or electric field. During an MEC event, a single charge carrier hops between two distant grains by transiting to virtual states in intermediate grains which ultimately remain unexcited.

To verify that our $G(T)$ data result from a MIC-to-MEC crossover, we fit a function of the form

$$G(T) = G_{MIC}(T) + G_{MEC}(T) \tag{3.4.7}$$

where

$$G_{MIC}(T) = G_{in} e^{-\sqrt{T_{in}/T}} \tag{3.4.8}$$

and

$$G_{MEC}(T) = G_{el} e^{-\sqrt{T_{el}/T}} \tag{3.4.9}$$

are MIC and MEC conductance terms. The best fit is obtained for $G_{in} = 6$ µs, $T_{in} \approx 700$ K, $G_{el} \approx 1.5$ nS, and $T_{el} \approx 6$ K. We now show that these

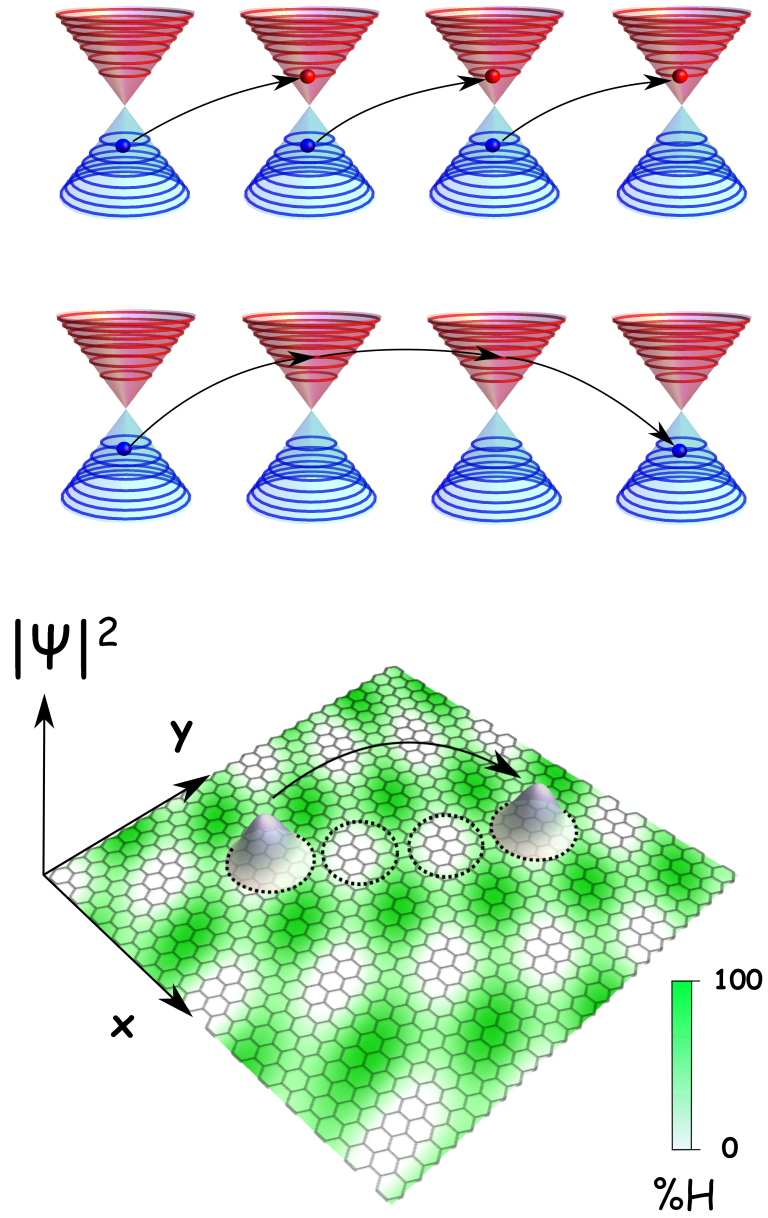

Figure 3.4.5: Cartoon representation of hydrogenated graphene sheets (bottom), MEC (centre) and MIC (top). Hydrogen clusters partition hydrogenated graphene into disconnected metallic graphene dots. Hydrogen concentration is encoded by shades of green, from white (hydrogen-poor) to green (hydrogen-rich). Hopping from initial to final localized state (grey) occurs by two possible mechanisms described in the main text: MIC (top) and MEC (centre). Cones represent graphene's energy spectrum within individual dots circled by dashed lines in the bottom panel. Discrete energy levels due to confinement are marked by red and blue circles. Red (blue) balls represent electrons (holes). Arrows correspond to tunneling events leaving the dots either in an excited state (top) or a ground state (bottom).

values match theoretical expectations for co-tunneling in granular graphene. We start with G_{in}, which is the total conductance in the $T \gg T_{in}$ limit and is related to the nearest-grain tunneling conductance g by $g \sim LG_{in}/W$, where $W \approx 7$ μm is sample D1 width. This leads to $g \sim 0.1 \ll 1$ in units of e^2/h, which is a characteristic of insulating GM. The inter-dot tunneling conductance g should also be compared to the intra-dot conductance g_{dot} [107]. Since before hydrogenation, our graphene samples have a typical mobility $\mu \approx 5000$ cm^2/V.s, the intra-dot mean-free path can be estimated to be $l \sim A\sqrt{n}$ with $A = \frac{h}{2e}\frac{\mu}{\sqrt{\pi}} \approx 6 \times 10^{-12}$ cm^2. A graphene grain of size $\sim \xi$ with at least one Dirac fermion, corresponding to an areal density of $\sim 5 \times 10^{10}$ cm^{-2}, should have a mean-free path $l > 13$ nm and a Thouless energy [108]

$$E_{Th} = \frac{\hbar v_F l}{2(\xi/2)^2} \tag{3.4.10}$$

larger than ~ 10 meV. Therefore, E_{Th} typically exceeds the dots mean energy level spacing [109]

$$\Delta \leq \frac{\hbar v_F}{\xi} \sim 10meV \tag{3.4.11}$$

so that

$$g_{dot} \approx \frac{2e^2}{h}\frac{E_{Th}}{\Delta} \tag{3.4.12}$$

is at least a few e^2/h. $g_{dot} \gg g$ is thus satisfied throughout the experimentally relevant range of densities. This is again perfectly consistent with an insulating granular metal behavior, and contrasts sharply with the case of homogeneously disordered systems [82], where $g_{dot} \approx g$. Next, we notice that $T_{in} \approx 700$ K is significantly larger than the charging energy of a grain

$$T_c = \frac{e^2}{4\pi\epsilon\epsilon_0\xi} \approx 100K \tag{3.4.13}$$

where $\epsilon \approx 3.5$ is the dielectric constant of the inter-granular medium [88]. This agrees with MIC theory [82] which predicts $T_{in} = \chi_{in}T_c$, where χ_{in} is a

logarithmically T-dependent coefficient. As $T \ll T_c$,

$$\chi_{in} = -4C \ln p_{in} \tag{3.4.14}$$

where C is a dimensionless constant of the order of unity, and p_{in} is the rate of elementary inelastic tunneling events introduced in sections 3.2.3.2 and 3.2.3.3. p_{in} is usually assumed to read [84]

$$p_{in} \approx 16\pi g \left(\frac{T}{T_c}\right)^2 \tag{3.4.15}$$

However, equation 3.4.15 is valid provided grains have an energy-independent density of states. For graphene grains, we expect to have a different temperature-dependence for p_{in}. Though deriving an analytical finite-temperature result for p_{in} is challenging for graphene (see equation 3.2.69), equation 3.2.75 strongly suggests a $\propto (T/T_c)^4$ behavior close to CNP, with a prefactor similar to the one in equation 3.4.15. Given the logarithmic dependence of χ_{in}, and the presence of a prefactor C close to unity but not precisely known, we opt for a conservative approach. We take $C = 1$ and use equation 3.4.15 to analyse the data. This leads to $\chi_{in} \approx 8$ at $T = 10 - 20$ K, and $T_{in,theory} \approx 800$ K, close to the experimental value. We finally focus on T_{el}, whose value extracted from figure 3.4.4 is one order of magnitude smaller than T_c. This remains true at all V_g despite fluctuations, and T_{el} averages to $\theta_{el} \approx 10$ K. More details on the statistics of T_{el} are reported in section 3.5.4. Theoretically,

$$T_{el} = -\frac{CT_c}{2} \ln p \tag{3.4.16}$$

where p is the probability of virtual transition to a neighboring grain [82, 83]. For conventional two-dimensional GMs, the DOS in each grain is constant and

the level spacing is small compared to the charging energy, leading to [82]

$$p \propto g\frac{\Delta}{T_c} \ll g \ll 1 \tag{3.4.17}$$

and T_{el} of the order of few T_c. Therefore, Schrödinger fermions cannot account for the observed $T_{el} \ll T_c$ behavior. Unlike MIC for which only states within $k_B T_{eff}$ around the Fermi level contribute to G, virtual transitions to high-energy states contribute to the MEC conductance and the band structure plays a key role. In the Dirac fermions case, the short life-time $\hbar/E$ of high-energy fermions is compensated by a DOS which increases linearly with energy E, making the contribution of high-energy virtual states significant. It remains true for chaotic dots with edges of random shape[86, 109]. We derived in section 3.2.4 an estimate for the virtual tunneling probability of graphene Dirac Fermions:

$$p_{el} \sim \frac{g}{2}\left(\ln\left(\frac{\Gamma}{k_B T_c}\right) - 1\right) \approx 0.3 \tag{3.4.18}$$

where Γ is the energy bandwidth. This is in accord with experimental statistics on p_{el} shown in inset of figure 3.4.4 and implies that $p_{in} \sim p_{el}$ just above T_{cross}, between 20K and 40K, thus providing strong evidence for MIC-to-MEC crossover.

A powerful way to gain further insight is to analyze the variations of G with V_g and V_{sd}, as each transport mechanism leaves its own mesoscopic fluctuations footprint [110, 111, 112, 113]. Figure 3.4.6(a) shows G measured at 3K for $-7.5V \leq V_g \leq 7.5V$ and $0 \leq V_{sd} \leq 200$ mV and exhibits vertical stripes of width $\Delta V_g \approx 200$ mV, corresponding to peaks and valleys in conductance reproduced at all measured V_{sd}. This is highlighted by figure 3.4.6(b), which shows four different traces extracted from figure 3.4.6(a) at $V_{sd} = 10$ mV, 80 mV, 120 mV and 175 mV. While overall the conductance increases with V_{sd}, the different fixed-V_{sd} $G(V_g)$ curves show reproducible peaks and valleys. To analyze these fluctuations quantitatively, we systematically extracted the

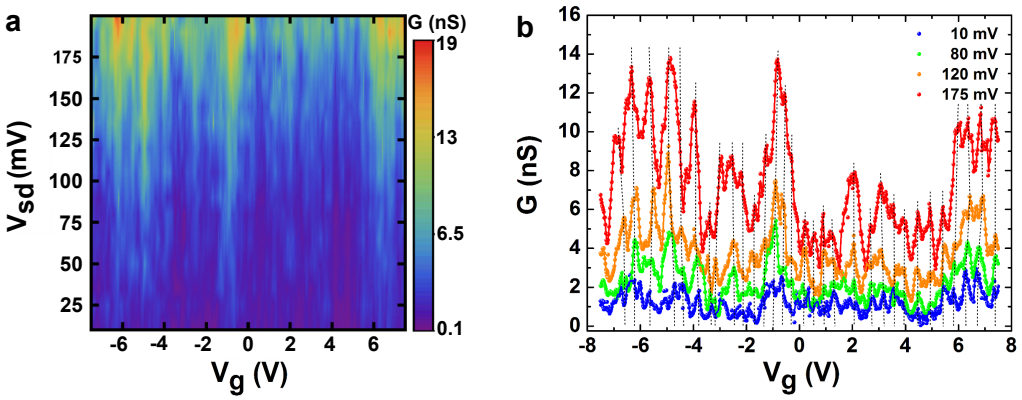

Figure 3.4.6: (a) Conductance as a function of V_g and V_{sd} at 3K. The linear color scale corresponds to the measured conductance in nS. (b) Conductance against V_g traces at 3K extracted from fig. 3.4.6(a): at $V_{sd} = 10$ mV (blue), $V_{sd} = 80$ mV (green), $V_{sd} = 120$ mV (orange), and $V_{sd} = 175$ mV (red). The vertical black dashed curves are guides to the eyes highlighting the reproducibility of the peaks in conductance across different voltage biases.

standard deviation of log-conductance $\sigma_{\ln G}$ at fixed source-drain bias from figure 3.4.6(a) and three other data sets shown in section 3.5.5. Figure 3.4.7 shows $\sigma_{\ln G}$ plotted against T_{eff} (see equation 3.4.2) from 3K up to 80K, in double-log scale. Two different regimes can be clearly distinguished. Below $T_{eff} = 10$ K, $\sigma_{\ln G}$ is weakly temperature-dependent while above 10K, $\sigma_{\ln G}$ decreases rapidly with T_{eff}. Quite remarkably, these two regimes coincide with the two distinct $G(T)$ regimes observed in figure 3.4.4. We start by analyzing the high-T_{eff} regime, where $\sigma_{\ln G}$ is very well described by the power-law

$$\sigma_{\ln G} \propto T_{eff}^{-2.1} \tag{3.4.19}$$

This behavior is clearly incompatible with Mott or ES VRH as such phenomena would lead to $\sigma_{\ln G} \propto T_{eff}^{-a}$with a < 1 [113]. We now compare the observed fluctuations above 10K to expected MIC-induced fluctuations. From a hopping percolation viewpoint [114], the fluctuations in log-conductance $\sigma_{\ln G}$ are related to the standard deviation s of log-conductance at the scale of a hopping distance r_{hop}, by

$$\sigma_{\ln G} = \frac{\kappa^{\nu}}{l} \tag{3.4.20}$$

where $\kappa = 2\sqrt{2}s$, $l = L/r_{hop}$ and $\nu \approx 4/3$ is the critical exponent in two dimensions. Since MIC is a fundamentally phase-incoherent process involving a different charge carrier for each intermediate transition (see figure 3.4.5), MIC-induced fluctuations in conductance do not originate from quantum interferences between electron wave functions. It must rather arise from fluctuations in inter-dot conductances accompanying changes in percolation network as gate voltage is tuned. From this perspective, we find - based on probabilistic arguments developed in section 3.2.3.4- that

$$s \propto \sqrt{\frac{N_{hop}}{N_{th}}} \tag{3.4.21}$$

where [82]

$$N_{hop} = \frac{r_{hop}}{\xi} \propto \sqrt{\frac{T_{in}}{T_{eff}}} \tag{3.4.22}$$

and N_{th} is the number of intra-grain energy levels within an energy $\sim k_B T_{eff}$ from the Fermi level ϵ_F. We emphasize that it is a good approximation to substitute T_{eff} to T in equations 3.2.55, 3.2.58, and 3.2.89, because at finite voltages, the Fermi-Dirac distribution can be replaced by the effective distribution $f_{eff}(\epsilon) \approx (1+\exp((\epsilon-\epsilon_F)/k_B T_{eff}))^{-1}$, as discussed in appendix (section 3.5.2). This not only guarantees the validity of equation 3.4.22, but also the pertinence of our analysis based on the effective temperature rather than the temperature. For a 2D GM with parabolic-band grains, $N_{th} \sim k_B T_{eff}/\Delta$ and hence $s \propto \sqrt{\Delta/k_B T_{eff}}(T_{in}/T_{eff})^{1/4}$. This corresponds to $\sigma_{\ln G} \propto T_{eff}^{-1.5}$, which does not satisfactorily fit the data. However, in graphene grains, energy levels are not evenly spaced. The n^{th} energy level from neutrality point has an expected value of energy

$$E_n \propto \Delta_0 \sqrt{n} \tag{3.4.23}$$

where $\Delta_0 = \hbar v_F/\xi$. Therefore - see appendix, section 3.5.6 -,

$$N_{th} \propto \left(\frac{k_B T_{eff}}{\Delta_0}\right)^2 \tag{3.4.24}$$

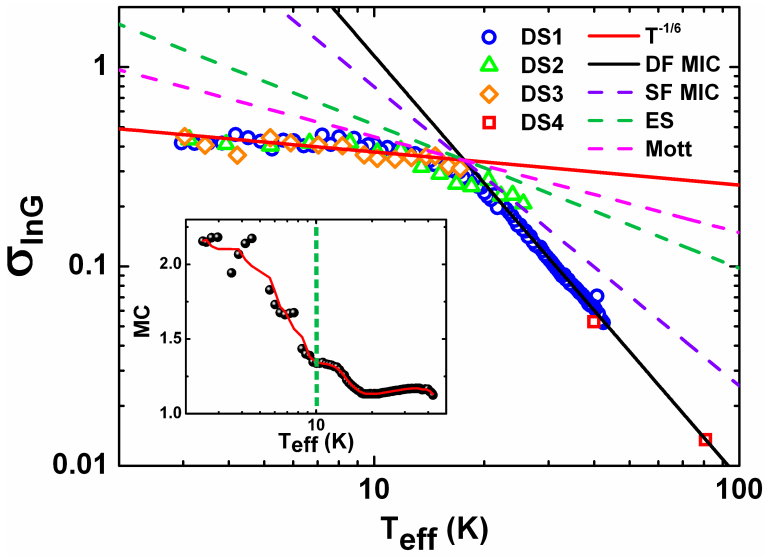

Figure 3.4.7: Standard deviation $\sigma_{\ln G}$ of the log-conductance as a function of T_{eff} (see Eq. 3.4.2). Data points were extracted from 4 distinct data sets - DS1, DS2, DS3, DS4, see section 3.5.5 - measured in sample D1. DS3 corresponds to fig. 3.4.6(a). Blue circles (DS1) were extracted from G vs V_{sd} curves taken at 3K for different V_g. Green triangles (DS2) and orange diamonds (DS3) were extracted from G vs V_g, V_{sd} plots. Red squares (DS4) correspond to G vs V_g curves taken at 6K and fixed source-drain current. Dashed and solid lines correspond to theoretically predicted power-laws for different transport mechanisms: Dirac fermions (DF) MIC (black), Schrödinger fermions (SF) MIC (violet), ES (green) and Mott VRH (pink), bottleneck-limited MEC (red). Inset shows the high-field MC at $V_g = 0$ V between 2K and 40K. Data points are shown in black. The solid red line is a guide to the eyes and the dashed green line indicates T_{cross}.

and

$$s \propto \frac{\Delta_0}{k_B T_{eff}} \left(\frac{T_{in}}{T_{eff}} \right)^{1/4} \propto T_{eff}^{-1.25} \tag{3.4.25}$$

This yields

$$\sigma_{\ln G}^{theory} \propto T_{eff}^{-2.16} \tag{3.4.26}$$

which agrees very well with the data. In other words, the unusually strong T_{eff}–dependence of $\sigma_{\ln G}$ above 10K can only be understood in terms of inelastic co-tunneling of Dirac fermions.

We now discuss the sub-T_{cross} regime, where $\sigma_{\ln G} \sim 0.5$ is weakly T-dependent, clearly ruling out MIC as dominant transport mechanism below 10K. This is perfectly consistent with figure 3.4.4 which indicates a crossover

to MEC below 10K. Since MEC is a phase-preserving process, it is tempting to assign this behavior to quantum interferences between distinct phase-coherent charge-carrier paths [115, 116], a phenomenon known to produce almost T_{eff}-independent conductance fluctuations of large magnitude. This view is supported by magneto-transport experiments carried out at 2.4K for $-500mV \leq V_{sd} \leq 500mV$. The inset of figure 3.4.7 shows the relative magneto-conductance $MC = G(8T)/G(0T)$ against T_{eff} from 2.4K up to 40K. MC is almost constant and close to 1 above T_{cross} where MIC dominates, reflecting its phase-incoherent nature, whereas MC rapidly increases to ≈ 2 below T_{cross}, a manifestation of quantum interferences [83, 116, 117] attributable to MEC. Moreover, figure 3.4.7 shows that the sub-T_{cross} data are well-described by $\sigma_{\ln G} \propto T_{eff}^{-\eta}$ with $\eta \approx 0.16$ or less, suggesting conduction is limited by a strongly resistive portion of the granular graphene film of size $\sim r_{hop}$, or "bottleneck". Such a situation systematically occurs in granular media at sufficiently low T_{eff} when $\sigma_{\ln G}$ approaches unity [113, 118], which is the case around T_{cross}. Since quantum interferences within a bottleneck must give the main contribution to $\sigma_{\ln G}$, the observed $\sigma_{\ln G} \propto T_{eff}^{-\eta}$ -behavior plausibly approximates the

$$\sigma_{\ln G} = \sqrt{AT_{eff}^{-1/3} + B} \tag{3.4.27}$$

law for systems of size close to the phase-coherence length [119, 120, 121]. In summary, both the significant increase in magneto-conductance and weak temperature-dependence of $\sigma_{\ln G}$ below 10K indicate the appearance of quantum interferences. The presence of such strong interferences only below T_{cross} is consistent with the existence of a crossover from phase-incoherent MIC above 10K to MEC below 10K.

3.4.4 Discussion

Our results show that doubly-hydrogenated graphene is not amorphous but has a granular structure instead. This finding is consistent with the tendency

of hydrogen atoms adsorbed on graphene to phase-separate [122] and form electrically insulating clusters. This observation is particularly interesting as graphane phases – or fully hydrogenated graphene regions – are predicted to be high-temperature superconductors [123]. From this perspective, hydrogenation of suspended graphene sheets appears as a viable route towards the synthesis of novel granular superconductors [82, 124] . The granularity of our doubly-hydrogenated graphene samples is reflected by the presence of Dirac fermions in this material, which can exist in graphene grains or dots, but not in amorphous media. Both the large crossover temperature from inelastic to elastic co-tunneling and the temperature dependence of the log-conductance fluctuations with gate voltage are signatures of the presence of Dirac fermions in our samples. In conclusion, we observed multiple elastic co-tunneling for the first time in a granular metal. In our granular graphene samples, both multiple inelastic and elastic co-tunneling mechanisms showed signatures of Dirac fermions. The presence of large high-order elastic co-tunneling currents in granular graphene establishes granular Dirac materials as ideal platforms for the study of vacuum fluctuations and quantum noise [125].

3.5 Appendix

3.5.1 Data from other samples

3.5.1.1 I-V characteristics for four devices of different lengths:

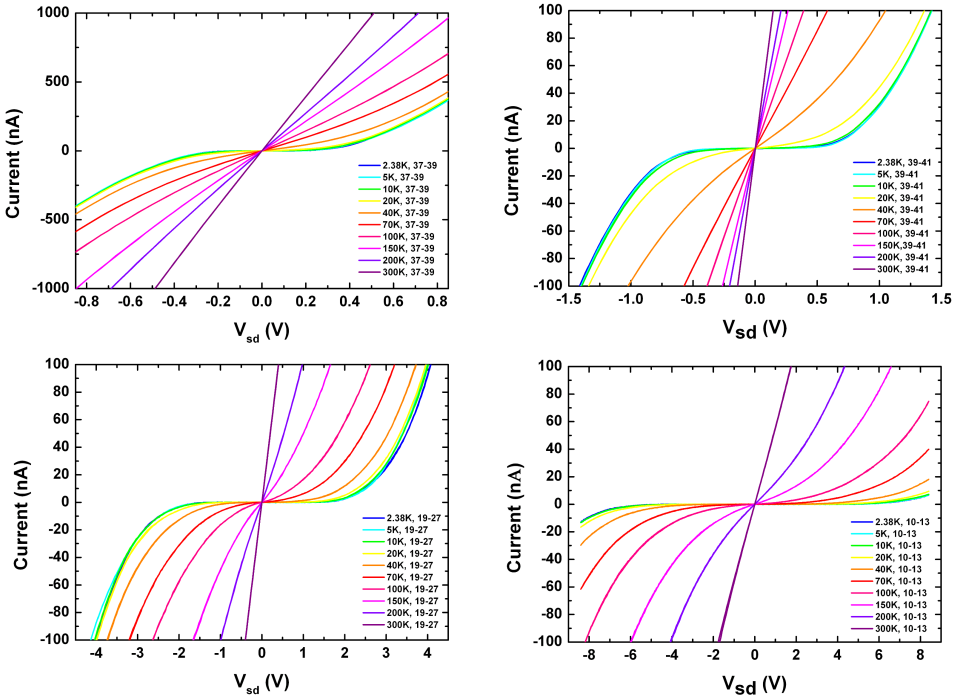

Figure 3.5.1: Source-drain current as a function of voltage bias for four different devices (namely D2, D3, D4 and D5), around the charge neutrality point. All devices show strongly non-linear I-V characteristics and exhibit threshold voltages of different values determined by channel length and localization length.

3.5.1.2 Temperature-dependence of the conductance

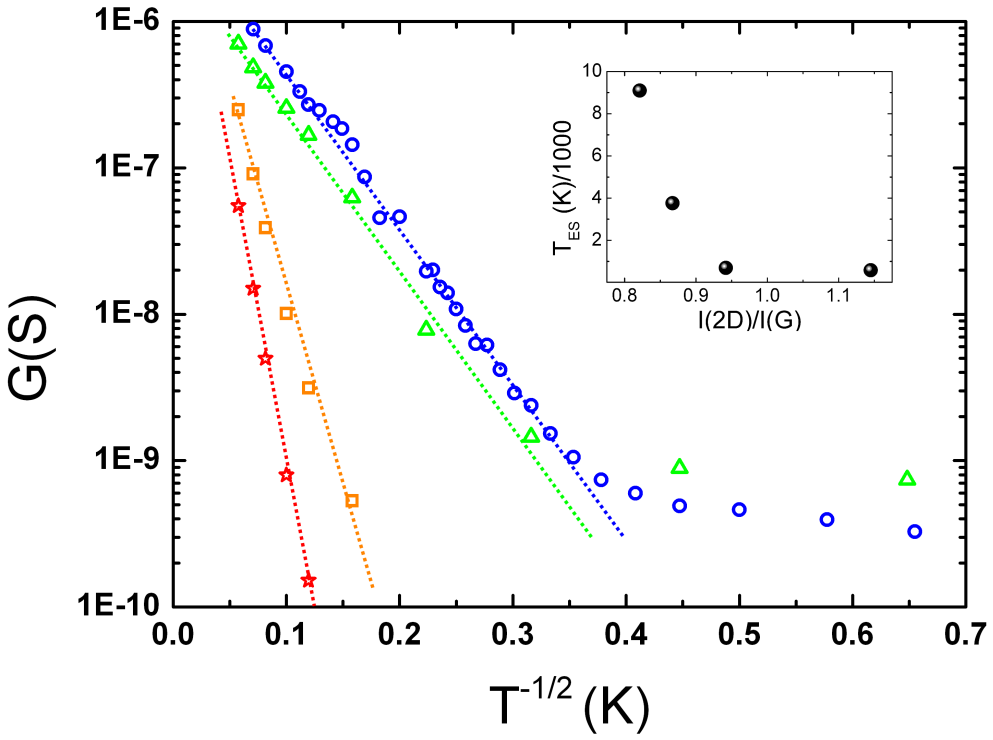

Figure 3.5.2: Low-bias conductance as a function of $T^{-1/2}$ around the charge neutrality point for four different samples (D2, D3, D4 and D5). The dashed lines are Efros-Shklovskii temperature-dependence fits to the data above 10K. The inset shows the characteristic temperature T_{ES} defined as $\ln(G/G(T \to \infty))) = -\sqrt{T_{ES}/T}$ plotted against the ratio $I(2D)/I(G)$ of 2D-to-G peak intensities extracted from the Raman spectrum of each sample. I(2D)/I(G) is a convenient measure of the degree of hydrogenation of a sample as it decreases monotonously with the number of sp^3bonds introduced in the graphene lattice [94]. This figure shows that the most hydrogenated samples have the largest T_{ES}. Their conductance decreases too rapidly as T decreases (red and orange curves), so that the slope break observed around 10K for the least hydrogenated samples (blue and green curves) cannot be observed, due to the limitations of our setup.

3.5.2 The concept of effective temperature

In sections 3.2.3.2, 3.2.3.3, 3.2.3.4, and 3.2.4 on multiple inelastic and elastic cotunneling, we expressed hopping probabilities $\mathcal{P}$ and conductivities $G_\square$ resulting from these transport phenomena as a function of either temperature T or electric field E_{sd}. Besides, we always implicitly assumed that the electric field E_{sd} was small enough to be almost at equilibrium, so that the electron

statistics was always close to the standard Fermi-Dirac distribution,

$$f_{FD}(\epsilon) = \frac{1}{1 + e^{\frac{\epsilon - E_F}{k_B T}}} \tag{3.5.1}$$

where E_F is the Fermi level. The results of these sections are thus valid in the $e\xi E_{sd} \ll k_B T$ limit at finite temperature, or at vanishingly small $e\xi E_{sd}$ at absolute zero temperature. In this section we deal with the situation where both E_{sd} and T are finite and comparable, and the standard Fermi-Dirac distribution 3.5.1 fails to describe electron and hole statistics properly. Several authors studied this difficult question for strongly localized systems such as disordered materials [93, 128, 126, 127] and good conductors in the quantum Hall regime [129]. Intuitively, a non-zero electric field offers more available sites to hop to for an electron moving in the field direction, and therefore enhences the conductivity. For a system whose typical localization length is $\sim \xi$, one thus expects $e\xi E_{sd}/k_B$ to play a role similar to the temperature T [93]. It has been proposed that T should be replaced by an effective temperature $T_{eff}(T, E_{sd})$ in equation 3.5.1, so that transport quantities $\mathcal{P}(T, E_{sd})$ and $G_\square(T, E_{sd})$ can be uniquely determined by T_{eff}, i.e. $\mathcal{P}(T_{eff}(T, E_{sd}))$ and $G_\square(T_{eff}(T, E_{sd}))$. Such an effective temperature T_{eff} should then verify basic properties:

(I) $G_\square(T_{eff}(T, E_{sd}))$ must be Ohmic as $E_{sd} \to 0$

(II) $T_{eff}(T, E_{sd}) \to T$ as $E_{sd} \to 0$

(III) $T_{eff}(T, E_{sd}) \to E_{sd}$ as $T \to 0$

If condition (I) is satisfied then at finite T and $E_{sd} = 0$, we have:

$$\frac{dG_\square}{dE_{sd}} = \frac{dG_\square}{dT_{eff}} \frac{dT_{eff}}{dE_{sd}} = 0 \tag{3.5.2}$$

leading to $\frac{dT_{eff}}{dE_{sd}} = 0$. By maximizing hopping probabilities of the form $\mathcal{P}_N \propto p^N e^{-\frac{\Delta}{k_B T}}$ with $\Delta \propto \frac{e^2}{\kappa N \xi} + eN\xi E_{sd}$, one would obtain conductivities $G_\square \left(T + \frac{e\xi E_{sd}}{k_B}\right)$ depending only on an effective temperature $T^*_{eff} = T + \frac{e\xi E_{sd}}{k_B}$. However, such

an effective temperature does not satisfy condition (I) as $\frac{dT^*_{eff}}{dE_{sd}} = e\xi/k_B$. This is because at finite electric field, the boltzmann factor $e^{-\frac{\Delta}{k_BT}}$ is incorrect. A possible method to find the steady-state distribution functions $f(\epsilon, E_{sd})$ replacing Fermi-Dirac distributions $f_{FD}(\epsilon)$ when an electric field $\vec{E}_{sd}$ is applied is to solve the balance equation [93, 128, 126]:

$$\sum_{j\neq i} f(\epsilon_i, E_{sd})\Gamma_{ij}(1 - f(\epsilon_j, E_{sd})) = \sum_{j\neq i} f(\epsilon_j, E_{sd})\Gamma_{ji}(1 - f(\epsilon_i, E_{sd})) \quad (3.5.3)$$

associated with a Miller-Abrahams network [70] for which a node i of real-space coordinates $\vec{r_i}$ corresponds to a state i of energy ϵ_i, and Γ_{ij} represents the transition rate from state i to state j and is given by:

$$\Gamma_{ij} = \Gamma_0 e^{-2\|\vec{r}_i - \vec{r}_j\|/\xi}\Theta_{ij} \quad (3.5.4)$$

where Θ_{ij} is equal to $\exp(-(\epsilon_j - \epsilon_i - e\vec{E}_{sd}.(\vec{r}_j - \vec{r}_i))/k_BT)$ if $\epsilon_j - \epsilon_i - e\vec{E}_{sd}.(\vec{r}_j - \vec{r}_i) \leq 0$ and $\Theta_{ij} = 1$ otherwise. Since the rates Γ_{ij} verify the detailed balance equation,

$$\frac{\Gamma_{ji}}{\Gamma_{ij}} = e^{\frac{\epsilon_j - \epsilon_i - e\vec{E}_{sd}.(\vec{r}_j - \vec{r}_i)}{k_BT}} \quad (3.5.5)$$

it is easy to check that the Fermi-Dirac distribution verifies, at $E_{sd} = 0$,

$$f_{FD}(\epsilon_i)\Gamma_{ij}(1 - f_{FD}(\epsilon_j)) = f_{FD}(\epsilon_j)\Gamma_{ji}(1 - f_{FD}(\epsilon_i)) \quad (3.5.6)$$

and hence solves equation 3.5.3 at zero electric field. At finite E_{sd} however, f_{FD} is generally not a solution of equation 3.5.3, and the standard approaches to solve the balance equation for the correct distribution $f(\epsilon, E_{sd})$ are numerical. Observing that effective temperatures of the form

$$T^{(\eta,\gamma)}_{eff}(T, E_{sd}) = (T^\eta + (\gamma e\xi E_{sd}/k_B)^\eta)^{1/\eta} \quad (3.5.7)$$

verify conditions (I), (II) and (III) provided $\eta > 1$, distribution functions of the form

$$f^{(\eta,\gamma)}(\epsilon) = \frac{1}{1 + \exp\left(\frac{\epsilon - E_F}{k_B T_{eff}^{(\gamma,\eta)}(T, E_{sd})}\right)} \tag{3.5.8}$$

are then usually fitted to the numerical data. Excellent fits are then obtained for values of η close to ~ 2 and γ of the order of unity. Values of η and γ nonetheless vary slightly with the assumed density of states $g(\epsilon)$ in the system described by the Miller-Abrahams network. Conventional strongly doped semiconductors have a density of midgap states $g(\epsilon) \propto e^{-\epsilon/\epsilon_0}$ exponentially decaying from the band edge into the gap, leading to an effective temperature $T_{eff}^{(\eta,\gamma)}(T, E_{sd})$ with $\eta = 2$ and $\gamma = 0.67$[93] provided the Fermi level lies deeply in the exponential tail of the density of midgap states and the temperature is small enough, $k_B T \ll \epsilon_0$. Other densities of states have been considered, such as Gaussian distributions $g(\epsilon) \propto e^{-\epsilon^2/2\sigma^2}$ describing disordered organic materials, leading to $\eta \approx 1.54$ and $\gamma \approx 0.64$ [127]. Effective temperatures $T_{eff}^{(\eta,\gamma)}$ with $\gamma \approx 0.6 - 0.7$ and $\eta \approx 1.5 - 2$ thus properly describe typical strongly localized systems in the Mott variable-range hopping regime. Are such effective temperatures applicable to other types of strongly localized materials, whose conduction is dominated by different transport mechanisms, such as Efros-Shklovskii variable-range hopping, multiple inelastic co-tunneling or multiple elastic co-tunneling? Irrespective of the hopping mchanism, strongly localized systems can be mapped to a Miller-Abrahams network with transition rates of the form given by equation 3.5.4. While for Mott and Efros-Shklovskii variable-range hopping mechanisms, the prefactor $\exp\left(-2\left\|\vec{r}_i - \vec{r}_j\right\|/\xi\right)$ originates from the overlap between exponentially decaying wave-functions describing localized states, this prefactor simply corresponds to $p_{in}^{N_{int}}$ or $p_{el}^{N_{int}}$ for MIC or MIC transition rates $\mathcal{P}_N^{MIC}$ and $\mathcal{P}_N^{MEC}$, which can easily be seen by introducing the

inelastic (elastic) co-tunneling effective localization length

$$\xi_{in/el} = \frac{2\xi}{\ln\left(\frac{1}{p_{in/el}}\right)}, \tag{3.5.9}$$

and $\|\vec{r}_i - \vec{r}_j\| \approx N_{int}\xi$. To check whether an effective temperature $T_{eff}^{(\eta,\gamma)}(T, E_{sd})$ with $\eta \sim 2$ and $\gamma \sim 1$ generally applies to disordered semiconductors dominated by Efros-Shklovskii variable-range hopping or to granular metals in the insulating regime, we now need to understand the behavior of the density of localized states $g(\epsilon)$ for such systems. In amorphous semiconductors dominated by Efros-Shklovskii VRH, the density of localized states $g(\epsilon)$ must be similar to the one observed in disordered semiconductors dominated by Mott VRH, except that $g(\epsilon)$ must vanish in the vicinity of the Fermi level, due to the presence of an Efros-Shklovskii Coulomb gap [60]. The case of granular metals is more complicated. The charging energy E_c of its dots deeply affects the density of states $g(\epsilon)$ at the scale of the entire granular metal [61], which as a result exhibits peaks in density of states with a periodicity equal to the average charging energy $\langle E_c \rangle$. These peaks are unavoidably broadened by charged impurities and random fluctuations in dots capacitance due to variations of the dots geometry [61]. It is expected that these random fluctations in turn give the peaks in $g(\epsilon)$ a Gaussian character and hence a finite density of states at the Fermi level, should we neglect the Efros-Shklovskii Coulomb gap. Regarding $g(\epsilon)$, the situation for granular metals therefore resembles the situation for above-mentioned materials whenever the Fermi levels lies between two peaks. It is therefore reasonable to expect the existence of an effective temperature T_{eff} of the form given by the heuristic formula 3.5.7 with $\eta \approx 2$ and $\gamma \sim 1$ for a wide range of Fermi energies. However, it is not clear to us to which extent the Efros-Shklovskii Coulomb gap affects T_{eff}. To the best of our knowledge, the literature lacks conclusive studies on this question, even if it can be confidently said that Coulomb glasses and granular metals expe-

rience an effective temperature $T_{eff} \approx \gamma e \xi E_{sd}/\gamma$ at high electric fields, with $\gamma \approx 0.5$. It is also worth noting that the concept of effective temperature was recently applied to strongly localized graphene nano-ribbons exhibiting an Efros-Shklovskii temperature-dependence by M.Y. Han, J.C. Brant, and P. Kim [130].

3.5.3 Reduced activation energy

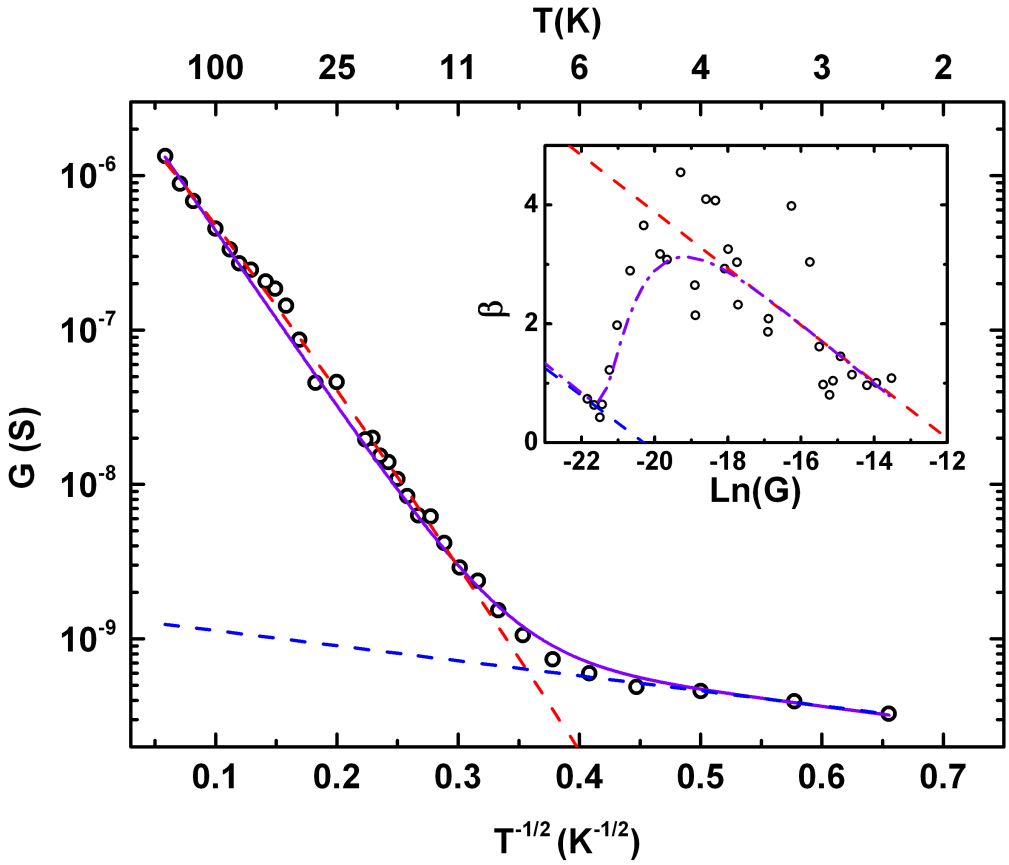

Figure 3.5.3: Low-bias G vs $T^{-1/2}$ at $V_g = 1.5$ V together with corresponding reduced activation energy β vs $\ln G$ shown in inset. $\beta(\ln G)$ was extracted from main graph using discrete derivatives. In inset, the red (resp. blue) dashed line is the best linear fit for $-19 < \ln G < -13$ (resp. between $-22 < \ln G < -21.5$), and was obtained for $\gamma \approx 0.5$. The violet dashed line corresponds to $\beta(\ln G)$ directly calculated from the fit (violet) of the main figure.

3.5.4 Fluctuations of $T_0 = T_{el}$ with V_g

While below $T \sim 10$ K, the low source-drain bias conductance has a

$$G(T) \propto \exp\left(-\sqrt{\frac{T_{el}}{T}}\right) \tag{3.5.10}$$

behavior at all gate voltages V_g, T_{el} exhibits large fluctuations with V_g. This phenomenon is highlighted by the following three figures.

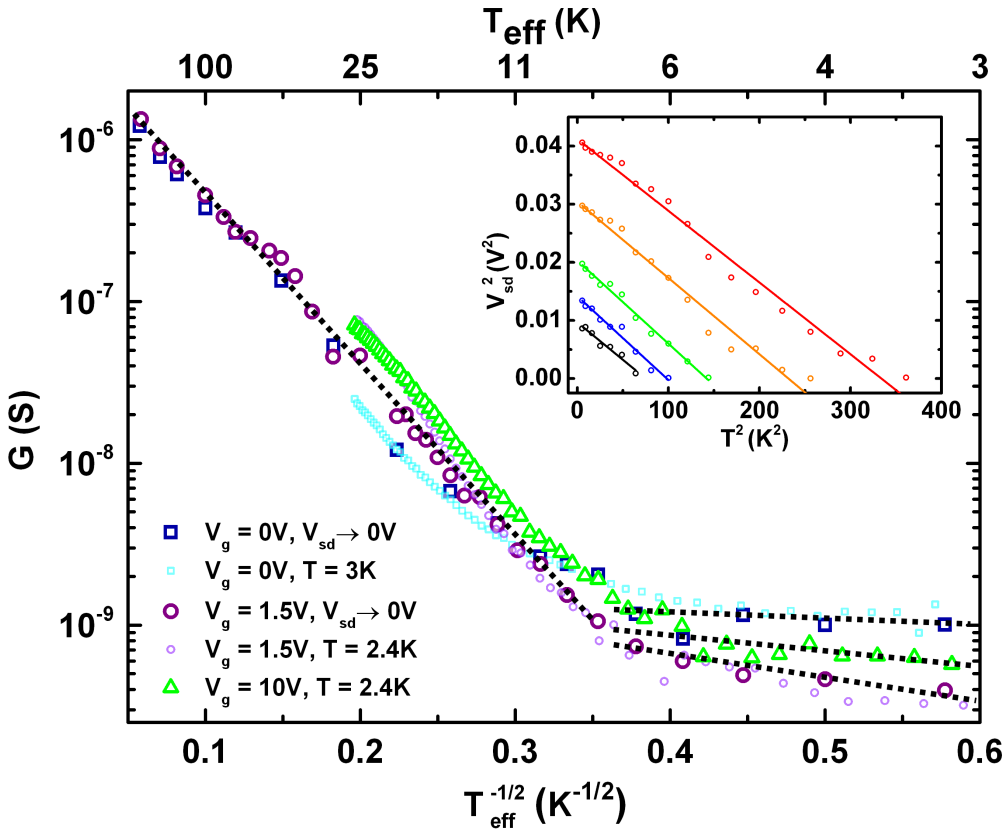

Figure 3.5.4: Conductance against the $T_{eff}^{-1/2}$, where T_{eff} is the effective temperature defined in the main text. The purple circles (resp. big blue squares) correspond to G vs. $T_{eff}^{-1/2}$ at low bias, variable T and $V_g = 1.5$ V (resp. $V_g = 0$ V). The small data points correspond to G vs. $T_{eff}^{-1/2}$ at fixed T and variable V_{sd}, at $V_g = 0$ V and 1.5 V . Small light blue squares: $T = 3$ K, $V_g = 0$ V; Small purple circles: $T = 2.4$ K, $V_g = 1.5$ V; Green triangles correspond to G vs. $T_{eff}^{-1/2}$ at fixed T and variable V_{sd} at $V_g = 10$ V. Black dashed lines are guide to the eyes. Inset shows V_{sd}^2 against T^2 at constant conductance G. Different G are represented: 1 nS (black), 2 nS (blue), 4 nS (green), 10 nS (orange), and 20 nS (red). The V_{sd}^2 against T^2 curves are well fitted by straight lines of same slope.

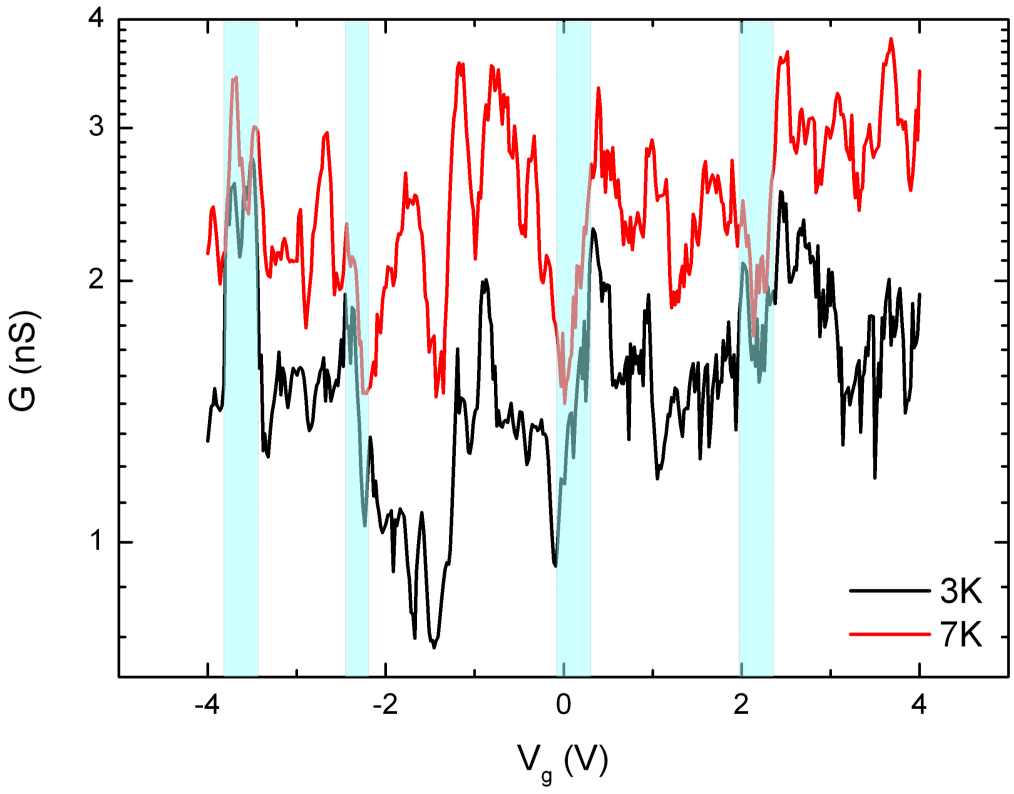

Figure 3.5.5: Conductance against gate voltage at $V_{sd} = 25$ mV. The black (resp. red) curve is measured at 3K (resp. 7K). The shaded regions correspond to ranges of gate voltages where the conductance is weakly temperature-dependent.

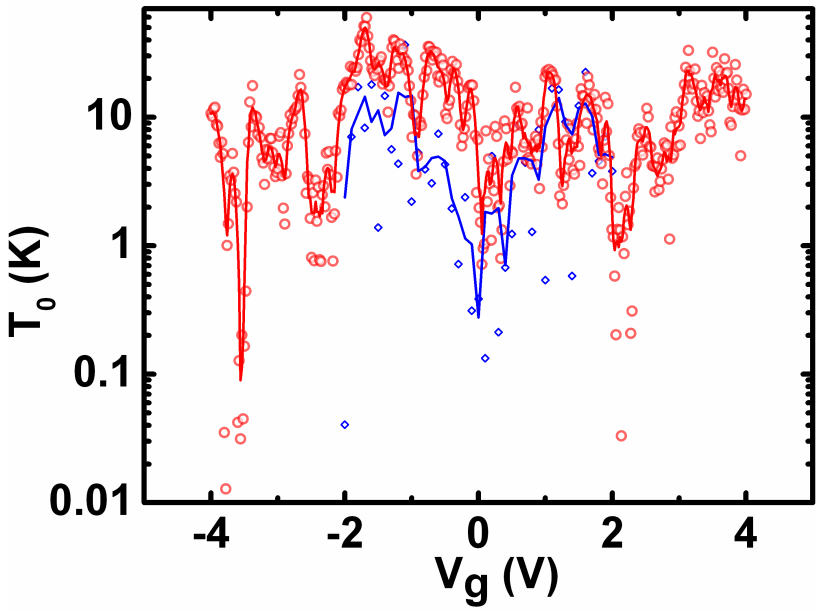

Figure 3.5.6: $T_0 = T_{el}$ vs V_g extracted by two different methods. The red points have been measured by sweeping the gate voltage at 3K and 7K and calculating $(\Delta \ln G/\Delta X_{eff})^2$ for all V_g, where $X_{eff} = T_{eff}^{-1/2}$ (see Figure 3.5.5). The blue dots have been obtained at fixed T by sweeping the bias voltage at different V_g, and systematically calculating the slope of $\ln G$ vs $T_{eff}^{-1/2}$ below 10K (see Figure 3.5.4). Solid lines are averages. The histogram shown in figure 3.4.4 has been plotted using the red data and the relation $T_{el} = -\frac{T_c}{2}\ln(p_{el})$.

3.5.5 Data sets used to plot $\sigma_{\ln G}$ vs T_{eff} in figure 3.4.7

In order to plot a meaningful $\sigma_{\ln G}$ vs T_{eff} graph (figure 3.4.7), we used large data sets from the same device. These data sets were measured in different regions of the three-dimensional (T, V_{sd}, V_g) parameter space. Standard deviations were systematically calculated from G vs V_g data series, at fixed T and V_{sd}. We show below the data sets used to plot $\sigma_{\ln G}$ vs T_{eff} in figure 3.4.7, apart from the $G(T = 3K, V_{sd}, V_g)$ data set (Data set 3), already shown in Figure 3.4.6.

3.5.5.1 Data set 1 (DS1):

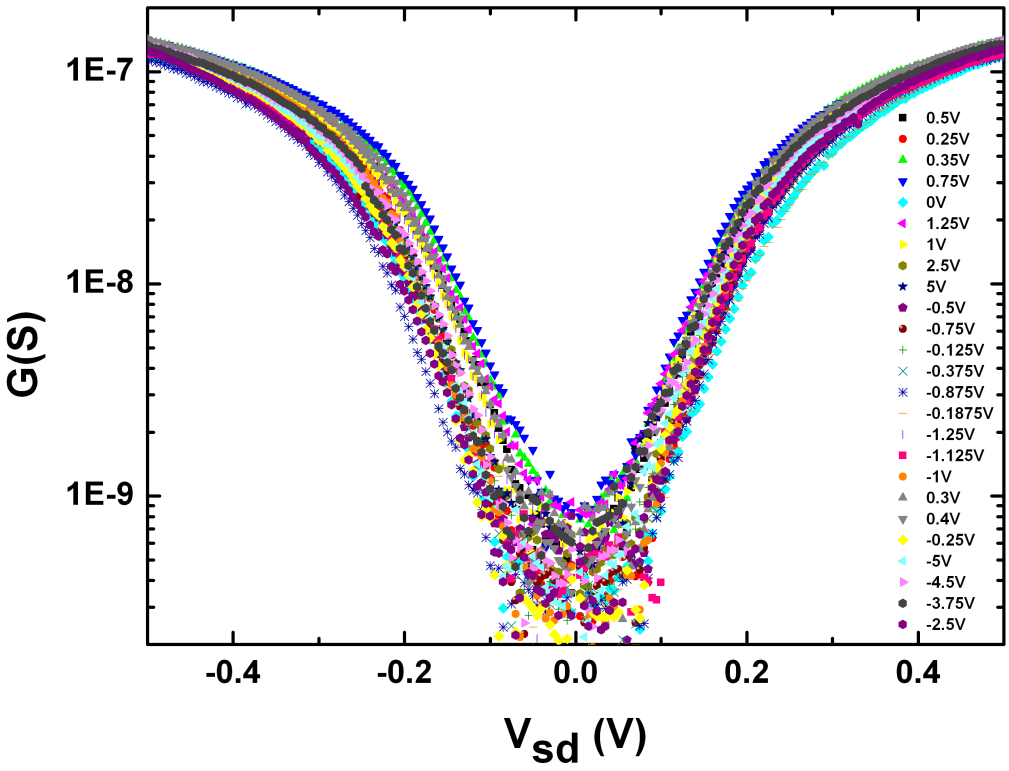

Figure 3.5.7: Conductance as a function of voltage bias for 25 different gate voltages, at $T = 2.42$ K. V_{sd} varies between -0.5V and 0.5V in steps of 5 mV. The 25 different V_g lie in the range [-5V,+5V]. The standard deviation of $\ln G$ shown as blue dots in Figure 3.4.7 has been systematically calculated at fixed V_{sd} = -0.5V, -0.495V,...,0.495V, 0.5V. For all $T_{eff} = \sqrt{T^2 + (\alpha e \xi V_{sd}/k_B L)^2}$, the standard deviation of the log-conductance is calculated as $\sigma_{\ln G}(T_{eff}) = (\sigma_{\ln G}(V_{sd}) + \sigma_{\ln G}(-V_{sd}))/2$.

3.5.5.2 Data set 2 (DS2):

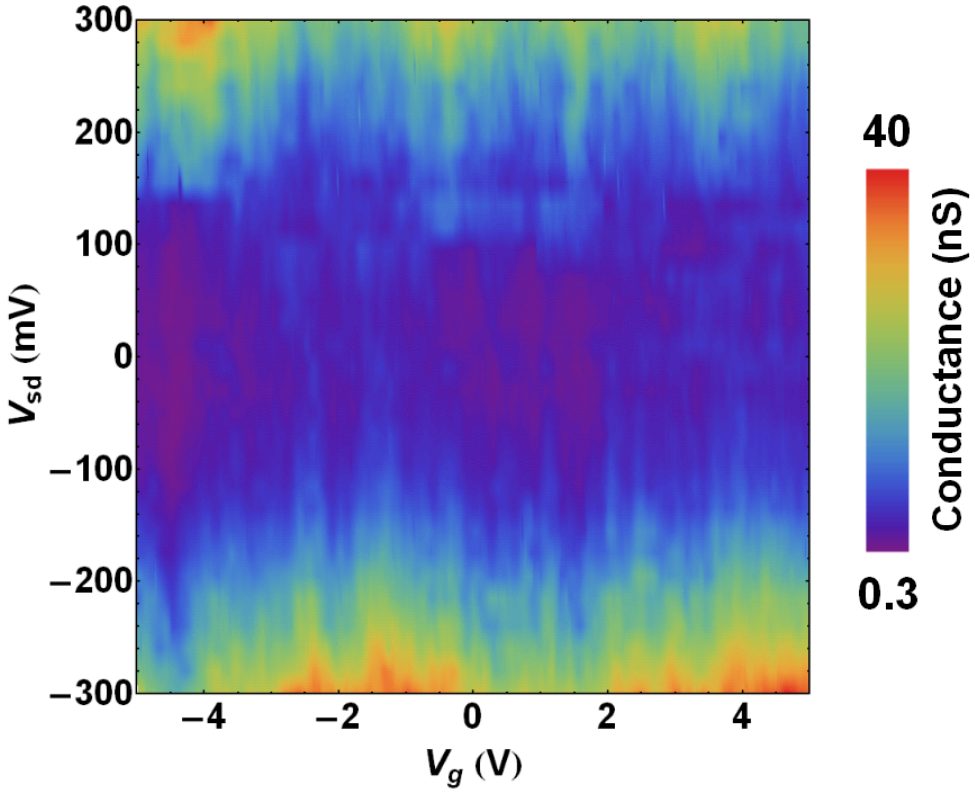

Figure 3.5.8: Conductance as a function of V_g and V_{sd} at 3K. The color scale corresponds to the measured conductance in nS. Here, the gate voltage is varied between -5V and 5V, while the bias voltage is varied between -300 mV and 300 mV. This data set is used to calculate the standard deviation of the log-conductance against T_{eff} points represented by green triangles in Figure 3.4.7.

3.5.5.3 Data set 4 (DS4):

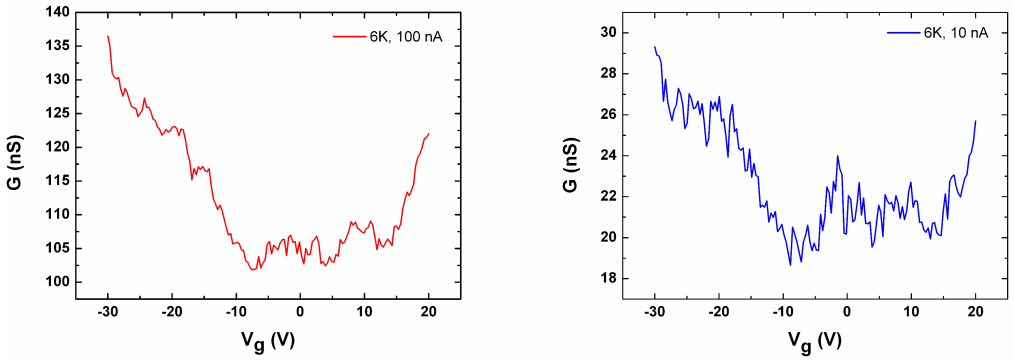

Figure 3.5.9: Conductance against gate voltage at 6K, measured at fixed source-drain current: 10 nA (blue) and 100 nA (red). The standard deviation of the log-conductance was calculated in both cases in the flat region around the charge neutrality point. The red squares in Figure 3.4.7 correspond to the fluctuations in log-conductance between -4V and 4V.

3.5.6 Dependence of N_{th} on T_{eff}

For graphene dots at Fermi energies comparable to or smaller than $k_B T_{eff}$, we have $N_{th} \propto T_{eff}^2$, since graphene dots' bulk charge carriers have a linear density of states. This is a reasonable assumption in our case, where the density of charge carriers is of the order of $\sim 10^{12}/\text{cm}^2$, or less. In other words, the number of electrons (or holes) per dot of linear size $\xi \sim 45$ nm is comparable to or smaller than 20. This is typically smaller than the number of low-energy edge-states existing in a dot of size $\xi \sim 45$ nm, which is of the order [137] of $\xi/a_0 \sim 100$, where a_0 is graphene lattice constant. Unlike bulk states which have a density of states $\rho_{bulk}(\epsilon) \sim \epsilon$, edge states have a density of states $\rho_{edge}(\epsilon) \sim 1/\epsilon$ [137]. Since the number of charge carriers per dot is typically smaller than the number of edge states, the Fermi energy is pinned around the zero-energy point. Numerical simulations reported in reference [137] suggest that in our case, the Fermi energy lies within few meV from charge-neutrality point, comparable to $k_B T_{eff}$ in the MIC regime (see Figure 3.4.7). The number of graphene dots extended bulk states within an energy interval of length $k_B T_{eff}$ must thus be $N_{th} \propto T_{eff}^2$.

Chapter 4

Engineering spin and anomalous Hall effects in graphene by means of spin-orbit active adatoms

4.1 Graphene spintronics

Graphene is widely seen as a promising material for spintronics given its low intrinsic spin-orbit coupling [132] of $\lambda_{int} \sim 1$ µeV and its ability to form sp^3 bonds with adatoms in a controllable way [90, 91]. While the former property in principle allows to use graphene as a spin-preserving channel, the latter gives the possibilty to locally enhance the spin-orbit coupling due to atomic-scale out-of-plane deformation of the lattice [149]. Therefore, it may become possible to engineer novel graphene-based spintronics devices, with spatially-varying spin-orbit coupling. Low spin-orbit interaction regions would be used to faithfully transport spins, while the high spin-orbit coupling ones would be used to manipulate spins. However, spin-transport experiments performed on pristine graphene [133] showed that spin diffusion lengths are orders of magni-

tude smaller than expected from the extremely small value of λ_{int}. Many early spin-transport experiments on graphene [133, 134] and its bilayer counterpart [135] were devoted to understand the main scattering mechanisms responsible for such unexpectedly low spin diffusion lengths. At the time of writing, this is still a mystery in spite of some notable advances [136].

Hybridization techniques to tune graphene' s spin-orbit coupling and allow new spin-processing possibilities are still in their infancy. While it was recently shown that hydrogenation of graphene could lead to spin Hall effect at zero magnetic fields [87], few other types of adatoms have been tried to functionalize graphene. Clearly, exploring Mendeleev's table more deeply could bring new exciting possibilities for spin-processing. In this purely theoretical chapter, we investigate the effects of non-magnetic heavy elements, which leave the lattice flat. We show that such species can induce large spin-orbit interactions if adsorbed in hollow- or top-position, but not in bridge-position. Exact spin-orbit coupling mechanisms depend not only on the position of adatoms on the lattice but also on their valence orbital type: s, p, d or f. Our calculations reveal that while hollow-position adatoms can induce large pure transverse spin currents and spin Hall effect, top-position adatoms produce no spin-currents but give rise to transverse charge currents, leading to anomalous Hall effect. Crucially, we show that tuning the Fermi level can not only switch these transverse currents on and off but also reverse their flow. This opens up new avenues for novel spintronics and electronics applications.

4.2 Constructing effective impurity Hamiltonians

We now derive Hamiltonians describing the action of adatoms on graphene's Dirac fermions. In previous works, graphene's adatoms have essentially been described as a Dirac-peak potential $V\delta(\vec{r})$, in order to estimate the conductivity

[139, 156] of defective graphene, and identify its dependence on charge carrier density. Though this approach proved successful experimentally[150, 151, 152], it does not capture subtle effects which we aim to investigate, in particular the impact of adatoms on charge carriers spin and valley degrees of freedom. In this section we seek to establish a continuum theory of atoms adsorbed on graphene, within which an adatom situated at the origin adds a localized effective-mass term $M\delta(\vec{r})$ to pristine graphene's Dirac Hamiltonian, and M is an 8×8 matrix which depends on the adatom's exact position in the lattice: at the center of a honeycomb hexagon - hollow position -, on top of a carbon atom - top position -, or in the middle of a carbon-carbon bond - bridge position -. For the continuum theory to incorporate the most important symmetries associated with these particular positions in the lattice, we first derive very general graphene-only single-electron level tight-binding Hamiltonians, and then take the limit of vanishingly small lattice spacing.

4.2.1 Adatoms in hollow position

We start by considering the case of a single adatom in the hollow position. Since we are primarily concerned with spin-orbit coupling, we decide to write our graphene-only hamiltonian in terms of creation and annihilation operators of states of well-defined angular momentum M, instead of the more conventional creation and annihilation operators of carbon p_z-orbital states. Since hopping integrals between the latter and the adatom decrease exponentially with distance from the adatom, the relevant states of angular momentum M can be written as superposition of all p_z-orbital states located at the 6 vertices of the hexagon occupied by the adatom, as depicted in FIG. 4.2.1.

Using the numbering of carbon atoms shown in Figure 4.2.1, and noting c_i the operator annihilating a p_z-orbital state of atom i, we focus on operators of the form $C = \sum_{i=1}^{6} \lambda_i c_i$. We also note $s_{l=0,x,y,z}$ the Pauli matrices acting on spin. Requiring C to have a given angular momentum, there exists an integer

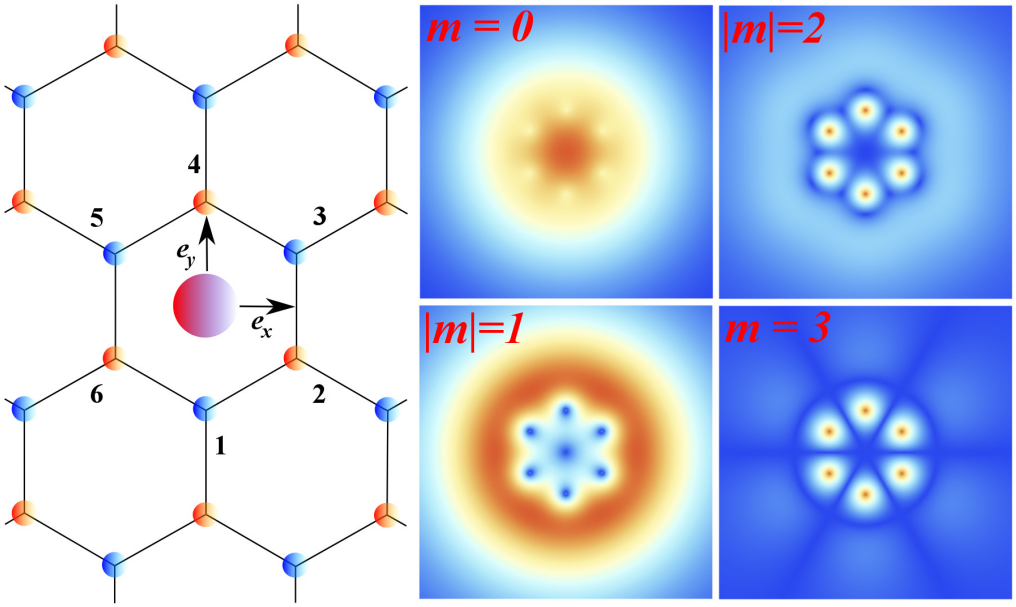

Figure 4.2.1: Schematic picture of an adatom (pink sphere) in a hollow position. A-sublattice (resp. B-sublattice) carbon atoms are represented as blue (resp. red). Right pannels show the modulus of wave functions $\psi_m(x, y)$ created by operators $\Omega_m^\dagger$, for $m = 0, \pm 1, \pm 2, 3$. Space coordinates (x, y) have the adatom as origin, and verify $(x, y) \in [-3.5, 3.5]^2$ in units of $a \approx 1.43$. The color scale is linear and reprsents $|\psi_m|$, from dark blue (lowest values) to red (highest values).

m such that C transforms into $e^{-is_z\pi/6}e^{-im\pi/3}C$ under in-plane rotation by $\pi/3$ around the adatom. This condition imposes that $\lambda_2 = \omega^m\lambda_1$, $\lambda_3 = \omega^{2m}\lambda_1$,..., $\lambda_6 = \omega^{5m}\lambda_1$, where $\omega = e^{-i\pi/3}$. In other words, the only possible operators annihilating a graphene quasiparticle state on the hexagonal plaquette hosting the adatom, and of well-defined angular momentum M around this adatom are, up to a scalar coefficient and unitary operator acting on spin, $\Omega_m = \sum_{i=1}^{6}\omega^{m(n-1)}c_n$ for $m = 0, \pm1, \pm2, 3$. By construction, operators Ω_m, already encountered in Ref. [154], carry angular momentum m, except Ω_3 which carries angular momentum 0. This can easily be seen by considering the time-reversed operator $s_y\Omega_3$ which has the same angular momentum. Since time-reversal transforms angular momentum $\vec{L} = \vec{r}\times\vec{p}$ into its opposite, it follows that Ω_3 has angular momentum zero. We also observe that the six operators Ω_m are linearly independent, since $\left[\omega^{m(n-1)}\right]_{(m,n)}$ is a Vandermonde matrix [155] and ω is a primitive sixth root of unity. Therefore, the most general graphene-only single-electron Hamiltonian term induced by a hollow-position adatom can be written in terms of operators annihilating "hexagonal" $\Omega_m^\dagger|0\rangle$ states:

$$\begin{aligned} H_{hollow} &= \sum_{m=-2}^{3}\Omega_m^\dagger X_m\Omega_m + \sum_{m=-2}^{1}\Omega_m^\dagger M_m\Omega_{m+1} \\ &+ \sum_{m=0,\pm1}\Omega_3^\dagger T_m\Omega_m + h.c. \end{aligned} \tag{4.2.1}$$

where X_m, M_m, and T_m are matrices acting on spin. These matrices connect operators Ω_i which have angular momenta differing by at most 1, by conservation of total angular momentum $J = L + S$. Conservation of J also implies that X_m and T_0 are diagonal matrices, while M_m and T_1 matrices are proportional to the spin-raising operator $s_+ = \frac{s_x+is_y}{2}$ and T_{-1} is proportional to the spin-lowering operator $s_- = \frac{s_x-is_y}{2}$. This means that under rotation by $\pi/3$, $\Omega_m^\dagger X_m\Omega_m$and $\Omega_m^\dagger M_m\Omega_{m+1}$ are invariant, while $\Omega_3^\dagger T_m\Omega_m$ terms are odd. The invariance of H_{hollow} under rotation by $\pi/3$ thus requires $T_{m=0,\pm1} = 0$. In

other words, zero-angular momentum states $\Omega_3^\dagger|0\rangle$ don't couple to any other hexagonal $\Omega_m^\dagger|0\rangle$ state and can be ignored. Moreover, since we consider non-magnetic and static impurities, H_{hollow} is time-reversal invariant, which implies that $s_y X_m^* s_y = X_{-m}$ and $s_y M_m^* s_y = M_{-m-1}^\dagger$. Finally, invariance of H_{hollow} under reflection $x \mapsto -x$ requires $s_x X_m s_x = X_{-m}$and $s_x M_m s_x = M_{-m-1}^\dagger$. Together, these conditions lead to the simplified form:

$$\begin{aligned} H_{hollow} &= \sum_{m=-2}^{2} \nu_m^+ \Omega_m^\dagger \Omega_m + \sum_{m=\pm1,\pm2} \nu_m^- \Omega_m^\dagger s_z \Omega_m \\ &+ i \sum_{m=-2}^{1} \Lambda_m (\Omega_m^\dagger s_+ \Omega_{m+1} - \Omega_{m+1}^\dagger s_- \Omega_m) \end{aligned} \tag{4.2.2}$$

where ν_m^+, ν_m^-, and Λ_m are real numbers verifying $\nu_m^+ = \nu_{-m}^+$, $\nu_{-m}^- = -\nu_m^-$ and $\Lambda_{-m-1} = -\Lambda_m$. It is important to note that eq. 4.2.2 is general at the single-electron level, provided that interactions between the adatom and graphene's p_z-orbitals are negligible outside the adatom's six nearest neighbors. The exact coupling mechansims between hexagonal states only affect the value of constants $\nu_m^\pm$ and Λ_m, but not the overall form of H_{hallow} given by eq. 4.2.2. Relations between these coupling constants and microscopic parameters such as energy levels and spin-orbit couplings of the adatom are derived in Appendix, in situations where a graphene electron or hole in state $\Omega_m^\dagger|0\rangle$ undergoes spin-dependent tunneling to an adatom orbital of same angular momentum, potentially flips its spin by intra-atomic spin-orbit interaction and tunnels back to the graphene sheet in another $\Omega_{m'}^\dagger|0\rangle$ state. In such cases, H_{hollow} describes the effect of impurity-graphene hybridization on graphene's Dirac fermions.

We now derive an expression for H_{hollow} in the continuum limit, where the carbon-carbon distance a_0 is seen as vanishingly small. In this limit, pristine

graphene's Hamiltonian reads [157]

$$H_0 = \int \frac{d^2\vec{r}}{A_{\hexagon}} \Psi^\dagger(\vec{r}) \mathcal{H}_0(\vec{r}) \Psi(\vec{r}) \tag{4.2.3}$$

where $\mathcal{H}_0 = v_F(\tau_z \sigma_x p_x + \sigma_y p_y)$ and $A_{\hexagon} = \frac{3\sqrt{3}a_0^2}{2}$ is the area of a unit cell. Here, $\tau_{l=0,x,y,z}$ and $\sigma_{l=0,x,y,z}$ are Pauli matrices acting respectively on valley- and sublattice-space. In eq. 4.2.3,

$$\begin{aligned} \Psi^\dagger(\vec{r}) \;\; = \;\; & (\Psi^\dagger_{\uparrow KA}(\vec{r}), \Psi^\dagger_{\uparrow KB}(\vec{r}), \Psi^\dagger_{\uparrow K'A}(\vec{r}), \Psi^\dagger_{\uparrow K'B}(\vec{r}), \\ & \Psi^\dagger_{\downarrow KA}(\vec{r}), \Psi^\dagger_{\downarrow KB}(\vec{r}), \Psi^\dagger_{\downarrow K'A}(\vec{r}), \Psi^\dagger_{\downarrow K'B}(\vec{r})) \end{aligned}$$

is an 1×8 creation operator whose components $\Psi^\dagger_{s\tau\sigma}(\vec{r})$ create a state with spin $s = \uparrow, \downarrow \equiv 1, -1$, valley $\tau = K, K' \equiv 1, -1$, in sublattice $\sigma = A, B \equiv 1, -1$ and at point $\vec{r}$. To account for both K and K' valleys, we write spin-s components of annihilation operators c_n as superpositions of $\Psi_{sK\sigma_n}(\vec{r}_n)$ and $\Psi_{sK'\sigma_n}(\vec{r}_n)$, where $\vec{r}_n$ and σ_n are the position vector and sublattice index corresponding to site n:

$$c_{n,s} = \sum_{\tau=\pm 1} e^{i\tau\overrightarrow{\Gamma K}.\vec{r}_n} \Psi_{s\tau\sigma_n}(\vec{r}_n) \tag{4.2.4}$$

Here, Γ denotes graphene's first Brillouin zone center, and taking the $a_0 \to 0$ limit, the spin-$s = \uparrow, \downarrow$ component of Ω_m becomes:

$$\Omega_{m,s} = \sum_\tau \left(\gamma^A_{m\tau} \Psi_{s\tau A}(\vec{0}) + \gamma^B_{m\tau} \Psi_{s\tau B}(\vec{0}) \right) \tag{4.2.5}$$

with $\gamma^A_{m\tau} = 1 + 2\cos((m-\tau)\frac{2\pi}{3})$ and $\gamma^B_{m\tau} = (-1)^m + 2\cos((m-2\tau)\frac{\pi}{3})$. Writing

$$H_{hollow} = \int \frac{d^2\vec{r}}{A_{\hexagon}} \Psi^\dagger(\vec{r}) \mathcal{H}_{hollow}(\vec{r}) \Psi(\vec{r}) \tag{4.2.6}$$

we obtain the following continuum-limit expression for $\mathcal{H}_{hollow}(\vec{r})$:

$$\begin{aligned}\mathcal{H}_{hollow} &= (V_0\mathbb{I} + \Delta\tau_x\sigma_x + V_{so}s_z\tau_z\sigma_z + \Delta_{so}s_z\tau_y\sigma_y \\ &+ \Lambda_R(s_x\sigma_y + s_y\tau_z\sigma_x))A_{\hexagon}\delta(\vec{r}) \end{aligned} \tag{4.2.7}$$

where $V_0 = 9(\nu_1^+ + \nu_2^+)$, $\Delta = 9(\nu_2^+ - \nu_1^+)$,$V_{so} = 9(\nu_1^- - \nu_2^-)$, $\Delta_{so} = 9(\nu_1^- + \nu_2^-)$ and $\Lambda_R = -9\Lambda_1$. From now on, $A_{\hexagon}$ is set to unity, unless specified otherwise. Eq. 4.2.7 is only valid in the vicinity of the Dirac point, as terms of order 1 or higher in momentum k have been neglected. It nonetheless gives insight regarding possible spin-orbit coupling mechanisms induced by hybridization. In addition to expected on-site potential $V_0\mathbb{I}$ [156] and Kane-Mele [158] intrinsic spin-orbit coupling $V_{so}s_z\tau_z\sigma_z$ terms discussed in Ref. [154], $\mathcal{H}_{hollow}$ contains a spin-independent intervalley term $\Delta\tau_x\sigma_x$ and a term $V_{so}s_z\tau_y\sigma_y$ which mixes both spin and valley degrees of freedom. The presence of $\Delta\tau_x\sigma_x$ reflects the fact that atomically small impurities tend to act as "white noise" [161] in momentum space and hence make intra-valley and inter-valley scattering processes equi-probable. Similar to intrinsic spin-orbit coupling term $V_{so}s_z\tau_z\sigma_z$, the term $V_{so}s_z\tau_y\sigma_y$ is even under $\mathcal{R}_z : z \mapsto -z$ reflection. However, the former differs from the latter by its valley-connecting character, itself a consequence of the short-range nature of adatoms. Importantly, $\mathcal{H}_{hollow}$ also contains a term $\mathcal{H}_R = \Lambda_R(s_x\sigma_y + s_y\tau_z\sigma_x)\delta(\vec{r})$ originating from couplings between hexagonal states of total angular momentum $J = \pm\frac{3}{2}$, namely $\Omega^\dagger_{\pm1}s_\pm\Omega_{\pm2}$ and $\Omega^\dagger_{\pm2}s_\mp\Omega_{\pm1}$ in equation 4.2.2. Since p-orbitals accomodate two states of angular momentum $\pm3/2$, p-orbital adatoms can in principle mediate spin-orbit interactions between hexagonal states $\Omega^\dagger_{1,\uparrow}|0\rangle$ and $\Omega^\dagger_{2,\downarrow}|0\rangle$, thereby leading to non-zero Λ_R. This is confirmed by calculations performed with Löwdin's method, shown in Appendix. However, Λ_R should be significantly enhanced in situations where spin-orbit coupling is mediated by d- or f -orbital adatoms, which host four states of angular momentum $\pm3/2$.

The symmerties of $\mathcal{H}_R$ are interesting in their own right. This term is odd under reflection $\mathcal{R}_z$ but differs from the well-known Bychkov-Rashba [159] Hamiltonian $\mathcal{H}_{BR} = \Lambda_{so}(s_x\sigma_y - s_y\tau_z\sigma_x)$ induced by an out-of-plane electric field, a possibility already pointed out by Ref. [160] for inversion symmetry breaking impurities. Similarly to the Bychkov-Rashba Hamiltonian, $\mathcal{H}_R$ is $SO(2)$-symmetric, as it should be for spin-orbit interactions induced by hollow-position adatoms, which preserve graphene's C_{6v}-symmetry. However, spinors $\psi(\vec{r})$ verifying $(\mathcal{H}_0 + \mathcal{H}_{hollow})\psi = E\psi$ transform under rotation by ϕ, noted $\mathcal{R}_\phi$, as

$$e^{+is_z\phi/2}e^{-i\tau_z\sigma_z\phi/2}\psi(\mathcal{R}_{-\phi}(\vec{r})) \tag{4.2.8}$$

instead of the conventional $e^{-is_z\phi/2}e^{-i\tau_z\sigma_z\phi/2}\psi(\mathcal{R}_{-\phi}(\vec{r}))$. As a result, $\tau\sigma - s$ is a conserved quantity, but *not* $\tau\sigma + s$.

Finally, let us mention that Hamiltonian $\mathcal{H}_{hollow}$ can easily be interpreted in terms of hopping between graphene's p_z orbitals closest to the adatom, as illustrated by Figure 4.2.2. While scalar potential $V_0\mathbb{I}$ and intrinsic spin-orbit coupling term $V_{so}s_z\tau_z\sigma_z$ are associated with on-site energies and hopping between second-nearest neighbors, inter-valley terms $\Delta\tau_x\sigma_x$ and $\Delta_{so}s_z\tau_y\sigma_y$ correspond to first- and third-nearest neighbor hopping respectively. In contrast with Bychkov-Rashba spin-orbit interaction $\mathcal{H}_{BR}$, the $\Lambda_R(s_x\sigma_y + s_y\tau_z\sigma_x)$ term is associated with *both* first- and third-nearest neighbor hopping.

4.2.2 Adatoms in top-position

Another important class of adatoms are species which can be physisorbed or chemisorbed in top position, *i.e.* on top of a graphene carbon atom belonging to the A- or B-sublattice, as depicted in Figure 4.2.3. Such an adatom breaks graphene's C_{6v} symmetry and hence induces spin-orbit coupling mechansims different from those introduced by adatoms in hollow position. In contrast with adatoms in hollow position, a top-position adatom has only one nearest neighbor, located directly below and numbered as 0, as well as three second

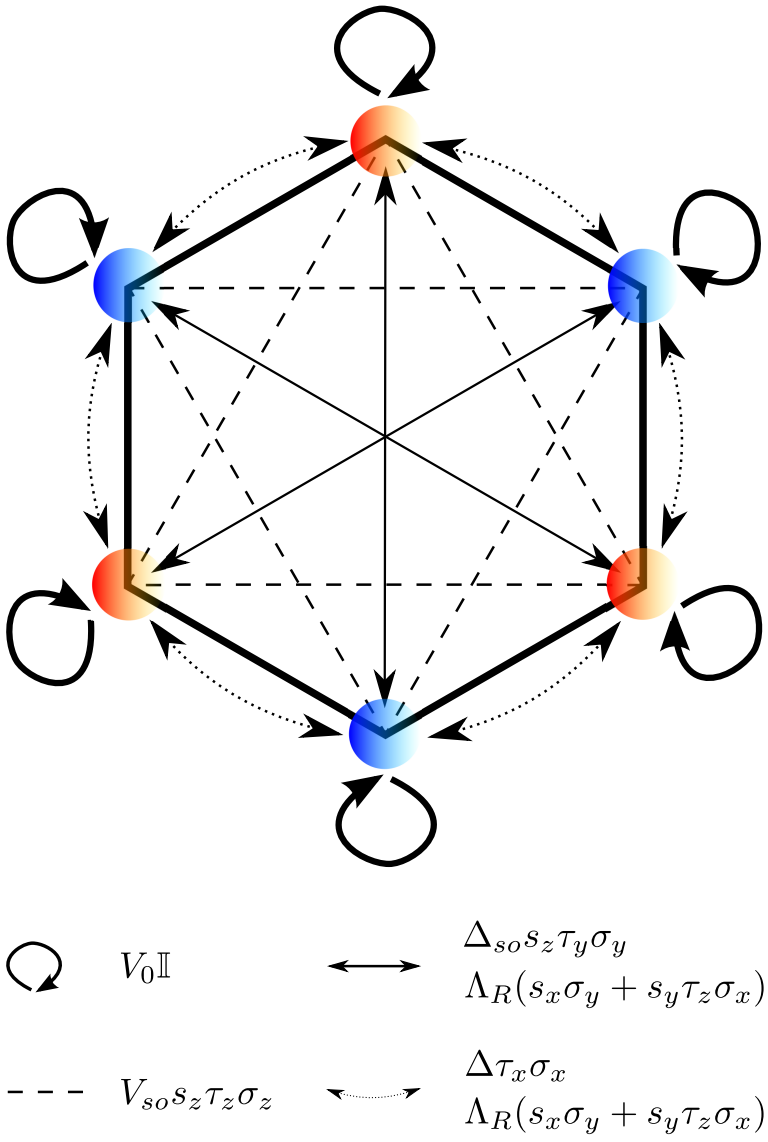

Figure 4.2.2: Interpretation of effective Hamiltonian $\mathcal{H}_{hollow}$ in terms of hopping between graphene's p_z-orbitals.

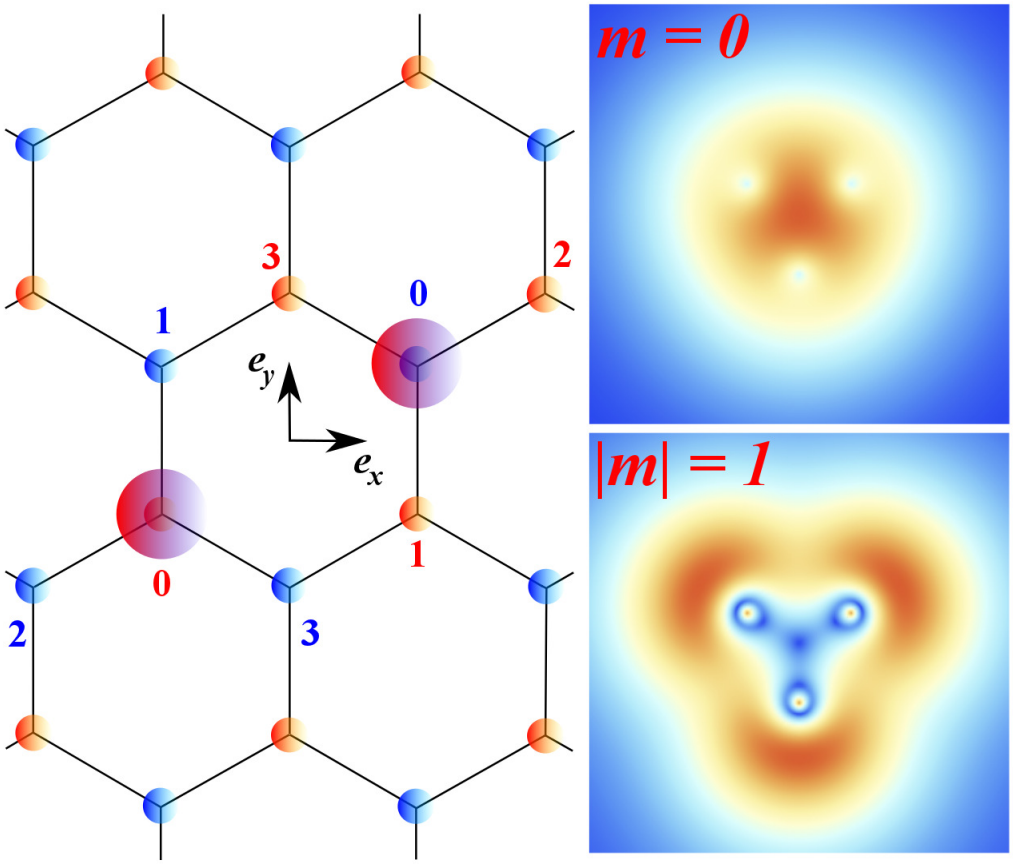

Figure 4.2.3: Schematic picture of adatoms (pink spheres) in top position, on an A-sublattice (blue) and B-sublattice (red) carbon atom. Sites numbering used in main text is shown for both cases, A- and B-sublattice. Right pannels show the modulus of wave functions $\phi_m(x, y)$ created around the A-sublattice adatom by operators $\Gamma_m^\dagger$, for $m = 0, \pm 1$. Space coordinates (x, y) have this adatom as origin, and verify $(x, y) \in [-3.5, 3.5]^2$ in units of $a \approx 1.43$. The color scale is linear and reprsents $|\phi_m|$, from dark blue (lowest values) to red (highest values).

nearest neighbors labelled 1,2 and 3 and situated at a distance of a_0 away from 0. The only electronic states with definite angular momentum m formed by linear combinations of p_z orbitals 1,2 and 3 are "triangular states" annihilated by operators $\Gamma_m = \sum_{n=1}^{3} \zeta^{m(n-1)} c_n$ where $m = 0, \pm 1$ and $\zeta = e^{-i2\pi/3}$, see Figure 4.2.3. In particular, states with angular momentum ± 2 are not supported. Since Γ_0, Γ_1 and Γ_{-1} are linearly independant, we can write the graphene-only impurity hamiltonian H_{top} describing the action of a top-position adatom in terms of operators c_0 and $\Gamma_{0,\pm 1}$ only, provided that interactions between the adatom and more distant carbon atoms are negligible. At the single-electron

level, the most general time-reversal invariant H_{top} conserving total angular momentum and preserving C_{3v}-symmetry reads:

$$\begin{aligned} H_{top} &= V_0 c_0^\dagger c_0 + V_1 \Gamma_0^\dagger \Gamma_0 + V_2 (c_0^\dagger \Gamma_0 + \Gamma_0^\dagger c_0) \\ &+ \Lambda_+ (\Gamma_1^\dagger \Gamma_1 + \Gamma_{-1}^\dagger \Gamma_{-1}) \\ &+ \Lambda_- (\Gamma_1^\dagger s_z \Gamma_1 + \Gamma_{-1}^\dagger s_z \Gamma_{-1}) \\ &+ i\mu (c_0^\dagger s_+ \Gamma_1 + c_0^\dagger s_- \Gamma_{-1} - h.c.) \\ &+ i\tau (\Gamma_0^\dagger s_+ \Gamma_1 + \Gamma_0^\dagger s_- \Gamma_{-1} - h.c.) \end{aligned} \tag{4.2.9}$$

where $V_{0,1,2}$, τ, μ and $\Lambda_\pm$ are reals. In the continuum limit $a_0 \to 0$, spin-s components of c_0 and Γ_m operators, are $c_{0,s} = \Psi_{sKA}(\vec{0}) + \Psi_{sK'A}(\vec{0})$ and $\Gamma_{m,s} = 3(1-\delta_{m,0})\Psi_{smB}(\vec{0})$ if the adatom is on top of an A-sublattice carbon atom, and $c_{0,s} = \Psi_{sKB}(\vec{0}) + \Psi_{sK'B}(\vec{0})$ and $\Gamma_{m,s} = 3(1-\delta_{m,0})\Psi_{s,-m,A}(\vec{0})$ otherwise. In the continuum, an adatom on top of an A,B-sublattice site thus induces the following $\mathcal{H}_{top}^{A,B}$ Hamiltonian:

$$\begin{aligned} \mathcal{H}_{top}^{A,B} &= (V_0(\tau_0 + \tau_x)\pi_{A,B} + v_0 \pi_{B,A} \pm \lambda_{so} s_z \tau_z \pi_{B,A} \\ &+ \Lambda_{so}(s_x \tau_x \sigma_y + s_x \sigma_y + s_y \tau_z \sigma_x \pm s_y \tau_y \sigma_y))\delta(\vec{r}) \end{aligned} \tag{4.2.10}$$

where $\pi_A = \frac{\sigma_0 + \sigma_z}{2}$ and $\pi_B = \frac{\sigma_0 - \sigma_z}{2}$ are projectors on A- and B-sublattice subspace respectively, and $v_0 = 9\Lambda_+$, $\lambda_{so} = 9\Lambda_-$ and $\Lambda_{so} = \frac{9}{2}\mu$. The term $V_0(\tau_0 + \tau_x)\pi_{A,B}\delta(\vec{r})$ of $\mathcal{H}_{top}^{A,B}$ in eq. 4.2.10 has already been derived for atomically sharp potentials on an A- or B-sublattice atom [161]. It induces intervalley scattering and is symmetric under $x \mapsto -x$ reflection $\mathcal{R}_x$, but breaks all rotational symmetries in the contiuum theory describing graphene Dirac fermions. This is best highlighted by local density of states maps in the vicinity of such impurities [162], exhibiting fringes perpendicular to $\overrightarrow{KK'}$ and hence to $\overrightarrow{e_x}$. Invariance of $\mathcal{H}_{top}^{A,B}$ under $\mathcal{R}_x$ is manifest, as $\mathcal{U}_x H_{top}^{A,B} \mathcal{U}_x = H_{top}^{A,B}$, where $\mathcal{U}_x = s_x \tau_x$ is

the unitary representation of $\mathcal{R}_x$ in the continuum theory described by $\mathcal{H}_{tot} = \mathcal{H}_0 + \mathcal{H}_{top}^{A,B}$. Importantly, one also has $\mathcal{U}_y \mathcal{H}_{top}^{A} \mathcal{U}_y = \mathcal{H}_{top}^{B}$, with $\mathcal{U}_y = s_y \sigma_x$. In other words, $\mathcal{H}_{top}^{A}$ transforms into $\mathcal{H}_{top}^{B}$ under $\mathcal{R}_y : y \mapsto -y$, faithfully reflecting the lattice geometry. This means that top-position adatoms induce different spin-orbit coupling terms, depending on the host sub-lattice. Both close cousins of graphene's intrinsic spin-orbit coupling, $\mathcal{R}_z$-even spin-orbit interaction mediated by top-position adatoms on A- and B-sublattice are $\lambda_{so} s_z \tau_z \pi_B \delta(\vec{r})$ and $-\lambda_{so} s_z \tau_z \pi_A \delta(\vec{r})$ respectively. The $\mathcal{R}_z$-odd component is more surprising. Beside the valley-preserving term $\propto (s_x \sigma_y + s_y \tau_z \sigma_x)\delta(\vec{r})$ already encoutered in eq. 4.2.7, a new valley-mixing term $\Lambda_{so}(s_x \tau_x \sigma_y \pm s_y \tau_y \sigma_y)\delta(\vec{r})$ emerges, $+$ for $\mathcal{H}_{top}^{A}$ and $-$ for $\mathcal{H}_{top}^{B}$. Since in the continuum limit, $\Gamma_0 = 0 + \mathcal{O}(a_0 k)$, spin-flipping processes coupling two triangular states are quenched, in contrast with those coupling a triangular state $\Gamma_{\pm 1}^{\dagger}|0\rangle$ with the central orbital $c_0^{\dagger}|0\rangle$, whose continuum limit is a superposition of K- and K'-valley states. This explains why top-position adatoms give rise to $\mathcal{R}_z$-odd spin-orbit interactions inducing both spin-flip and inter-valley scattering.

Continuum-limit hamiltonian $\mathcal{H}_{top}^{A,B}$ can be interpreted in terms of hopping between $p_z$orbitals $i = 0, 1, 2, 3$, as shown in Figure 4.2.4. While spin-independent terms $V_0(\tau_0 + \tau_x)\pi_{A,B}$ and $v_0 \pi_{B,A}$ correspond to on-site energies on central site 0 and neighboring orbitals $i = 1, 2, 3$ respectively, the $\mathcal{R}_z$-even spin-orbit coupling term $\pm\lambda_{so} s_z \tau_z \pi_{B,A}$ is associated with hopping between orbitals $i = 1, 2, 3$. Finally, the $\mathcal{R}_z$-odd term $\Lambda_{so}(s_x \tau_x \sigma_y + s_x \sigma_y + s_y \tau_z \sigma_x \pm s_y \tau_y \sigma_y)$ arises from spin-dependent hopping between the central site 0 and its first nearest neighbors.

4.2.3 Adatoms in bridge position

We now consider the case of adatoms in the bridge position, depicted in Figure 4.2.5. The only states of definite angular momentum m which can be formed with p_z-orbitals of atoms 1 and 2 are, up to a scalar and a unitary matrix

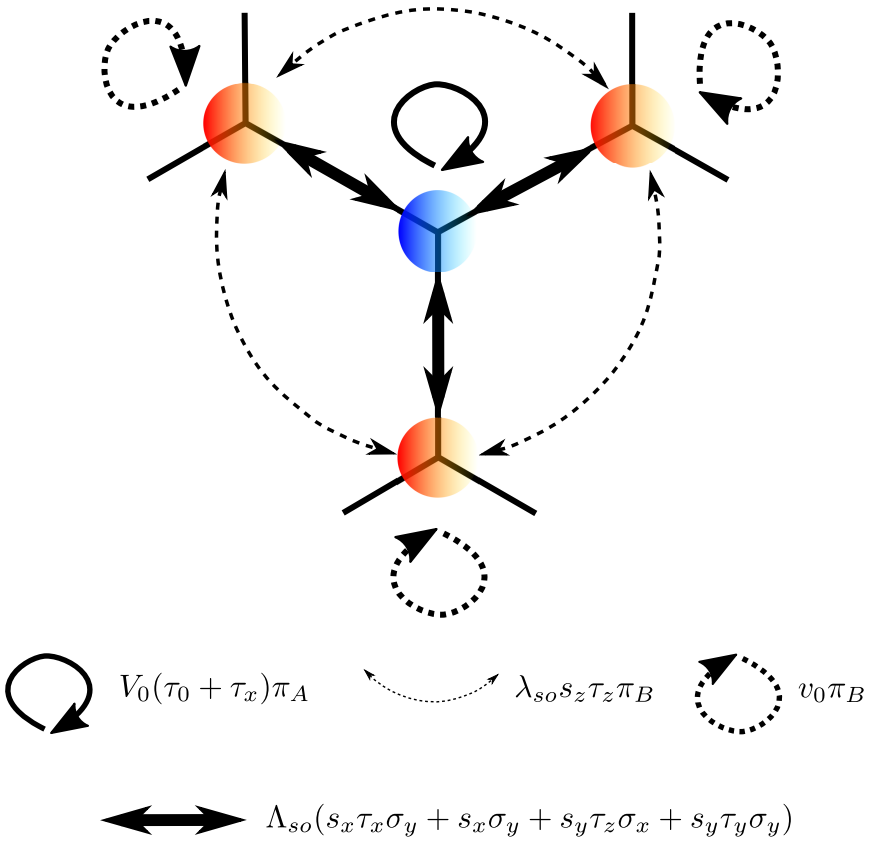

Figure 4.2.4: Interpretation of effective Hamiltonian $\mathcal{H}^A_{top}$ in terms of hopping between graphene's p_z-orbitals.

acting on spins: $(c_1^\dagger \pm c_2^\dagger)|0\rangle$. However, these states have angular momentum zero. Other possible definite-m linear combinations including further p_z-orbitals would also have $m = 0$, because the only rotational symmetry preserved by the bridge configuration is the rotation by π. As a result, $\mathcal{R}_z$-odd spin-orbit coupling mechanisms induced by graphene-adatom hybridization is forbidden in absence of electric field. Furthermore, the impurity Hamiltonian H_{bridge} induced by any non-magnetic, static bridge-position adatom must respect hermicity, time-reversal symmetry and $\mathcal{R}_y$. At the single electron level, and limiting ourselves to orbital 1 and 2, these conditions constrain H_{bridge} to read:

$$H_{bridge} = V_b(c_1^\dagger c_1 + c_2^\dagger c_2) + \beta(c_2^\dagger c_1 + c_1^\dagger c_2) \tag{4.2.11}$$

where V_b and β are reals. Clearly, H_{bridge} does *not* have any spin-orbit coupling term, but for completeness, we derived the continuum limit of H_{bridge}, using

$c_{1,s} \to \Psi_{sKB}(\vec{0}) + \Psi_{sK'B}(\vec{0})$ and $c_{2,s} \to \Psi_{sKA}(\vec{0}) + \Psi_{sK'A}(\vec{0})$. We obtain:

$$\mathcal{H}_{bridge} = (V_b(\tau_0 + \tau_x) + \beta(\tau_0 + \tau_x)\sigma_x)\delta(\vec{r}) \tag{4.2.12}$$

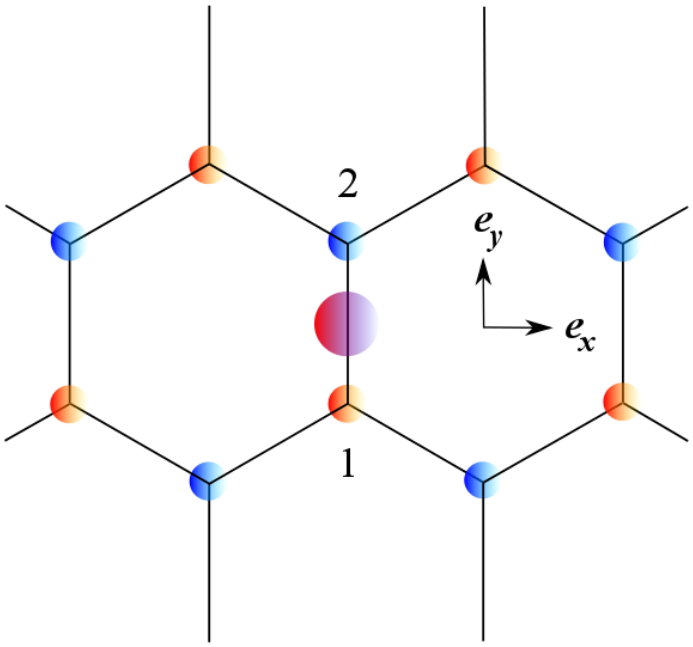

Figure 4.2.5: Adatom (pink sphere) in bridge position. A-sublattice and B-sublattice carbon atoms are shown in blue and red respectively. Relevant atoms are numbered as in main text.

In summary, adatoms in hollow, top and bridge positions give rise to a mass-term in the continuum limit Hamiltonian describing graphene quasi-particles:

$$\mathcal{H}_{tot} = v_F(\tau_z\sigma_x p_x + \sigma_y p_y) + M\delta(\vec{r}) \tag{4.2.13}$$

where $M = M_{el} + M_{ev} + M_{odd}$ are, close to the Dirac point, momentum-independent 8×8 hermitian matrices. Here, M_{el} describes the spin-independent part, of pure electrostatic origin, while M_{ev} and M_{odd} correspond to the $\mathcal{R}_z$-even and $\mathcal{R}_z$-odd spin-orbit coupling contributions. Expressions for these matrices in previously-discussed cases are compared in table 4.1.

Effective mass	Hollow	Top (A or B)	Bridge
M_{el}	$V_0\mathbb{I} + \Delta\tau_x\sigma_x$	$V_0(\tau_0 + \tau_x)\pi_{A,B} + v_0\pi_{B,A}$	$V_b(\tau_0 + \tau_x) + \beta(\tau_0 + \tau_x)\sigma_x$
M_{ev}	$V_{so}s_z\tau_z\sigma_z + \Delta_{so}s_z\tau_y\sigma_y$	$\pm\lambda_{so}s_z\tau_z\pi_{B,A}$	0
M_{odd}	$\Lambda_R(s_x\sigma_y + s_y\tau_z\sigma_x)$	$\Lambda_{so}(s_x\tau_x\sigma_y + s_x\sigma_y + s_y\tau_z\sigma_x \pm s_y\tau_y\sigma_y)$	0

Table 4.1: Table comparing effective masses M_{el}, M_{ev}, and M_{odd} induced by spin-independant, $\mathcal{R}_z$-even and $\mathcal{R}_z$-odd terms of impurity Hamiltonians originating from adatoms in hollow, top (on A- or B-sublattice) and bridge positions. Results are valid for s-, p-, d-, and f- orbital adatoms.

4.3 Scattering theory

4.3.1 Scattering cross-section formalism

We consider a hollow- or top-position adatom on graphene, centered at the origin and inducing an effective mass $M\delta(\vec{r})$. The impurity induces elastic scattering, i.e. an incoming Dirac plane wave $\phi_{\vec{k}}^{s,\tau}(\vec{r})$ of spin s, valley τ, momentum $\vec{k}$ and energy $E = s_E\hbar v_F k$, where $s_E = \pm 1$, is scattered to an outgoing wave $\phi_{out}(\vec{r})$, giving rise to a total wave $\Phi(\vec{r}) = \phi_{\vec{k}}^{s,\tau}(\vec{r}) + \phi_{out}(\vec{r})$ of energy E. The outgoing and incoming waves are related by the the Lippmann-Schwinger equation [163]:

$$\phi_{out}(\vec{r}) = G_0^{\pm}(\vec{r}, E)T(E)\phi_{\vec{k}}^{s,\tau}(\vec{0}) \tag{4.3.1}$$

where $G_0^{\pm}(\vec{r}, E) = \langle\vec{r}|(E - \mathcal{H}_0 \pm i\eta)^{-1}|\vec{0}\rangle$ is pristine graphene' s advanced (-) or retarded (+) Green's function, depending on the energy sign: (+) if $\omega > 0$

and (-) otherwise. The matrix T satisfies the equation:

$$T(E) = M(\mathbb{I} - g(E)M)^{-1} \tag{4.3.2}$$

In eq. 4.3.2, $g(E)$ corresponds to the Green's function evaluated at the origin, which is a scalar:

$$g(E) = \frac{E}{2\pi} \ln\left(\frac{|E|}{E_c}\right) - i\frac{E}{4} \tag{4.3.3}$$

where E_c is graphene half band-width and $\hbar v_F \equiv 1$ has been set. For the sake of simplicity, we write the T-matrix and $G_0^{\pm}(\vec{r}, E)$ in the following basis of states:

$$\begin{aligned} &\{|\uparrow KA\rangle, |\uparrow KB\rangle, |\uparrow K'B\rangle, |\uparrow K'A\rangle, \\ &|\downarrow KA\rangle, |\downarrow KB\rangle, |\downarrow K'B\rangle, |\downarrow K'A\rangle\} \end{aligned} \tag{4.3.4}$$

where the Green's function takes the simple asymptotic form, as $r \to +\infty$:

$$G_0^{\pm}(\vec{r}, E) = -\sqrt{\frac{is_E k}{8\pi}} \frac{e^{ikr}}{\sqrt{r}} e^{i\tau_z \overrightarrow{\Gamma K}.\vec{r}} (\mathbb{I} + s_0 \tau_z \sigma_\theta) \tag{4.3.5}$$

with $\sigma_\theta = \begin{pmatrix} 0 & e^{-i\theta} \\ e^{i\theta} & 0 \end{pmatrix}$ and $\theta = \angle(\vec{e}_x, \vec{r})$. In eq. 4.3.5, the diagonal matrix $e^{i\tau_z \overrightarrow{\Gamma K}.\vec{r}}$ encodes the phase difference between waves at K and K' points. In basis 4.3.4, we write T in block form:

$$T = \begin{pmatrix} T_{\uparrow K,\uparrow K} & T_{\uparrow K',\uparrow K} & T_{\downarrow K,\uparrow K} & T_{\downarrow K',\uparrow K} \\ T_{\uparrow K,\uparrow K'} & T_{\uparrow K',\uparrow K'} & T_{\downarrow K,\uparrow K'} & T_{\downarrow K',\uparrow K'} \\ T_{\uparrow K,\downarrow K} & T_{\uparrow K',\downarrow K} & T_{\downarrow K,\downarrow K} & T_{\downarrow K',\downarrow K} \\ T_{\uparrow K,\downarrow K'} & T_{\uparrow K',\downarrow K'} & T_{\downarrow K,\downarrow K'} & T_{\downarrow K',\downarrow K'} \end{pmatrix} \tag{4.3.6}$$

and we note, for valleys $\tau, \tau'$and spins s, s'

$$T_{s\tau,s'\tau'} = \begin{pmatrix} T^{11}_{s\tau,s'\tau'} & T^{12}_{s\tau,s'\tau'} \\ T^{21}_{s\tau,s'\tau'} & T^{22}_{s\tau,s'\tau'} \end{pmatrix} \tag{4.3.7}$$

With these notations, the outgoing wave ϕ_{out} reads, away from the impurity:

$$\phi_{out}(\vec{r}) = -\sqrt{\frac{is_E k}{8\pi}} \frac{e^{ikr}}{\sqrt{r}} e^{i\tau_z \overrightarrow{\Gamma K}.\vec{r}} \sum_{s',\tau'} c_{s\tau,s'\tau'}(\theta) u^{s',\tau'}_{k\vec{e}_r}(\theta) \tag{4.3.8}$$

where $\vec{e}_r = \vec{r}/r$, $u^{s',\tau'}_{k\vec{e}_r}(\theta) = \frac{1}{\sqrt{2}}|s'\rangle \otimes |\tau'\rangle \otimes \begin{pmatrix} 1 \\ s_E \tau' e^{i\theta} \end{pmatrix}$ in basis 4.3.4, and

$$\begin{aligned} c_{s\tau,s'\tau'}(\theta) &= T^{11}_{s\tau,s'\tau'} + \tau T^{12}_{s\tau,s'\tau'} \\ &+ \tau' e^{-i\theta} \left(T^{21}_{s\tau,s'\tau'} + \tau T^{22}_{s\tau,s'\tau'} \right) \end{aligned} \tag{4.3.9}$$

Accounting for both spin and valley degrees of freedom, the radial probability density current associated with the outgoing wave reads

$$\begin{aligned} \mathcal{J}_r &= v_F \phi^\dagger_{out} s_0 \tau_z \sigma_\theta \phi_{out} \\ &= \frac{k}{8\pi r} v_F \sum_{s',\tau'} |c_{s\tau,s'\tau'}(\theta)|^2, \end{aligned} \tag{4.3.10}$$

while the tangential component of the probability density current is

$$\mathcal{J}_\theta = v_F \phi^\dagger_{out} s_0 \tau_z \partial_\theta \sigma_\theta \phi_{out} = 0, \tag{4.3.11}$$

so that the probability density current is radial, $\vec{\mathcal{J}}(\vec{r}) = \mathcal{J}_r \vec{e}_r$. The current associated with scattering of an incoming Dirac fermion of spin s and valley τ is thus the sum of currents $\vec{\mathcal{J}}_{s\tau,s'\tau'} = \frac{k}{8\pi r} v_F |c_{s\tau,s'\tau'}(\theta)|^2 \vec{e}_r$ arising from all possible $s\tau \to s'\tau'$ transitions, and the corresponding differential cross-sections $\sigma_{s\tau,s'\tau'}(\theta)$ are:

$$\sigma_{s\tau,s'\tau'}(\theta) = \frac{k}{8\pi} |c_{s\tau,s'\tau'}(\theta)|^2 \tag{4.3.12}$$

An asymptotic formula for $\sigma_{s\tau,s'\tau'}(\theta)$ can easily be derived from equation 4.3.9:

$$\sigma_{s\tau,s'\tau'}(\theta) = \frac{k}{8\pi}(\mathcal{C}^2_{s\tau,s'\tau'} + \mathcal{M}_{s\tau,s'\tau'}\cos(\theta + \varphi_{s\tau,s'\tau'})) \tag{4.3.13}$$

where

$$\begin{aligned} \mathcal{C}^2_{s\tau,s'\tau'} &= |T^{11}_{s\tau,s'\tau'} + \tau T^{12}_{s\tau,s'\tau'}|^2 \\ &+ |T^{21}_{s\tau,s'\tau'} + \tau T^{22}_{s\tau,s'\tau'}|^2 \end{aligned} \tag{4.3.14}$$

$$\begin{aligned} \mathcal{M}_{s\tau,s'\tau'} &= 2\tau' |T^{11}_{s\tau,s'\tau'} + \tau T^{12}_{s\tau,s'\tau'}| \\ &\times |T^{21}_{s\tau,s'\tau'} + \tau T^{22}_{s\tau,s'\tau'}| \end{aligned} \tag{4.3.15}$$

and

$$\begin{aligned} \varphi_{s\tau,s'\tau'} &= \arg(T^{11}_{s\tau,s'\tau'} + \tau T^{12}_{s\tau,s'\tau'}) \\ &- \arg(T^{21}_{s\tau,s'\tau'} + \tau T^{22}_{s\tau,s'\tau'}) \end{aligned} \tag{4.3.16}$$

It is important to note that $\sigma_{s\tau,s'\tau'}(\theta)$ generally has a phase $\varphi_{s\tau,s'\tau'}$, which can give rise to skew-scattering and hence spin Hall effect or anomalous Hall effect, provided $\varphi_{s\tau,s'\tau'} \neq 0$ and $\mathcal{M}_{s\tau,s'\tau'} \neq 0$. Establishing conditions under which skew scattering is significant is the object of the remaining paragraphs. This study can be conveniently carried out by comparing the integrated skew cross-sections

$$\Sigma^{\perp}_{s\tau,s'\tau'} = \int_0^{2\pi} d\theta \sin\theta \sigma_{s\tau,s'\tau'}(\theta), \tag{4.3.17}$$

which measure the skewness of $s\tau \to s'\tau'$ scattering mechanisms, to the integrated transport cross-sections:

$$\Sigma^{\parallel}_{s\tau,s'\tau'} = \int_0^{2\pi} d\theta (1 - \cos\theta)\sigma_{s\tau,s'\tau'}(\theta) \tag{4.3.18}$$

From a semi-classical view point, these integrated cross-sections directly relate to the relevant microscopic currents

$$\begin{aligned} J^{\perp}_{s\tau,s'\tau'} &= s_E \int_0^{2\pi} \vec{\mathcal{J}}_{s\tau,s'\tau'}.\vec{e}_y r d\theta \\ &= s_E v_F \Sigma^{\perp}_{s\tau,s'\tau'} \end{aligned} \tag{4.3.19}$$

and

$$\begin{aligned} J^{\parallel}_{s\tau,s'\tau'} &= s_E \int_0^{2\pi} \vec{\mathcal{J}}_{s\tau,s'\tau'}.(\vec{e}_r - \vec{e}_x) r d\theta \\ &= s_E v_F \Sigma^{\parallel}_{s\tau,s'\tau'} \end{aligned} \tag{4.3.20}$$

which respectively describe the transverse and deflected currents due to $s\tau \rightarrow s'\tau'$ processes.

4.3.2 Scattering with hollow-position adatoms

We now focus on scattering mechanisms induced by an adatom in the hollow position. Using table 4.1, the calculated T-matrix in basis 4.3.4 reads:

$$T_{hollow} = \begin{pmatrix} T^{\uparrow\uparrow}_{hollow} & T^{\downarrow\uparrow}_{hollow} \\ T^{\uparrow\downarrow}_{hollow} & T^{\downarrow\downarrow}_{hollow} \end{pmatrix} \tag{4.3.21}$$

with 4×4 blocks:

$$T^{ss}_{hollow} = \begin{pmatrix} \alpha_s & 0 & \gamma_s & 0 \\ 0 & \beta_s & 0 & \delta_s \\ \gamma_s & 0 & \alpha_s & 0 \\ 0 & \delta_s & 0 & \beta_s \end{pmatrix} \tag{4.3.22}$$

where $s = \uparrow, \downarrow$, and:

$$T^{\uparrow\downarrow}_{hollow} = -{}^tT^{\downarrow\uparrow}_{hollow} = \begin{pmatrix} 0 & 0 & 0 & 0 \\ \tau_f & 0 & 0 & 0 \\ 0 & 0 & 0 & 0 \\ 0 & 0 & -\tau_f & 0 \end{pmatrix} \tag{4.3.23}$$

Matrix elements appearing in equations 4.3.22 and 4.3.23 verify:

$$\tau_f = \frac{2i\Lambda_R}{d} \tag{4.3.24}$$

$$\alpha_\uparrow = \beta_\downarrow = \frac{\chi - pg}{d} \tag{4.3.25}$$

$$\alpha_\downarrow = \beta_\uparrow = \frac{\chi' - qg}{d'} \tag{4.3.26}$$

$$\gamma_\uparrow = \delta_\downarrow = \frac{\Delta - \Delta_{so}}{d} \tag{4.3.27}$$

$$\gamma_\downarrow = \delta_\uparrow = \frac{\Delta + \Delta_{so}}{d'} \tag{4.3.28}$$

where we set $\chi = V_0 + V_{so}$, $\chi' = V_0 - V_{so}$, $p = (V_0 + V_{so})^2 - (\Delta - \Delta_{so})^2 - 4\Lambda_R^2$ and $q = (V_0 - V_{so})^2 - (\Delta + \Delta_{so})^2$. We also defined:

$$d = 1 - 2g\chi + pg^2 \tag{4.3.29}$$

and

$$d' = 1 - 2g\chi' + qg^2 \tag{4.3.30}$$

Strikingly, T-matrix elements for intervalley-scattering events involving spin-flip are null. However, intra-valley spin-flips, spin-preserving inter-valley scattering and pure momentum scattering events are allowed, and we shall describe them in more detail in the following paragraphs.

Using equations 4.3.9 and 4.3.12, we found that differential cross-sections $\sigma_{\uparrow K,\downarrow K}(\theta)$, $\sigma_{\uparrow K',\downarrow K'}(\theta)$,$\sigma_{\downarrow K,\uparrow K}(\theta)$, and $\sigma_{\downarrow K',\uparrow K'}(\theta)$ are equal and isotropic, leading to:

$$\Sigma_{s\tau,-s\tau} = \frac{k|\tau_f|^2}{4}, \tag{4.3.31}$$

and null skew cross-sections. In other words, spin-flip does not give rise to transverse spin-currents.

This contrasts sharply with the case of spin-preserving scattering. In particular, inter-valley scattering cross-sections are characterized, for $\tau \neq \tau'$, by:

$$\mathcal{M}_{s\tau,s\tau'} = \tau' \mathcal{M}_{inter} \tag{4.3.32}$$

$$\varphi_{s\tau,s\tau'} = s\Theta_{inter} - (1-\tau)\frac{\pi}{2} \tag{4.3.33}$$

with

$$\mathcal{M}_{inter} = 2\frac{\Delta^2 - \Delta_{so}^2}{|d'd|} \tag{4.3.34}$$

and

$$\begin{aligned} \Theta_{inter} &= \arctan\left(\frac{\Im d'}{\Re d'}\right) - \arctan\left(\frac{\Im d}{\Re d}\right) \\ &+ \pi H(-\Re d') - \pi H(-\Re d) \end{aligned} \tag{4.3.35}$$

where H is the Heaviside step function. Generally, both $\mathcal{M}_{inter} \neq 0$ and $\Theta_{inter} \neq 0$ and hence inter-valley scattering induced by a hollow-position adatom is skewed. The case of spin-preserving intra-valley scattering is similar:

$$\mathcal{M}_{s\tau,s\tau} = \tau \mathcal{M}_{intra} \tag{4.3.36}$$

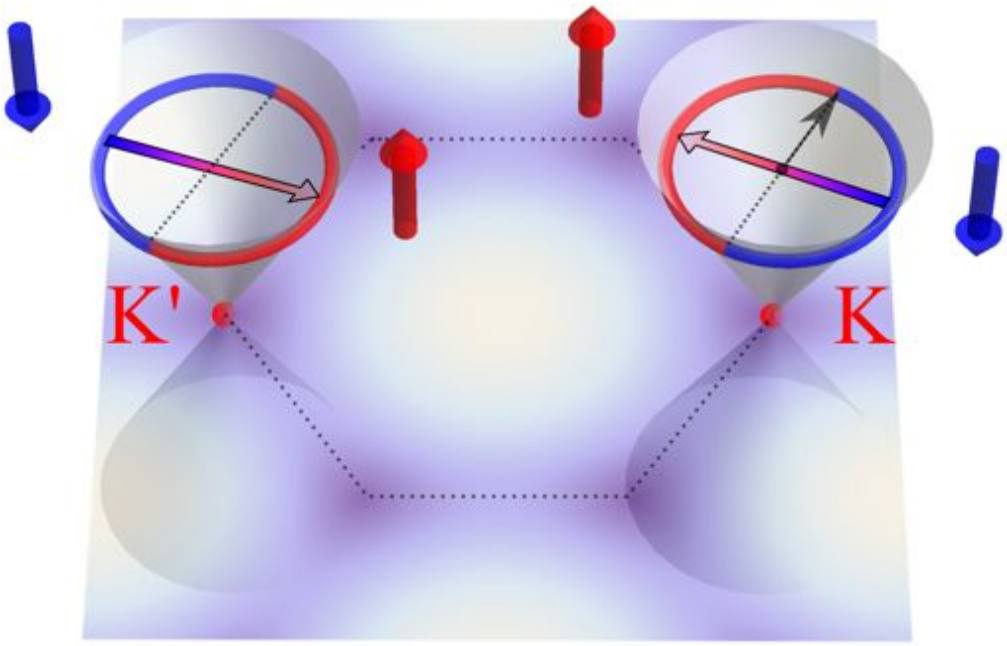

Figure 4.3.1: Schematic representation of skew-scattering induced by adatoms in hollow position. The black arrow represents the momentum $\vec{k}_{in}$ of an incoming quasi-particle in K-valley. Blue (resp. red) half circles correspond to the region of the Fermi line where the outgoing momentum $\vec{k}_{out}$ is most likely to be after a scattering event, if the incoming charge-carrier has spin down (resp. spin up). Resulting pure spin currents are depicted as blue and red planar arrows. Spin currents in K and K' valleys associated with intra- and inter-valley scattering tend to oppose each other.

$$\varphi_{s\tau,s\tau} = s\Theta_{intra} - (1-\tau)\frac{\pi}{2} \tag{4.3.37}$$

with

$$\mathcal{M}_{intra} = \frac{2|\chi' - qg||\chi - pg|}{|d'd|} \tag{4.3.38}$$

and

$$\begin{aligned}\Theta_{intra} - \Theta_{inter} &= \arctan\left(\frac{\Im g}{\Re g - \frac{\chi}{p}}\right) \\ &- \arctan\left(\frac{\Im g}{\Re g - \frac{\chi'}{q}}\right) \\ &+ \pi H\left(\Re g - \frac{\chi}{p}\right) \\ &- \pi H\left(\Re g - \frac{\chi'}{q}\right)\end{aligned} \tag{4.3.39}$$

These results trivially lead to a zero transverse charge current

$$J_Q^{\perp} = e \sum_{s,\tau,\tau'} J^{\perp}_{s\tau,s\tau'} = 0, \tag{4.3.40}$$

but to a generally non-zero transverse spin current

$$\begin{aligned} J_S^{\perp} &= \sum_{s,\tau,\tau'} s J^{\perp}_{s\tau,s\tau'} \\ &= \frac{k s_E v_F}{2} \mathcal{M}_{inter} \Big\{ \sin\Theta_{inter} - \mathcal{F} \sin\Theta_{intra} \Big\} \end{aligned} \tag{4.3.41}$$

where

$$\mathcal{F} = \frac{\mathcal{M}_{intra}}{\mathcal{M}_{inter}} \tag{4.3.42}$$

The key parameters controlling the magnitude of the transverse spin current $J_S^{\perp}$ are thus the phase difference $\vartheta = \Theta_{intra} - \Theta_{inter}$ and the $\mathcal{F}$ factor. They depend on hopping energies characterizing the adatom-graphene hybridization, and are thus expected to depend strongly on the valence orbital type. Since s-orbital adatoms lack $J = \pm 3/2, \pm 5/2$ total angular momentum states necessary to couple hexagonal states of angular momentum $m = \pm 2$, they induce zero $\nu_2^{\pm}$. This directly leads to $p = q = 0$. As a result, $\vartheta = 0$, $\mathcal{F} = 1$ and hence $J_S^{\perp} = 0$. Interestingly, p-orbital adatoms are a limit case. They host exactly two orbital states $J = \pm 3/2$ and no $J = \pm 5/2$ states. Therefore, $\Omega^{\dagger}_{\pm 2}|0\rangle \longrightarrow \Omega^{\dagger}_{\pm 2}|0\rangle$ transitions require double spin-flips, leading to small $\nu_2^{\pm} \propto w_2^2$ couplings, where w_2 is the hopping energy between graphene's $\Omega^{\dagger}_{\pm 2,\downarrow/\uparrow}|0\rangle$ state and adatom's p-orbital with angular momentum ± 1 and spin-$\uparrow,\downarrow$, see Appendix. p-orbital adatoms are thus expected to yield negligible ϑ, $\mathcal{F} \approx 1$ and hence small $J_S^{\perp}$. The case of d- and f-orbital adatoms are noticeably different as they offer spin-preserving channels for $\Omega^{\dagger}_{\pm 2}|0\rangle \longrightarrow \Omega^{\dagger}_{\pm 2}|0\rangle$ transitions, generally leading to appreciable $\nu_2^{\pm}$ couplings. In the low-energy limit $|g| \ll \frac{\chi}{p}$, the $\mathcal{F}$ factor then

becomes

$$\mathcal{F} \approx \left(\frac{\nu_1^+ + \nu_2^+}{\nu_1^+ - \nu_2^+} \right)^2 \neq 1 \tag{4.3.43}$$

where couplings corresponding to spin-dependent processes are neglected. Clearly, this opens up the possibility of having large $J_S^{\perp}$ provided Θ_{inter} and/or ϑ are finite, leading to spin Hall effect [165, 166, 167, 168]. ϑ vanishes in the vicinity of the Dirac point, reflecting the fact that intra- and inter-valley scattering mechanisms tend to yield transverse spin currents of opposite signs, as depicted by 4.3.1. However, ϑ can become significant under certain conditions. A natural question is thus whether ϑ can become large close to the Dirac point for some physically meaningful values of p, q, χ and χ'. Typically, ϑ peaks when $\Re g$ lies between $x = \frac{\chi}{p}$ and $x' = \frac{\chi'}{q}$. Conditions $\Re g = x, x'$ are fulfilled for Fermi levels $E_{X=x,x'}$ verifying

$$\frac{E_X}{E_c} \ln \left| \frac{E_X}{E_c} \right| = \frac{2\pi E_{\hexagon}^2 X}{E_c} \tag{4.3.44}$$

where constants $\hbar v_F$ and $A_{\hexagon}$ have been restored, and $E_{\hexagon} = \frac{\hbar v_F}{\sqrt{A_{\hexagon}}}$. Peak values of ϑ are thus attained close to the Dirac point provided $2\pi E_{\hexagon}^2 |X| \ll E_c$, in which case

$$\frac{E_X}{E_c} = \mathcal{L}\left(\frac{2\pi E_{\hexagon}^2 X}{E_c} \right) \tag{4.3.45}$$

Here, $\mathcal{L}$ is a function defined by means of the lower branch of the Lambert W-function, $\mathcal{W}_{-1}$:

$$\begin{aligned} \mathcal{L}(y) &= \frac{y}{\mathcal{W}_{-1}(-|y|)} \\ &\approx \frac{y}{\ln|y|} \left(1 + \frac{\ln|\ln|y||}{\ln|y|} + \frac{\ln^2|\ln|y||}{\ln^2|y|} - \frac{\ln|\ln|y||}{\ln^2|y|} \right) \end{aligned} \tag{4.3.46}$$

We now determine under which conditions, $2\pi E_{\hexagon}^2 |X| \ll E_c$ is verified. Parameters p, q, χ and χ' can be expressed in terms of the adatom's energy

levels as well as tight-binding parameteres connecting hexagonal states to the adatoms valence orbital. If the Fermi energy lies far away from the adatom's valence orbital energy levels,

$$\chi \approx 9\left(\frac{\sigma_1^2}{E_{3/2}^+}+\frac{\sigma_2^2}{E_{3/2}^-}\right) \tag{4.3.47}$$

$$\chi' \approx 9\left(\frac{\sigma_1^2}{E_{1/2}^-}+\frac{\sigma_2^2}{E_{5/2}^+}\right) \tag{4.3.48}$$

$$p \approx 324\frac{\sigma_1^2\sigma_2^2}{E_{3/2}^-E_{3/2}^+} \tag{4.3.49}$$

$$q \approx 324\frac{\sigma_1^2\sigma_2^2}{E_{1/2}^-E_{5/2}^+} \tag{4.3.50}$$

where $E_J^{\pm}$ are energy levels valence orbitals would have in absence of intra-atomic spin-flip, $\sigma_m = u_m + \nu_m$ and u_m and ν_m are hopping integrals connecting hexagonal states and adatom's orbitals of same angular momentum m, see appendix. We thus have

$$\frac{2\pi E_{\hexagon}^2 x}{E_c} \approx \frac{\pi E_{\hexagon}^2}{18E_c}\left(\frac{E_{3/2}^+}{\sigma_1^2}+\frac{E_{3/2}^-}{\sigma_2^2}\right) \tag{4.3.51}$$

and

$$\frac{2\pi E_{\hexagon}^2 x'}{E_c} \approx \frac{\pi E_{\hexagon}^2}{18E_c}\left(\frac{E_{1/2}^-}{\sigma_1^2}+\frac{E_{5/2}^+}{\sigma_2^2}\right) \tag{4.3.52}$$

which are small provided $E_c\sigma_{1,2}^2/E_{\hexagon}^2$ are significantly larger than the adatom's valence orbital energy levels.

In addition, Θ_{inter} exhibits resonances of its own, which typically occur in energy windows where real parts of d and d' are small. The real parts of d and d' vanish close to the Dirac point at energies $E_{D=d,d'}$ which relate to $X = x, x'$ and $C = c, c' = \frac{p}{\chi^2}, \frac{q}{\chi'^2}$ by

$$\frac{E_D}{E_c} \approx \mathcal{L}\left(\frac{2\pi E_{\hexagon}^2 X}{E_c}[1-\sqrt{1-C}]\right) \tag{4.3.53}$$

Θ_{inter} exhibits resonances close to the Dirac point provided $2\pi E_{\hexagon}^2|X| \ll E_c$ or $C \ll 1$. The former condition is valid whenever both $E_c\sigma_1/E_{\hexagon}^2$ and $E_c\sigma_2/E_{\hexagon}^2$ are large compared to adatom energy levels, whereas, the latter condition is fulfilled if $\sigma_1 \gg \sigma_2$ or $\sigma_2 \gg \sigma_1$. More precisely, $c, c' \propto (\sigma_2/\sigma_1)^2$ whenever $\sigma_1 \gg \sigma_2$ and $c, c' \propto (\sigma_1/\sigma_2)^2$ in the opposite limit.

Figure 4.3.2(a) shows $J_S^{\perp}$ as a fraction of total outgoing current

$$J_{tot}^{\parallel} = s_E v_F \sum_{s,\tau,s',\tau'} \Sigma_{s\tau,s'\tau'}^{\parallel} \tag{4.3.54}$$

against Fermi energy E_F, for realistic values of hopping integrals and atomic energy levels. While the adatom energy levels are kept fixed, $J_S^{\perp}/J_{tot}^{\parallel}$ is plotted for different pairs of couplings (σ_1, σ_2), corresponding to points A, B, C and D shown in figure 4.3.2(b). 4.3.2(a) illustrates the strong dependence of $J_S^{\perp}/J_{tot}^{\parallel}$ on couplings between the adatom valence orbitals and graphene hexagonal states. At point A, the transverse spin current is negligible compared to $J_{tot}^{\parallel}$, whereas points B and C yield transverse spin currents as large as $\sim 20\%$ of the total outgoing current at resonance. In situation D, $J_S^{\perp}/J_{tot}^{\parallel}$ exhibits giant peak-values of up to 40 in magnitude. 4.3.2(b) connects the existence of peaks in $J_S^{\perp}/J_{tot}^{\parallel}$ for particular (σ_1, σ_2) points to previously discussed resonant energies $E_{x,x',d,d'}$. It highlights that $E_{x,x',d,d'}$ and resulting peaks in transverse spin currents exist at low energy for sufficiently high σ_1 or σ_2. However, peak values of $J_S^{\perp}/J_{tot}^{\parallel}$ become significant provided both σ_1 and σ_2 exceed $\sim E_{\hexagon}(E_J^{\pm}/E_c)^{1/2}$.

While transverse spin currents arising from skew scattering of graphene Dirac fermions with a hollow-position adatom can exhibit large resonances, eq. 4.3.41 suggests that $J_S^{\perp}$ possesses another interesting property. Since $J_S^{\perp}$ results from competing transverse spin currents originating from intra- and inter-valley scattering, one expects $J_S^{\perp}$ to change sign for particular Fermi

energies, such that

$$\tan\Theta_{inter} = \frac{\mathcal{F}\sin\vartheta}{1-\mathcal{F}\cos\vartheta} \tag{4.3.55}$$

The existence of such levels close to the Dirac point would open up interesting technological prospects, as simple field-effect would allow to reverse spin-current flows. Intriguingly, eq. 4.3.55 admits low energy solutions for sufficiently large σ_1 or σ_2. For the sake of clarity, points (σ_1, σ_2) such that the solution E_{inv} of minimum magnitude is equal to a tenth of graphene half bandwidth are shown in Figure 4.3.2(b), as a yellow dashed line. Energies E_{inv} closer to the Dirac point are obtained away from the origin, beyond the yellow curve. This is illustrated by point D, whose corresponding $J_S^{\perp}/J_{tot}^{\parallel}$ against E_F curve is shown in 4.3.2(a), and exhibits a sharp inversion in transverse spin current flow around $E_F \approx 50$ meV.

Finally, let us highlight further the specificities of the above-discussed spin currents. Though spin Hall effects of intrinsic [172] and extrinsic [87] types have already been observed in graphene, they differ drastically from the spin Hall effect discussed in our work. While in Ref. [172], spin Hall effect necessitates a strong magnetic field and relies on Zeeman splitting at the Dirac point [173], correlating spin $\uparrow,\downarrow$ and charge $\mp e$, spin Hall effect observed in Ref. [87] is induced by the deformation of graphene lattice due to the presence of sp^3-bonds [149]. Our theory describes spin Hall effect arising from hybridization of graphene with d- or f-orbital adatoms in hollow position, and predicts the appearance of large spin currents around resonant energies $E_{x,x'}$ and $E_{d,d'}$ The nature of these resonances is graphene-specific: the peaks in ϑ and Θ_{inter} reflect an anomalous dephasing of the A- and B-sublattice components of Dirac spinors after spin-conserving scattering with the adatom. This phenomenon is unrelated to the previously-observed enhancement of spin-orbit coupling occuring when the Fermi level lies close to an impurity level [174] or a large spin-orbit coupling energy band [175]. Last but not least, a very interesting and distinct feature of the resonant regime illustrated by Figure

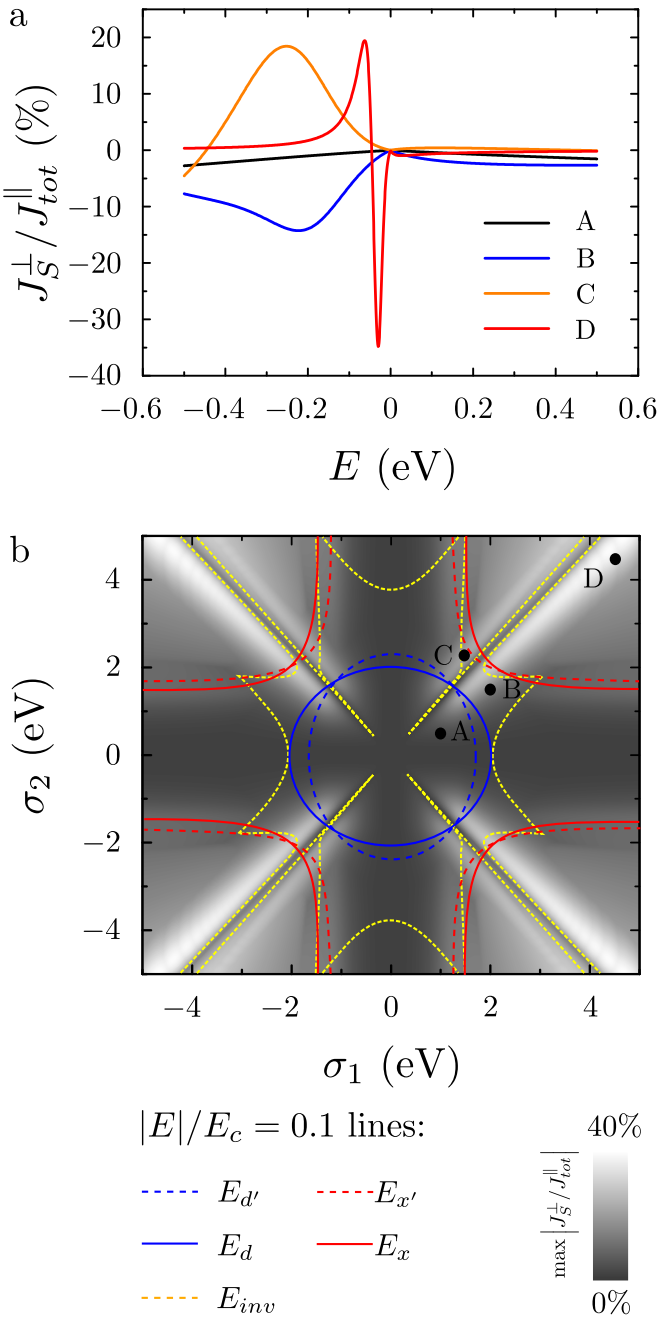

Figure 4.3.2: (a)$J_S^{\perp}/J_{tot}^{\parallel}$ (in %) against Fermi energy (in eV), for hollow-position adatoms with fixed $E_{1/2}^{\pm} = 1$ eV, $E_{3/2}^{\pm} = 1.5$ eV, and $E_{5/2}^{\pm} = 2$ eV and different (σ_1, σ_2), corresponding to points A, B, C and D shown in the lower panel. (b) Maximum of $|J_S^{\perp}/J_{tot}^{\parallel}|$ for $|E_F| \leq 0.5$ eV, against σ_1 and σ_2. $|E|/E_c = 0.1$ lines are shown for $E = E_{x,x',d,d'}, E_{inv}$. Each line partitions (σ_1, σ_2)-space into regions, whose farthest from the origin corresponds to $|E|/E_c < 0.1$.

4.3.2 is the possibility to change the sign of $J_S^{\perp}$ upon tuning the Fermi level around specific "inversion energies" E_{inv}. A direct consequence is the ability to convert a charge current into a large transverse spin current in a certain energy range, and to reverse its flow by tuning the gate voltage around critical values, enabling novel spin-based logic devices.

4.3.3 Scattering with top-position adatoms

We now deal with scattering mechanisms induced by an adatom in top position. We start with adatoms on top of an A-sublattice carbon atom. Using table 4.1, the corresponding T-matrix in basis 4.3.4 reads:

$$T_{top,A} = \begin{pmatrix} T_{top,A}^{\uparrow\uparrow} & T_{top,A}^{\downarrow\uparrow} \\ T_{top,A}^{\uparrow\downarrow} & T_{top,A}^{\downarrow\downarrow} \end{pmatrix} \tag{4.3.56}$$

with 4×4 blocks:

$$T_{top,A}^{ss} = \begin{pmatrix} a & 0 & 0 & a \\ 0 & b_s & 0 & 0 \\ 0 & 0 & b'_s & 0 \\ a & 0 & 0 & a \end{pmatrix} \tag{4.3.57}$$

where $s = \uparrow, \downarrow$ and

$$T_{top,A}^{\uparrow\downarrow} = -{}^tT_{top,A}^{\downarrow\uparrow} = \begin{pmatrix} 0 & 0 & -t & 0 \\ t & 0 & 0 & t \\ 0 & 0 & 0 & 0 \\ 0 & 0 & -t & 0 \end{pmatrix} \tag{4.3.58}$$

The T-matrix elements in equations 4.3.57 and 4.3.58 verify the following identities:

$$t = \frac{2i\Lambda_{so}}{1 - Ug + 2wg^2} \tag{4.3.59}$$

$$a = \frac{V_0 - wg}{1 - Ug + 2wg^2} \tag{4.3.60}$$

$$b_\uparrow = b'_\downarrow = \frac{v_0 + \lambda_{so}}{1 - g(v_0 + \lambda_{so})} \tag{4.3.61}$$

$$b_\downarrow = b'_\uparrow = \frac{v_0 - \lambda_{so} - 2wg}{1 - Ug + 2wg^2} \tag{4.3.62}$$

where we set $U = 2V_0 + v_0 - \lambda_{so}$ and $w = (v_0 - \lambda_{so})V_0 - 4\Lambda_{so}^2$. The T-matrix $T_{top,B}$ for an adatom on top of a B-sublattice site is easily obtained from $T_{top,A}$ by reflection $\mathcal{R}_y$,

$$T_{top,B} = \mathcal{U}_y T_{top,A} \mathcal{U}_y \tag{4.3.63}$$

Matrix elements $t^{\sigma,\sigma'}_{s\tau,s'\tau'}$ and $\widetilde{t}^{\sigma,\sigma'}_{s\tau,s'\tau'}$ of $T_{top,A}$ and $T_{top,B}$ associated with $s\tau\sigma \to s'\tau'\sigma'$ transitions are thus related by:

$$\widetilde{t}^{\sigma,\sigma'}_{s\tau,s'\tau'} = ss' t^{\overline{\sigma},\overline{\sigma}'}_{-s\tau,-s'\tau'} \tag{4.3.64}$$

with $\overline{A} = B$ and $\overline{B} = A$. We next describe possible scattering mechanims induced by an adatom on top of a σ_0-sublattice site, $\sigma_0 = A, B$, by calculating corresponding cross-sections $\sigma^{\sigma_0}_{s\tau,s'\tau'}$. Since $T_{top,A}$ transforms into $T_{top,B}$ under $\mathcal{R}_y$, the following relation holds:

$$\sigma^B_{s\tau,s'\tau'}(\theta) = \sigma^A_{-s\tau,-s'\tau'}(-\theta) \tag{4.3.65}$$

so that we can focus on computing $\sigma^A_{s\tau,s'\tau'}(\theta)$ cross-sections only.

From this perspective, we first describe scattering mechanisms which do not conserve spin and valley quantum numbers. Equation 4.3.57 directly implies that intra-valley spin-flip and spin-preserving inter-valley scattering induced by top-position adatoms are isotropic mechanisms, as

$$\sigma^A_{s\tau,-s\tau} = \frac{k|t|^2}{8\pi}, \tag{4.3.66}$$

and for $\tau \neq \tau'$,

$$\sigma^{A}_{s\tau,s\tau'} = \frac{k|a|^2}{8\pi} \tag{4.3.67}$$

Unlike adatoms in hollow position, top-position adatoms induce inter-valley spin-flip scattering processes. In particular, for adatoms on the A-sublattice, corresponding differential cross-sections read, for $s \neq s'$ and $\tau \neq \tau'$:

$$\sigma^{A}_{s\tau,s'\tau'}(\theta) = \frac{k|t|^2}{2\pi} \cos^2\left(\frac{\theta}{2}\right) \delta_{s+\tau} \tag{4.3.68}$$

Therefore, scattering mechanisms originating from top-position adatoms yield zero transverse currents, i.e. $J^{A\perp}_{s\tau,s'\tau'} = 0$, whenever $s \neq s'$ or $\tau \neq \tau'$.

Next, we study spin-preserving intra-valley scattering. Irrespective of the valley τ and spin s, T-matrix elements $t^{A,A}_{s\tau,s\tau}$are equal. This contrasts with $t^{B,B}_{s\tau,s\tau}$ elements, which generally verify:

$$t^{B,B}_{\uparrow K,\uparrow K} = t^{B,B}_{\downarrow K',\downarrow K'} \neq t^{B,B}_{\uparrow K',\uparrow K'} = t^{B,B}_{\downarrow K,\downarrow K} \tag{4.3.69}$$

As a result, spin-preserving intra-valley scattering cross-sections for $\uparrow K$ and $\downarrow K'$ charge carriers differ from those for $\downarrow K$ and $\uparrow K'$ quasi-particles, and $\sigma_{s\tau,s\tau}(\theta)$ is determined by the conserved quantity $s+\tau$. We start by considering the $s+\tau = \pm 2$ case, and note $\mathcal{M}_2 = \mathcal{M}^{A}_{\uparrow K,\uparrow K} = \mathcal{M}^{A}_{\downarrow K',\downarrow K'}$ and $\varphi_2 = \varphi^{A}_{\uparrow K,\uparrow K} = \varphi^{A}_{\downarrow K',\downarrow K'}$, which verify:

$$\mathcal{M}_2 = \frac{2|v_0 + \lambda_{so}|.|V_0 - wg|}{|1 - Ug + 2wg^2|.|1 - g(v_0 + \lambda_{so})|} \tag{4.3.70}$$

and:

$$\begin{aligned}\varphi_2 &= \arctan\left(\frac{U\Im g - 2w\Im(g^2)}{1 - U\Re g + 2w\Re(g^2)}\right) \\ &+ \arctan\left(\frac{(v_0+\lambda_{so})\Im g}{(v_0+\lambda_{so})\Re g - 1}\right) \\ &+ \arctan\left(\frac{w\Im g}{w\Re g - V_0}\right) \\ &+ \pi H\left(w\Re g - V_0\right) + \pi H\left((v_0+\lambda_{so})\Re g - 1\right) \\ &- \pi H\left(U\Re g - 2w\Re(g^2) - 1\right)\end{aligned} \tag{4.3.71}$$

The case of Dirac fermions for which $s+\tau=0$ is markedly different. Noting $\mathcal{M}_0 = \mathcal{M}^A_{\downarrow K,\downarrow K} = \mathcal{M}^A_{\uparrow K',\uparrow K'}$ and $\varphi_0 = \varphi^A_{\downarrow K,\downarrow K} = \varphi^A_{\uparrow K',\uparrow K'}$, we obtain

$$\mathcal{M}_0 = \frac{2|V_0 - wg|.|v_0 - \lambda_{so} - 2wg|}{|1 - Ug + 2wg^2|^2} \tag{4.3.72}$$

and

$$\begin{aligned}\varphi_0 &= \arctan\left(\frac{w\Im g}{V_0 - w\Re g}\right) \\ &- \arctan\left(\frac{2w\Im g}{v_0 - \lambda_{so} - 2w\Re g}\right) \\ &+ \pi H\left(2w\Re g + \lambda_{so} - v_0\right) - \pi H\left(w\Re g - V_0\right)\end{aligned} \tag{4.3.73}$$

Crucially, currents $J^{A\perp}_{\uparrow K,\uparrow K} + J^{A\perp}_{\uparrow K',\uparrow K'}$ and $J^{A\perp}_{\downarrow K,\downarrow K} + J^{A\perp}_{\downarrow K',\downarrow K'}$ are equal, so that spin-preserving intra-valley scattering does not give rise to any transverse spin current. The same holds true for spin-preserving intra-valley scattering induced by an adatom on the B-sublattice, but owing to relation 4.3.65,

$$J^{B\perp}_{s\tau,s\tau} = -J^{A\perp}_{-s\tau,-s\tau} \tag{4.3.74}$$

However, the transverse charge current arising from scattering with a single

top-position adatom on sublattice $\sigma = A, B$

$$J_Q^{\sigma\perp} = e \sum_{s,\tau} J_{s\tau,s\tau}^{\sigma\perp} \tag{4.3.75}$$

is generally non-zero, and eq. 4.3.74 directly implies $J_Q^{A\perp} = -J_Q^{B\perp}$. Macroscopically, top-position adatoms thus give rise to anomalous Hall effect [176], provided the populations of adatoms on A- and B-sublattice differ by type or number. Let us now study transverse charge currents $J_Q^{\sigma\perp}$ in more detail. Using equations 4.3.75, 4.3.19 and 4.3.13, we obtain:

$$J_Q^{\sigma\perp} = -\sigma \frac{eks_E v_F}{4} (\mathcal{M}_0 \sin\varphi_0 + \mathcal{M}_2 \sin\varphi_2) \tag{4.3.76}$$

It is interesting to note that the magnitude of $J_Q^{\sigma\perp}$ is modulated by $\mathcal{M}_0$ and $\mathcal{M}_2$, which are proportional to $|v_0 - \lambda_{so} - 2wg|$ and $|v_0 + \lambda_{so}|$ respectively. While the dependence on λ_{so} is expected, as spin-orbit interaction is a well-known cause of anomalous Hall effect [176], the dependence on v_0, a scalar potential acting on graphene triangular states $\Gamma_{m,s}^\dagger|0\rangle$, is more surprising. However, this v_0-dependence has a trivial geometrical explanation: the $v_0\pi_{B,A}$ term of Hamiltonian $\mathcal{H}_{top}^{A,B}$ is the continuum-theory counterpart of the trigonal potential which affects the three graphene p_z-orbitals neighboring the adsorption site, and trigonal potentials clearly scatter charges anisotropically.

We next describe the energy-dependence of $J_Q^{\sigma\perp}$. In neutral graphene, phases φ_0 and φ_2 are null. However, they exhibit large resonances at finite Fermi energies, such that

$$\Re g = 1/\omega_{i=1,2,3} \tag{4.3.77}$$

where:

$$\omega_1 = v_0 + \lambda_{so} \tag{4.3.78}$$

$$\omega_2 = v_0 - \lambda_{so} - \frac{4\Lambda_{so}^2}{V_0} \tag{4.3.79}$$

$$\omega_3 = 2V_0 - \frac{8\Lambda_{so}^2}{v_0 - \lambda_{so}} \tag{4.3.80}$$

Equation 4.3.77 has a low-energy root $|\mathcal{E}_i| \ll E_c$ provided $|\omega_i| \gg 2\pi E_{\hexagon}^2/E_c$, in which case (see Eq. 4.3.46):

$$\frac{\mathcal{E}_i}{E_c} = \mathcal{L}\left(\frac{2\pi E_{\hexagon}^2}{E_c \omega_i}\right) \tag{4.3.81}$$

Another resonance is reached whenever

$$\Re(g^2) - \frac{U}{2w}\Re g + \frac{1}{2w} = 0 \tag{4.3.82}$$

Equation 4.3.82 admits a low energy solution $\mathcal{E}_4$ verifying

$$\frac{\mathcal{E}_4}{E_c} \approx \mathcal{L}\left(\frac{2\pi E_{\hexagon}^2}{E_c U}\right) \tag{4.3.83}$$

provided $8|w| \ll U^2$ and $|U| \gg 2\pi E_c$.

We now write conditions for the existence of resonant energies close to the Dirac point, in terms of tight-binding parameters connecting central and triangular states to the top-position adatoms. We first consider the marginal case of s-orbital adatoms, which only host states of total angular momentum $J = \pm 1/2$. Couplings between triangular states of angular momentum $m = \pm 1$ are thus necessarily mediated by double spin-flip through an available adatom orbital. Using the Appendix notations as well as equations 4.5.29 and 4.5.31 within, this results in $v_0 = -\lambda_{so} \approx \frac{9}{2}\frac{l_{so,1}^2}{E_{1/2}^+}$ and $\Lambda_{so} \approx \frac{9}{2}\frac{l_{so,1}\gamma}{E_{1/2}^+}$. Therefore, $\omega_1 = 0$ and resonant energy $\mathcal{E}_1$ is infinite. Besides, the hopping integral $l_{so,1}$ connecting triangular states $\Gamma_{\pm 1,\downarrow/\uparrow}^\dagger|0\rangle$ to s-orbitals of opposite spin is expected to be small compared to $E_{1/2}^+$ and graphene half-bandwidth E_c, leading to $|\omega_{2,3}| \ll 2\pi E_{\hexagon}^2/E_c$ and $|\mathcal{E}_{2,3}| \gg E_c$. Resonant energies $\mathcal{E}_{1,2,3}$ are thus experimentally irrelevant. However, $U \approx \frac{2\gamma^2}{E_{1/2}^+}$ and $\mathcal{E}_4$ is the only resonance which can possibly be observed, provided $\frac{\gamma^2}{E_{1/2}^+} \gg \pi E_c$.

For all other types of valence orbitals, i.e. p, d, and f, the existence

of spin-preserving channels coupling triangular states of angular momentum $m = \pm 1$ gives rise to enhanced v_0, λ_{so} and Λ_{so} energy scales, making resonant energies $\mathcal{E}_{i=1,2,3}$ accessible under certain conditions. Equations 4.5.29 and 4.5.31 directly lead to:

$$V_0 \sim \frac{\gamma^2}{E^+_{1/2}} \tag{4.3.84}$$

$$v_0 \sim \frac{9}{2}\theta_1^2 \left(\frac{1}{E^-_{1/2}} + \frac{1}{E^+_{3/2}} \right) \tag{4.3.85}$$

$$\lambda_{so} \sim \frac{9}{2}\theta_1^2 \left(\frac{1}{E^+_{3/2}} - \frac{1}{E^-_{1/2}} \right) \tag{4.3.86}$$

$$\Lambda_{so} \sim -\frac{9}{2} \frac{\gamma \theta_1 \Lambda^1_{so}}{E^-_{1/2} E^+_{1/2}} \tag{4.3.87}$$

Therefore, equation 4.3.77 holds for $i = 1, 2$ or 3 if $\theta_1^2/|E^+_{3/2}| \gg E^2_{\hexagon}/E_c$, $\theta_1^2/|E^-_{1/2}| \gg E^2_{\hexagon}/E_c$ or $\gamma^2/|E^+_{1/2}| \gg 2\pi E^2_{\hexagon}/E_c$ respectively. Moreover,

$$U \sim \frac{2\gamma^2}{E^+_{1/2}} + \frac{9\theta_1^2}{E^-_{1/2}} \tag{4.3.88}$$

and assuming Λ_{so} is much smaller than V_0, v_0 and λ_{so}, we have:

$$w \sim \frac{9\theta_1^2\gamma^2}{E^-_{1/2}E^+_{1/2}} \tag{4.3.89}$$

so that equation 4.3.83 is valid provided $|\gamma| \gg |\theta_1|$ or $|\gamma| \ll |\theta_1|$, and $2\gamma^2/E^+_{1/2} + 9\theta_1^2/E^-_{1/2} \gg 2\pi E^2_{\hexagon}/E_c$.

Figure 4.3.3(a) shows the transverse charge current $J_Q^{A\perp}$ as a fraction of total outgoing current

$$J^{A\parallel}_{tot} = e s_E v_F \sum_{s,\tau,s',\tau'} \Sigma^{A\parallel}_{s\tau,s'\tau'} \tag{4.3.90}$$

against Fermi energy E_F, for fixed values of atomic energy levels $E^{\pm}_{1/2}$, and $E^{\pm}_{3/2}$, and various (γ, θ_1) points, labelled as A, B, C, D and E. While for small

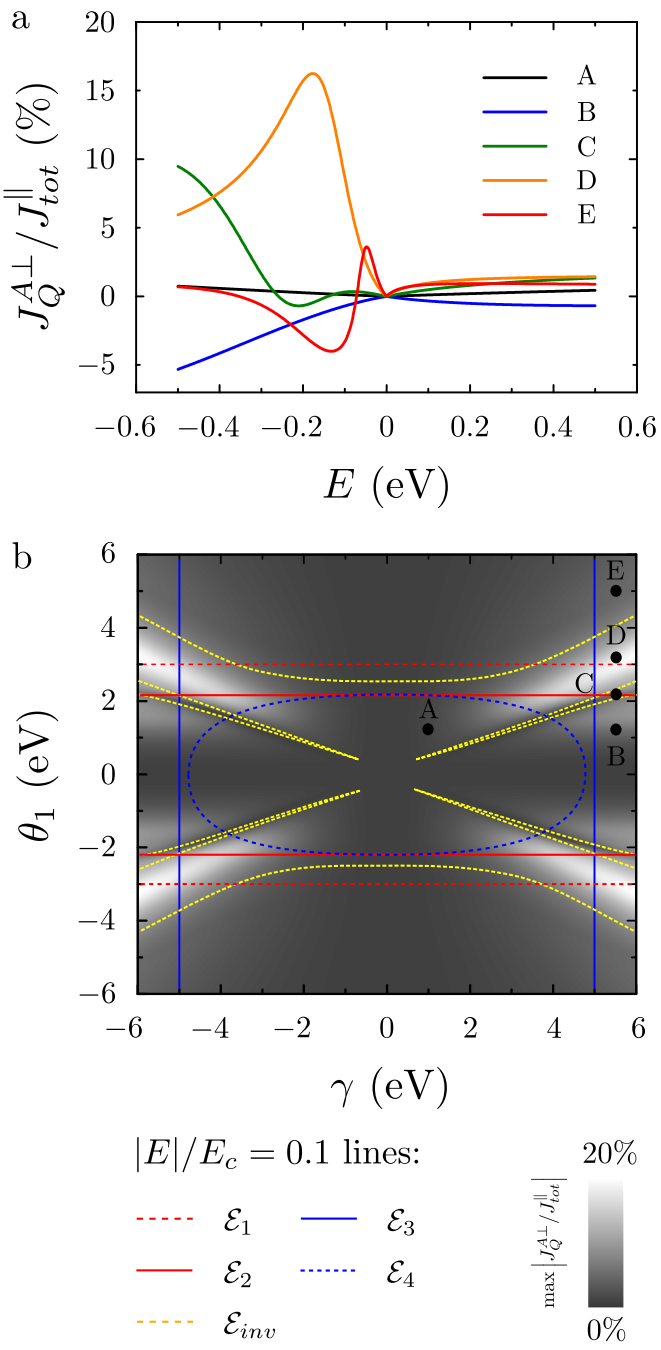

Figure 4.3.3: (a)$J_Q^{A\perp}/J_{tot}^{A\parallel}$ (in %) against Fermi energy (in eV), for top-position adatoms with fixed $E_{1/2}^{\pm} = 1$ eV and $E_{3/2}^{\pm} = 1.5$ eV and different (σ_1, σ_2), corresponding to points A, B, C, D and E shown in lower panel. (b) Maximum of $|J_Q^{A\perp}/J_{tot}^{A\parallel}|$ for $|E_F| \leq 0.5$ eV, against σ_1 and σ_2. $|E|/E_c = 0.1$ lines are shown for $E = \mathcal{E}_{1,2,3,4}, \mathcal{E}_{inv}$. Each line partitions (σ_1, σ_2)-space into regions, whose farthest from the origin corresponds to $|E|/E_c < 0.1$.

γ and θ_1 (situation A), the transverse charge current is negligible compared to $J_{tot}^{A\parallel}$, significant $J_Q^{A\perp}$ currents are obtained for values of γ and θ_1 of the order of few eV (points B, C, D, E in Figure 4.3.3(b)), up to 20%. In addition, the transverse charge current can change direction for some values of Fermi energy, as illustrated by curves C and E in figure 4.3.3(a). Such "inversion" energies can exist close to the Dirac point for finite values of γ and θ_1 only. Noting $\mathcal{E}_{inv}$ the inversion energy closest to the Dirac point for a given (γ, θ_1) couple, figure 4.3.3(b) shows $|\mathcal{E}_{inv}(\gamma, \theta_1)| = E_c/10$ lines, which partition (γ, θ_1)-space into regions whose farthest from the origin corresponds to $|\mathcal{E}_{inv}|/E_c < 0.1$. Clearly, $|\mathcal{E}_{inv}|/E_c < 0.1$ domains overlap with regions of large $J_Q^{A\perp}/J_{tot}^{A\parallel}$ magnitude, making the existence of $\mathcal{E}_{inv}$ relevant for applications. Similar to transverse spin currents arising from scattering with hollow-position adatoms, we believe that the possibility of changing the sign of $J_Q^{\sigma\perp}$ by field effect can lead to interesting novel logic devices, with new functionalities. However, the observation of significant anomalous Hall effect due to scattering with top-position adatoms appears more challenging than the observation of large spin Hall effect due to hollow-position adatoms, due to the necessity of having an imbalance between A- and B-sublattice. Nevertheless, it should be noted that sublattice ordering driven by RKKY-type interactions below a critical temperature was predicted by several authors [177, 178, 179, 180], so that the above-discussed anomalous Hall effect may in principle be observed in an experiment.

4.4 Concluding remarks

We have shown that both position in the lattice and valence orbital type are critical to determine the action of an adatom on graphene's Dirac fermions. Our study of non-magnetic elements adsorbed on graphene, valid when the Fermi energy is detuned from the adatoms valence orbital spectrum, established that while bridge-position adatoms do not induce spin-orbit coupling, hollow- and

top-position adatoms induce spin-orbit interaction, in such a way that spin and valley quantum numbers are strongly intertwined. The low-energy continuum theories constructed for hollow- and top-position species allowed to derive the corresponding electron scattering mechanisms. Quite surprisingly, these two categories of adatoms give rise to transverse currents of drastically different nature: pure spin currents for the former, and non-polarized charge currents for the latter. They nonetheless have two key characteristics in common: they can be switched on and off and their flow can be reversed by tuning the Fermi energy. We anticipate that such properties will find technological applications in the fields of spintronics- and electronics-based logic devices and memories. While we believe our scattering theory to be essentially correct, we expect the existence of complementary effects originating from the neglected momentum dependence of effective-mass terms $M\delta(\vec{r})$. This is beyond the scope of this work, and will be discussed in a future paper.

4.5 Appendix

In this appendix, we re-derive the impurity Hamiltonians of section I, for adatoms in hollow- and top-positions, accounting for adatoms' internal degrees of freedom. From this perspective, we describe the "graphene + adatom" system with a tight-binding Hamiltonain $H_{tot} = H_{gr} + H_{ad} + H_{gr-ad}$ where H_{gr} is pristine graphene's Hamiltonian, H_{ad} is the adatoms' Hamiltonian, and H_{gr-ad} is the graphene-adatom hybridization term. We write H_{gr} as the following first-nearest neighbors tight-binding Hamiltonian:

$$H_{gr} = -t \sum_{i \in \mathcal{A}} \sum_{\langle i,j \rangle} a_i^\dagger b_j + h.c. \tag{4.5.1}$$

where $\mathcal{A}$ describes graphene's A-sublattice carbon atoms, $a_i^\dagger$ (b_j) creates an A-sublattice electron at atom $i \in \mathcal{A}$ (annihilates an electron from B-sublattice site j). Here, $\langle i,j \rangle$ refers to nearest neighbors *j* of site *i*, and *t* is the hop-

ping energy between nearest neighbors. Next, we derive single-electron tight-binding Hamiltonians for H_{ad} and H_{gr-ad} by symmetry arguments [154], and then trace these terms out of full Hamiltonian H_{tot} by Löwdin's transformation [164]. Taking the continuum limit then yields the results of Table 4.1. Beside confirming results obtained in section I, this approach has the advantage of relating couplings - V_0, V_{so}, Δ, Δ_{so}, Λ_R, ...- appearing in Table 4.1 to microscopic parameters -hopping integrals, atomic spin-orbit couplings and energy levels- and the Fermi energy of graphene.

We start by writing the solution of Schrödinger equation $H_{tot}|\psi\rangle = E|\psi\rangle$ as a sum of waves $|\psi\rangle = |\psi_{ad}\rangle + |\psi_{\mathcal{N}}\rangle + |\psi_{\infty}\rangle$ where $|\psi_{ad}\rangle$, $|\psi_{\mathcal{N}}\rangle$ and $|\psi_{\infty}\rangle$ are projections of $|\psi\rangle$ on the adatom valence $l-$orbital, its immediate vicinity -where graphene's p_z- orbitals couple strongly to the adatom's valence orbital - and further graphene's p_z-orbitals respectively. We note $d^{\dagger}_{m,s}$ the operator creating an adatom's l-orbital of angular momentum m and spin s, and write $d^{\dagger}_{m,s}|0\rangle = |m,s\rangle_{ad}$. In the case of an adatom in hollow position, $|\psi_{\mathcal{N}}\rangle$ is a linear combination of hexagonal states $\Omega^{\dagger}_{m,s}|0\rangle = |m,s\rangle_{\mathcal{N}}$. For top-position adatoms, $|\psi_{\mathcal{N}}\rangle$ is a linear combination of triangular states $\Gamma^{\dagger}_{m,s}|0\rangle$ and $c^{\dagger}_{0}|0\rangle$. Here, we explain the method used in the case of an adatom in hollow position, the top-position case being analogous. We write $|\psi_{ad}\rangle$, $|\psi_{\mathcal{N}}\rangle$ as:

$$|\psi_{\mathcal{N}}\rangle = \sum_{s,m} \alpha_{m,s}|m,s\rangle_{\mathcal{N}} \tag{4.5.2}$$

$$|\psi_{ad}\rangle = \sum_{s,m} \beta_{m,s}|m,s\rangle_{ad} \tag{4.5.3}$$

The projection of Schrödinger equation $H_{tot}|\psi\rangle = E|\psi\rangle$ on $|m,s\rangle_{ad}$ gives:

$$\begin{aligned} \sum_{s',m'} \beta_{m',s'\,ad}\langle m,s|H_{ad}|m',s'\rangle_{ad} \quad + \\ \sum_{s',m'} \alpha_{m',s'\,ad}\langle m,s|H_{gr-ad}|m',s'\rangle_{ad} \quad = \quad \beta_{m,s}\delta_{m,m'}\delta_{s,s'}E \end{aligned} \tag{4.5.4}$$

Noting $\hat{\mathcal{Z}}$ the square matrix $({}_{ad}\langle m,s|H_{ad}|m',s'\rangle_{ad})_{(m,s),(m',s')}$ and $\hat{\mathcal{T}}$ the rectangular matrix $({}_{ad}\langle m,s|H_{gr-ad}|m',s'\rangle_{\mathcal{N}})$, equation 4.5.4 leads to:

$$B = (E\mathbb{I} - \hat{\mathcal{Z}})^{-1}\hat{\mathcal{T}}A \tag{4.5.5}$$

where A and B are vectors $(\alpha_{m,s})_{(m,s)}$ and $(\beta_{m,s})_{(m,s)}$ respectively. Setting $H_{imp} = H_{ad} + H_{gr-ad}$, we next project vector $H_{imp}|\psi\rangle$ on $|m,s\rangle_{\mathcal{N}}$-states. This gives:

$${}_{\mathcal{N}}\langle m,s|H_{imp}|\psi\rangle = \sum_{m',s'} \alpha_{m',s'\,\mathcal{N}}\langle m,s|\hat{\mathcal{S}}|m',s'\rangle_{ad} \tag{4.5.6}$$

where

$$\hat{\mathcal{S}} = \hat{\mathcal{T}}^{\dagger}(E\mathbb{I} - \hat{\mathcal{Z}})^{-1}\hat{\mathcal{T}} \tag{4.5.7}$$

Equation 4.5.6 can be interpreted as the projection of vector $\tilde{H}_{imp}(|\psi\rangle_{\mathcal{N}}+|\psi\rangle_{\infty})$ on state $|m,s\rangle_{\mathcal{N}}$, where $\tilde{H}_{imp}$ is the *graphene-only* Hamiltonian:

$$\tilde{H}_{imp} = \sum_{m,s}\sum_{m',s'} \hat{\mathcal{S}}_{(m,s),(m',s')}\Omega^{\dagger}_{m,s}\Omega_{m',s'} \tag{4.5.8}$$

Tracing H_{ad} out hence consists in replacing H_{imp} by $\tilde{H}_{imp}$ in the full Hamiltonian H_{tot}.

We now derive a single-electron tight-binding Hamiltonian H_{ad} describing an l-orbital adatom either in hollow- or top-position, thereby generalizing a result of Ref. [154]. We start with an ansatz Hamiltonian H_{ad} which manifestly conserves total angular momentum,

$$\begin{aligned} H_{ad} &= \sum_{m=-l}^{l} \epsilon_m d^{\dagger}_m d_m + \sum_{m=-l}^{l} \lambda^m_{so} d^{\dagger}_m s_z d_m \\ &+ \sum_{m=-l}^{l-1} \Lambda^m_{so}(d^{\dagger}_m s_+ d_{m+1} + d^{\dagger}_{m+1} s_- d_m) \end{aligned} \tag{4.5.9}$$

This Hamiltonian is invariant under rotation by $\pi/3$, so that choosing en-

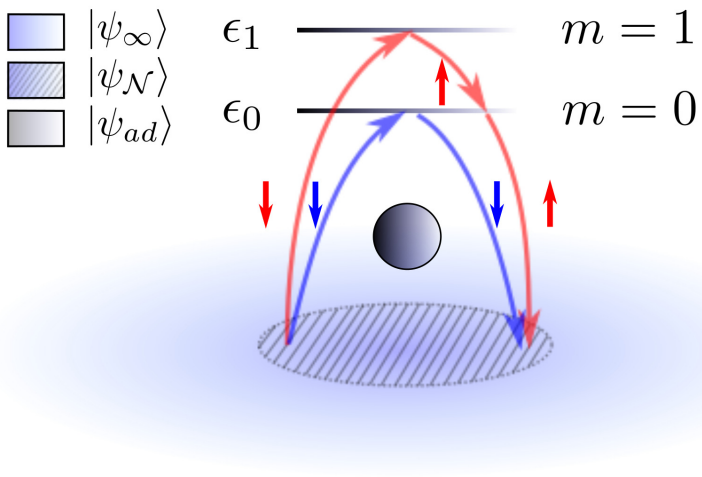

Figure 4.5.1: Cartoon representation of typical spin-flip (red) and spin-conserving (blue) processes induced by a p-orbital adatom (gray) on graphene (light blue). Energy levels ϵ_0 and ϵ_1 of adatom's p-orbitals $m = 0$ and $m = \pm 1$ are represented as gray solid lines. Core orbitals are depicted as a black ball. Shaded region corresponds to the adatom's immediate vicinity, where carbon atoms p_z-orbitals couple strongly to the adatoms valence p-orbital. Red (blue) straight vertical arrows represent the spin of an electron transiting between graphene and the adatom while flipping (conserving) its spin. Partial waves $|\psi_\infty\rangle$, $|\psi_\mathcal{N}\rangle$ and $|\psi_{ad}\rangle$ introduced in appendix are associated with the blue area, dashed area and adatom's valence orbital respectively.

ergies ϵ_m, λ_{so}^m, and Λ_{so}^m such that H_{ad} is time-reversal invariant and symmetric under $\mathcal{R}_x : x \mapsto -x$ reflection makes it suitable for describing *both* hollow- and top-position l-orbital adatoms, $l = p, d, f$. Since in spherical coordinates, $\langle\theta, \phi|d_m^\dagger|0\rangle = Y_l^m(\theta, \phi)$, where $Y_l^m(\theta, \phi)$ are conventional spherical harmonics, d_m transforms into $s_x d_{-m}$ under $\mathcal{R}_x$, which sends ϕ to $\pi - \phi$. Enforcing $\mathcal{R}_x$-symmetry thus requires $\epsilon_m = \epsilon_{-m}$, $\lambda_{so}^{-m} = -\lambda_{so}^m$ and $\Lambda_{so}^{-m-1} = \Lambda_{so}^m$. Moreover, time-reversal symmetry requires ϵ_m, λ_{so}^m, and Λ_{so}^m to be reals. We end up with:

$$\begin{aligned} H_{ad} &= \sum_{m=-l}^{l} \epsilon_{|m|} d_m^\dagger d_m + \sum_{m=1}^{l} \lambda_{so}^m (d_m^\dagger s_z d_m - d_{-m}^\dagger s_z d_{-m}) \\ &+ \sum_{m=0}^{l-1} \Lambda_{so}^m (d_m^\dagger s_+ d_{m+1} + d_{-m-1}^\dagger s_+ d_{-m} + h.c.) \end{aligned} \tag{4.5.10}$$

which describes the adatom Hamiltonian for both hollow- and top-position. However, hybridization terms H_{gr-ad} differ in the hollow- and top-position cases. We first treat the hollow-position situation, in which total angular mo-

mentum conservation constrains H_{gr-ad} to take the form

$$\begin{aligned} H_{gr-ad}^{hollow} &= \sum_{m=-2}^{2} t_m d_m^\dagger \Omega_m + \sum_{m=-2}^{2} \tau_m d_m^\dagger s_z \Omega_m \\ &+ \sum_{m=-2}^{2} (W_{so}^m d_{m-1}^\dagger s_+ \Omega_m + V_{so}^m d_{m+1}^\dagger s_- \Omega_m) + h.c. \end{aligned} \tag{4.5.11}$$

Since $\Omega_m \mapsto s_x \Omega_{-m}$ under $\mathcal{R}_x$, we must have $t_m = t_{-m}$, $\tau_m = -\tau_{-m}$ and $W_{so}^m = V_{so}^{-m}$. Enforcing time-reversal symmetry requires t_m, τ_m and W_{so}^m to read $t_m = i^{|m|} u_{|m|}$, $\tau_m = i^m \nu_{|m|}$ and $W_{so}^m = i^m w_m$where $u_{|m|}$, $\nu_{|m|}$ and w_m are reals. Finally,

$$\begin{aligned} H_{gr-ad}^{hollow} &= \sum_{m=-2}^{2} i^{|m|} u_{|m|} d_m^\dagger \Omega_m \\ &+ \sum_{m=1}^{2} i^m \nu_{|m|} (d_m^\dagger s_z \Omega_m - d_{-m}^\dagger s_z \Omega_{-m}) \\ &+ \sum_{m=-2}^{2} i^m w_m (d_{m-1}^\dagger s_+ \Omega_m + d_{-m+1}^\dagger s_- \Omega_{-m}) + h.c. \end{aligned} \tag{4.5.12}$$

A similar treatment allows to derive H_{gr-ad} for top-position adatoms. Enforcing symmetry under $\mathcal{R}_x$, time-reversal symmetry and total angular momentum conservation, we obtain:

$$\begin{aligned} H_{gr-ad}^{top} &= \sum_{m=-1}^{1} i^{|m|} \theta_{|m|} d_m^\dagger \Gamma_m + i\tau (d_1^\dagger s_z \Gamma_1 - d_{-1}^\dagger s_z \Gamma_{-1}) \\ &+ \sum_{m=0,1} i^m l_{so,m} (d_{m-1}^\dagger s_+ \Gamma_m + d_{-m+1}^\dagger s_- \Gamma_{-m}) \\ &+ L_{so} (d_{-1}^\dagger s_+ c_0 + d_1^\dagger s_- c_0) + \gamma d_0^\dagger c_0 + h.c. \end{aligned} \tag{4.5.13}$$

where θ_m, τ, $l_{so,m}$, L_{so} and γ are reals. We can now derive graphene-only Hamiltonians for adatoms in hollow- or top-position using equations 4.5.7 and 4.5.8. We write the $\hat{\mathcal{Z}}$-matrix, similar for both hollow- and top-position

adatoms, in a basis $\mathcal{B}_l$ of $2(2l+1)$ states $|m,s\rangle_{ad}$ arranged in ascending total angular momentum $J = m + s$ order:

$$\begin{aligned}\mathcal{B}_l = \{&|-l,\downarrow\rangle_{ad}, |-l,\uparrow\rangle_{ad}, |-l+1,\downarrow\rangle_{ad},\\ &|-l+1,\uparrow\rangle_{ad}, ..., |l,\downarrow\rangle_{ad}, |l,\uparrow\rangle_{ad}\}\end{aligned} \tag{4.5.14}$$

In basis $\mathcal{B}_l$, the $\hat{\mathcal{Z}}$-matrix is simply block-diagonal and reads:

$$\hat{\mathcal{Z}} = \begin{pmatrix} \hat{\mathcal{Z}}_{-l-\frac{1}{2}} & 0 & \cdots & 0 & 0 \\ 0 & \hat{\mathcal{Z}}_{-l+\frac{1}{2}} & \cdots & 0 & 0 \\ \vdots & \vdots & \ddots & \vdots & \vdots \\ 0 & 0 & \cdots & \hat{\mathcal{Z}}_{l-\frac{1}{2}} & 0 \\ 0 & 0 & \cdots & 0 & \epsilon_l + \lambda_{so}^l \end{pmatrix} \tag{4.5.15}$$

where $\hat{\mathcal{Z}}_{-l-\frac{1}{2}} = \hat{\mathcal{Z}}_{l+\frac{1}{2}} = \epsilon_l + \lambda_{so}^l$. If $|J| \neq l + \frac{1}{2}$, then $\hat{\mathcal{Z}}_J$ are 2×2 matrices acting on total-angular momentum J subspace:

$$\hat{\mathcal{Z}}_J = \begin{pmatrix} E_J^+ & \Delta_J \\ \Delta_J & E_J^- \end{pmatrix} \tag{4.5.16}$$

where $E_J^+ = \epsilon_{s_J(J-\frac{1}{2})} + s_J \lambda_{so}^{s_J(J-\frac{1}{2})}$, $E_J^- = \epsilon_{s_J(J+\frac{1}{2})} - s_J \lambda_{so}^{s_J(J+\frac{1}{2})}$, $\Delta_J = \Lambda_{so}^{|J|+\frac{1}{2}}$, $s_J = J/|J|$ and $\lambda_{so}^0 = 0$. Using basis $\mathcal{B}_\Omega$ of hexagonal states in ascending-J order:

$$\begin{aligned}\mathcal{B}_\Omega = \{&|-2,\downarrow\rangle_{\mathcal{N}}, |-2,\uparrow\rangle_{\mathcal{N}}, |-1,\downarrow\rangle_{\mathcal{N}},\\ &|-1,\uparrow\rangle_{\mathcal{N}}, ..., |2,\downarrow\rangle_{\mathcal{N}}, |2,\uparrow\rangle_{\mathcal{N}}\}\end{aligned} \tag{4.5.17}$$

the "hybridization" matrix $\hat{\mathcal{T}}$ for a hollow-position adatom is also a sparse matrix. Its only non-zero elements are in 2×2 and 1×2 blocks $\hat{\mathcal{T}}_J$ connecting

subspaces of hexagonal and adatom orbital states of same total angular momentum J. 2×2 $\hat{\mathcal{T}}_J$ blocks read:

$$\hat{\mathcal{T}}_J = i^{J-\frac{1}{2}} \begin{pmatrix} a_J u_{|J-\frac{1}{2}|} + \nu_{|J-\frac{1}{2}|} & iw_{J+\frac{1}{2}} \\ i^{-2J+1} w_{-J+\frac{1}{2}} & b_J u_{|J+\frac{1}{2}|} + i\nu_{|J+\frac{1}{2}|} \end{pmatrix} \tag{4.5.18}$$

where $a_J = i^{|J-\frac{1}{2}|-J+\frac{1}{2}}$ and $b_J = i^{|J+\frac{1}{2}|-J+\frac{1}{2}}$, while 1×2 blocks are appropriate sub-matrices of the 2×2 blocks shown in eq. 4.5.18. As a result, the $\hat{\mathcal{S}}$-matrix is block-diagonal and for instance, the f-orbital adatom graphene-only Hamiltonian reads:

$$\tilde{H}_{hollow} = \sum_{m=-l}^{l} (\Omega^\dagger_{m\uparrow}, \Omega^\dagger_{m+1\downarrow}) \hat{\mathcal{S}}_{m+\frac{1}{2}} \begin{pmatrix} \Omega_{m\uparrow} \\ \Omega_{m+1\downarrow} \end{pmatrix} \tag{4.5.19}$$

with

$$\hat{\mathcal{S}}_J = \hat{\mathcal{T}}_J^\dagger (E\mathbb{I} - \hat{\mathcal{Z}}_J)^{-1} \hat{\mathcal{T}}_J \tag{4.5.20}$$

Similar results are straightforwardly obtained for p- and d-orbital adatoms. The connection with the Hamiltonian of equation 4.2.2 is easily made, as:

$$\hat{\mathcal{S}}_{m+\frac{1}{2}} = \begin{pmatrix} \nu^+_m + \nu^-_m & i\Lambda_m \\ -i\Lambda_m & \nu^+_{m+1} - \nu^-_{m+1} \end{pmatrix} \tag{4.5.21}$$

We now write the "hybridization" matrix $\hat{\mathcal{T}}_{top}$ for top-position adatoms, using a basis $\mathcal{B}_{top}$ of states arranged in ascending J-order:

$$\begin{aligned} \mathcal{B}_{top} = \{&\Gamma^\dagger_{-1,\downarrow}|0\rangle, \Gamma^\dagger_{-1,\uparrow}|0\rangle, \Gamma^\dagger_{0,\downarrow}|0\rangle, c^\dagger_{0,\downarrow}|0\rangle, \\ &c^\dagger_{0,\uparrow}|0\rangle, \Gamma^\dagger_{0,\uparrow}|0\rangle, \Gamma^\dagger_{1,\downarrow}|0\rangle, \Gamma^\dagger_{1,\uparrow}|0\rangle\} \end{aligned} \tag{4.5.22}$$

Unlike $\mathcal{B}_\Omega$, $\mathcal{B}_{top}$ comprises 6 states of total angular momentum $\pm 1/2$ due to the presence of central states $c^\dagger_{0,\uparrow/\downarrow}|0\rangle$in addition to triangular states $\Gamma^\dagger_{0,\uparrow/\downarrow}|0\rangle$. Correspondingly, the only non-zero elements of $\hat{\mathcal{T}}_{top}$ are in blocks $\hat{\mathcal{T}}_{top,J}$ connecting states of total angular momentum J. Irrespective of the adatom's valence orbital - p, d, or f-, we have:

$$\hat{\mathcal{T}}_{top,-\frac{1}{2}} = \begin{pmatrix} i\theta_{-1} + i\tau & l_{so,0} & L_{so} \\ il_{so,1} & \theta_0 & \gamma \end{pmatrix} \tag{4.5.23}$$

$$\hat{\mathcal{T}}_{top,\frac{1}{2}} = \begin{pmatrix} \gamma & \theta_0 & il_{so,1} \\ L_{so} & l_{so,0} & i\theta_1 - i\tau \end{pmatrix} \tag{4.5.24}$$

Other blocks $\hat{\mathcal{T}}_{top,J}$ depend on the adatom's valence orbital, but are appropriate sub-arrays of:

$$\hat{\mathcal{T}}_{top,-\frac{3}{2}} = \begin{pmatrix} -il_{so,-1} \\ i\theta_1 + i\tau \end{pmatrix} \tag{4.5.25}$$

$$\hat{\mathcal{T}}_{top,\frac{3}{2}} = \begin{pmatrix} i\theta_1 + i\tau \\ -il_{so,-1} \end{pmatrix} \tag{4.5.26}$$

The $\hat{\mathcal{S}}$-matrix for top-position adatoms is block-diagonal,

$$\hat{\mathcal{S}}_{top} = \begin{pmatrix} \hat{\mathcal{S}}_{top,-\frac{3}{2}} & 0 & 0 & 0 \\ 0 & \hat{\mathcal{S}}_{top,-\frac{1}{2}} & 0 & 0 \\ 0 & 0 & \hat{\mathcal{S}}_{top,\frac{1}{2}} & 0 \\ 0 & 0 & 0 & \hat{\mathcal{S}}_{top,\frac{3}{2}} \end{pmatrix} \tag{4.5.27}$$

with $\hat{\mathcal{S}}_{top,J} = \hat{\mathcal{T}}^\dagger_{top,J}(E\mathbb{I} - \hat{\mathcal{Z}}_J)^{-1}\hat{\mathcal{T}}_{top,J}$ as in equation 4.5.20. The graphene-only

top-position Hamiltonian thus reads:

$$\begin{aligned}\tilde{H}_{top} &= \hat{\mathcal{S}}_{top,-\frac{3}{2}}\Gamma^{\dagger}_{-1,\downarrow}\Gamma_{-1,\downarrow} + \hat{\mathcal{S}}_{top,\frac{3}{2}}\Gamma^{\dagger}_{1,\uparrow}\Gamma_{1,\uparrow} \\ &+ (\Gamma^{\dagger}_{-1,\uparrow}, \Gamma^{\dagger}_{0,\downarrow}, c^{\dagger}_{0,\downarrow})\hat{\mathcal{S}}_{top,-\frac{1}{2}} \begin{pmatrix} \Gamma_{-1,\uparrow} \\ \Gamma_{0,\downarrow} \\ c_{0,\downarrow} \end{pmatrix} \\ &+ (c^{\dagger}_{0,\uparrow}, \Gamma^{\dagger}_{0,\uparrow}, \Gamma^{\dagger}_{1,\downarrow})\hat{\mathcal{S}}_{top,\frac{1}{2}} \begin{pmatrix} c_{0,\uparrow} \\ \Gamma_{0,\uparrow} \\ \Gamma_{1,\downarrow} \end{pmatrix} \end{aligned} \tag{4.5.28}$$

This is exactly the Hamiltonian of equation 4.2.9 with the following correspondence:

$$\hat{\mathcal{S}}_{top,-\frac{3}{2}} = \hat{\mathcal{S}}_{top,\frac{3}{2}} = \Lambda_+ + \Lambda_- \tag{4.5.29}$$

$$\hat{\mathcal{S}}_{top,-\frac{1}{2}} = \begin{pmatrix} \Lambda_+ - \Lambda_- & -i\tau & -i\mu \\ i\tau & V_1 & V_2 \\ i\mu & V_2 & V_0 \end{pmatrix} \tag{4.5.30}$$

$$\hat{\mathcal{S}}_{top,\frac{1}{2}} = \begin{pmatrix} V_0 & V_2 & i\mu \\ V_2 & V_1 & i\tau \\ -i\mu & -i\tau & \Lambda_+ - \Lambda_- \end{pmatrix} \tag{4.5.31}$$

Chapter 5

Conclusion

In this thesis, we presented our experimental and theoretical results showing that graphene properties can be considerably modified upon ultra-high doping or atom adsorption. By using a polymer-electrolyte technique, we demonstrated that graphene's density of states and electron-phonon coupling can be dramatically enhanced so that the temperature-dependence of its resistivity is deeply modified. Improving this technique to new levels could perhaps lead to the first observation of strictly two-dimensional intrinsic superconductivity in a crystal. At the time of writing, no research groups could achieve this result, despite numerous attempts, but the objective of observing intrinsic superconductivity in graphene at high charge carrier densities still looks attainable. In another series of experiments and theoretical development, we showed that graphene could be effectively transformed into a granular metal by heavy sp^3 hybridization. Originally a semi-metal, graphene could be transformed into a granular Dirac material whose conduction is mediated by sequences of virtual tunneling events, with characteristics specific to the Dirac nature of its grains. Though surprising at first, this result is a consequence of the well-known theory of neutrino billiards developed by Berry and Mondragon. From a technological viewpoint, the possibility of fabricating elastic granular materials such as granular graphene opens up the way to novel strain sensors. Finally,

we theoretically studied the possibility to engineer spin Hall effect and anomalous Hall effect in graphene by adding a small concentration of adatoms of various valence orbitals, s, p, d and f. We studied the impact of the adsorption position on the spintronic and electronic properties, and concluded that they affect significantly the transverse spin and charge currents generated by scattering of charge carriers with the adatoms. While hollow-position adatoms tend to induce gate-tunable spin Hall effect and no transverse charge currents, top-position adatoms favor the occurrence of anomalous Hall effects instead of spin Hall effects.

Bibliography

[1] Novoselov K. S., Geim A. K., Morozov S. V., Jiang D., Zhang Y., Dubonos S. V., Grigorieva I. V. and Firsov A. A.,Science **306**, 666 (2004).

[2] A.H. Castro Neto, F. Guinea, N.M.R. Peres, K.S. Novoselov, and A.K. Geim, Rev. Mod. Phys. **81**, 109 (2009).

[3] Young A. F. and Kim P. Nat. Phys. **5**, 222 (2009).

[4] Novoselov K. S., Geim A. K., Morozov S. V., Jiang D., Katsnelson M. I., Grigorieva I. V., Dubonos S. V. and Firsov A. A., Nature **438**, 197 (2005).

[5] Castro Neto A. H., Guinea F., Peres N. M. R., Novoselov K. S. and Geim A. K., Rev. Mod. Phys. **81**, 109 (2009).

[6] C. Lee, X. Wei, J.W. Kysar, and J. Hone, Science **321**, 385 (2008).

[7] A.K. Geim and I.V. Grigorieva, Nature **499**, 419 (2013).

[8] L.A. Ponomarenko, R.V. Gorbachev, G.L. Yu, D.C. Elias, R. Jalil, A.A. Patel, A. Mishchenko, A.S. Mayorov, C.R. Woods, J.R. Wallbank, M. Mucha-Kruczynski, B.A. Piot, M. Potemski, I.V. Grigorieva, K.S. Novoselov, F. Guinea, V.I. Fal'ko, and A.K. Geim, Nature **497**, 594 (2013).

[9] R.V. Gorbachev, A.K. Geim, M.I. Katsnelson, K.S. Novoselov, T. Tudorovskiy, I.V. Grigorieva, A.H. MacDonald, S.V. Morozov, K. Watanabe, T. Taniguchi, and L.A. Ponomarenko, Nat. Phys. **8**, 896 (2012).

[10] L. Britnell, R.M. Ribeiro, A. Eckmann, R. Jalil, B.D. Belle, A. Mishchenko, Y.-J. Kim, R.V. Gorbachev, T. Georgiou, S.V. Morozov, A.N. Grigorenko, A.K. Geim, C. Casiraghi A.H. Castro Neto, and K.S. Novoselov, Science **340**, 1311 (2013).

[11] L. Britnell, R.V. Gorbachev, R. Jalil, B.D. Belle, F. Schedin, A. Mishchenko, T. Georgiou, M.I. Katsnelson, L.Eaves, S.V. Morozov, N.M.R. Peres, J. Leist, A.K. Geim, K.S. Novoselov, and L.A. Ponomarenko, Science 335, 947 (2012).

[12] L. Britnell, R.V. Gorbachev, A.K. Geim, L.A. Ponomarenko, A. Mishchenko, M.T. Greenaway, T.M. Fromhold, K.S. Novoselov, and L. Eaves, Nat. Commun. **4**, 1794 (2013).

[13] T. Georgiou, R. Jalil, B.D. Belle, L. Britnell, R.V. Gorbachev, S.V. Morozov, Y-J. Kim, A. Gholinia, S.J. Haigh, O. Makarovsky, L. Eaves, L.A. Ponomarenko, A.K. Geim, K.S. Novoselov, and A. Mishchenko, Nat. Nanotechnol. **8**, 100 (2013).

[14] A.C. Ferrari, Nat. Nanotechnol. **8**, 235 (2013).

[15] A.C. Ferrari, Solid State Commun. **143**, 47 (2007).

[16] M. Huang, H. Yan, T.F. Heinz, and J. Hone, Nano Lett. **10**, 4074 (2010).

[17] A.C. Ferrari, J.C. Meyer, V. Scardaci, C. Casiraghi, M. Lazzeri, F. Mauri, S. Piscanec, D. Jiang, K.S. Novoselov, S. Roth, and A.K. Geim, Phys. Rev. Lett. **97**, 187401 (2006)

[18] F. Tuinstra and J.L. Koenig, J. Chem. Phys. **53**, 1126 (1970).

[19] K.S. Kim, Y. Zhao, H. Jang, S.Y. Lee, J.M. Kim, K.S. Kim, J-H. Ahn, P. Kim, J-Y. Choi, and B.H. Hong, Nature **457**, 706 (2009).

[20] P.R. Wallace, Phys. Rev. **71**, 622 (1947).

[21] Y. Barlas, R. Côté, J. Lambert, A.H. MacDonald, Phys. Rev. Lett. **104**, 096802 (2010).

[22] S. Das Sarma, S. Adam, E.H. Hwang, and Enrico Rossi, Rev. Mod. Phys. **83**, 407 (2011).

[23] E.H. Hwang and S. Das Sarma, Phys. Rev. B **77**, 115449 (2008).

[24] K. Kaasbjerg, K.S. Thygesen, and K.W. Jacobsen, Phys. Rev. B **85**, 165440 (2012).

[25] T. Stauber, N.M.R. Peres, and F. Guinea, Phys. Rev. B **76**, 205423 (2007).

[26] McChesney J. L., Bostwick A., Ohta T., Seyller T., Horn K., Gonzalez J. and Rotenberg E., Phys. Rev. Lett. **104**, 136803 (2010).

[27] Grüneis A., Attacalite C., Wintz L., Shiozawa H., Saito R., Pichler T. and Rubio A., Phys. Rev. B **78**, 205425 (2008).

[28] Abrikosov A. A., Campuzano J. C. and Gofron K., Physica C **214**, 73 (1993).

[29] Blake P., Hill E. W., Castro Neto A. H., Novoselov K. S., Jiang D., Yang R., Booth T. J. and Geim A.K., Appl. Phys. Lett. **91**, 063124 (2007).

[30] Kim S. N., Junghyo Jo I., Shahrjerdi D., Colombo L., Yao Z., Tutuc E. and Banerjee S. K., Appl. Phys. Lett. **94**, 062107 (2009).

[31] Das A., Pisana S., Chakraborty B., Piscanec S., Saha S. K., Waghmare U. V., Novoselov K. S., Krishnamurthy H. R., Geim A. K. Ferrari A. C. and Sood A. K., Nat. Nanotech. **3**, 210 (2008).

[32] Yan J., Villarson T., Henriksen T. A., Kim P. and Pinczuk A. Phys. Rev. B **80**, 241417 (2009).

[33] Ozel T., Gaur A., Rogers J. A. and Shim M., Nanolett. **5**, 205 (2005).

[34] Ueno K., Nakamura S., Shimotani H., Ohtono A., Kimura N., Nojima T., Aoki H., Iwasa Y. and Kawasaki M., Nat. Mater. **7**, 855 (2008).

[35] Konar A., Fang T. and Jena D., arXiv:0902.0819v1.

[36] Stauber T., Peres N. M. R. and Guinea F., Phys. Rev. B **76**, 205423 (2007).

[37] Chen J. H., Jan C., Xiao S., Ishigami M. and Fuhrer M. S., Nat. Nanotech. **3**, 206 (2008).

[38] Adam S., Hwang E. H., Galitski V. M. and Sarma S. D., PNAS **104**, 18392 (2007).

[39] Kilic M. S., Bazant M. Z. and Ajdari A., Phys. Rev. E **75**, 021501 (2007).

[40] Sarma S. D., Adam S., Hwang E. H. and Rossi E., arXiv:1003.4731v1.

[41] Morozov S. V., Novoselov K. S., Katsnelson M. I., Schedin F., Elias D. C., Jaszczak J. A. and Geim A. K., Phys. Rev. Lett. **100**, 016602 (2008).

[42] Li G., Luican A. and Andrei E. Y., Phys. Rev. Lett. **102**, 176804 (2009).

[43] Tse W. -K. and Sarma S. D., arXiv:0707.3651v2.

[44] Pereira V. M., Lopes dos Santos J. M. B. and Castro Neto A. H., Phys. Rev. B **77**, 115109 (2008).

[45] Hu B. Y. -K., Hwang E. H. and Sarma S. D., Phys. Rev. B **78**, 165411 (2008).

[46] Barlas Y., Pereg-Barnea T., Polini M., Asgari R. and McDonald A. H., Phys. Rev. Lett. **98**, 236601 (2007).

[47] Calandra. M, and Mauri F., Phys. Rev. B **76**, 205411 (2007).

[48] Mahan G. D.,Many-particle Physics,Kluwer Academic/Plenum Publishers, New York (2000).

[49] Attacalite C. and Rubio A., Phys. Stat. Solidi B **246**, 2523 (2009).

[50] N.W. Ashcroft and N.D. Mermin, Solid State Physics (Cengage Learning, 1976).

[51] B. Abeles, Ping Sheng, M. Coutts, and Y. Arie, Adv. in Phys. **24**, 407 (1975).

[52] I. Beloborodov, A. Lopatin, V. Vinokur, and K. Efetov, Rev. Mod. Phys. **79**, 469 (2007).

[53] A. Gerber, A. Milner, G. Deutscher, M. Karpovsky, and A. Gladkikh, Phys. Rev. Lett **78**, 4277 (1997).

[54] C. Collier, T. Vossmeyer, and J. Heath, Annu. Rev. Phys. Chem. **49**, 371 (1998).

[55] C. Murray, C. Kagan, and M. Bawendi, Annu. Rev. Mater. Sci. **30**, 545 (2000).

[56] X. Lin, H.M. Jaeger, C. Sorensen, and K. Klabunde, J. Phys. Chem. B **105**, 3353 (2001).

[57] C. Gomez-Navarro, R.T. Weitz, A.M. Bittner, M. Scolari, A. Mews, M. Burghar, and K. Kern, Nano Lett. **7**, 3499 (2007).

[58] C. Gomez-Navarro, J.C. Meyer, R.S. Sundaram, A. Chuvilin, S. Kurasch, M. Burghard, K. Kern, and U. Kaiser, Nano Lett. **10**, 1144 (2010).

[59] A.I. Yakimov, A.V. Dvurechenskii, V.V. Kirienko, Y.I. Yakovlev, A.I. Nikiforov, and C.J. Adkins, Phys. Rev. B 61, 10868 (2000).

[60] A.L. Efros and B.I. Shklovskii, J. Phys. C: Solid State Phys. **8**, L49 (1975).

[61] J. Zhang and B.I. Shklovskii, Phys. Rev. B **70**, 115317 (2004).

[62] I.L. Aleiner, and L.I. Glazman, Mesoscopic Fluctuations of Elastic Cotunneling, Phys. Rev. Lett. 77, 2057 (1996).

[63] M.V. Berry, and R.J. Mondragon, Neutrino Billiards: Time-Reversal Symmetry-Breaking Without Magnetic Fields, Proc. R. Soc. A **412**, 53 (1987).

[64] D. Averin, and Yu. N. Nazarov, Phys. Rev. Lett. **65**, 2446 (1990).

[65] I.L. Aleiner, P.W. Brouwer, and L.I. Glazman, Phys. Rep. **358**, 309 (2002).

[66] M.H. Devoret, D. Esteve, H. Grabert, G.-L. Ingold, H. Pothier, and C. Urbina, Phys. Rev. Lett. **64**, 1824 (1990).

[67] G.-L. Ingold, and H. Grabert, Europhys. Lett.**14**, 371 (1991).

[68] N.M. Chtchelkatchev, V.M. Vinokur, and T.I. Baturina, Phys. Rev. Lett. **103**, 247003 (2009).

[69] N.F. Mott, Philos. Mag. **19**, 835 (1969).

[70] A. Miller, and E. Abrahams, Phys. Rev. **120**, 745 (1960).

[71] W. Regan, N. Alem, B. Aleman, B. Geng, C. Girit, L. Maserati, F. Wang, M. Crommie, and A. Zettl, Appl. Phys. Lett. **96**, 113102 (2010).

[72] J. Moser, H. Tao, S. Roche, F. Alzina, C.M. Sotomayor Torres, and A. Bachtold, Phys. Rev. B **81**, 205445 (2010).

[73] M. E. Peskin and D.V. Schroeder. An Introduction to Quantum Field Theory. (Addison-Wesley Publishing Company, Reading, 1995).

[74] M.O. Scully and M.S. Zubairy, Quantum Optics. (Cambridge University Press, Cambridge, 1997).

[75] A.W. Rodriguez, F. Capasso and S.G. Johnson, Nature Photon. **5**, 211-221 (2011).

[76] S.W. Hawking, Nature **248**, 30-31 (1974).

[77] C.M. Wilson et al., Nature **479**, 376-379 (2011).

[78] D. Averin, and Y. Nazarov, Phys. Rev. Lett. **65**, 2446-2449 (1990).

[79] T. Fujisawa, Science **282**, 932-935 (1998).

[80] S. De Franceschi et al., Phys. Rev. Lett. **86**, 878-881 (2001).

[81] S. Gustavsson et al., Phys. Rev. B **78**, 155309 (2008).

[82] I. Beloborodov, A. Lopatin, V. Vinokur, and K. Efetov, Rev. Mod. Phys. **79**, 469-518 (2007).

[83] M.V. Feigel'man and A.S. Ioselevich, JETP Lett. **81**, 341-347 (2005).

[84] I. Beloborodov, A. Lopatin, and V. Vinokur, Phys. Rev. B **72**, 125121 (2005).

[85] M.I. Katsnelson, EPJ B **51**, 157-160 (2006).

[86] M.V. Berry, and R.J. Mondragon, Proc. R. Soc. A **412**, 53-74 (1987).

[87] J. Balakrishnan, G.K.W. Koon, M. Jaiswal, A.H. Castro Neto, and B. Özyilmaz, Nat. Phys. **9**, 284-287 (2013).

[88] D. Joung, L. Zhai, S.I. Khondaker, Phys. Rev. B **83**, 115323 (2011).

[89] S. Bae et al., Nature Nanotech. **5**, 574-578 (2010).

[90] D.C. Elias et al., Science **323**, 610-613 (2009).

[91] M. Jaiswal et al., ACS Nano **5**, 888-896 (2011).

[92] B.R. Matis et al., ACS Nano **6**, 17-22 (2012).

[93] S. Marianer and B. Shklovskii, Physical Review B **46**, 13100-13103 (1992).

[94] R.R. Nair et al., Small **6**, 2877-2884 (2010).

[95] A.C. Ferrari, Solid State Commun. **143**, 47-57 (2007).

[96] M.M. Lucchese et al., Carbon **48**, 1592-1597 (2010).

[97] E.H. Martins Ferreira et al., Phys. Rev. B **82**, 125429 (2010).

[98] S. Ryu, J. Maultzsch, M. Han, P. Kim and L.E. Brus, ACS Nano **5**, 4123-4130 (2011).

[99] A. Eckmann et al., Nano Lett. **12**, 3925-3930 (2012).

[100] R. Saito, M. Hofmann, G. Dresselhaus, A. Jorio, and M.S. Dresselhaus, Adv. Phys. **60**, 413-550 (2011).

[101] T.G. Rappoport, B. Uchoa, and A.H. Castro Neto, Phys. Rev. B **80**, 245408 (2009).

[102] S. Kim et al., Appl. Phys. Lett. **102**, 053108 (2013).

[103] C. Casiraghi et al., Nano Lett. **9**, 1433-1441 (2009).

[104] B.I. Shklovskii and A.L. Efros, Electronic Properties of Doped Semiconductors. (Springer-Verlag, Berlin, New York, 1984).

[105] G. Liu, and H. Soonpaa, Phys. Rev. B **48**, 5682-5684 (1993).

[106] T. Tran et al., Phys. Rev. B **78**, 075437 (2008).

[107] T. Tran, et al., Phys. Rev. Lett. **95**, 076806 (2005).

[108] J.T. Edwards, and D.J. Thouless, J. Phys. C: Solid State Phys. **5**, 807-820 (1972).

[109] L.A. Ponomarenko et al., Science **320**, 356-358 (2008).

[110] I.L. Aleiner and L.I. Glazman, Phys. Rev. Lett. **77**, 2057-2060 (1996).

[111] F. Milliken and Z. Ovadyahu, Phys. Rev. Lett. **65**, 911-914 (1990).

[112] S.M. Cronenwett, S.R. Patel, C.M. Marcus, K. Campman and A.C. Gossard, Phys. Rev. Lett. **79**, 2312-2315 (1997).

[113] M. Raikh, and I. Ruzin, Phys. Rev. B **42**, 11203-11207 (1990).

[114] Y. Strelniker, S. Havlin, R. Berkovits, and A. Frydman, Phys. Rev. E **72**, 016121 (2005).

[115] I. Beloborodov, A. Lopatin, and V. Vinokur, Phys. Rev. B **70**, 205120 (2004).

[116] V.L. Nguyen, B.Z. Spivak, and B.I. Shklovskii, JETP Lett. **43**, 44-47 (1986).

[117] H.L. Zhao, B.Z. Spivak, M.P. Gelfand, and S. Feng, Phys. Rev. B **44**, 10760-10767 (1991).

[118] Y. Strelniker, R. Berkovits, A. Frydman, and S. Havlin, Phys. Rev. E **69**, 065105 (2004).

[119] A. Somoza, M. Ortuño, and J. Prior, Phys. Rev. Lett. **99**, 116602 (2007).

[120] J. Prior, A. Somoza, and M. Ortuño, Phys. Rev. B **72**, 024206 (2005).

[121] D.H. Choe and K.J. Chang, Nano Lett. **12**, 5175-5180 (2012).

[122] A.L. Rakhmanov, A.V. Rozhkov, A.O. Sboychakov, and F. Nori, Phys. Rev. B **85**, 035408 (2012).

[123] G. Savini, A.C. Ferrari, and F. Giustino, Phys. Rev. Lett. **105**, 037002 (2010).

[124] A. Allain, Z. Han, and V. Bouchiat, Nature Mater. **11**, 590-594 (2012).

[125] A.A. Clerk, M.H. Devoret, S.M. Girvin, F. Marquardt, and R.J. Schoelkopf, Rev. Mod. Phys. **82**, 1155-1208 (2010).

[126] B. Cleve, B. Hartenstein, S.D. Baranovskii, M. Scheidler, P. Thomas, and H. Baessler, Phys. Rev. B **51**, 16705 (1995).

[127] F. Jansson, S.D. Baranovskii, F. Gebhard, and R. Österbacka, Phys. Rev. B **77**, 195211 (2008).

[128] S.D. Baranovskii, B. Cleve, R. Hess, and P. Thomas, J. Non-Cryst. Solids **164-166**, 437 (1993).

[129] D.G. Polyakov, and B.I. Shklovskii, Phys. Rev. Lett. **70**, 3796 (1993).

[130] M.Y. Han, J.C. Brant, and P. Kim, Phys. Rev. Lett **104**, 056801 (2010).

[131] K. S. Novoselov, A. K. Geim, S. V. Morozov, D. Jiang, Y. Zhang, S. V. Dubonos, I. V. Grigorieva, and A. A. Firsov, Science **306**, 666 (2004).

[132] D. Huertas-Hernando, F. Guinea, and A. Brataas, Phys. Rev. B **74**, 155426 (2006).

[133] N. Tombros, C. Jozsa, M. Popinciuc, H.T. Jonkman, and B.J. van Wees, Nature **448**, 571 (2007).

[134] N. Tombros, S. Tanabe, A. Veligura, C. Jozsa, M. Popinciuc, H.T. Jonkman, and B.J. van Wees, Phys. Rev. Lett **101**, 046601 (2008).

[135] T.-Y. Yang, J. Balakrishnan, F. Volmer, A. Avsar, M. Jaiswal, J. Samm, S.R. Ali, A. Pachoud, M. Zeng, M. Popinciuc, G. Güntherodt, B. Beschoten, and B. Özyilmaz, Phys. Rev. Lett **107**, 047206 (2011).

[136] B. Dlubak, M-B. Martin, C. Deranlot, B. Servet, S. Xavier, R. Mattana, M. Sprinkle, C. Berger, W.A. De Heer, F. Petroff, A. Anane, P. Seneor, and A. Fert, Nat. Phys. **8**, 557 (2012).

[137] M. Wimmer, A.R. Akhmerov, and F. Guinea, Robustness of edge states in graphene quantum dots, Phys. Rev. B **82**, 045409 (2010).

[138] J.P. Hobson and W.A. Nierenberg, Phys. Rev. **89**, 662 (1953).

[139] N.M.R. Peres, F. Guinea, and A.H. Castro Neto, Phys. Rev. B **73**, 125411 (2006).

[140] T. Ando, J. Phys. Soc. Jpn. **75**, 074716 (2006).

[141] K.S. Novoselov, A. K. Geim, S. V. Morozov, D. Jiang, M. I. Katsnelson, I. V. Grigorieva, S. V. Dubonos, and A. A. Firsov, 2005, Nature **438**, 197.

[142] A. Pachoud, M. Jaiswal, P.K. Ang, K.P. Loh, and B. Özyilmaz, Europhys. Lett. **92**, 27001 (2010).

[143] D.K. Efetov and P. Kim, Phys. Rev. Lett. **105**, 256805 (2010).

[144] R.R. Nair, W. Ren, R. Jalil, I. Riaz, V.G. Kravets, L. Britnell, P. Blake, F. Schedin, A.S. Mayorov, S. Yuan, M.I. Katsnelson, H-M. Cheng, W. Strupinski, L.G. Bulusheva, A.V. Okotrub, I.V. Grigorieva, A.N. Grigorenko, K.S. Novoselov, and A.K. Geim, Small **6**, 2877 (2010).

[145] A. Pachoud, M. Jaiswal, Y. Wang, B-H. Hong, J-H. Ahn, K.P. Loh, and B. Özyilmaz, Sci. Rep. **3**, 3404 (2013).

[146] R.R. Nair, M. Sepioni, I-L. Tsai, O. Lehtinen, J. Keinonen, A.V. Krasheninnikov, T.Thomson, A.K. Geim, and I.V. Grigorieva, Nat. Phys. **8**, 199 (2012).

[147] R.R. Nair, I-L. Tsai, M. Sepioni, O. Lehtinen, J. Keinonen, A.V. Krasheninnikov, A.H. Castro Neto, M.I. Katsnelson, A.K. Geim, and I.V. Grigorieva, Nat. Commun. **4**, 2010 (2013).

[148] B. Uchoa, V.N. Kotov, N.M.R. Peres, and A.H. Castro Neto, Phys. Rev. Lett. **101**, 026805 (2008).

[149] A.H. Castro Neto and F. Guinea, Phys. Rev. Lett. **103**, 026804 (2009).

[150] M. Jaiswal, C. Haley Yi Xuan Lim, Q. Bao, C.T. Toh, K.P. Loh, and B. Özyilmaz, ACS Nano **5**, 888 (2011).

[151] Z.H.Ni, L.A. Ponomarenko, R.R. Nair, R. Yang, S. Anissimova, I.V. Grigorieva, F. Schedin, P. Blake, Z.X. Shen, E.H. Hill, K.S. Novoselov, and A.K. Geim, Nano Lett. **10**, 3868 (2010).

[152] J-H. Chen, W.G. Cullen, C. Jang, M.S. Fuhrer, and E.D. Williams, Phys. Rev. Lett. 102, 236805 (2009).

[153] D. Marchenko, A. Varykhalov, M. R. Scholz, G. Bihlmayer, E. I. Rashba, A. Rybkin, A. M. Shikin & O. Rader. Nature Comm. **3**, 1232 (2012).

[154] C. Weeks, J. Hu, J. Alicea, M. Franz, and R. Wu, Phys. Rev. X **1**, 021001 (2011).

[155] R.A. Horn and C.R. Johnson, *Topics in matrix analysis*, Cambridge University Press (1991).

[156] A. Ferreira, J. Viana-Gomes, J. Nilsson, E. R. Mucciolo, N. M. R. Peres, and A. H. Castro Neto, Phys. Rev. B **83**, 165402 (2011).

[157] G.W. Semenoff, Phys. Rev. Lett. **53**, 2449 (1984).

[158] C.L. Kane and E.J. Mele, Phys. Rev. Lett. **95**, 226801 (2005).

[159] Y. A. Bychkov and E. I. Rashba, J. Phys. C **17**, 6039 (1984).

[160] E. McCann and V.I. Fal'ko, Phys. Rev. Lett. **108**, 166606 (2012).

[161] T. Ando, T. Nakanishi, and M. Igami, J. Phys. Soc. Jpn. **68**, 3994 (1999).

[162] C. Bena and S.A. Kivelson, Phys. Rev. B **72**, 125432 (2005).

[163] B.A. Lippmann and J. Schwinger, Phys. Rev. **79**, 469 (1950).

[164] P.O. Löwdin, J. Chem. Phys **19**, 1396 (1951).

[165] M. I. Dyakonov, and V. I. Perel, JETP Lett. **13**, 467 (1971).

[166] J. E. Hirsch, Phys. Rev. Lett. **83**, 1834 (1999).

[167] S. Zhang, Phys. Rev. Lett. **85**, 393 (2000).

[168] T. Jungwirth, J. Wunderlich, and K. Olejnik, Nature Mat. **11**, 382 (2012).

[169] J. Martin, N. Akerman, G. Ulbricht, T. Lohmann, J.H. Smet, K. von Klitzing, and A. Yacoby, Nat. Phys. **4**, 144 (2008).

[170] J. Xue, J. Sanchez-Yamagishi, D. Bulmash, P. Jacquod, A. Deshpande, K. Watanabe, T. Taniguchi, P. Jarillo-Herrero and B.J. LeRoy, Nature Mater. **10**, 282 (2011).

[171] J. Balakrishnan, G. Kok Wai Koon, M. Jaiswal, A.H. Castro Neto, and B. Özyilmaz, Nat. Phys. **9**, 284 (2013).

[172] D.A. Abanin, S.V. Morozov, L.A. Ponomarenko, R.V. Gorbachev, A.S. Mayorov, M.I. Katsnelson, K. Watanabe, T. Taniguchi, K.S. Novoselov, L.S. Levitov, and A.K. Geim, Science **332**, 328 (2011).

[173] D.A. Abanin, R.V. Gorbachev, K.S. Novoselov, A.K. Geim, and L.S. Levitov, Phys. Rev. Lett. **107**, 096601 (2011).

[174] B. Gu, I. Sugai, T. Ziman, G.Y. Guo, N. Nagaosa, T. Seki, K. Takanashi, and S. Maekawa, Phys. Rev. Lett. **105**, 216401 (2010).

[175] C. Brüne, A. Roth, E.G. Novik, M. König, H. Buhmann, E.M. Hankiewicz, W. Hanke, J. Sinova, and L. Molenkamp, Nat. Phys. **6**, 448 (2010).

[176] N. Nagaosa, J. Sinova, S. Onoda, A.H. MacDonald, and N.P. Ong, Rev. Mod. Phys. **82**, 1539 (2010).

[177] D.A. Abanin, A.V. Shytov, and L.S. Levitov, Phys. Rev. Lett. **105**, 086802 (2010).

[178] V.V. Cheianov, O. Syljuasen, B.L. Altshuler, and V. Fal'ko, Phys. Rev. B **80**, 233409 (2009).

[179] V.V. Cheianov, O. Syljuasen, B.L. Altshuler, and V.I. Fal'ko, Europhys. Lett. **89**, 56003 (2010).

[180] S. Kopylov, V. Cheianov, B.L. Altshuler, and V.I. Fal'ko, Phys. Rev. B **83**, 201401 (2011).